SELECTED GROWTH AND INTERACTION CHARACTERISTICS OF SEAFLOOR FAULTS IN THE CENTRAL MISSISSIPPI CANYON OFFSHORE CONTINENTAL SHELF (OCS) AREA, NORTHERN GULF OF MEXICO

A Thesis

by

SCOTT ASHLEY WEGNER

Submitted to the Office of Graduate Studies of
Texas A&M University
in partial fulfillment of the requirements for the degree of

MASTER OF SCIENCE

May 2006

Major Subject: Geology

SELECTED GROWTH AND INTERACTION CHARACTERISTICS OF SEAFLOOR FAULTS IN THE CENTRAL MISSISSIPPI CANYON OFFSHORE CONTINENTAL SHELF (OCS) AREA, NORTHERN GULF OF MEXICO

A Thesis

by

SCOTT ASHLEY WEGNER

Submitted to the Office of Graduate Studies of
Texas A&M University
in partial fulfillment of the requirements for the degree of

MASTER OF SCIENCE

Approved by:

Chair of Committee,	Christopher C. Mathewson
Committee Members,	John H. Spang
	Jean-Louis Briaud
	Kerry J. Campbell
Head of Department,	Richard Carlson

May 2006

Major Subject: Geology

ABSTRACT

Selected Growth and Interaction Characteristics of Seafloor Faults
in the Central Mississippi Canyon Offshore Continental Shelf (OCS) Area,
Northern Gulf of Mexico. (May 2006)
Scott Ashley Wegner, B.S., Texas A&M University
Chair of Advisory Committee: Dr. Christopher Mathewson

The characteristics of some shallow faults in the Gulf of Mexico interpreted to be active are poorly understood. A better understanding of these faults will increase our understanding of formerly and presently active geologic processes in the Gulf. Specifically, the characteristics of growth, interaction, and linkage of faults are of interest. Most of the Gulf has seen continuous clastic sediment deposition since the end of continental rifting in the middle Mesozoic. The Gulf is a tectonically quiescent basin, with the only major structural processes being salt diapirism and subsidence. Numerous styles of faulting have been observed in the Gulf, with each style being related to a specific type of deformation. Numerous authors have concluded that fault growth processes generally involve tipline propagation and linkage of faults. Evidence of these processes has been observed in seismic data sets. This investigation uses a HR 3-D seismic data set to characterize growth, interaction, and linkage of a fault set in the northern Gulf of Mexico. This work shows that linked and interacting faults are present in the study area. These conclusions were reached using measurements of throw on horizons offset by several faults and interpreting the throw data using a model of fault growth and interaction based on separate processes of growth by tipline propagation and growth by linkage of smaller faults. The ratio of these parameters for a fault population can be described by a power law relationship. For the fault set considered here, the power law was found to be valid.

DEDICATION

"The mind is not a vessel to be filled, but a fire to be lighted."
- Col. David R. Scott, Commander, Apollo 15

This thesis document is a record of the hard work put forth by the student. In addition, and more importantly, this thesis represents the efforts of numerous individuals who will receive no academic degree for their hard work. I would like to dedicate this work to my family. My mother, La Verna A. Wegner, my father, John L. Wegner, and my sister, Amy D. Wegner, all deserve my deepest appreciation for the love they have shown me not only with regard to this academic project, but with all aspects of my life. I consider myself enviably lucky to have them.

I would also like to dedicate this work to my own personal set of heroes, America's pioneering astronauts selected in the first four groups from 1959 to 1965. These men displayed faith, intellect, sheer bravery, and a competitive sense of camaraderie that transformed America's dreams of a space-faring society into a reality. I have had the high honor of meeting three of their number, one of which is no longer living at the time of this writing. These men gave of themselves for a purpose in which they believed completely. I looked to these men and told myself, "If they can do great things, then so can I."

ACKNOWLEDGEMENTS

My appreciation to my family cannot be overstated. It is the greatest wish of my parents that I reach my goals in life, and that I live a positive life. In achieving this milestone, I hope that I am fulfilling their desire. For all that my parents and my sister have done for me, I cannot properly state my thanks in mere words. I would also like to express my thanks to my academic advisor, Dr. Christopher Mathewson, who is a very dynamic and gifted individual. He is, in my opinion, one of the most valuable educators at Texas A&M University. I witnessed him teach countless engineering students how to appreciate and accommodate geology, and in this, he clearly demonstrates his commitment to his profession and to the education of the next generation of engineering and geologic professionals.

My appreciation is also extended to Drs. John Spang and Jean-Louis Briaud, both members of my academic committee. Mr. Kerry J. Campbell of Fugro, also a member of my academic committee, provided the research idea, guidance, and much motivation. Fugro GeoServices, Inc. provided data storage space, a seismic workstation for my use, and other support. Shell, BP, ExxonMobil, and ConocoPhillips graciously allowed me to use their Princess high-resolution 3-D seismic data set for this research. Their important contribution to this research is greatly appreciated. My thanks also goes to Dr. Peter Trabant, who has enthusiastically provided me much useful help and guidance.

TABLE OF CONTENTS

Page

LIST OF FIGURES

Figure Page

Figure Page

INTRODUCTION

Numerous geological conditions are regarded as potentially hazardous for seafloor and shallow subsurface engineering projects in the marine environment. These conditions are collectively termed *geohazards*. Bryant and Roemer (1983) and Campbell (1997a, 1997b, and 1999) supply several examples of geohazards, including unstable slopes and submarine mass movements, active and inactive channels, irregular seafloor topography, gas hydrates at the seafloor and within sediments, overpressured water-flow sands at shallow depths (shallow-water-flow), erosion and deposition of sediments by bottom currents, weak or laterally variable shallow soils, salt diapirism, and active faults that may or may not breach the seafloor. These geohazards receive varying degrees of attention from geologists and engineers who specialize in the mitigation or avoidance of such hazardous conditions. The Gulf of Mexico has been described by Campbell (1999) as one of the more challenging and complex oil and gas provinces in the world, with respect to geological conditions of potential affect to drilling and engineering projects. This challenging geologic environment is largely the result of salt diapirism and the unique structures and strata resulting from the lateral and vertical movements of salt in the subsurface. All of these conditions are present at some location on the continental shelf and continental slope of the Gulf.

Unstable slopes and the potential for mass movements have received much attention from hazards specialists, and can be reliably predicted through engineering analysis of slope conditions and by examining the proposed development area for evidence of recent mass movements. Gas hydrates, soil erosion or deposition related to bottom currents, mechanical characteristics of the soil and soft sediments, and shallow-water-flow have similarly received much attention. These conditions are either easily detectable with the proper geophysical and geotechnical tools, or they are easily predicted by incorporating experiences from previous work

---

This thesis follows the style and format of The American Association of Petroleum Geologists Bulletin.

done at nearby locations. Inactive channels are commonly buried by younger deposits, and present difficulties in that they represent lateral soil variations (i.e., a channel incises a sandy soil and is later infilled with clay). Active channels experience episodic failure of their banks, and the main hazard here is the proximity of the structure or development to such a failure.

The level of activity of faults breaching the seafloor (seafloor faults) cannot be determined directly from geophysical or geotechnical data and cannot generally be inferred to be the same from one location to another. Programs to instrument faults for the purpose of obtaining direct data on movement of potentially active faults are not known to have been performed in the Gulf of Mexico. For some structures that must be placed in the vicinity of faults, a study is done of the expected displacement of the fault within the design life of the structure (Fenton et al., 2002, K. J. Campbell, 2004, personal communication). The preferred method for dealing with potentially active seafloor faults is avoidance—placing the seafloor facility, structure foundation, pilings, or pipeline in such a way that the potential for damage to the infrastructure is well within design limits for the design lifetime. The engineer will often go a further step and recommend that the infrastructure be sited far enough away such that the risk of damage resulting from fault movement is zero. Thus, because the needs of industry often push research in marine geology, the issue of active faulting as it relates to engineering projects has not received much attention and is not well understood in this context. Even on land in areas with known faulting and associated problems (i.e., earthquakes) such as southern California, only recently has work been done to characterize several blind thrust fault systems that produced damaging earthquakes in Los Angeles and its suburbs. Blind thrust faults related to the 1987 West Los Angeles and 1994 Northridge earthquakes were unstudied until they had caused severe damage and deaths (Pratt et al., 1998, Pratt et al., 2002).

A better understanding of active faulting in the deep marine environment of the northern Gulf of Mexico continental slope is necessary as more oil and gas exploration and associated engineering works are planned for this area. For long-lived projects, faulting can damage foundations, bend or sever well casings, reduce the capacities of tension pilings and other

moorings, and cause pipelines to fail where they span seafloor fault scarps. Such failures or difficulties would add to project costs, reduce the economic return from the project, and introduce delays.

Problem and Hypothesis

The problems that active faulting in the marine environment can cause for engineering projects are symptomatic of the relatively poor understanding of these faults. From a purely scientific viewpoint, it is desirable to understand how the faults within a set of active faults grow and interact, whether the faults conform to models of fault growth and interaction, and whether or not these determinations can be made using a procedure of throw mapping along the strikes of faults mapped within a high-resolution 3-D seismic data set. The hypothesis of this work is that high-resolution 3-D seismic data can be used to confirm that study area faults do grow and interact in accordance with a generally-accepted model.

Objectives

The main objective of this study is to describe the displacement and growth characteristics of seafloor-offsetting faults within a study area located on the northern Gulf of Mexico continental slope. Displacement characteristics investigated here include the type of fault movement, distribution of slip along fault strike and in the down-dip direction, and fault geometry. Growth characteristics include the degree to which faults are linked and the degree to which faults interact to restrict or enhance the other's growth. Characterizations of the relationships that exist between interacting and linked faults follow from this. These main study objectives are facilitated by the following secondary objectives:

1. Evaluation of a high-resolution 3-D seismic data set acquired at a deepwater location on the northern Gulf of Mexico continental slope where seafloor fault scarps are known to exist. The data are to be evaluated for their applicability to this study, and for the basic geophysical characteristics of the data set. These characteristics affect interpretations made using the data set.

2. Interpretation of the high-resolution 3-D seismic data to produce a set of mapped stratigraphic horizons and a set of mapped faults. Accurately mapped horizons and faults are necessary for accurate determinations of fault movement characteristics.
3. Measurements of fault throw made at regular intervals along the faults in vertical seismic sections oriented parallel to fault dip.
4. Analysis of the measurement data to yield numerical results describing the along-strike and down-dip variations in fault offset for individual faults and for the entire set of faults studied.
5. Comparison of the results with expected results and results yielded from similar studies done by other investigators.

GEOLOGICAL SETTING

Physiography of the Northern Gulf of Mexico

The Gulf of Mexico is a tectonically stable, small ocean basin characterized by a complex sedimentary and structural history. This basin opened during a Triassic-Jurassic rifting event associated with the opening of the Atlantic Ocean, and records a complex history of sedimentation, subsidence, and structural change brought about by mobile Jurassic-age salt. Several modern physiographic provinces can be identified in the Gulf, with each province drawing its unique characteristics from past geological processes and those that occur in the present. Uchupi (1975) divides the Gulf of Mexico into two fundamental units on the basis of dominant sedimentation processes and structures. Bryant et al. (1991) provides a detailed description of the recognized subdivisions of these two units. The terrigenous province is characterized by dominantly siliciclastic sedimentation derived from the interior of North America, and covers the larger, western portion of the Gulf. The carbonate province is characterized by dominantly organic *in situ* production of carbonate sediments in the form of platforms and fringing reefs (Figure 1).

Terrigenous Province. The terrigenous province can be further subdivided. The Mexico, Texas-Louisiana, and Mississippi-Alabama Shelves stretch from the southwestern Gulf to the Florida panhandle, and constitute an essentially flat, shallow continental shelf that varies from about 8 miles to 105 miles in width. At a water depth of about 600 feet, the continental shelf gives way to the continental slope. The Texas-Louisiana Slope and Campeche Knolls are both characterized by “hummocky” seafloor, as described by Bryant et al. (1991). This seafloor topography consists of numerous uplifts and intervening fault-bounded basins caused by salt diapirs. The seafloor of the East Mexico Slope is characterized by structurally-controlled and regularly-spaced ridges paralleling the shoreline, thought to be the topographic expression of massive submarine gravity slides (Bryant et al., 1991). The Rio Grande Slope shows characteristics of both the Texas-Louisiana and East Mexico Slopes, and the Veracruz Tongue

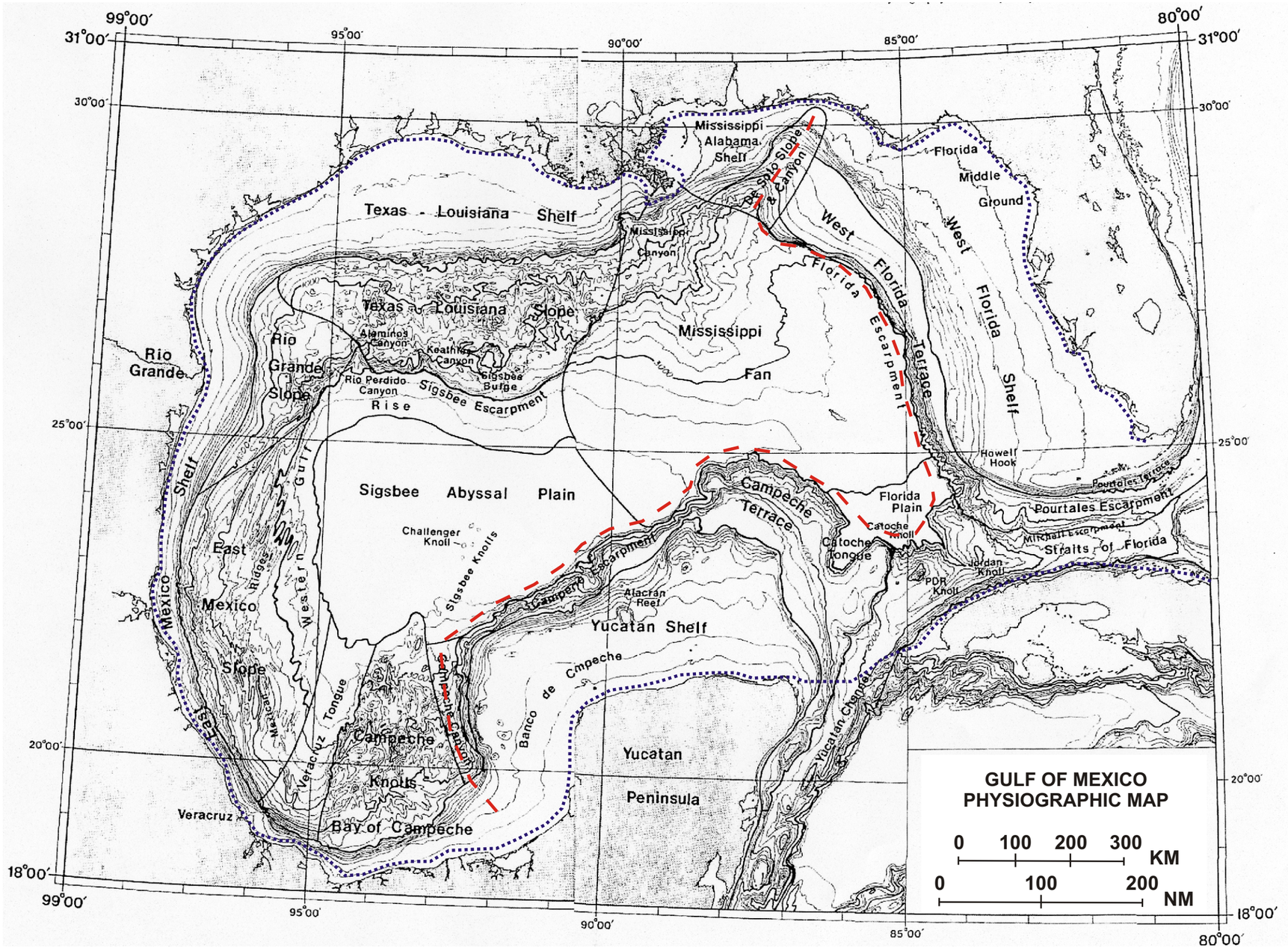

FIGURE 1: Physiographic and bathymetric map of the Gulf of Mexico. Modified from Bryant et al. (1991). The red, dashed line roughly divides the clastic province (to the west) from the carbonate province (to the east). The shoreline is outlined by a blue, dotted line to aid visibility. Names of sub-provinces and features are as shown.

is an unusually flat stretch of the slope. The Desoto Slope is cut off from the other slope divisions by the Mississippi Fan and is characterized by the erosive Desoto Canyon.

From the continental slope, the basin floor slopes down gently onto the Sigsbee Abyssal Plain by way of the Western Gulf Rise. The boundary between the Texas-Louisiana Slope and the abyssal plain is marked by the Sigsbee Escarpment, a steep scarp representing the southern edge of the continental slope and also the southern edge of seafloor topography related to subsurface salt diapirism (Uchupi, 1975, Amery, 1978). The abyssal plain is an expansive, exceptionally flat surface interrupted only by the Sigsbee Knolls, identified as the surface expression of diapiric salt structures.

At the eastern end of the terrigenous province is the Mississippi Fan, a relatively young and vast submarine fan stretching from the modern Birdfoot Delta to the Campeche Terrace and the Florida Plain. The western margin of the fan borders the Texas-Louisiana Slope and the Sigsbee Abyssal Plain and has blanketed the eastern extents of the Sigsbee Escarpment to the point that it has no topographic expression.

Carbonate Province. The carbonate province consists of the remaining eastern portion of the Gulf, and consists primarily of two broad carbonate platforms: the West Florida Shelf and the Yucatan Shelf. Each of these shelves is a low-relief carbonate platform having maximum widths of about 145 miles each. These carbonate platforms are characterized by primary deposition of carbonates formed *in situ* by reefal organisms and by secondary sedimentation of marine evaporites (Uchupi, 1975). Seaward of the platforms are carbonate terraces, which are characterized by shallow basinward gradients and are often channelized and show evidence for slumping.

The edges of the two carbonate platforms are marked by escarpments—the Florida Escarpment and the Campeche Escarpment. These scarps are not related to diapiric salt as with the Sigsbee Escarpment. Rather, they represent the basinward extent of reefs and the extensive carbonate build-ups they produce (Bryant et al., 1991). The Florida Escarpment is one of the steepest submarine scarps in the world, at about 45°, and is the confining eastern

boundary of the Mississippi Fan. The western extent of the Campeche Escarpment borders the Sigsbee Abyssal Plain, and the eastern extent forms another portion of the boundary of the Mississippi Fan. Other physiographic features include the Florida Plain, an abyssal plain beyond the distal extent of the Mississippi Fan; the Pourtales Escarpment, which is the southern boundary of the Florida Peninsula and carbonate platform; and the Straits of Florida, a deep submarine channel connecting the Gulf of Mexico to the Atlantic Ocean.

Depositional History of the Northern Gulf of Mexico

The Gulf of Mexico Basin was formed in the Mesozoic by the same extensional forces that split present-day Europe and Africa from North and South America and opened the Atlantic Ocean. Since the end of crustal extension that initially formed the basin and the subsequent emplacement of oceanic crust near the basin center, the Gulf has been a tectonically quiescent portion of North America for all of the Cenozoic (Martin, 1977). Gulf geologic structures are largely a consequence of the complex depositional history of the basin. An in-depth discussion of the geologic history of the basin is well beyond the scope of this study, so a summary of the late Mesozoic and Cenozoic depositional history and related structures will be given. Emphasis will be placed on the northern portion of the Gulf (Figures 1 and 2).

Depositional History. The Gulf of Mexico represents a complex accumulation of siliciclastic, carbonate, and evaporitic sediments deposited in different settings under varying depositional conditions. The earliest sediments deposited in the basin are early Jurassic post-rift terrigenous to shallow marine clastics that infilled lows in the rift topography (Martin, 1977). Later, middle Jurassic evaporites were deposited in topographically lower areas of the shallow basin as a result of episodic isolation of the Gulf's waters from circulation with the rest of the open ocean and subsequent desiccation of the resulting land-locked sea. For the entire Cenozoic, deposition in the clastic-deficient northeastern Gulf consisted of primary carbonate deposition and secondary evaporite deposition on the subsiding Florida Platform and Terrace. The following discussion describes the dominating siliciclastic sedimentation and processes in the much larger, western remainder of the Gulf of Mexico (refer to Figure 2).

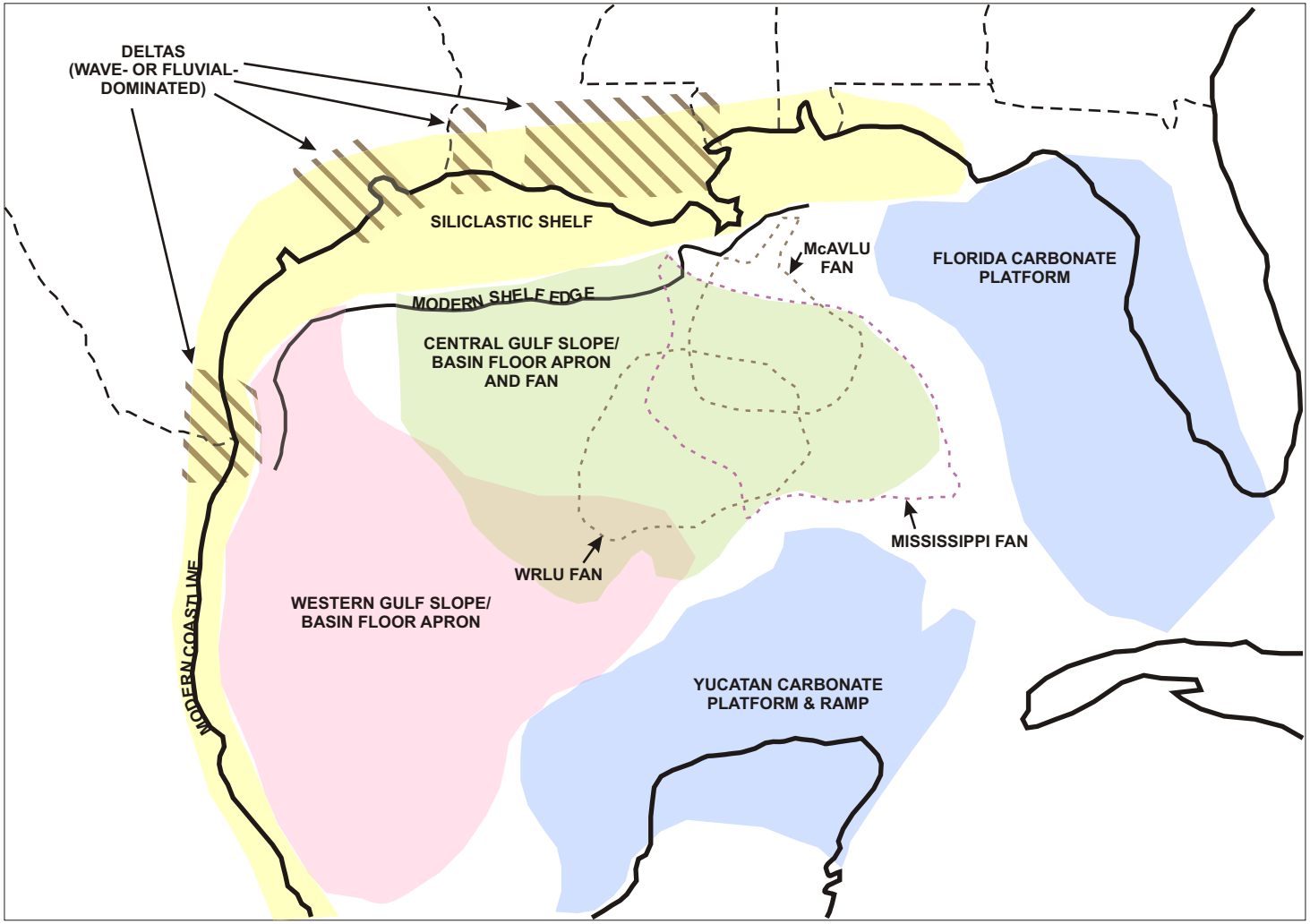

FIGURE 2: Regional map of the Gulf of Mexico's major sedimentary depositional systems and depositional environments. The features shown are generalized, and represent areas of varying influences of dominant modes of deposition. Thus, boundaries shown varied during the Cenozoic, as depositional systems shown were either dominant or subordinate. (Based on Figures 5-18 of Galloway et al., 2000).

Late Jurassic to early Cretaceous sedimentation consisted largely of shallow marine carbonate formation with relative sediment starvation of the subsiding basin center. During the middle Cretaceous, a scarcity of clastic sedimentation from North American continental sources allowed reefs to flourish and almost completely ring the basin. A significant rise in relative sea level during this period led to a landward shift in position of these reefs. This resulted in a wide carbonate reef build-up transgressing almost the entire pre-Cretaceous Mesozoic section of the American Gulf Coast (Martin, 1977). Late Cretaceous time saw an increase in the supply of clastic sediments to the basin and a continuation of basinal subsidence that began after the opening of the basin.

Cretaceous to Paleocene Laramide orogenic activity in the western continental United States and Mexico spurred the production of unprecedented volumes of clastic fluvial sediments that reached the Gulf of Mexico basin by way of the Houston and Holly Springs (Central Mississippi) depositional axes. These sediments constituted the first major pulse of siliciclastic sediments of the Cenozoic in the Gulf and both infilled the shallow marine carbonate platform behind the late Cretaceous reef and deposited on the basin floor (Galloway et al., 2000).

The early Eocene sediment supply was reduced from Paleocene levels, reflecting relative quiescence of the continental interior. Sedimentation continued on the western Gulf basin floor in the form of a sediment apron fed by slope-bypassing, fluvially-derived clastics. The central and eastern portions of the deep basin were sediment starved during the early Eocene. Middle to late Eocene crustal heating in the Mexican Cordillera led to the shedding of much clastic sediment that found its way to the western Gulf by way of the Rio Grande, Tuxpan (southwestern Gulf), and Houston depositional systems. This resulted in the clastic deposition on the western Gulf continental shelf and slope and continued feeding of the basin floor apron. The area of the basin affected by this greater influx of sediment from the west increased, and thus the area of the basin characterized by sediment starvation shrank (Galloway et al., 2000). Relatively slow subsidence continued across the basin as a whole.

Crustal heating continued into the Oligocene, and associated uplift in the southwest United States and in Mexico led to the shedding of a vast supply of clastic sediment. This sediment was transported eastward to the Gulf principally via the Rio Grande and Houston fluvial axes and to a lesser extent by the Central Mississippi fluvial axis, which was beginning to grow in importance as a sediment outlet to the Gulf (Galloway et al., 2000). This sediment accumulated primarily on the western Gulf basin floor apron and basin floor fan, with some accompanying progradation of the shelf edge and sedimentation on the continental slope. Massive shelf edge failures along the western Gulf margin briefly interrupted margin outbuilding and basinal sedimentation patterns (Galloway, et al., 2000). Carbonate and evaporite deposition extended farther west of the Florida Platform into the deep basin than it had previously. Portions of the deep basin floor continued to be sediment starved through Oligocene time.

In the early Miocene, the beginning of Basin and Range extension and accompanying uplift of the Edwards Plateau provided new sources of clastic sediment to the continental fluvial drainage systems. Fluvial systems gradually shifted to the east, changing the dynamics of sediment transport in North America. Consequently, the Rio Grande depositional axis shrank in prominence, the Houston axis was abandoned in favor of the Red River axis, and the Central Mississippi axis continued to gain prominence. During this period, the margin along the Central Mississippi delta prograded about 40 to 50 miles (Woodbury et al., 1973, Galloway et al., 2000; see Figure 3). Middle Miocene time saw massive slope failures on the northwest Gulf margin and the deposition of extensive sandy basin floor fan deposits across the entire basin floor to the Campeche Escarpment. The main western Gulf depositional axis during this period was the Corsair, which provided clastics derived from the Edwards Plateau to the margin and basin floor. In the northeastern Gulf, between and seaward of the Texas-Louisiana Shelf and the northwestern Florida Platform, the McAVLU Fan (acronym formed from Mississippi Canyon, Atwater Valley, and Lund areas) was deposited. This fan system resulted from bypass of clastic sediments derived from uplifted areas in the eastern US across the northeast Gulf continental shelf to deepwater depocenters on the continental slope (Galloway et al., 2000).

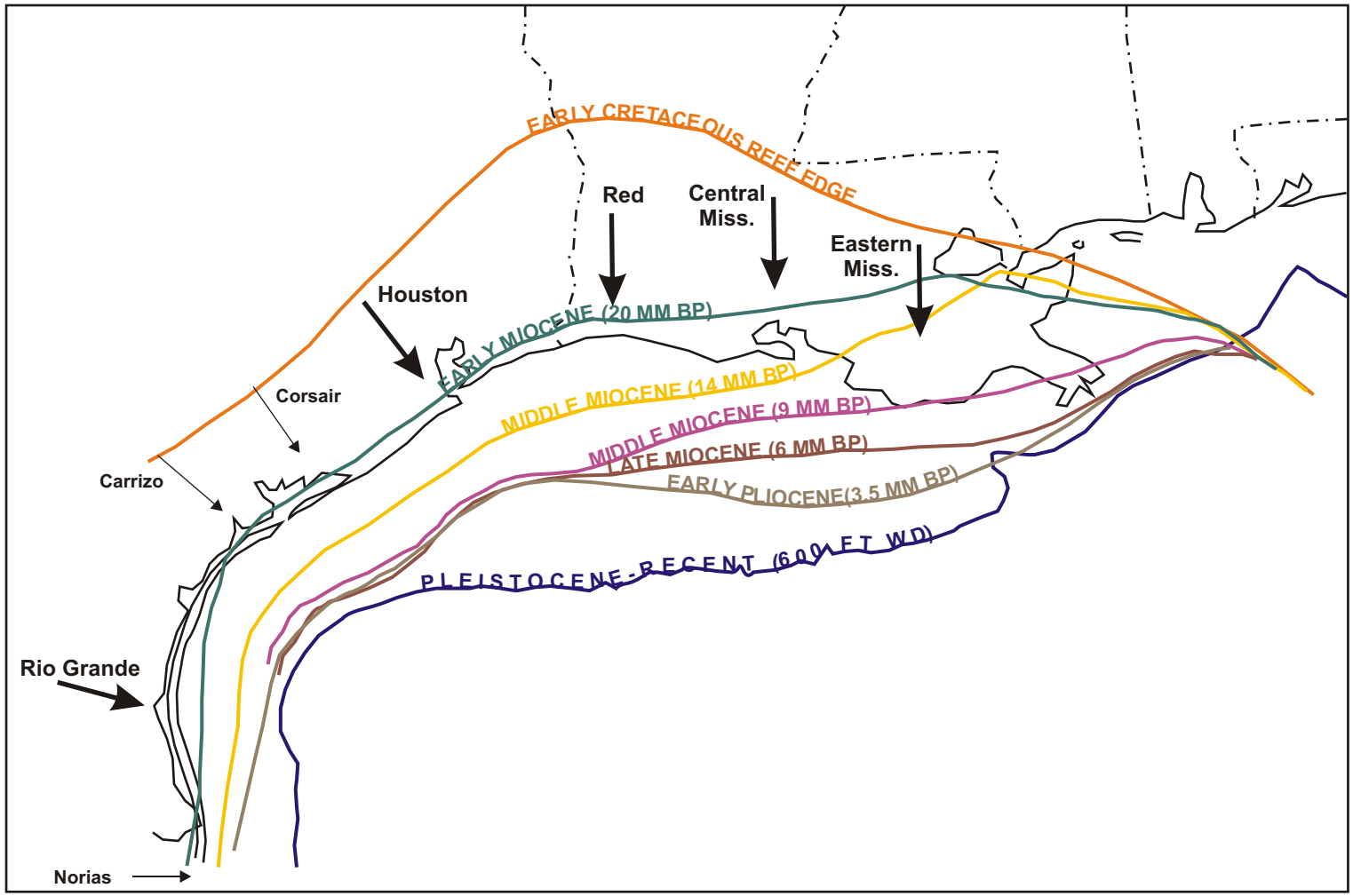

FIGURE 3: Regional map of the Gulf of Mexico showing major clastic sedimentary depositional axes and episodes of shelf-edge expansion. Period of time is Miocene to Recent. Depocenters are located at points of greatest expansion of the shelf edge, and are most prominent offshore of the Red, Central Mississippi, and Eastern Mississippi axes. (Based on Figure 3 of Galloway et al., 2000, and Figure 3 of Woodbury et al., 1973).

By the late Miocene, waning influence of the western Gulf depositional axes was still sufficient to prograde the margin several miles. The north-central Gulf was still the site of prolific shelf and slope outbuilding (Woodbury et al., 1973; see Figure 3), as sediments from the still-uplifting central and eastern US interior fed the Central Mississippi axis. These sediments also aggraded the Central Gulf and McAVLU fans. A major marine transgression in the late Miocene briefly disrupted these depositional patterns. Upon their reestablishment, sediment transport was almost exclusively centered on the Central and East Mississippi axes, and deposition onto the McAVLU fan was terminated.

Subsidence of the Gulf basin continued during the Miocene. Those portions of the deep basin described as sediment-starved also increased in area, covering vast stretches of the eastern and southern deep basin outboard of the Florida and Campeche Escarpments (Galloway et al., 2000).

Early Pliocene time began with a dramatic reduction in the supply of clastic sediment. Although the Red and Central Mississippi axes still dominated deposition, their deltas were wave-dominated as opposed to fluvial-dominated, and depocenters were smaller and were located landward of their Miocene predecessors. Shelf progradation ceased, and the northern Gulf basin margin suffered a period of retrogradation and mass wasting (megaslides are recorded on the northwestern shelf/slope). Even though more than half of the deep basin floor is sediment-starved (greatest since the Eocene), the WRLU Fan (Walker Ridge and Lund) was deposited on the northern slope. The deposition of this fan indicates that sediment was still being sourced from the eastern US and was bypassing the shelf for a deeper depocenter (Galloway et al., 2000).

In the middle Pliocene, sediment supply increased to the point that the combined Red/Central Mississippi/East Mississippi delta complex again prograded the shelf (Woodbury et al., 1973; see Figure 3), and sediment bypassing to the east continued to feed the WRLU Fan. Late Pliocene time brought the first Quaternary pulse of glacial sediment and meltwater. The abundant sediment supply and continuing shelf bypass through submarine

canyons led to the initiation of the Mississippi Fan on the lower eastern Texas-Louisiana Slope (Bryant et al., 1991, Galloway et al., 2000). The huge fluvial sediment supply also prograded the shelf, infilled basins on the slope, and supplied huge volumes of clastics in the form of mass movements and turbidites to the deep basin floor.

In the Pleistocene, glaciation induced rapid fluctuations in relative sea level and yielded vast quantities of clastic sediment to the dominating Red and Central Mississippi fluvial axes. As a result of this, highstand periods of prolific shelf progradation were countered with lowstand periods of submarine canyon incision that allowed fluvial sediments to bypass the shelf (Galloway et al., 2000). These same canyons also eroded the constructional continental shelf and funneled the sediments to deepwater depocenters. The Mississippi Fan grew to its immense size during this period of about 1.8 million years. The East Mississippi and Bryant Fans are minor, peripheral fans that also formed during the Pleistocene (Bouma et al., 1984, Bryant et al., 1991).

Holocene sedimentary processes are largely restricted to carbonate deposition, episodic mass movements, minor deposition of sand on the continental shelf, and hemi-pelagic and pelagic clay deposition on the Gulf margin and in the deep basin. Across most of the basin, Holocene sediments are less than 10 feet to a few tens of feet thick.

In summary, Cenozoic clastic sedimentation in the northern Gulf prograded the continental shelf by about 240 miles along the north-central margin (Figure 3). Bypassing of the continental shelf in the Pliocene and Pleistocene led to the formation of voluminous lower slope and basin floor fans. Sedimentation on the Florida Platform consisted mostly of carbonate formation.

Structural Geology of the Northern Gulf of Mexico

Gulf of Mexico structural geology is heavily influenced by the tectonic and sedimentary events that transpired during and after supercontinent break-up that occurred during late Triassic time. The extended continental crust forming the margins of the basin was, by Jurassic time, beginning to accumulate marine sediments in the form of shallow water evaporites

(Peel et al., 1995). Later, during the final phase of rifting, oceanic crust formed in the basin center. Initial basin subsidence was caused by thermal equilibration of the lithosphere as the extended crust thickened and cooled.

The voluminous Cenozoic supply of clastic sediments loaded the crust underlying the major depocenters, causing the crust to isostatically subside. The resulting subsidence was focused on these depocenters, and was therefore localized. Unlike even, basin-wide subsidence, this localized subsidence resulted in regional gradients and gravitationally-induced deformation of the Cenozoic sediment cover. Crustal loading and subsidence represent the only basin-wide structural modifications to crust underlying the Gulf of Mexico since the end of rifting. The Gulf basement has been remarkably quiescent in the tectonic sense during the Cenozoic (Rowan et al., 1999). The observed structures within the Cenozoic basin fill are the result of gravitational influence in the forms of the density contrast between salt and clastic sediments and basinward creep of the Cenozoic sedimentary cover (Worrall and Snelson, 1989).

Our understanding of the structure of the Cenozoic Gulf basin fill has improved markedly since the early 1970's. Up to that time, salt structures and faults were simplistically and separately described in terms of type, morphology, and distribution. Seismic data was plentiful covering the continental shelf off Texas, Louisiana, Alabama, and Mississippi, but was largely proprietary in ownership. As oil exploration moved into the deep waters of the continental slope, large volumes of 3-D seismic data were acquired over these areas, and some data owners saw the advantages of allowing public use of selected data to address geological issues in the vastly more complicated deepwater environment. Thus, a renaissance in the understanding of Gulf of Mexico Cenozoic structures began.

Allochthonous Salt. By the late 1960's, it was widely known that the amount of allochthonous salt present in the Cenozoic section generally increases from north to south across the northern Gulf margin (Figure 4). It was also known that this salt tended to move vertically, piercing upward through progressively younger siliciclastic sediments (Woodbury et al., 1973). Later, investigators such as Martin (1977) and Amery (1978) noted that

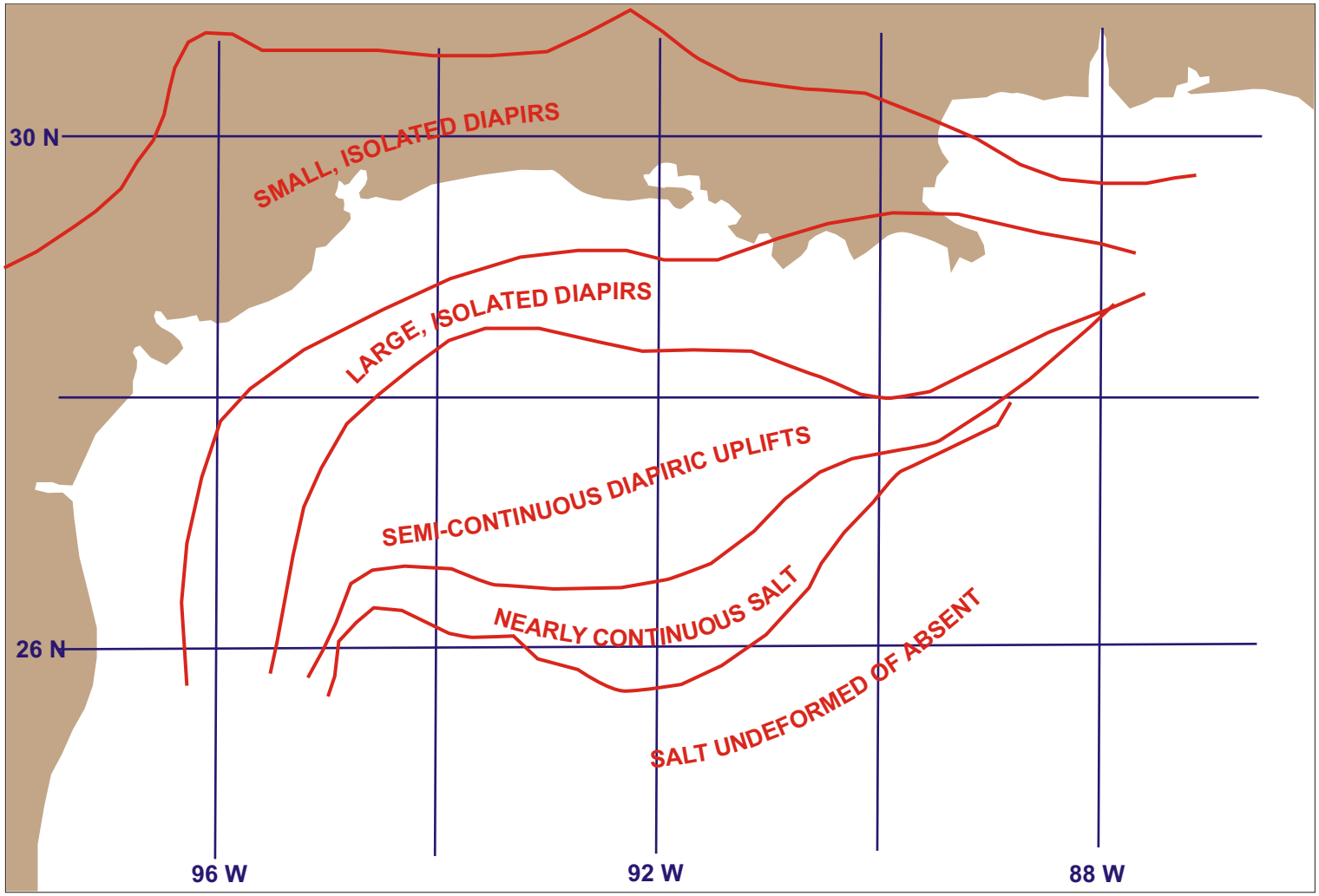

FIGURE 4: Distribution of salt in the north-central and northwestern Gulf of Mexico. This distribution, along with the well-understood progradational history of the continental shelf by clastic depositional systems, shows that salt has migrated southward as allochthonous bodies throughout the Cenozoic. (Based on Figure 11, Amery, 1978).

salt was apparently moving laterally in a southerly direction on geologic scales of time. This indicated a trend of downdip movement toward the basin center. This discovery helped to account for the distribution of salt and explained the observed lack of salt and salt-related structures in the center of the basin—that salt has not migrated that far south at present.

Today, modern and extensive 3-D seismic data coverage of the northern Gulf of Mexico has allowed for a good understanding of the relationships between salt bodies and the clastic sediment cover they intrude and deform. Peel et al. (1995) mapped salt structures across the northern Gulf of Mexico and produced palinspastic restorations of several regional cross-section lines in order to derive a history of the evolution of salt and faulting in the Gulf. Their work has resulted in the recognition of six regions characterized by salt with different emplacement and withdrawal histories. These regions are termed canopies, and represent salt that was injected into the shallow sediments from below at a common time and has seen the same basic history of structural deformation (Worrall and Snelson, 1989). These canopies are designated by Roman numerals on Figure 5.

Canopy I underlies the upper continental slope south of the modern Mississippi Delta and is characterized as a large, intact salt body injected into shallow sediments in the Miocene. Much of the growth faulting updip (landward) of this canopy and contractional folding in the Mississippi Fan foldbelt downdip of the canopy are also Miocene in age (Peel et al., 1995). Miocene clastic sedimentation of the northern continental margin produced great thicknesses of sediments in depocenters located in modern day southeastern Louisiana. This mass of overburden initiated lateral outflow of allochthonous salt in the downdip direction to form Canopy I.

Canopy II (IIa and IIb on Figure 5) is a large canopy that underlies the continental slope south of Louisiana. The northern portion of this canopy (upper slope) is partially withdrawn, with the salt flowing into the less-withdrawn southern portion (middle slope). As with Canopy I, withdrawal and southward lateral movement of salt is a response to sediment loading by Miocene- to Pleistocene-age shelf and slope depocenters. Salt withdrawal basins on the upper

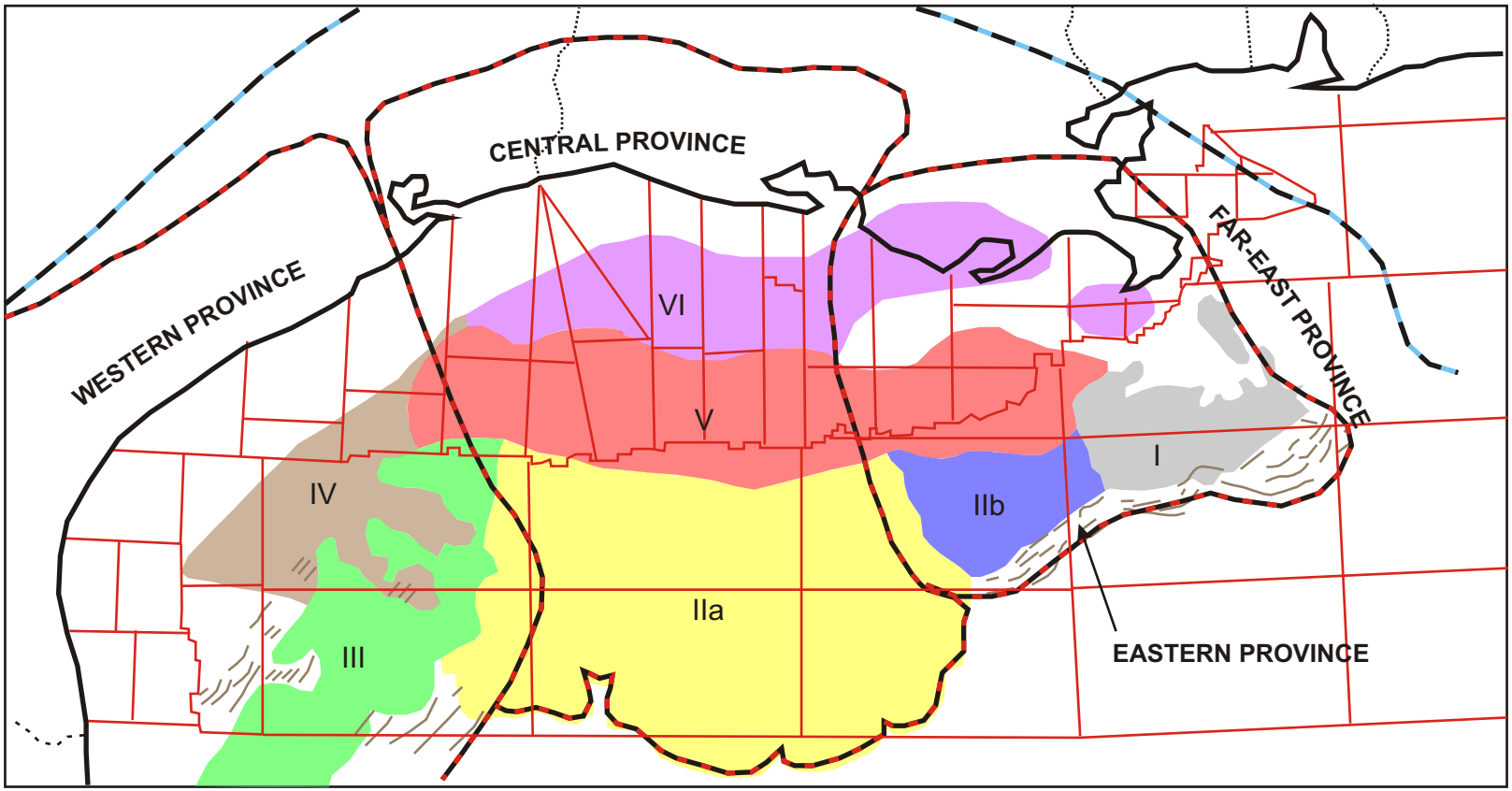

FIGURE 5: Map of north-central and northwestern Gulf of Mexico showing generalized extents of salt canopies. Roman numerals (canopy designations) relate to the text. Gray lines south of canopies I and IIb represent the Mississippi Fan Foldbelt. Gray lines west and east of canopy III represent the Perdido and Port Isabel Foldbelts, respectively. Thin red lines mark boundaries of oil and gas lease areas. Shown for reference. Black and red dashed lines mark approximate boundaries of the structural provinces of Peel et al., 1995. Black and blue dashed lines mark lower Cretaceous shelf edge and the offshore Florida Escarpment. (Based on Figures 9 and 12 of Peel et al., 1995).

slope are mature and are filled with thin Miocene and thick Pliocene-Pleistocene sediments. On the middle slope, the salt withdrawal basins are less mature, with Pliocene-Pleistocene infills. Lower slope withdrawal basins are comparatively younger and shallower, indicating the initial stages of salt withdrawal on the lower slope (Peel et al., 1995).

Canopy III underlies the western Gulf continental slope and is largely intact, showing little salt withdrawal and a correspondingly immature state of withdrawal basin formation. This canopy was emplaced from Paleocene to Miocene time.

Canopy IV is a paleocanopy initially formed in the Eocene and subsequently withdrawn into Canopy III (Peel et al., 1995). Canopy IV is represented by salt welds and by Oligocene and Miocene sediments that initiated and infilled salt withdrawal basins, and were later intensely contractionally deformed.

Canopy V is present along the northern Gulf lower continental shelf and uppermost slope. Canopy VI is the farthest landward of the canopies identified and underlies the upper continental shelf from offshore of Galveston to onshore southeastern Louisiana. Canopies V and VI are mostly withdrawn and are represented by sparsely distributed salt bodies, salt welds, and deep, fault-bounded basins infilled with Miocene-Pleistocene clastic sediments. Canopy VI is interpreted to predate Canopy V, with the latter inferred to have intruded between Miocene and Pliocene time, and the former inferred to have intruded in the Eocene to Oligocene time frame.

Taken together, the allochthonous salt canopies describe a history of southward migration and emplacement of salt (Diegel et al., 1995). This migration was forced by updip loading by clastic deposition. Salt withdrew under this sediment load, furnishing locales to the south on the modern-day middle and lower slope with generally unbroken bodies of salt. The upper slope contains remnant salt in the form of welds, salt stocks, and isolated sheets. Farther to the north, on the modern continental shelf and in onshore areas of southeast Texas and southern Louisiana, salt is present only as sparsely-distributed stocks and welds. The complete

absence of salt in these areas may be indicated by regional or counterregional listric faults marking the former location of mini-basin ringing salt bodies.

Fault Classes. The major mechanism of brittle deformation in the Cenozoic sediment cover of the northern Gulf of Mexico basin is extensional (normal) faulting. Numerous classifications exist for normal faults observed in the Gulf of Mexico, and most classify faults on the basis of either geometric or genetic parameters. Rowan et al. (1999) classify faults on the basis of geometry and include several classes of extensional faults along with a few classes of contractional faults and strike-slip faults. A fourth class of fault-like features, consisting of salt pinch-outs containing small remnant bodies of salt left after a larger salt body has been withdrawn, is included. These features are termed salt welds and may behave as faults in that strata move in opposite relative directions across the weld.

Extensional faults accommodate tensile stress within the Cenozoic sediment column and consist of several types (Figure 6). *Peripheral faults* are located along and parallel to the updip limit of Jurassic Louann Salt which extends from central Texas, through Louisiana, and into Mississippi and Alabama (Martin, 1977). These faults are typically planar in shape and form symmetric grabens that accommodate gravity sliding (Rowan et al., 1999), as shown in Figure 6. *Crestal faults* form symmetric grabens of planar growth faults along the crests of salt uplifts and accommodate extension of the clastic overburden. *Keystone faults* are geometrically similar to crestal faults because they form symmetric grabens and are planar. However, keystone faults are non-growth faults that do not root into salt and are commonly found at the crests of anticlines and along rollover monoclines (Rowan et al., 1999).

Roller faults are common in the Gulf of Mexico and are regional (dipping toward the basin) growth faults that sole onto the tops of salt bodies or onto salt welds. The fault hanging wall is characterized by a rollover monocline or anticline, with sediments infilling seafloor topographic lows. This results in the formation of an expanded section that thickens toward the fault (growth strata). Roller faults are arcuate in map view and accommodate much of the extension in the updip portion of the northern Gulf margin caused by gravity sliding and salt

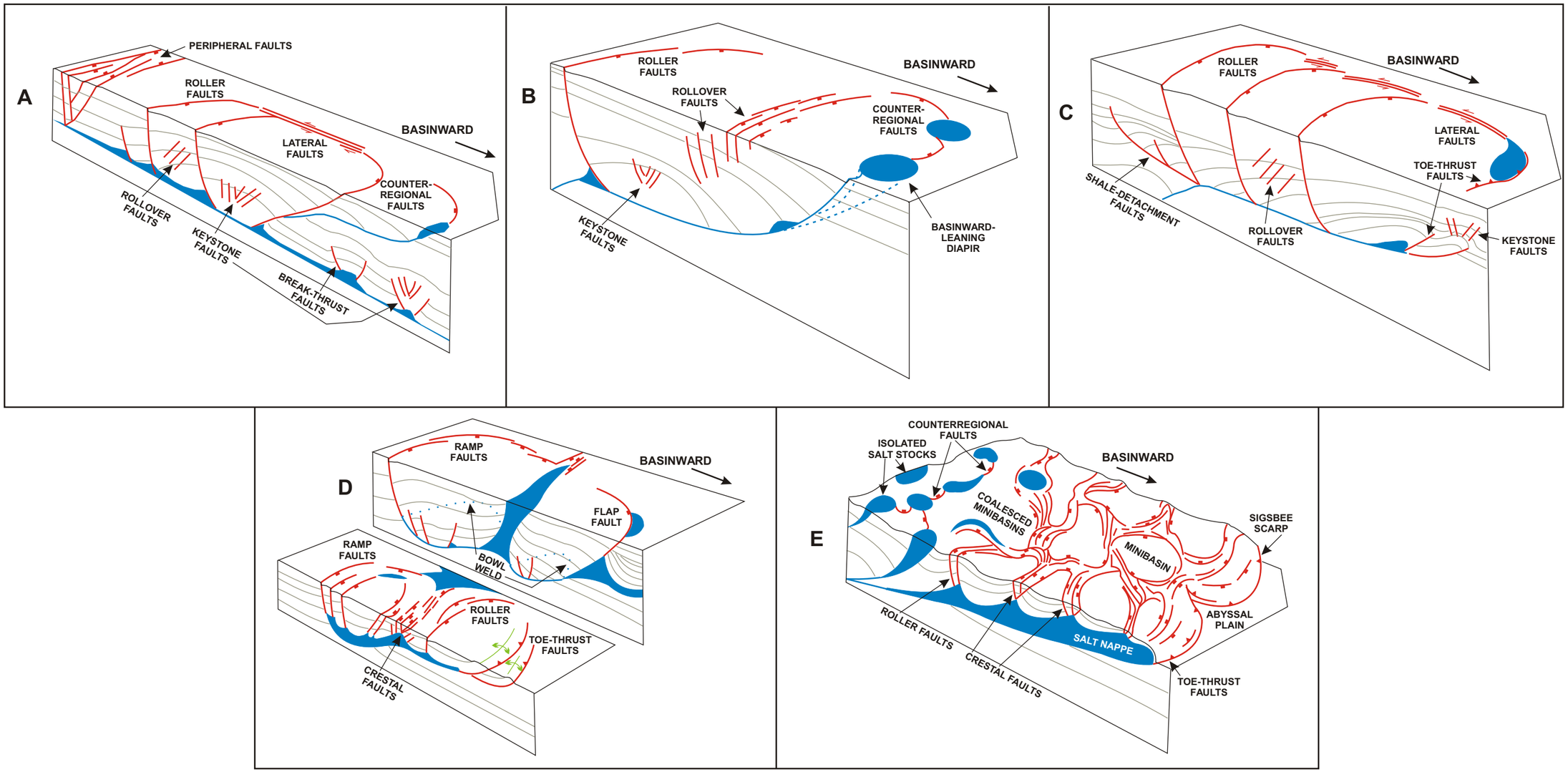

FIGURE 6: Idealized linked structural systems. (A) Autochthonous salt linked system. Extensional, contractional, and lateral fault types present. (B) Counterregional linked system. Major fault type is counterregional. (C) Roho linked system. Main fault type is roller (extensional). Contraction is accommodated by thrust faulting, folding, and movement of salt upward and laterally. (D) Salt-stock canopy linked system. Immature system (foreground) and more mature system (background) show how salt evacuation is accommodated by roller and counterregional faults and increased sedimentation in the minibasin. (E) Salt nappe linked system. System matures moving in the landward direction. Most basinward portion contains salt spreading and thrusting, with subsiding minibasins bounded by crestal fault families. More landward portion displays isolated salt stocks linked by counterregional faults. Red lines indicate faults. Rectangles denote hanging wall of normal fault, and triangles denote hanging wall of thrust fault. Blue indicates salt. Green lines represent fold axes. (Based on Rowan et al., 1999).

withdrawal from the fault hanging wall (Rowan et al., 1999). *Ramp faults* differ from roller faults in that they are highly arcuate in map view, they are typically younger, and they accommodate much less extension. *Shale detachment faults* are regional extensional faults that display a strong listric geometry and sole onto diapiric shale bodies or shale detachments. These faults are typically found landward of the major allochthonous salt bodies in nearshore and onshore coastal Texas and Louisiana (Martin, 1977). *Counterregional faults* are listric growth faults that dip in the landward direction, are arcuate in map view, and typically connect allochthonous salt bodies. The hanging walls of counterregional faults are characterized by monoclinal or anticlinal rollovers and basinward-thickening expanded sedimentary sections. Counterregional faults accommodate little extension because they form in response to salt withdrawal from the hanging wall, as opposed to gravity sliding (Rowan et al., 1999).

Flap faults are listric growth faults that typically display counterregional dip and contain a salt diapir in the footwall. Active diapirism causes intrusion of salt upward, uplifting the overlying footwall strata and exposing them to erosion as a local positive relief feature on the seafloor. The salt movement creates accommodation space in the hanging wall that is infilled by clastic strata that thicken toward the diapir (Rowan et al., 1999). *Rollover faults* are planar, non-growth faults that accommodate extensional deformation on monoclinal rollovers in fault or salt weld hanging walls. These faults are antithetic to the main fault or weld and are similar to keystone faults, but do not form symmetric families of faults.

Contractional faults help to accommodate extension that occurs in the updip portions of the Gulf margin. *Toe-thrust faults* display counterregional dips, are located down-dip of allochthonous salt within foldbelts, and display ramp-like geometry in dip sections. *Break-thrust faults* dip either regionally or counterregionally. These planar reverse faults are located within foldbelts and accommodate shortening after the initial phase of folding (Rowan et al., 1999).

Strike-slip faults are the last class of faults. These faults are oriented roughly parallel to the regional dip and form linear or en echelon arrays of faults in map view. In vertical section, strike-slip faults are observed rooting into allochthonous or autochthonous salt and display

steep, near vertical dips. Arrays of these faults may also form positive (transpressional) or negative (transtensional) flower structures (Peel et al., 1995, Rowan et al., 1999).

Fault welds, also known as salt welds, are detachment surfaces formed when salt has evacuated an area, leaving the clastics formerly above and below the salt in contact across a narrow zone of remnant salt. Six types of fault welds are recognized, and they are related to faults already discussed. They include *primary*, *roho*, *counterregional*, *bowl*, *thrust*, and *wrench welds*.

Linked Systems. Autochthonous and allochthonous salt, the Cenozoic clastic sediment column, and the faults just described form linked structural systems that represent varying responses to gravity sliding. Linked systems exist adjacent to one another and are bounded laterally by faults or welds. Their upper boundaries are the seafloor and their lower boundaries are detachment surfaces, commonly salt or shale bodies or welds (Rowan et al., 1999). Examples of linked structural system end-members are presented conceptually in Figure 6. For these figures, lateral dimensions are on the order of tens or hundreds of miles, and vertical dimensions are on the order of hundreds to thousands of feet. Linked structural systems encountered in the Gulf margin may resemble those shown, or may constitute hybrids between two or more end-members.

The diagrammatic structural systems show how various classes of faults work together with salt to accommodate basinward gravity sliding and also demonstrate the hierarchical relationships between structures. Salt and shale are both active and passive components of the system, performing several important functions. These mobile materials provide a detachment surface for faults—essentially linkages to downdip contraction—and accommodate contraction by extruding upward (i.e., the Sigsbee Salt Nappe) or laterally (Peel et al., 1995). These mobile substrata may also actively cause structural deformation, especially in the case of flap faults. Finally, the evacuation of salt or shale creates small basins. When these basins are infilled with clastic sediments, the extra overburden depresses the crust and squeezes any salt or shale radially away from the basin. Peripheral faults, roller faults, and shale detachment faults are the

primary means of accommodating extension in the Cenozoic overburden. Toe-thrust faults, folding, and salt movement are the primary agents that accommodate contraction. Other fault types act subordinately, to relieve mechanical strains caused by movement along the primary faults within the intervening rock packages. Rollover, keystone, crestal, and break-thrust faults fall into this group.

In the context of large-scale salt flowage within the northern Gulf of Mexico, the recognized linked structural systems can be placed into a geographic framework. Counterregional systems and roho systems are characteristic of the modern continental shelf and upper continental slope, where salt withdrawal and basinward gravity gliding are the large-scale deformational phenomena. Where salt canopies are only partially withdrawn, salt-stock canopy systems prevail. Such conditions exist on the upper and middle continental slope. Salt nappe systems occur where active salt movement and net salt intrusion (rather than net salt withdrawal) occur. A modern example of such a system is the lower continental slope west of the Mississippi Fan. This area—the Sigsbee Salt Nappe—represents active basinward allochthonous salt movement under a thin clastic sediment cover (Amery, 1978, Bryant et al., 1991). Autochthonous salt systems are found in those areas where allochthonous salt (or shale) is no longer present in significant quantities (the upper continental shelf), or has had no appreciable presence.

Structural Provinces. The various linked structural systems may be grouped into larger structural provinces, which are thought to represent the major structural subdivisions of the Cenozoic stratigraphic package. These structural provinces are areas that share common histories of salt canopy emplacement, salt withdrawal, structural deformation, and clastic sediment input. As with linked structural systems, structural provinces are thought to border each other along transitional boundaries that may include some component of lateral offset (Peel et al., 1995). Inspection of Figure 5 demonstrates the imperfect geographical correlation between salt canopies and the structural provinces, and a comparison with Figure 2 shows the relationship with episodes of clastic input.

The Far-East Province is located in an area characterized by a general lack of Cenozoic gravity-induced tectonics (Figure 5). This relatively undeformed area saw little Cenozoic clastic input, and therefore lacks the sediment-loading mechanism needed to drive large-scale sale flowage. The Eastern Province is characterized by extension under southern Louisiana and the continental shelf connected to downdip contractional folding in the Mississippi Fan Foldbelt. The age of these features, as well as the time of emplacement of Canopy I, is taken to be middle to late Miocene (Peel et al., 1995). Major updip sedimentation occurred locally during Miocene to Pliocene time, providing the overburden weight necessary to initiate salt flowage.

The Central Province is dominated by Canopy II, which has the contractional Sigsbee Salt Nappe as its basinward structural feature. Major clastic influx on the continental shelf and upper continental slope, and much of the gravity sliding and salt flowage occurred during Miocene to Pliocene time. Updip, near-shore and onshore extensional faulting occurred primarily during late Cretaceous to Oligocene time.

Western Province Eocene to middle Miocene extension occurred onshore and on the continental shelf and the continental slope. Contraction is accommodated by the Port Isabel Foldbelt of the middle slope, the Perdido Foldbelt located on the lower slope, and possibly by lateral evacuation of salt from Canopy III, which was emplaced in the middle slope between the two foldbelts (Peel et al., 1995). Major clastic sediment influx to depocenters on the western Gulf margin crested by Oligocene time, and had waned by Miocene time.

Northeastern Gulf Margin. The northeastern Gulf margin consists of the Florida Carbonate Platform. The only Cenozoic structural activity known for this portion of the Gulf of Mexico is subsidence. Relatively little seismic date exists in the public domain for this area and correspondingly less is known about the structure of the Florida Platform than other areas of the Gulf. Researchers, including Martin (1977), indicate that more than two miles of subsidence and attendant carbonate and evaporite sedimentation have occurred since late Cretaceous time.

Study Area Geological Setting

Seafloor. The study area is located on the northern Gulf of Mexico continental slope offshore of Louisiana. The study area conforms to the bounds of a rectangular high-resolution 3-D seismic data set (HR 3-D), shown in Figure 7, and measures approximately 49,530 ft long by 34,920 ft wide (9.38 miles by 6.61 miles). Water depths range from about 3,100 ft to 4,200 ft below sea surface (BSS) within the study area, and the seafloor dips regionally to the southeast at about 2.3% (1.3°).

Seafloor features found within the study area include seafloor-offsetting normal faults, two structural grabens, minor furrows, a significant seafloor channel, and several hydrocarbon fluid expulsion sites. These features are shown in Figure 7.

The main body of seafloor faults is found within and marks the boundary of a symmetric, northwest to southeast-trending structural graben with dimensions of about 30,000 ft by 10,700 ft (about 5.7 miles by 2.0 miles) within the study area. The graben is known to extend to the southeast beyond the study area; however, no data is available for this area. The numerous faults have generally northerly to northwesterly strikes and display variable dips. The seafloor faults strike approximately 35° relative to the axis of the graben. North-striking faults dip to the east or west, and northwesterly-striking faults dip either to the northeast or southwest. The direction of fault dip is dependent on position within the structural graben: those faults on the northeast side of the graben preferentially dip to the west or southwest, while those faults on the southwest side of the graben dip to the east or northeast (Figure 8). Dips of individual faults are estimated to range between about 45° to 60°, with an average of about 54°. The graben faults display *en echelon* geometry as a group, and are individually either linear or arcuate in map view. Seafloor fault traces range in length between about 1,220 ft and 13,890 ft and display observed maximum relief of about 140 ft. The faults are interpreted to be active presently or in the recent past because they have seafloor scarps. The available data suggests that recent,

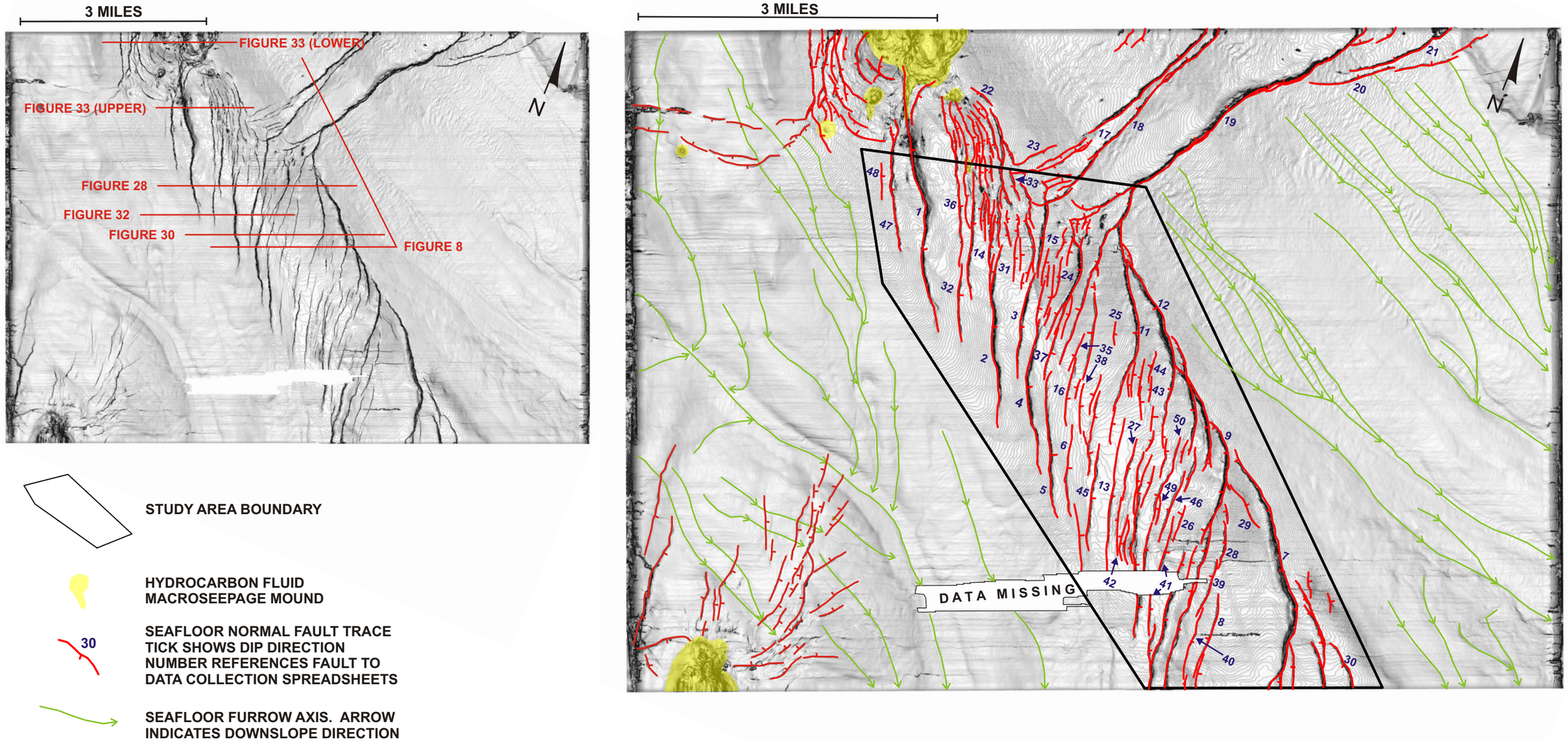

FIGURE 7: Grey-scale seafloor rendering maps of the study area. Areas of locally steep seafloor gradients (fault scarps, edges of furrows) appear as dark, generally linear features. Maps were generated from the seafloor horizon pick on the HR 3-D seismic data set. Dark areas on left- and right-hand edges of maps are data artifacts related to the terminations of the seismic inlines. Left-hand map is uninterpreted, but shows locations of vertical section data example figures. Right-hand map shows interpretation of seafloor fault scarps, assigned fault numbers, and interpretation of other seafloor features such as hydrocarbon seepage mounds and furrows.

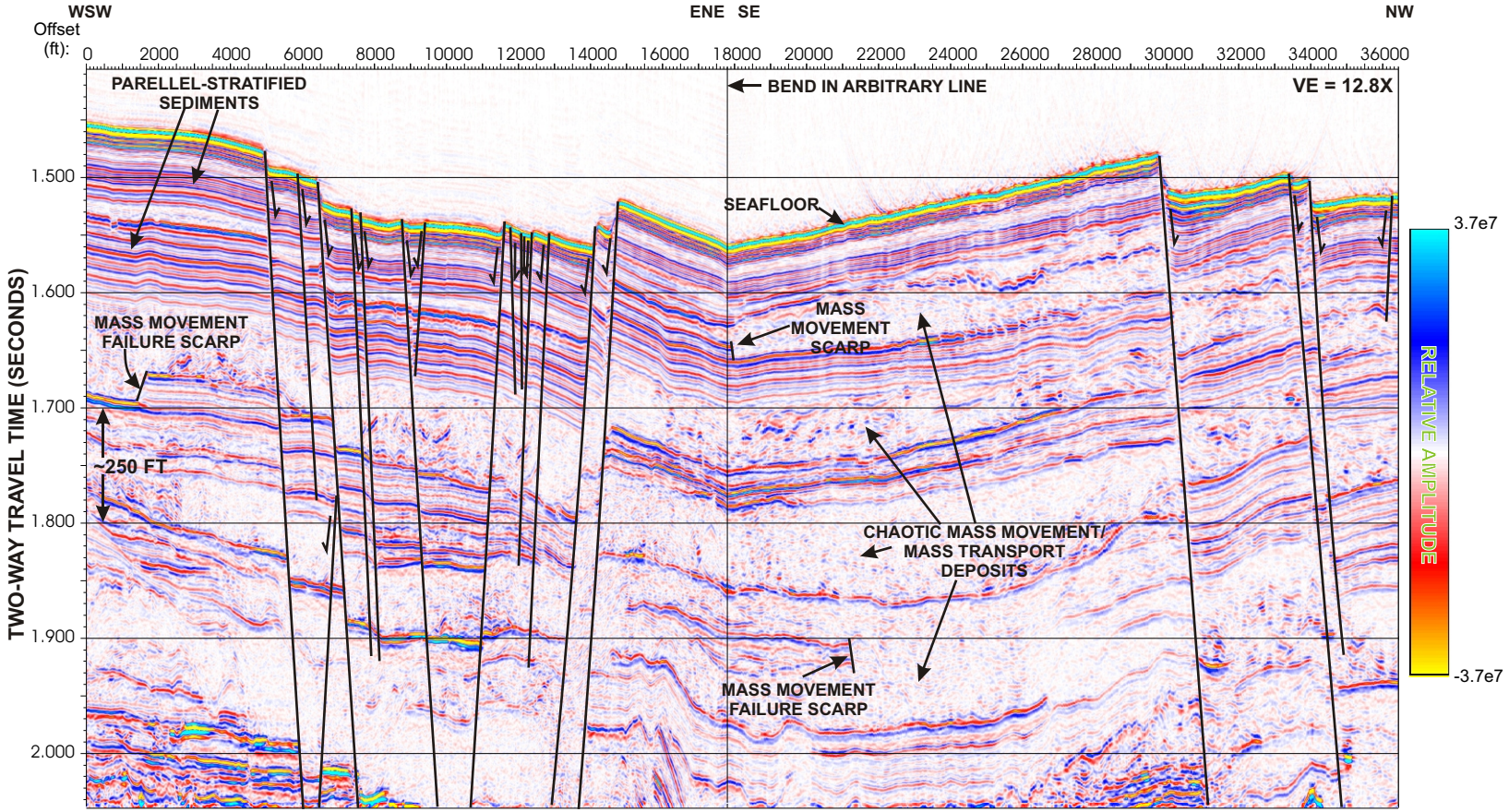

FIGURE 8: High-resolution 3-D seismic arbitrary line showing subsurface conditions. These include the graben, faulting, the shallow stratigraphy, and mass movement scarps. Location of this figure shown on Figure 7.

thin, undisturbed marine draping clays are not present across the fault scarps. This is indicative of recent or continuing activity (K. J. Campbell, 2004, personal communication).

Fault trace geometries at the graben edges (Figure 8) show that coalescence, or linkage, of faults has occurred to varying degrees within the study area. At the northeastern edge of the graben faults have coalesced into a well-defined segmented fault that marks the edge of the graben. The southwestern boundary of the graben is poorly defined. There, fault traces die out and no evidence of fault coalescence into a graben-bounding fault is present at the seafloor.

Another smaller graben is located to the southwest of the major graben. This smaller graben is characterized by a north-south axis, and dimensions of about 9,500 ft by 2,050 ft (about 1.8 miles by 0.39 miles). Faults associated with this graben are either bounding faults or interior faults, and generally strike parallel to the graben trend. As with the larger graben, the faults tend to dip toward the graben center. The faults comprising this graben are generally smaller than those associated with the larger graben, and show roughly the same ratio of trace length to maximum seafloor relief.

A set of northeast-striking, northwest-dipping normal faults extends from the northern end of the graben to beyond the study area. These faults appear to belong to a structural graben located well to the northeast of the study area, based on an inspection of NOAA's regional Seabeam bathymetry data.

Several furrows and a relatively wide seafloor channel are present on either side of the major graben. The widths and depths of the furrows generally cannot be measured from the 3-D HR seismic data, but are estimated to be on the order of tens of feet deep by a few tens of feet wide. Lengths of furrows are variable, ranging from a few hundred to more than 28,000 ft (more than 5.4 miles) long. Those furrows located northeast of the graben display a geometry analogous to a terrestrial parallel stream drainage pattern and follow the regional downdip direction to the southeast. The furrows located southwest of the major graben display a

terrestrial dendritic drainage pattern. All furrows within this area feed into a northwest-southeast trending channel that is several times wider than a furrow.

Several examples of hydrocarbon fluid expulsion sites are contained within the study area (Figure 7). These sites are characterized dominantly by a mound-like morphology, but one example of a shallow depression caused by fluid expulsion is present. Maximum relief measured on a hydrocarbon fluid expulsion mound is about 175 ft, with a maximum measured diameter of about 5,500 ft. An inspection of seafloor amplitudes revealed that most of the fluid expulsion sites display anomalously high amplitudes, and one case of anomalously low amplitudes. Hydrocarbon fluid expulsion sites are often characterized by the formation of authigenic carbonate build-ups (mounds) at the seafloor (K. J. Campbell, 2004, personal communication). The carbonates are harder than the surrounding soft clastic seafloor sediments and therefore display locally higher seafloor amplitudes. Where amplitudes are lower than the surrounding seafloor, very soft or gassy muds may be present at the seafloor.

The expulsion features are closely associated with faulting. An annular family of faults is present southwest of the northernmost mound, and a series of radial faults are present at the southernmost mound. The mounds themselves are the seafloor expression of hydrocarbon fluid escape from the subsurface. Large accumulations of gas are necessary for such expulsion features, and this gas was likely sourced from deeper reservoirs of thermogenic gas. The study area and vicinity are highly and complexly faulted, and these faults have likely acted as conduits for the upward migration of thermogenic gas (K. J. Campbell, 2004, personal communication).

Shallow Subsurface. The shallow subsurface geology of the study area (to the depth limit of this study, Horizon C) is dominated by the presence of generally stratified, predominantly fine-grained Pliocene-Pleistocene marine sediments that have been partitioned by faulting. Intervening packages of generally fine-grained mass movement transport complexes that range in geometric character from uniform thickness to variable thickness across the study area are also present. Several examples of erosional scarps produced by slope failures and mass movement scour are visible on Figure 8. At subsurface depths between Horizons B and C, the

shallow sediments are chaotically bedded and display generally higher amplitudes than the younger, overlying sediments. In the shallow section of the northern Gulf of Mexico, this seismic signature is often associated with the presence of predominantly coarse-grained (sandy) sediments deposited within successions of submarine distributary channel complexes and mass movement transport complexes (including turbidites). These are analogous to terrestrial infilled stream channels, levee and overbank deposits, and mass movement run-outs.

Deeper Subsurface. The shallow clastic section is underlain by a deeper and older Pliocene-Pleistocene clastic package and an allochthonous salt body. This salt body is interpreted to be related to and possibly interconnected at depth with Canopy I. Within the study area, allochthonous salt is generally present within the lower third of or below the base of the available conventional 3-D seismic data volume. This corresponds to a minimum subsurface depth of about 3.0 seconds TWT below the local seafloor. An exception to this is a ridge of salt that protrudes upward from the main body of allochthonous salt. This salt ridge parallels the trend of and directly underlies the structural graben and associated seafloor faults within the main study area. A series of 3-D images showing the upper surface of the allochthonous salt body, mapped fault planes, and the seafloor are shown in Figure 9. These images were generated from the 3-D seismic data sets available for this study (discussed later).

From Figure 9, it is apparent that the upper surface of allochthonous salt is characterized by dramatic structural relief. The salt ridge is connected to a much deeper, basin-shaped salt body located to the northeast. The relationship between the graben, its faults, and the salt ridge is interpreted to be one of cause and effect. Upward intrusion of allochthonous salt as a ridge induced extensional deformation in the overlying clastic sediments. The formation of a generally symmetric set of normal faults accommodated this deformation, resulting in the formation of a graben. The larger faults have detectable offset at the seafloor and root into shallow salt. Based on the classification of Rowan et al. (1999) this structural combination of shallow salt and an overlying fault set may be formally described as a crestal fault set.

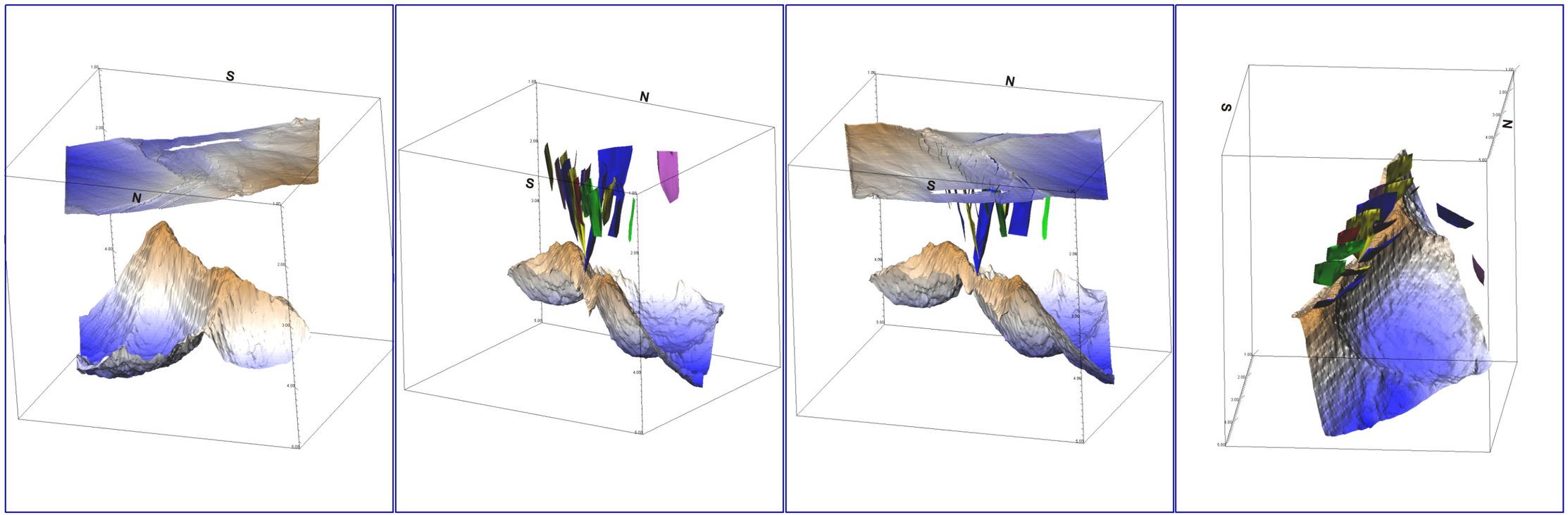

FIGURE 9: Four 3-D views of seafloor and subsurface conditions. Views show seafloor, fault planes, the top of shallow salt, and the relationship between salt, faulting, and seafloor topography. The first figure shows seafloor and top of shallow salt. Note the correspondence between the axes of the salt ridge and the seafloor graben. The second figure shows the relationship between faults (colored planes) and the top of salt. Note that most of the faults root into the salt ridge. The third figure shows seafloor, top of salt, and fault planes looking from the southeast, along the axis of the salt ridge. The fourth figure shows a high-angle view of fault planes and the salt surface. Note the angular relationship between the axis of the salt ridge and the strike of the individual faults. Color bar shows relative elevation on the top of salt and seafloor horizons. Fault coloration has no special meaning other than to allow the reader to differentiate between different faults.

BACKGROUND INFORMATION ON FAULTING AND PREVIOUS SIMILAR WORK BY OTHER AUTHORS

This section gives limited background information on faulting, with special emphasis given to seafloor-offsetting normal faults that show various stages of linkage along strike. Similar studies conducted previously by other authors are also discussed here. These works cover faulting on varying scales, from studies conducted on meso-scale faults observed in surface exposures to macro-scale faults investigated either in surface outcrops or with seismic data sets.

Background Information on Faulting

This discussion focuses primarily on sets of normal faults that offset the free surface (in this case, the seafloor) and display varying degrees of overlap and linkage along strike. However, the basic characteristics of faults discussed here apply equally to reverse and thrust faults, strike-slip faults, and to down-dip overlap and linkage of faults. All of the faults investigated in this study are normal faults, and the resolution at depth of the available data does not support the investigation of fault linkage down dip.

Fault Geometry and Displacement Characteristics. Numerous authors have described the tipline geometry, dimensions, and displacement characteristics of single-segment, *unrestricted faults*. Unrestricted faults are those that do not interact with other faults, or with free surfaces such as the ground surface, the seafloor, or bodies of material like salt that display very low shear strength over geologic periods of time. For such faults, the tipline geometry when observed in a plane parallel to the strike direction is essentially elliptical. This geometry is considered to be the result of smooth, generally constant rates of outward propagation of the fault tipline as the fault grows within a stress field from an initial crack in the rock volume. Displacement is at a maximum at or near the center of the fault and decreases smoothly (generally linearly, resulting in a nearly constant displacement gradient) in all directions to the fault tipline (Barnett et al., 1987, Chapman and Meneilly, 1991, Cartwright, et al., 1995, Needham et al., 1996, Nichol et al., 1996b, Cartwright et al., 1998, Contreras et al., 2000,

Willemse and Pollard, 2000). The elliptical shape of the tipline, with the semi-major axis of the ellipse generally subhorizontal for most observed cases of unrestricted normal faults, is the effect of mechanical anisotropy within the rock volume. Within most sedimentary successions that have not been deformed by tectonic or orogenic activity, sediments are deposited in horizontal to subhorizontal layers. Differences in the mechanical properties of the layers arise from their varying lithologic composition and from any diagenetic processes that may have occurred, including compaction, cementation, and/or dissolution. Together, these factors act to preferentially impede fault propagation perpendicular to the layering (in the dip direction) relative to propagation along strike, which is generally parallel to the layering (Barnett et al., 1987, Cartwright, et al., 1995, Nichol et al., 1996b). The result is slightly higher displacement gradients perpendicular to bedding than parallel to bedding.

More often, faults are observed to interact with each other, free surfaces, and materials such as salt that have vastly reduced mechanical competence over geologic periods of time. Such faults are said to be *restricted*. Restricted faults typically display complex geometries and highly variable displacement gradients not observed on unrestricted faults. Figure 10 shows idealized examples of unrestricted and restricted faults. In the unrestricted case, the fault shape is approximated by an ellipse, with displacement decreasing smoothly from a maximum at the center of the fault to zero at the tipline. In each other case the faults are restricted either laterally or vertically by the free surface, a layer with different mechanical properties, or by other faults. The result is a deviation from an elliptical shape and a departure from a smooth displacement gradient across the fault in favor of a relatively more complex distribution of displacement (Cartwright et al., 1995, Cartwright et al., 1996, Mansfield and Cartwright, 1996, Nichol et al., 1996b, Willemse and Pollard, 2000). Two important generalizations can be stated with regard to the boundary conditions and other faults that influence restricted faults. First, restriction by other faults causes a fault to display an underpropagated tipline and unusually high displacement gradients in the vicinity of the restricting fault, as in part C of Figure 10 and Figure 11. Second, restriction by a free surface boundary causes the tipline geometry of the

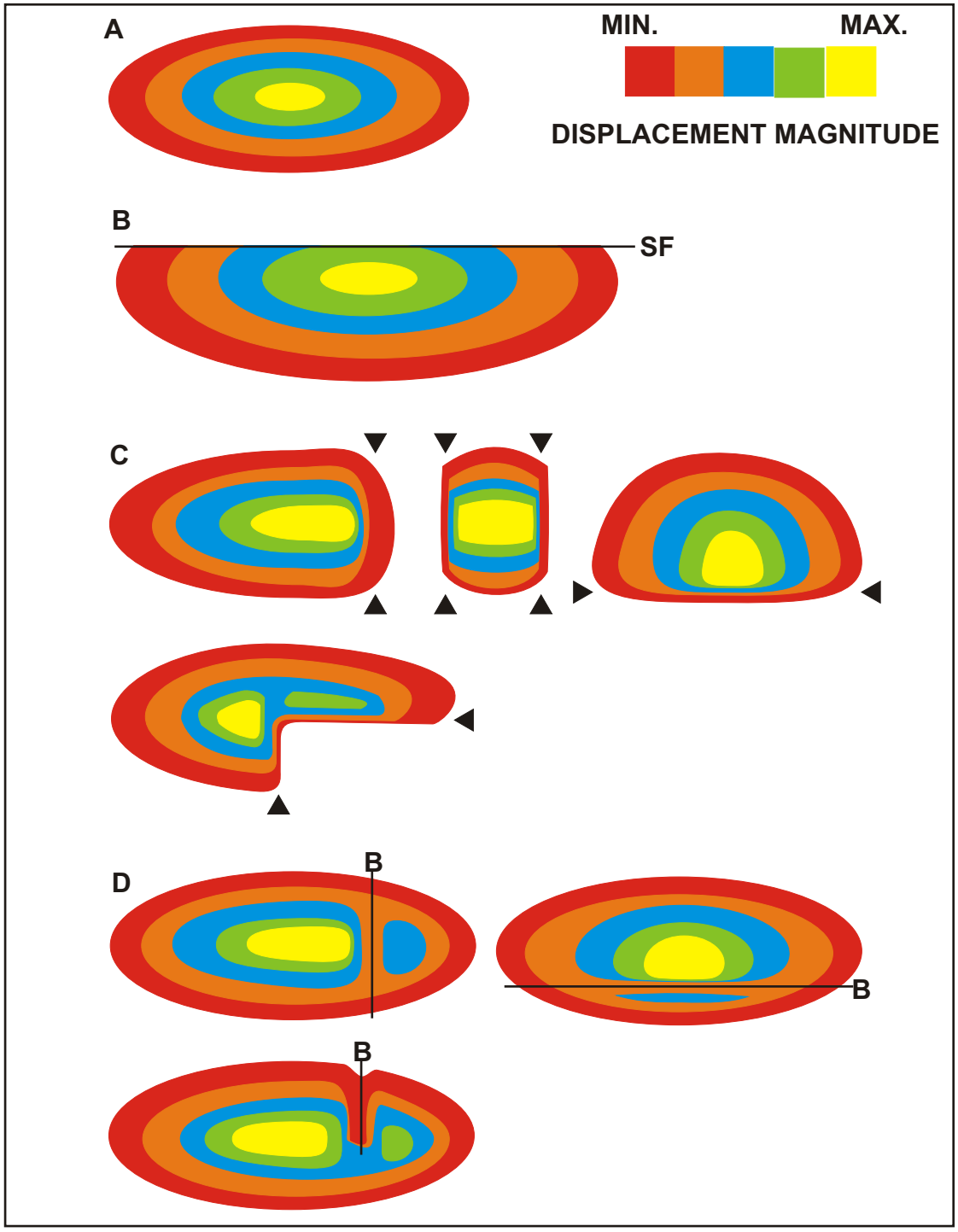

FIGURE 10: Strike projections of fault geometries and displacement (slip) distributions. A. Unrestricted fault. B. Fault restricted by the seafloor (SF). C. Faults restricted laterally and vertically by other faults (indicated by triangles). D. Fault geometries and displacement distributions preturbed by laterally and vertically branching faults (B). (Based on Figure 4, Willemse and Pollard, 2000).

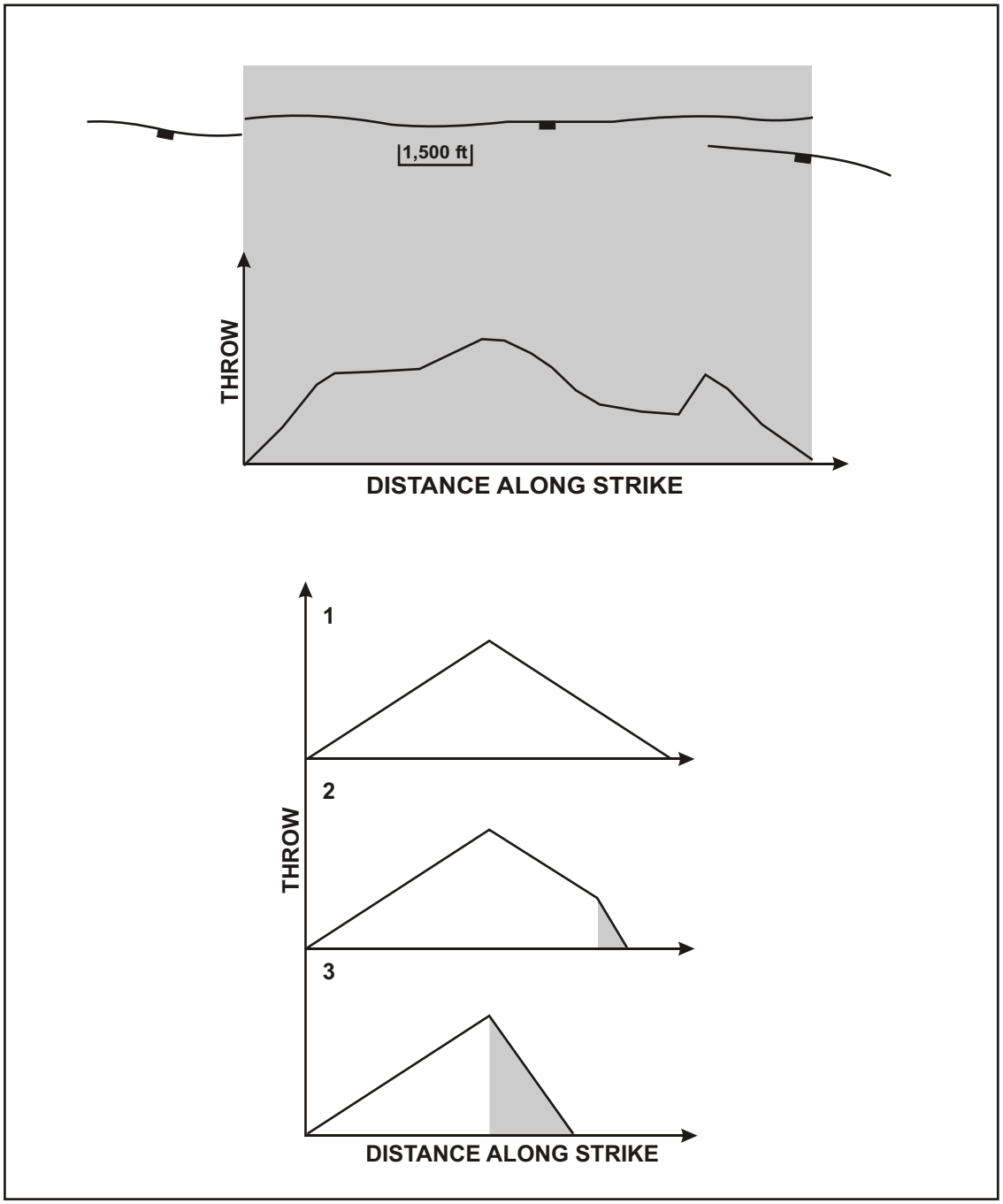

FIGURE 11: Map view and distance versus throw plots for restricted faults. Upper portion of figure shows a map view of a fault that is restricted at both tips by other faults, and a possible plot of throw (displacement) versus distance along strike for the long fault. Gray shading indicates the distance over with the fault is restricted by the two smaller faults. Lower portion of figure shows three example plots of throw versus distance along strike of a fault. In 1, the fault is unrestricted and shows the expected smooth distribution of throw along trace. In 2 and 3, the fault is restricted by another fault either at its tip (2), or along about half of its length (3). Restricted portions of the throw versus strike trace distance are shaded gray. (Based on Figure 2, Nichol et al., 1996).

fault to deviate from an ellipse without a corresponding deviation in the fault's displacement pattern (part B of Figure 10). This means that free surfaces represent *displacement discontinuities* where no tipline exists, yet the fault has a physical bound. Consequently, faults that form near a free surface boundary and grow to intersect the free surface tend to display maximum values of trace length and displacement at the free surface (Barnett et al., 1987).

Several authors have found an important relationship between fault trace length and maximum displacement (Barnett et al., 1987, Cartwright, et al., 1995, Cartwright et al., 1996, Mansfield and Cartwright, 1996, Nichol et al., 1996a and b, Willemse and Pollard, 2000). This relationship was developed for populations of unrestricted, single-segment faults, but has also been found to hold for restricted and segmented faults. This includes faults that intersect a free surface. The relationship is a power law stated as follows:

$$D = cL^n \quad (1)$$

D is maximum displacement on the fault, L is fault trace length, c is displacement axis intercept, and n is the power law exponent, which typically ranges between values of 1 and 2 in the literature (Cartwright et al., 1996).

Growth and Interaction of Faults. Fault growth occurs by two interrelated processes. These processes are considered to be independent of scale, occurring on faults of various sizes. The presence or absence of outside influences on growth such as interaction with other faults, free surfaces, and mechanical anisotropies within the subsurface rock mass determine which of the growth processes is dominant at any particular time on a fault.

Fault Growth by Tipline Propagation. The first of these growth processes is the enlargement of single-segment faults by continued displacement and consequent outward propagation of the tipline. This process has been described by numerous authors, including Barnett et al. (1987), Nichol et al. (1996b), and Willemse and Pollard (2000), and is the means by which fault segments grow in response to the continued accumulation of displacement on the fault. Outward expansion of the tipline (tipline propagation) is the dominant process by which faults grow only in the case where the fault does not interact with another fault.

Fault formation and growth are the brittle deformational response to the influence of a stress field that acts within the rock body. As displacement aggregates along a fault, the rock body surrounding the fault must accept the accompanying strain. Initially, this strain is elastic in nature, representing the potential energy transferred to the rock mass through the expenditure of kinetic energy in producing displacement along the fault. Through time, elastic strain is relaxed into permanent strain in the form of volume strain and shear strain (Barnett et al., 1987). Volume strains are those that require a change in the rock volume, and occur parallel to fault slip. Such strains may be accommodated by compaction, pressure solution, grain breakage, dilation, the formation of secondary antithetic or synthetic faults, or other processes. Commonly observed examples of volume strain are drag in the fault hanging wall and uplift in the footwall (Barnett et al., 1987, Chapman and Meneilly, 1991, Mansfield and Cartwright, 1996). Shear strains do not require a volume change and may be accommodated by some of the same processes as are volume strains. Other processes operating on scales ranging from relatively small-scale mineral dislocation and grain rotation to larger-scale formation of antithetic and synthetic secondary faults may act to accommodate shear strain.

The actual process of fault growth by tipline expansion outward from the fault center is related to perturbations of the stress field in the vicinity of the fault tipline. The results of numerous model and experimental investigations of stress fields in the vicinity of a crack have been extended to faults. These results show that stress is localized within a zone of unfaulted rock just beyond the fault tipline. There, the magnitude of the stress exceeds the average stress level within the rock mass containing the fault (Figure 12). In this case, a stress concentration exists. Conversely, those areas of the rock mass that are in the immediate vicinity of the fault plane away from the tip areas are characterized by stress magnitudes that are less than the average stress level within the rock mass, and a stress deficiency exists. The result of this uneven stress distribution is the tendency for a fault to grow by tipline propagation in the direction of the stress concentration. Propagation of the fault tipline locally reduces the state of stress in the rock body as the stress is converted into displacement and strain. Tipline

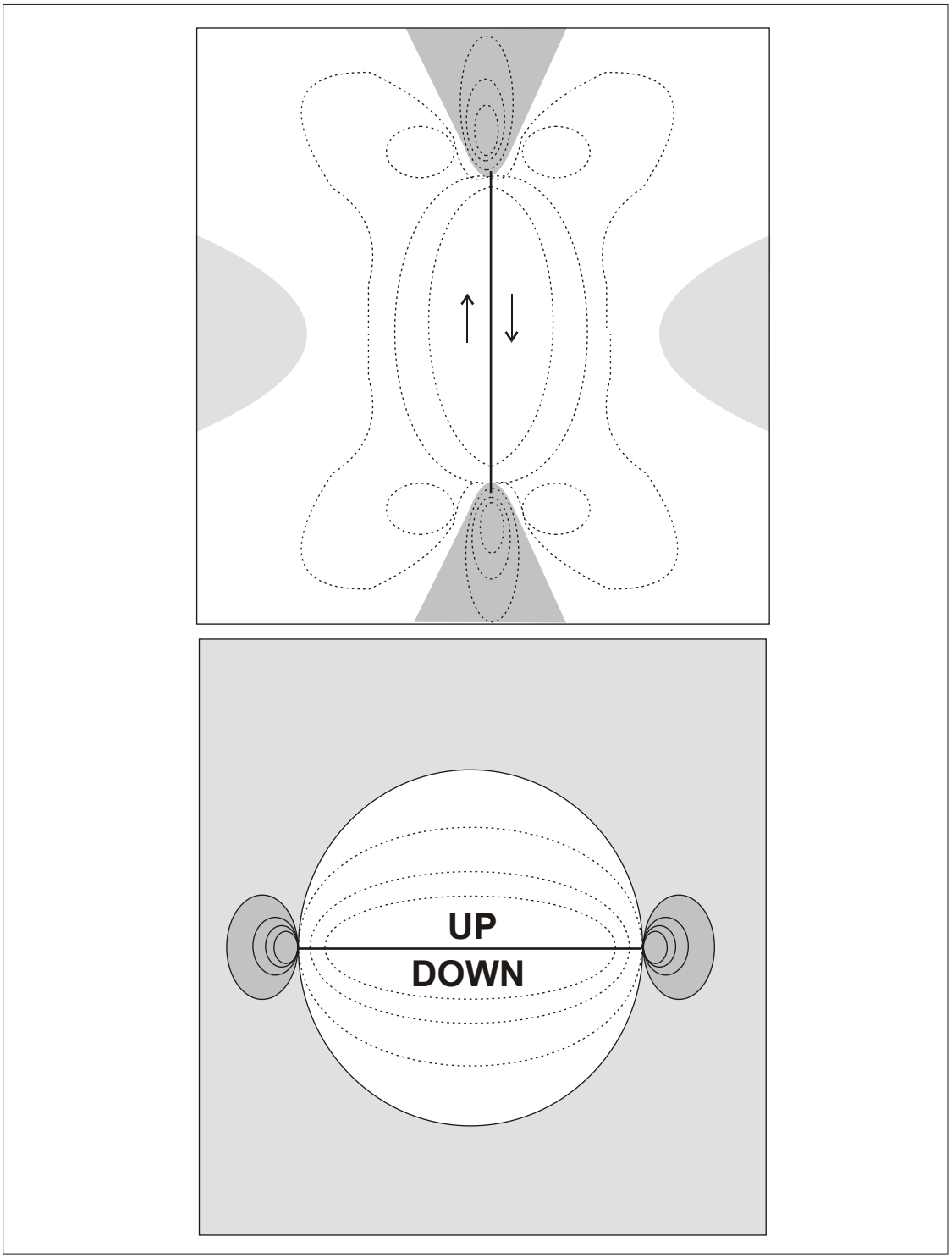

FIGURE 12: Vertical (upper) and horizontal (lower) sections through a single-segment fault. Dotted curves are shear stress contours. Dark shading represents areas of enhanced shear stress, and white areas are characterized by a drop in shear stress (stress shadow). Light shading represents areas of normal shear stress. (Based on Figure 5, Willemse and Pollard, 2000).

propagation continues to occur as long as the stress field within the rock body is of sufficient magnitude to cause the rock to locally rupture (propagate the fault through the rock). If the stress field magnitude is reduced, or if the fault encounters a layer with significantly contrasting mechanical properties, growth of the fault by tipline propagation may be less likely or may stop (Barnett et al., 1987, Burgmann and Pollard, 1994, Willemse and Pollard, 2000).

Fault Interaction and Linkage. It is common in nature that many faults exist within a body of rock in close proximity to one another, and because of this, these faults interact with each other when they grow. Interacting faults may be described as being either *soft linked* or *hard linked*. Soft-linked faults are not connected and therefore do not represent a continuous discrete discontinuity or zone of discontinuity in the rock body that characterizes a through-going fault. The connection between soft-linked faults lies in the interaction between the faults' stress fields. This interaction allows for displacement to be shared between the faults and for the individual faults to continue to accommodate strain. The unfaulted rock between the faults also accommodates some of this strain because no physical linkage is present to transmit strain between the faults (Burgmann and Pollard, 1994, Trudgill and Cartwright, 1994, Cartwright et al., 1995, Cartwright et al., 1996). Hard-linked faults have interconnected stress fields and are also physically connected together. The point of connection of hard-linked faults represents a through-going discontinuity in the rock body.

Numerous authors have shown that fault interaction and linkage are processes that ultimately lead to the enlargement of faults. This occurs as unlinked faults grow in size until they begin to interact, when they are considered to be soft linked. The growth of soft-linked faults leads to hard linkage, and continued displacement on hard-linked faults culminates in the formation of a fault that behaves as a single-segment fault (Cartwright et al., 1995, Dawers and Anders, 1995, Cartwright et al., 1996, Contreras et al., 2000). The following sections describe processes that occur as faults begin to interact and link and is based on observations and models presented by numerous authors.

Soft Linkage. Two faults must be situated within a minimum separation distance if interaction is to occur between then. If the faults grow in such a way that this condition is never met, then no interaction will occur between the faults and they will exist independent of each other. However, if the two faults grow to the point that their tiplines are within about a fault radius of each other, their stress fields begin to interact and exert influence on one another (Burgmann and Pollard, 1994, Cartwright et al., 1996, Willemse and Pollard, 2000). The orientation of the faults with respect to each other and the positions of their tiplines determines whether this interaction is positive (locally promotes fault growth), or negative (locally retards growth).

A review of Figure 12 shows that stress concentrations exist within the unfaulted rock adjacent to a fault tipline, and a stress shadow exists in the rock body adjacent to the fault and behind the tipline. Consider the case of two faults with essentially the same strike and sense of offset that are initially separated so far apart that their stress fields do not interact (part A of Figure 13). Also, the faults are positioned so that lateral propagation of one or both faults will cause eventual interaction. The faults will accommodate displacement in response to stress within the rock body and their tiplines will expand as a result. As the faults grow, the portions of the faults located closest to each other begin to encounter the concentrated stress in the region beyond the tipline. As a result of this interaction, the faults are considered to be in the early stage of soft linkage. This condition locally enhances the tendency for propagation, and the faults will preferentially grow toward each other. If the fault tiplines are arranged geometrically so that continued propagation will directly join the two faults into one discontinuity, then the faults will link into one larger fault.

If fault geometry dictates that the tiplines will not directly meet as tipline propagation proceeds, then the tiplines will begin to propagate past one another. In this case, the interacting portions of the two faults will continue to grow in this enhanced condition until the tiplines pass out of the areas of concentrated stress and into the stress shadows. Now, the portions of the faults within the stress shadows have a very low tendency for growth and tipline propagation is locally retarded. Those portions of the fault outside the stress shadows will continue to grow

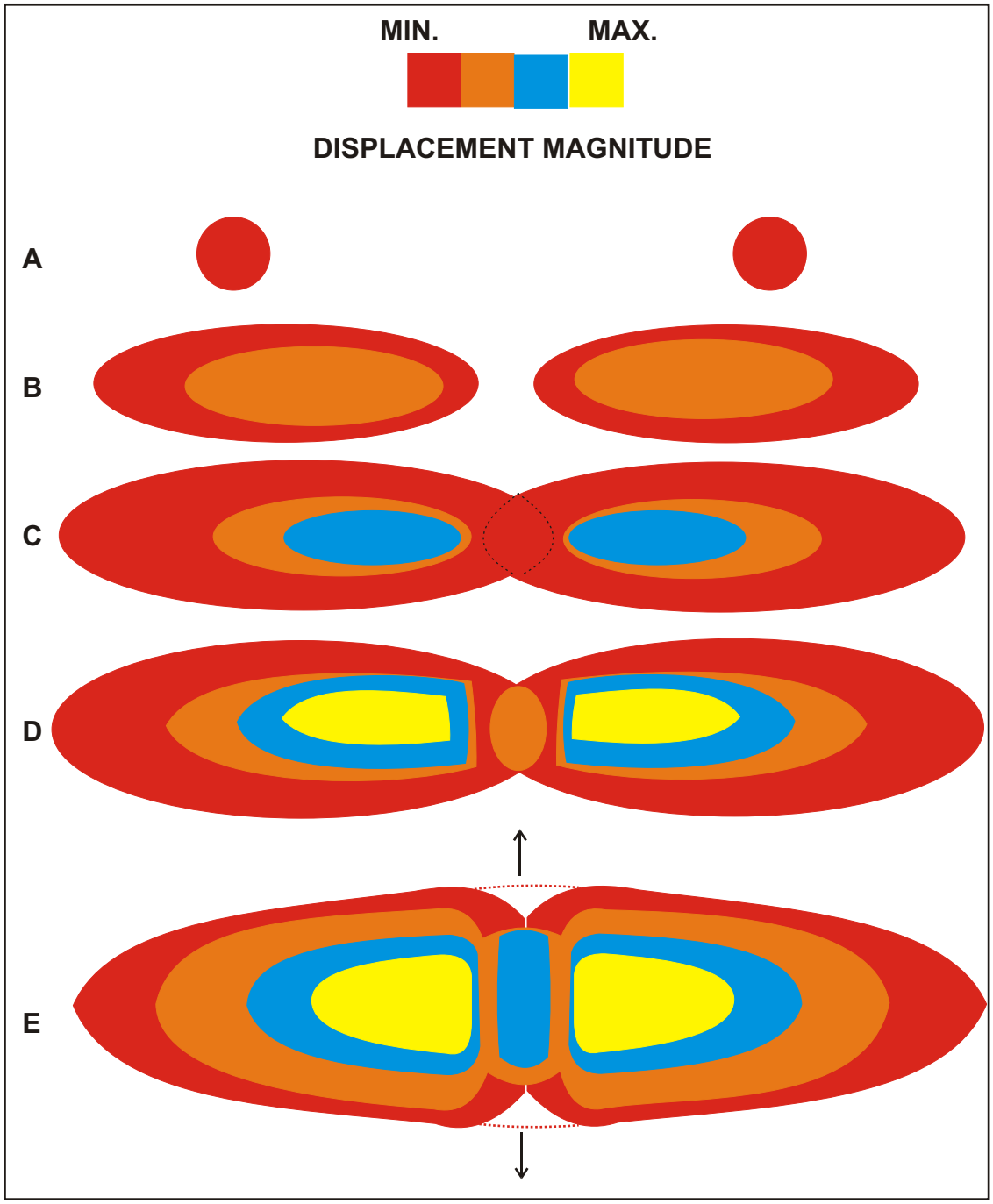

FIGURE 13: Strike projection views of fault growth and coalescence. A. Initial stage of two circular flaws. B. Two elliptical, underlapping faults. C. Faults overlap in a small zone and propogation is arrested. Lateral propogation tendendy is enhanced just above and below this zone. D. Relay zone forms where faults overlap. Tiplines are locally steeply-plunging, and displacement gradients are locally high. E. High tendency for propogation exists above, below, and immediately beside the relay zone. With continued displacement, the relay zone breaks down and a smooth displacement distribution is re-established. (Based on Figure 11, Willemse and Pollard, 2000).

normally, and where the faults are within stress concentrations growth will continue to be enhanced. This tendency toward localized retarded and enhanced growth patterns is shown for several cases of fault interaction in Figure 14, where growth tendency is plotted as a function of angular position on the tipline. This distribution of growth tendency results in modification of the fault shape in the zone where the two faults overlap. Work by several authors, including Dawers and Anders (1995), Nichol et al. (1996b), Contreras et al. (2000), and Willemse and Pollard (2000), has shown that tiplines become flatter perpendicular to the direction of interaction. This change in tipline shape represents a major departure from the inferred elliptical shape of unrestricted faults and their characteristic smooth displacement gradients. In the zone of overlap, displacement gradients increase as more and more displacement is accommodated over a relatively short portion of the fault length (parts B-D of Figure 13). Considering the two faults together, the amount of displacement per unit length of the two-fault system increases because growth is retarded on the interacting portion of each of the faults.

As non-overlapping portions of the faults continue to grow, the soft linked overlapping portions must accommodate the accumulating displacement by applying inelastic strains to the intervening rock body and by forming secondary deformational structures (Barnett et al., 1987, Burgmann and Pollard, 1994, Trudgill and Cartwright, 1994, Mansfield and Cartwright, 1996, Walsh et al., 1999). These secondary structures may include relay ramps and smaller antithetic or synthetic faults and are symptomatic of the inability of the intervening unfaulted rock body to accommodate any more inelastic strain without failing.

Hard Linkage. If the faults continue to accumulate displacement and grow in their non-overlapping areas, processes of inelastic deformation and the accommodation of displacement on secondary structures will also continue to occur in the soft-linked overlap zone. At some finite level of strain, the intervening rock in the overlap zone will fail such that a through-going fault connects the formerly soft-linked faults. The faults are now hard linked, and the former stress conditions existing between the two separated faults are modified to reflect the

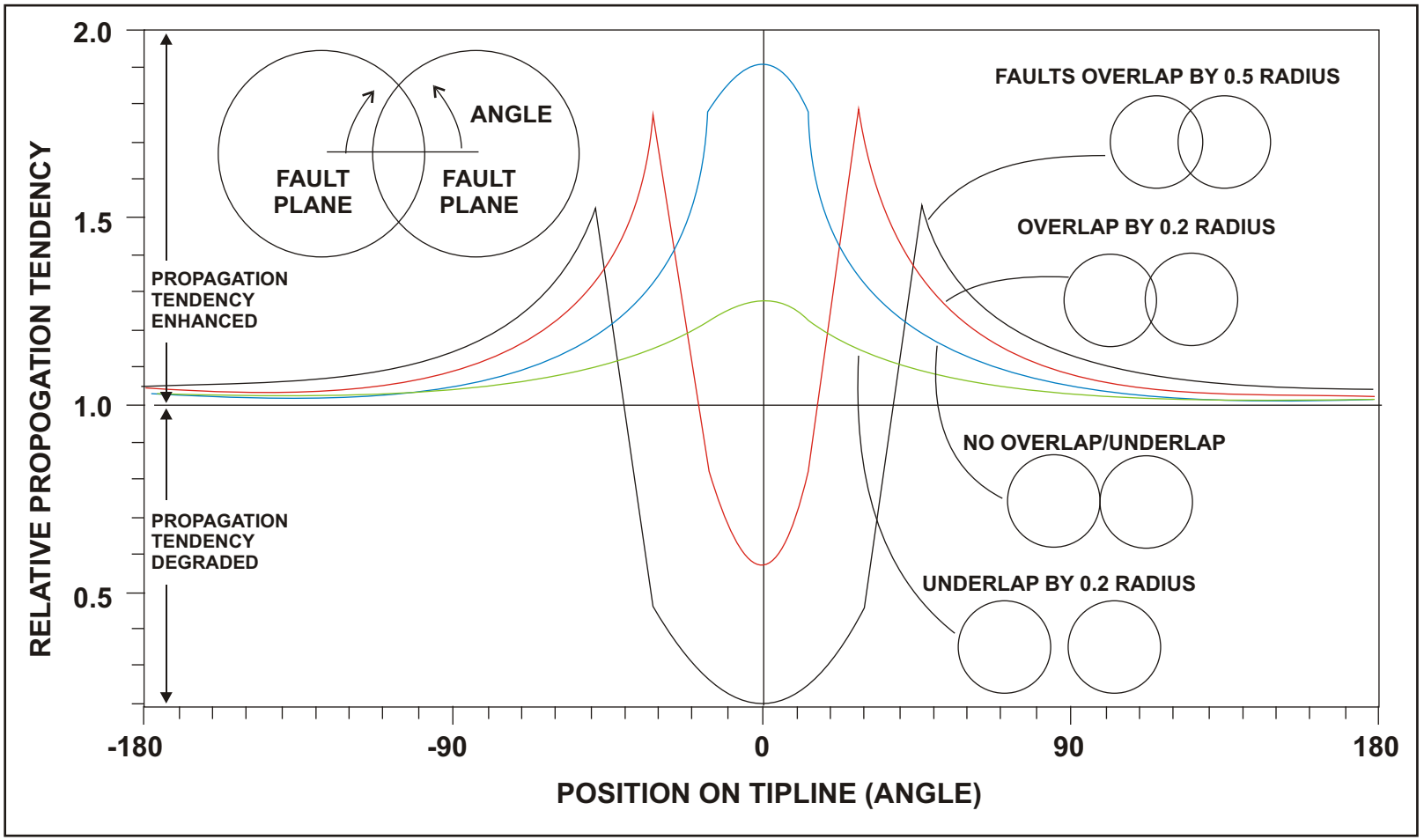

FIGURE 14: Graphic display of the fault propagation tendency for interacting faults. Relative tendency for propagation of faults in close proximity or overlapping is shown as a function of angular position on the fault tipline. Propagation tendency in enhanced as faults grow closer together, but is greatly reduced in areas of fault overlap. (Based on Figure 9, Willemse and Pollard, 2000).

identity of one fault. The length of the combined faults may exceed the length that a single-segment fault with the same maximum displacement might have.

Authors who have compared the characteristics of seismic faults to models of fault linkage, including Mansfield and Cartwright (1996) and Nichol et al. (1996b), have noted that seismic slip events typically occur on a small portion of a fault, usually one or two segments. Segment boundaries of these seismic faults may consist of offsets, bends, or breached relay structures and represent locations on the fault where the mechanical strength of the rock body exceeds the tendency for a seismic rupture event to spread from one segment to another. Thus, for the case of zones of hard linkage between two faults, the area of linkage may retain some of its former strength. Large faults are thought to represent a patchwork of smaller linked faults that have been assimilated together into a larger structure. Through conclusions reached in numerous studies, it is widely accepted that most large faults display relatively smooth displacement distributions that are similar to a single fault segment, as opposed to a distribution similar to that of numerous faults linked at comparatively strong zones. This means that as the regional stress field continues to promote growth of the hard-linked faults, the processes that accommodate strain in the rock body around the fault and along the fault surface act to destroy the remnant geometry and strength of the former two- or multi-fault system and to smooth out any other sources of roughness on the fault surface that resist displacement (Dawers and Anders, 1995, Cartwright et al., 1996, Nichol et al., 1996b). Figure 13 shows diagrammatically how these processes of linkage occur between two initially separate faults.

Cycles of Fault Linkage. As the result of the coalescence of smaller faults into larger ones through growth processes, and because fault growth periodically places fault tips in such a position that interaction occurs, then it follows that fault linkage must happen cyclically. This cyclic pattern of growth processes comprises the model of fault growth by tipline propagation and fault segment interaction. Within a given faulted area, it is expected that faults of varying sizes and varying stages of interaction will exist. These processes may manifest themselves

visibly on the seafloor or land surface as ranges in fault trace length, ranges in fault scarp relief, and unique trace geometries resulting from fault linkage and branching.

Effects of Fault Linkage on Fault Dimensions and Displacement. Interaction of faults with each other, free surfaces, or layers with mechanically contrasting properties are all causes of perturbations in the dimensions and displacement characteristics of faults. These deviations from the idealic smooth displacement gradients and elliptical tipline shape can be detected and characterized by examining selected key fault dimensions. One of the most commonly discussed relationships between fault dimensions is the power law equation relating maximum displacement to trace length, described earlier. Another useful relationship is the ratio of the fault's strike dimension to dip dimension (Nichol et al., 1996b).

A quantitative characterization of the dimensions of the fault group would likely yield scatter in the results rather than close agreement between data points (the individual faults) because unrestricted and restricted faults and faults in different stages of interaction and linkage may exist in the same area. Cartwright et al. (1995), Cartwright et al. (1996), Mansfield and Cartwright (1996), Nichol et al. (1996a and b), and Cartwright et al. (1998) state that measurement errors may account for some of this observed scatter, but the remainder of the scatter is real and is the result of interactions and linkage. For laterally-restricted faults, the lateral dimension is restricted, and ratios of strike dimension to dip dimension are skewed toward lower than average values. The reverse is true for vertically-restricted faults, where the dip dimension is restricted by interactions or layering. This is shown for faults from various geologic provinces in Figure 15 and Figure 16. Similar scatter would be expected in maximum displacement versus trace length data for the same sets of faults. Figure 17 shows an idealized example of how maximum displacement and trace length vary for two cycles of linkage on a growing fault, and Figure 18 shows how the two parameters vary when growth by linkage is compared to growth by tipline propagation.

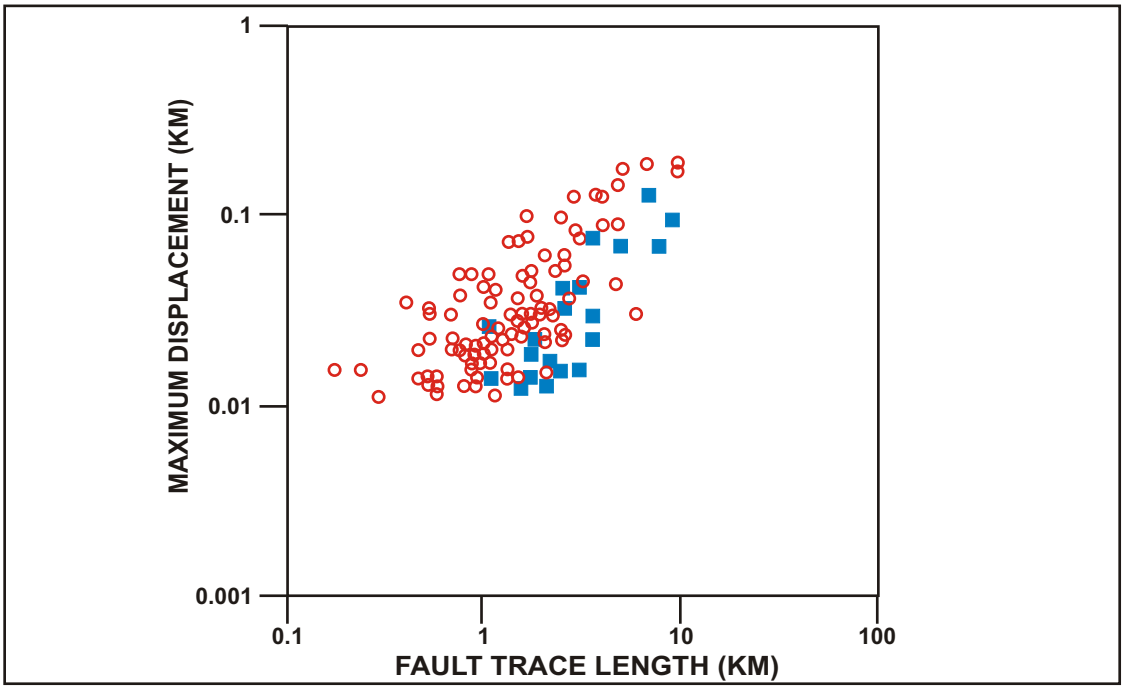

FIGURE 15: Maximum displacement versus fault trace length for 167 faults from the Timor Sea. Laterally restricted faults (red circles) display higher length-scaled maximum displacement than do laterally unrestricted faults (blue squares). (Based on Figure 15, Nichol et al., 1996a).

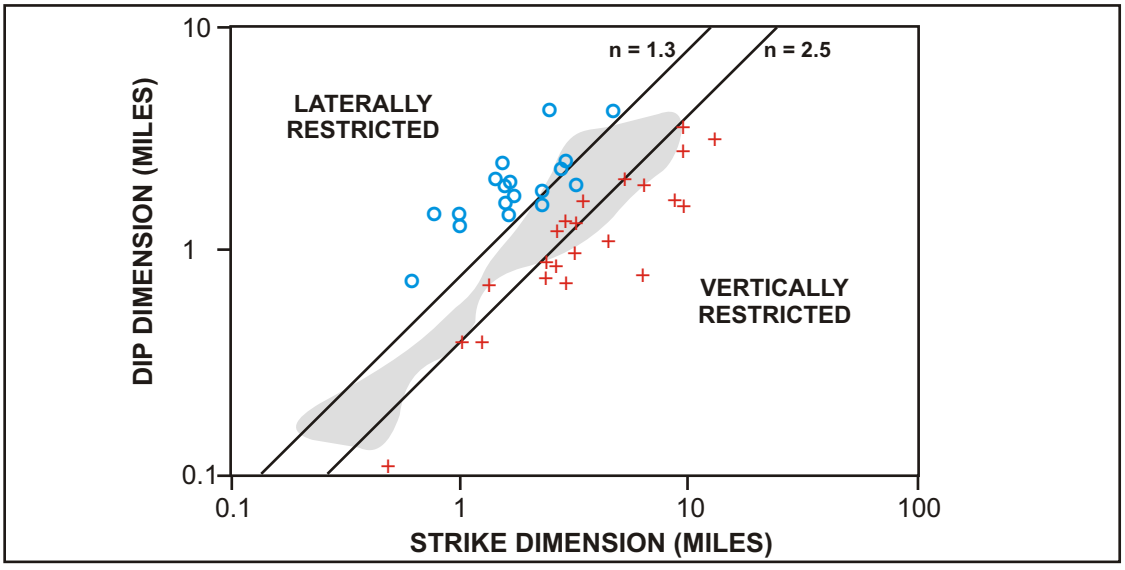

FIGURE 16: Dip dimension versus strike dimension for 39 faults from four different geologic provinces: British coal mines, Timor Sea, Gulf Coast, and North Sea. Laterally restricted faults are blue circles and vertically restricted faults are red crosses. Unrestricted faults plot in the shaded area. Here n is the aspect ratio of strike dimension to dip dimension and distinguishes between lateral restriction and vertical restriction. (Based on Figure 12, Nichol et al., 1996a).

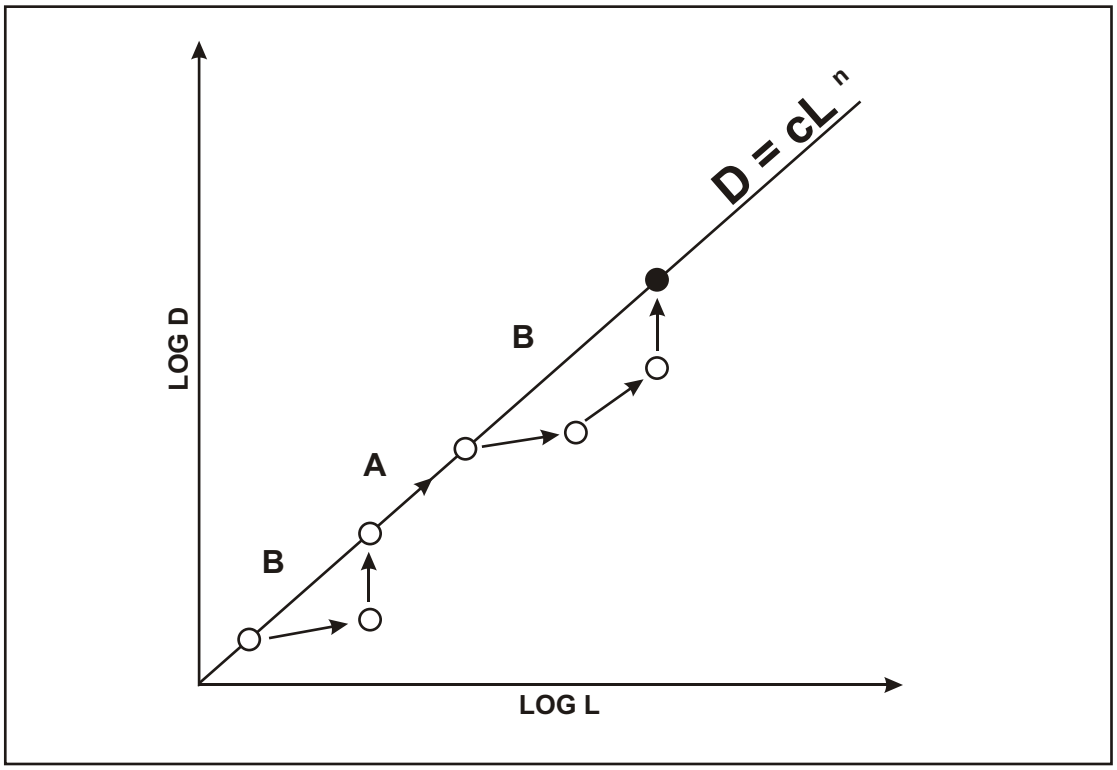

FIGURE 17: Idealized plot of log D vs. log L for a fault growing by cycles of radial tipline propagation and segment linkage. Tipline propagation tends to obey the power law relationship, and follows the line (segment A). Periods of growth by segment linkage deviate from the power law relationship during linkage and converge with the power law relationship after linkage has been accomplished (segments B). (Based on Figure 5, Cartwright et al., 1995).

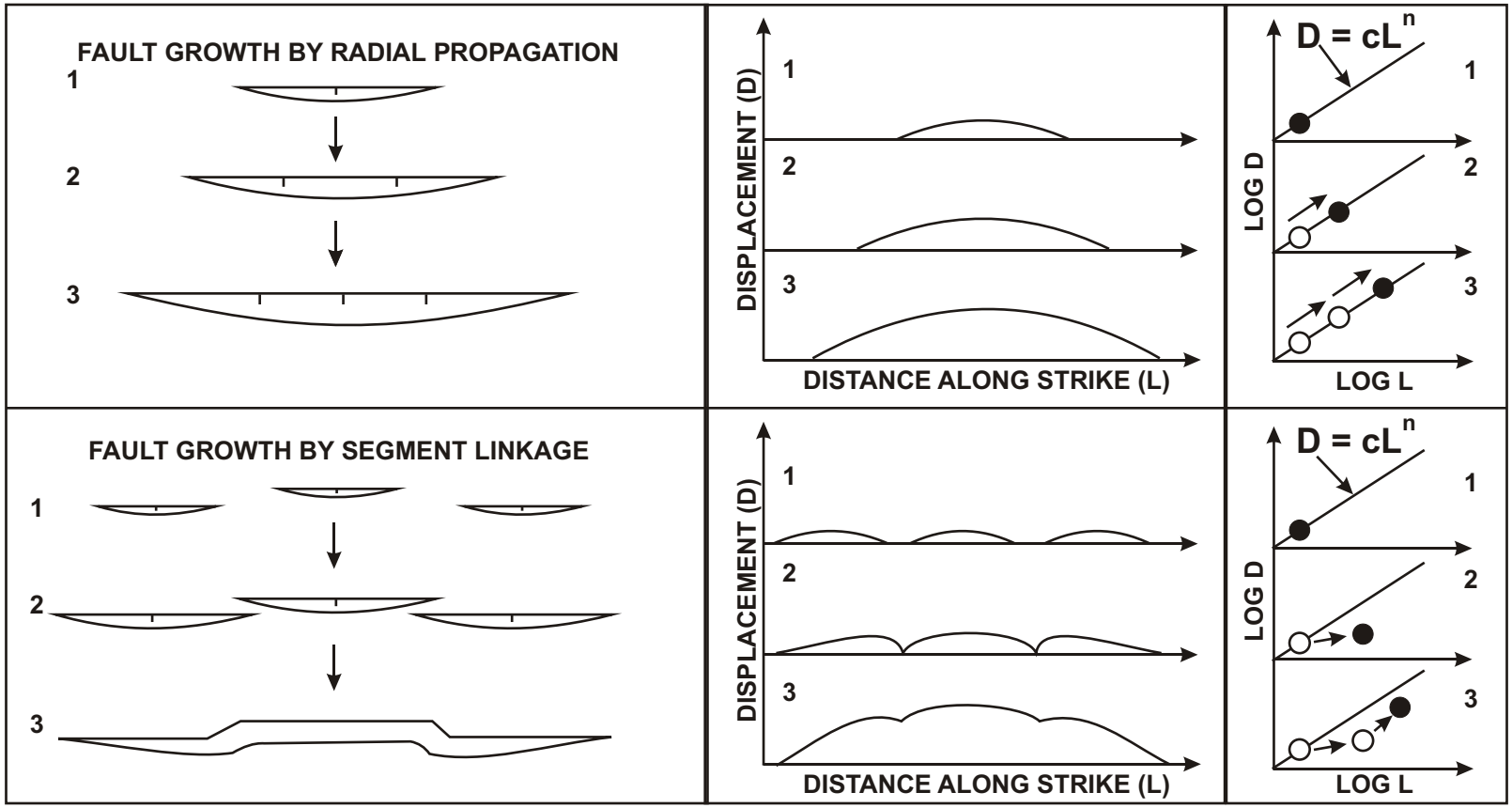

FIGURE 18: Two models of fault growth: radial propagation of the tipline and growth by fault segment linkage. As displacement proceeds, the fault or fault segments grow. This is shown in map view in the left-hand panels. Middle panels show displacement as a function of position along strike (along trace) of the fault or faults. Right-hand panels show relationship between displacement (D) and trace length (L) for the three-step growth progression. Each previous growth step is represented by an open circle. Dark circles represent the final growth step. Growth by tipline propagation displays a linear progression. Growth by fault linkage displays a progression that deviates from the power law equation slope. These deviations indicate that the length of linked fault exceeds the displacement on the linked fault predicted by the power law. Continued displacement with slowed lateral propagation continues until the ratio of log D to log L again falls on the power law line. (Based on Figure 4, Cartwright et al., 1995).

Previous Similar Work by Other Authors

Numerous authors have conducted studies of normal faults using various methods of measuring fault displacement along strike and down dip. The faults range in size from hundreds of feet to several tens of miles in length and are located in widely spaced geologic provinces. The methods used to measure displacements were partly a function of the goals of the study, and partly dictated by circumstance. In some cases, direct field measurements were taken without difficulty at surface scarps and within underground mine adits. Seismic data were used in other cases for faults located in the marine environment or when measurements of displacements at subsurface horizon offsets were desired. Selected examples of published works in which the measurement of throw was used to characterize faulting are discussed here.

Field Measurement Studies. In field studies of faults, the investigator is generally not able to make measurements of displacement or its components over the entire fault surface. Most studies of this type are limited to the uppermost portions of the fault that are exposed at the surface.

Work done by Trudgill and Cartwright (1994), Cartwright et al. (1995), and Cartwright et al. (1996) focused on the use of surface mapping of fault throw at normal fault scarps within the Canyonlands Grabens of Utah. This area contains numerous faulted grabens that have been interpreted to date to late Pleistocene time. Incision of a canyon by the Colorado River to the west of the Canyonlands area at that time promoted flow of Pennsylvanian-age Paradox evaporites at shallow subsurface depths toward the unloaded and unbounded riverbed where removal of the evaporites by dissolution occurred. As the evaporitic substrate was evacuated, the lithified siliciclastic overburden suffered gravitational collapse into the voided spaces in the form of near-vertical normal faulting.

Initial fault mapping was done on aerial photographs. Field observations and measurements were made at about 165 ft and 330 ft (about 50 m and 100 m) spacings along fault traces by surveying the vertical distance between correlable strata present in both the hanging wall and footwall. The authors indicate that erosion is expected to cause no appreciable

error in the results, since the faults are relatively young, the arid environment suppresses significant weathering, and allowances for minor erosion of hanging wall scarps and accumulation of alluvium and colluvium in the fault footwalls were made. A total of 97 faults were investigated in their study area, and many of these faults displayed visual indications of imminent or past interaction, including the presence of relay ramps and apparent displacement variations along strike.

Figure 19 and Figure 20 show results from the Canyonlands Grabens fault study. Figure 19 shows a displacement (throw) versus trace length plot for a graben fault identified as containing several linked and branching segments. Overall shape of the plot resembles the expected distribution of throw for a single segment, but the details reveal the true nature of the fault's numerous localized throw maxima and minima. Figure 20 shows a maximum displacement (maximum throw) versus trace length plot for several of the Canyonlands Grabens faults. The left-hand portion of the figure demonstrates the scatter in D versus L values for the faults, while the right-hand portions shows that this scatter is within expectations for a population of faults when data from numerous other areas are considered.

The authors concluded that displacement mapping along fault traces is a valuable tool in the investigation of fault linkage, and that the graben faults within their study area display several different stages of interaction. Relay ramps between some interacting faults accommodate soft linkage and some of the inelastic strain in the relay zone. The strain is manifested in distributed deformations such as distortion and twisting of the rock, and cracking. On some faults displaying relay structures, fault growth continued as soft linkages matured into hard linkages. Relay ramps were internally deformed to the point that they were breached by through-going faults (Figure 21). These connecting faults allowed displacement to become evenly distributed across the lateral extent of the newly hard-linked fault. With continued displacement and fault growth, the displacement distribution more closely resembled that of a single fault segment. Figure 22 summarizes the authors' conclusions on the evolution of the grabens based on their work.

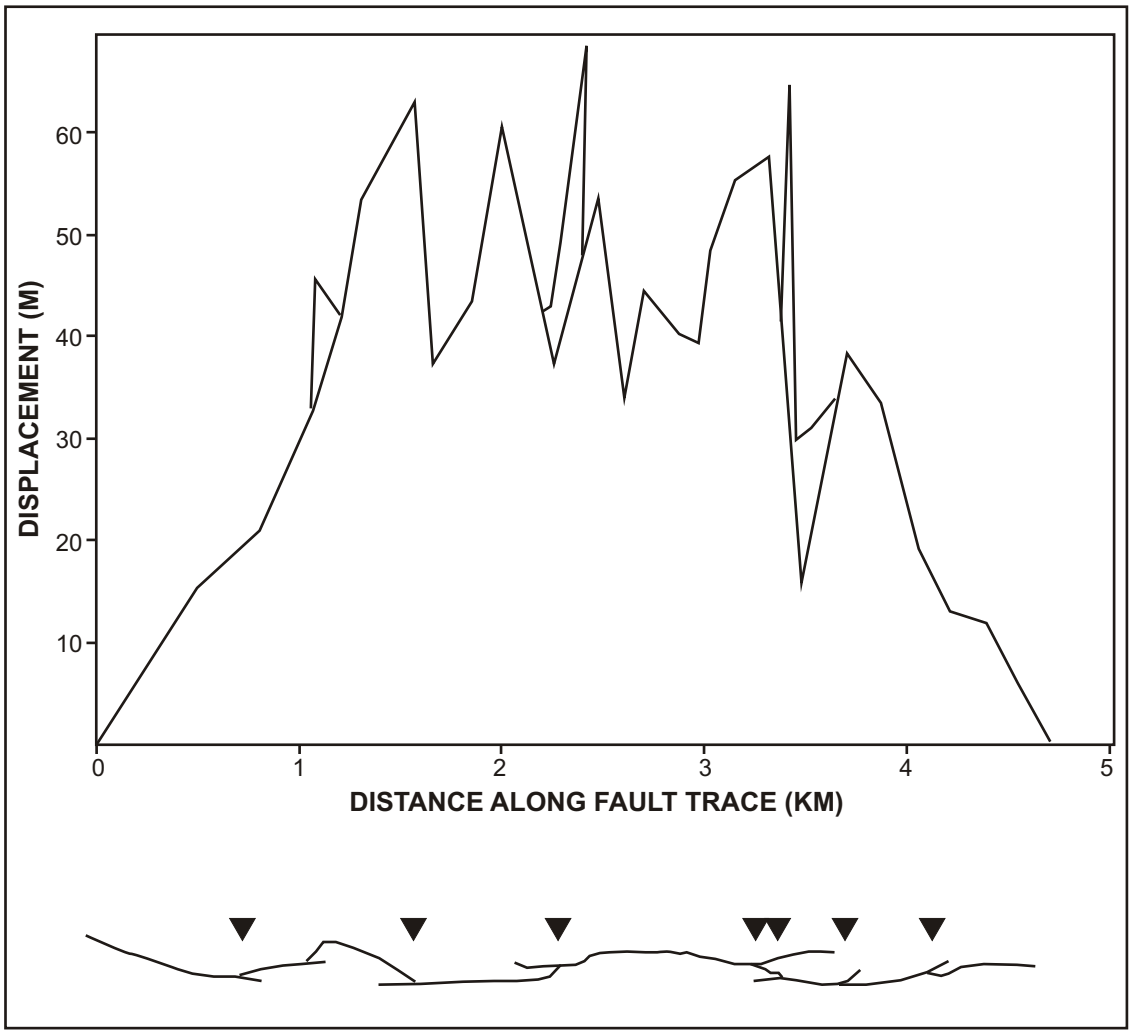

FIGURE 19: Plot of displacement versus distance along trace for a fault in the Canyonlands Grabens of the Colorado Plateau in Utah. A map view representation of the fault trace is shown below the plot, with triangles marking the locations of mappable branch points. Individual segments of the larger fault are obvious in the plot as the individual spikes in displacement. In an overall sense, and disregarding the individual spikes, the form of the plot is similar that expected for a single-segment fault. (Based on Figure 9, Cartwright et al., 1996).

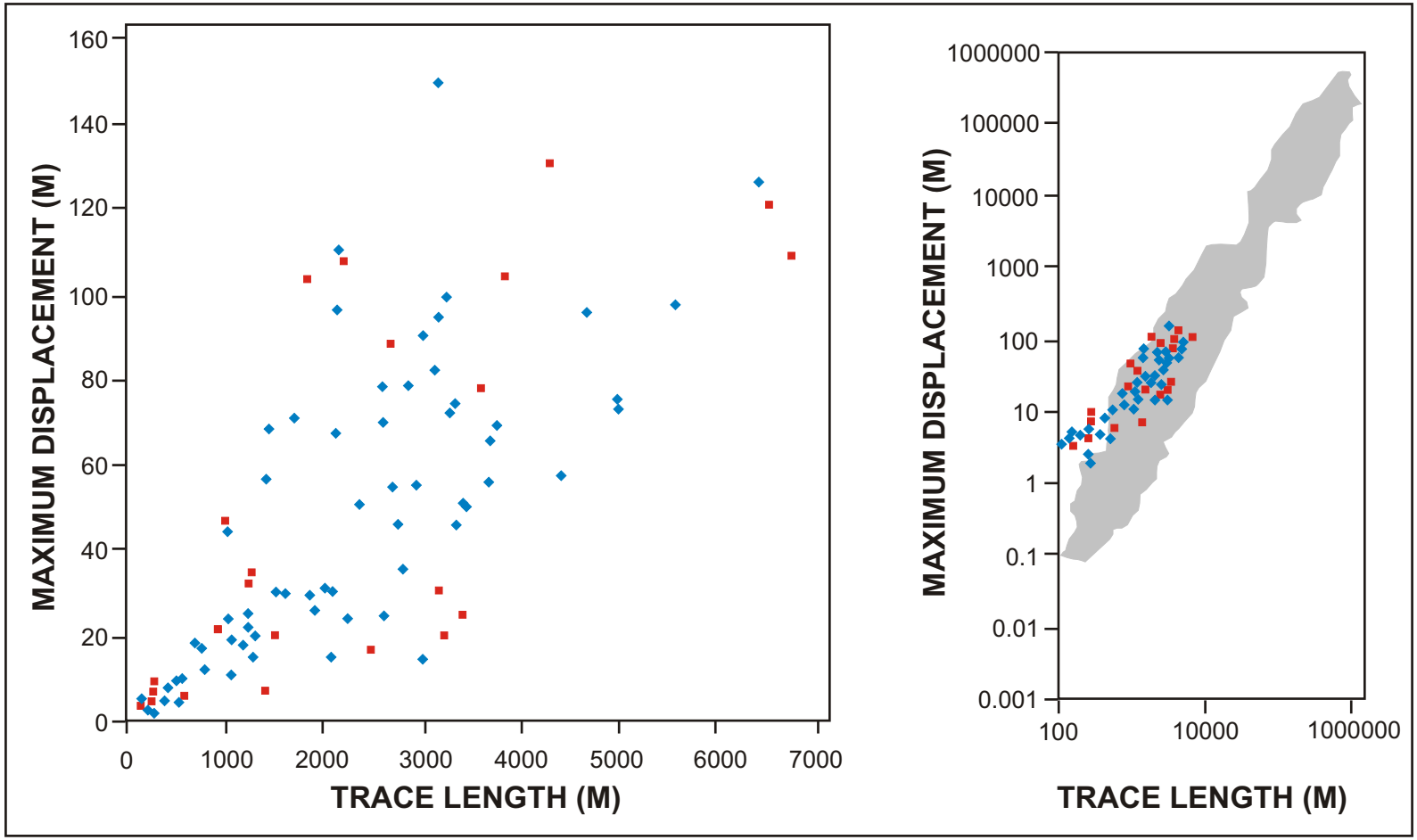

FIGURE 20: Plots of maximum displacement versus trace length for faults from two different areas of the Canyonlands Grabens (red and blue). Left-hand plot shows scatter in the data in normal space. Right-hand plot shows this data in log-log space and in comparison to a compilation of displacement versus trace length data from many different stratigraphic/tectonic settings around the world, shown in grey. A close correspondence is observed between the Canyonlands Grabens faults and those from other locales. (Based on Figure 11, Cartwright et al., 1996).

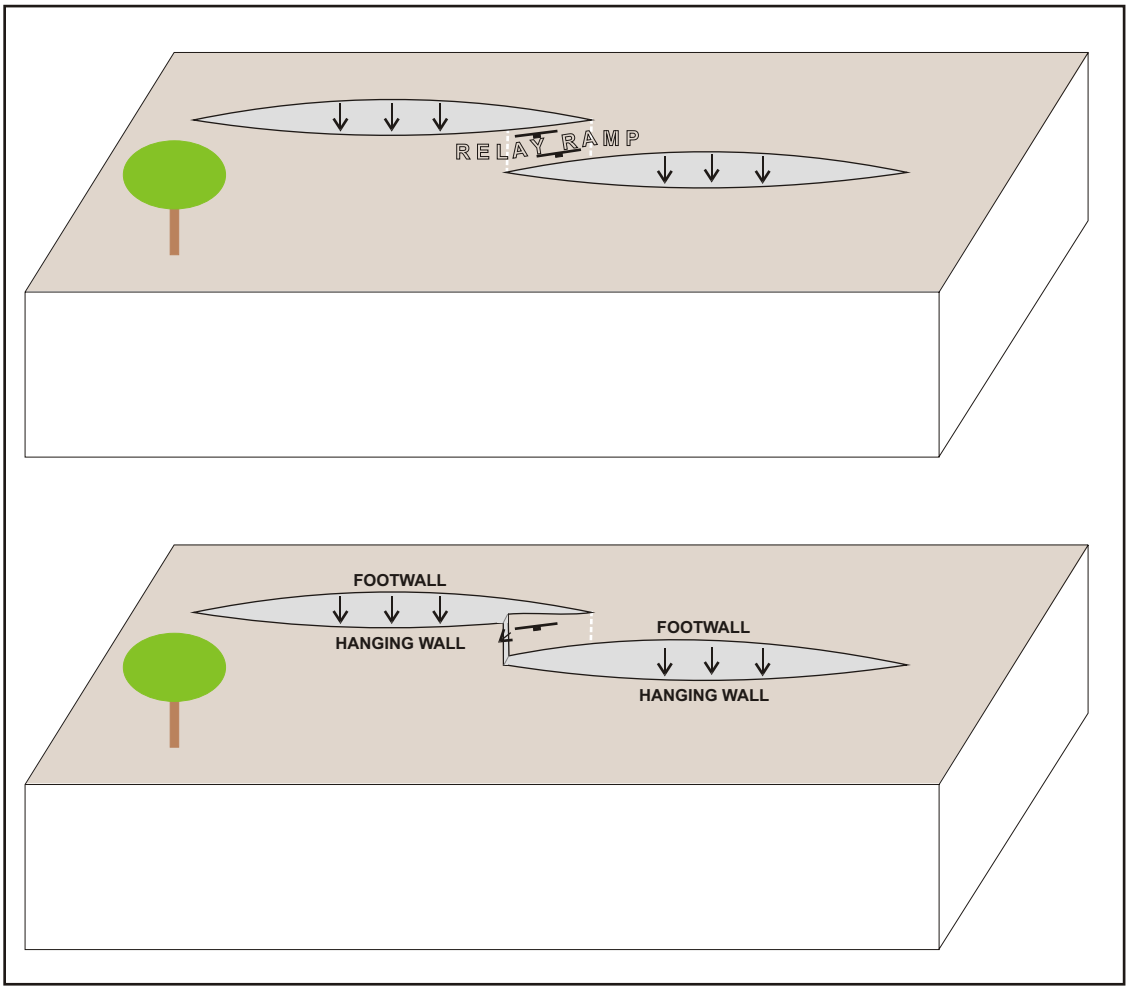

FIGURE 21: Block diagrams showing a relay zone between two interacting normal faults. Upper diagram shows a relay ramp formed in the overlap zone between two interacting, soft-linked normal faults that breach the ground surface. The relay zone may contain highly strained, rotated, and faulted rock, but represents a discontinuity between the two faults. The lower diagram shows hard linkage of the two faults by breaching of the relay ramp. A through-going fault connects the two faults at the hanging wall end of the ramp. A breach could have also developed at the footwall end of the relay ramp, in the vicinity of the white, dashed line.

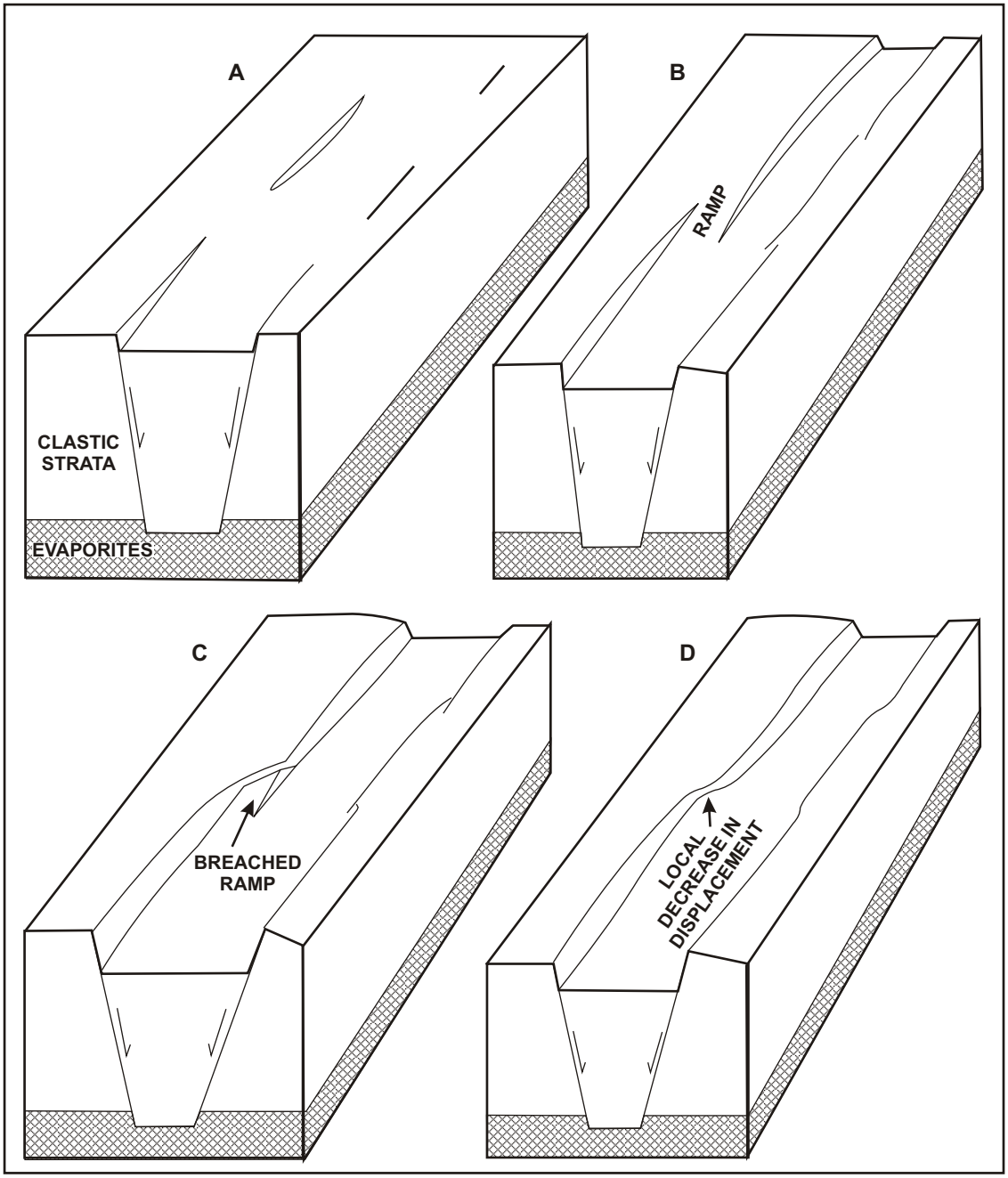

FIGURE 22: Evolutionary model of fault growth by segment linkage in the Canyonlands Grabens. In A, isolated faults grow by tipline propagation. In B, segment overlap leads to soft linkage and development of relay ramp structures. Continued fault growth shown in C leads to breaching of relay ramps as the faults become hard linked. Lastly, in D, displacement profiles along present-day grabens are marked by displacement lows which correspond to the original areas of fault linkage. (Based on Figure 10, Trudgill and Cartwright, 1994).

Contreras et al. (2000) conducted a fault displacement study of the Usisaya bounding fault system of the Lake Malawi Basin, East African Rift. Field studies were supplemented by a very widely spaced grid of 2-D lines (main lines spaced 5 miles apart and tie lines spaced 9.3 miles apart) that was used to map a set of prominent unconformities marking the boundaries of several lacustrine depositional intervals deposited within the basin spanning the period from late Miocene to Pleistocene time. Gridded isopach maps of these intervals were used to estimate increments of basin fill thickness for a given time period adjacent to the bounding faults. The authors assumed that sediment deposition was fault controlled, sediments were continuously supplied to the basin, and that the water level within the basin has represented a relatively constant point between the top of the fault footwall and the top of the hanging wall in the basin through time. With these assumptions dictating the magnitude of possible errors in the results, the authors used thickness variations in the basin fill to determine the displacement history of the Usisaya bounding faults. Results of this work are summarized in Figure 23.

Contreras et al. (2000) were able to establish from the displacement mapping that the three faults segments within their study area have interacted to a progressively greater extent since late Miocene time, and that displacement has been unevenly distributed among the segments during this time period. They also state that displacement gradients increase in the areas of fault segment overlap through time, and that the summed displacements between the central and southern segments is anomalously high in their region of overlap (lower portion of Figure 23). The authors conclude that the bounding fault zone has developed into a linked system having a displacement distribution that increasingly mimics that of a single fault segment.

3-D Seismic Workstation Studies. Several investigations of fault displacement distributions and associated fault characteristics have been undertaken with 2-D or 3-D seismic data. Most of the seismic data that has been used for these studies consists of either sets of exploration (standard resolution) or high-resolution 2-D lines or 3-D exploration seismic volumes, and interpretation was conducted on seismic interpretation workstations.

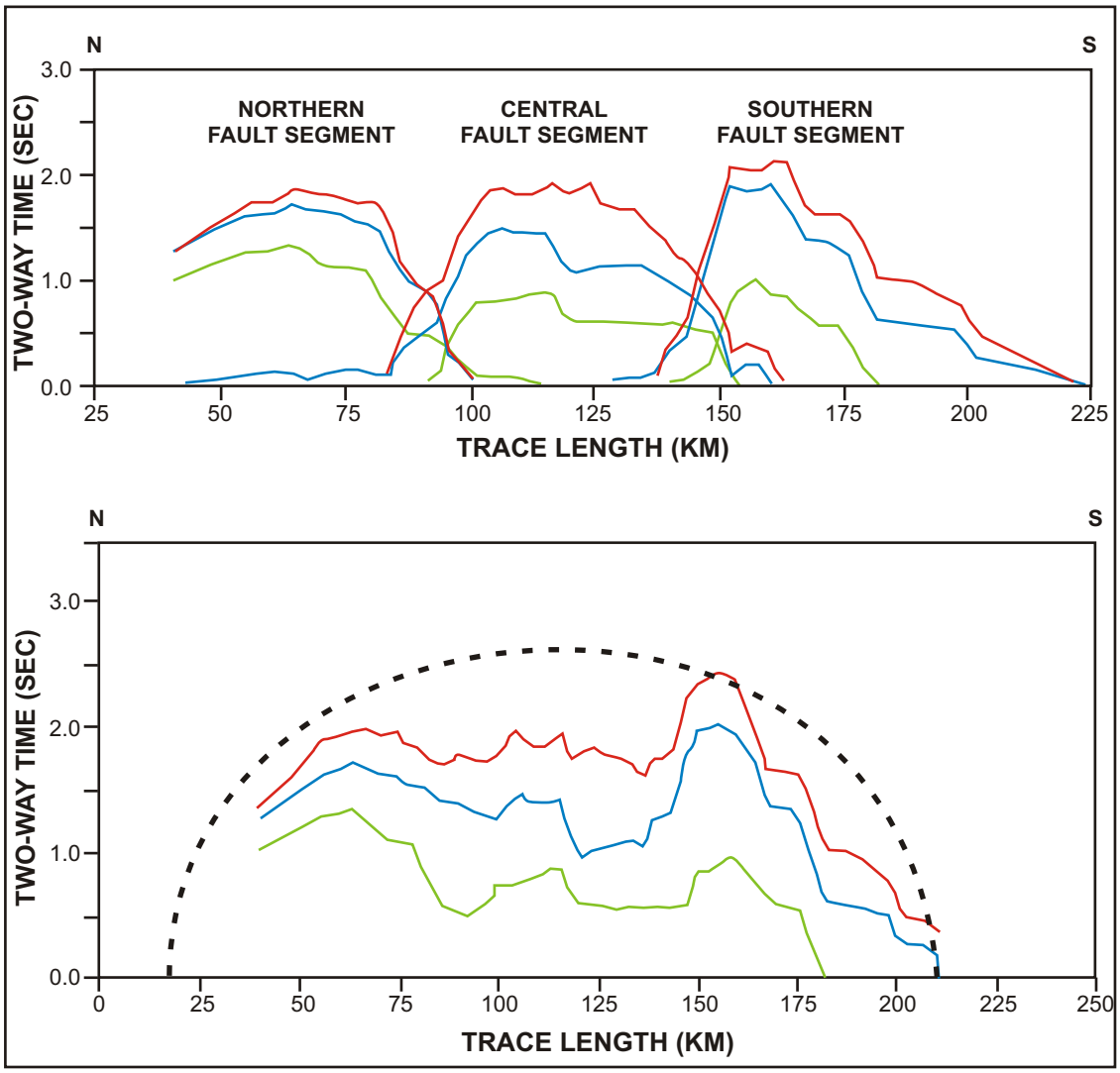

FIGURE 23: Displacement distribution on a large fault in the East African Rift. Upper plot shows the distribution of cumulative displacement along three fault segments within the Malawi Basin of the East African Rift. The colored lines represent the cumulative displacement accommodated during the deposition of the preceding sequences for each subsequent bounding unconformity at which measurements of displacement were taken. In order, the green, blue, and red lines represent younger and younger unconformities. Note that displacement is severely restricted where fault segments overlap. Lower plot shows same information, with the exception that cumulative displacements on adjacent fault segments are summed where the segments overlap. The result is a representation of the cumulative displacements at successive unconformities along the fault. Dashed line is an idealized displacement versus trace length distribution for a single-segment fault. A rough correspondence is apparent between this idealized curve and the actual fault displacement versus trace length data. (Based on Figures 5 and 7, Contreras et al., 2000).

Chapman and Meneilly (1990, 1991) used displacement mapping in a 3-D seismic volume to produce displacement contour diagrams for a pair of prominent faults in the Mesozoic sedimentary section of the North Sea. The main goal of this work was to demonstrate that one of these faults is a reverse-reactivated, former normal fault. More than 300 throw measurements were taken at regular intervals along each fault at selected mapped reflectors offset by the faults. Hanging wall deformation consisting of normal drag was observed, and was corrected-for when throw measurements were taken. This correction ensured that any displacement lost to folding was restored and was therefore recorded in their investigation. Measured values of throw were plotted on a vertical projection of the fault plane and were contoured to produce a display of the fault surface with the distribution of displacement shown by a series of constant displacement contours (Figure 24). The authors noted that the contours showed a general horizontal elongation, and thus the highest displacement gradients are oriented vertically. This indicates that slip was dominantly vertical (dip slip). Reconstructions of the fault during earlier periods in its history involved flattening selected horizons on the workstation, thereby “restoring” the fault to an earlier period when a given horizon was at the seafloor by simulating the case of no offset at the flattened horizon. Sequential restorations allowed the authors to estimate displacement accrued between the deposition of subsequent horizons. This work suggested a complex history of displacement consistent with an initial phase of normal dip slip, followed by inactivity, and later reactivation of slip in the reverse sense.

The authors concluded that their program of displacement mapping was crucial to uncovering the true history of fault movement, and that a large number of throw measurements serves to minimize the effects of possible measurement errors and to provide more complete characterization of the displacement distribution on the fault surface. Displacement mapping is also suggested as a means of verifying seismic interpretations in the vicinity of faults, where horizon mapping may be uncertain.

Mansfield and Cartwright (1996) undertook a study of dip linkage of faults using 3-D seismic data on a workstation. A large number of throw measurements of subsurface horizons

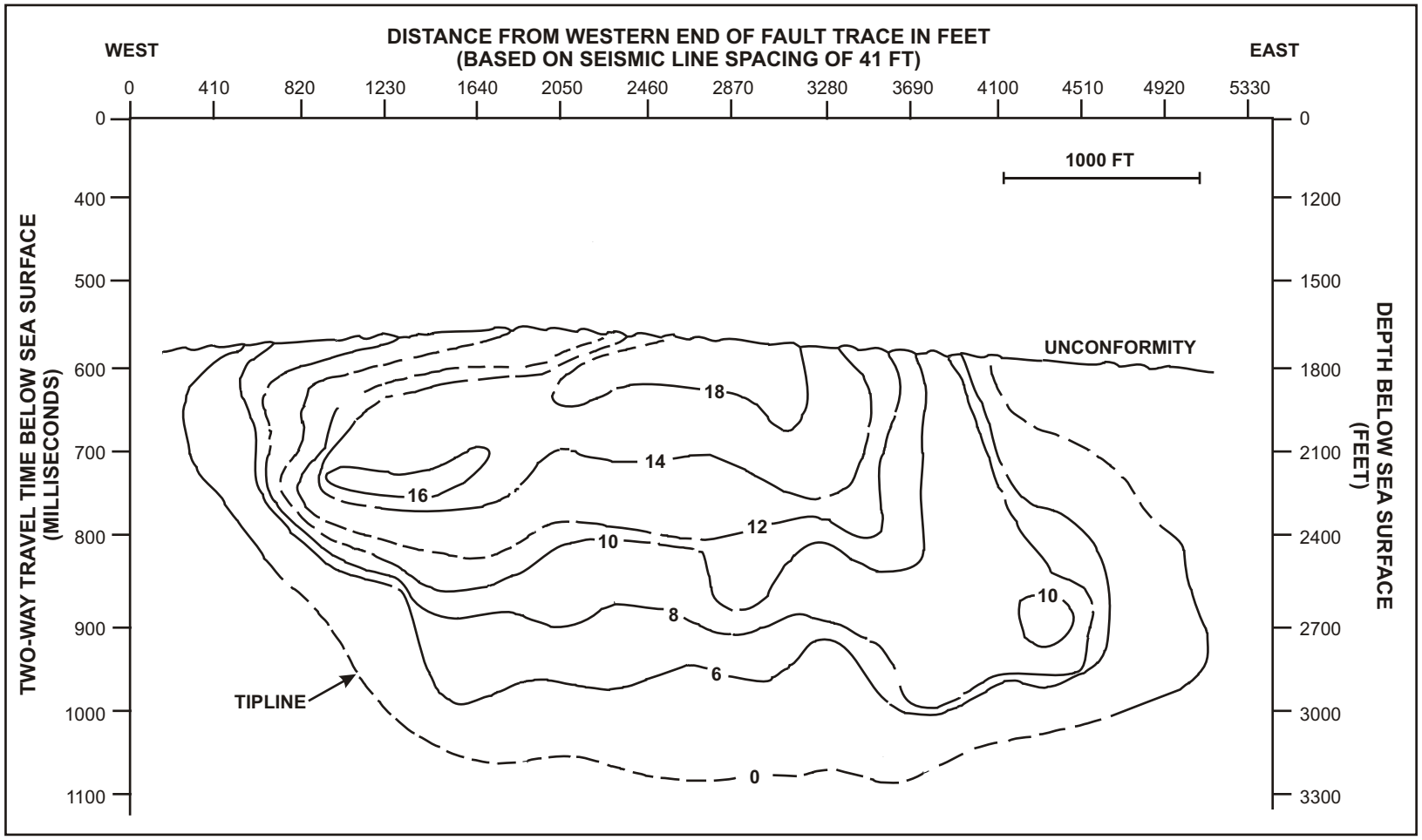

FIGURE 24: Vertical displacement diagram for a normal fault. Values of vertical displacmemnt are given in two-way travel time in milliseconds. Depths are given in two-way travel time in milliseconds below sea surface on the left-hand axis, and in feet below sea surface on the right-hand axis. An assumed seismic velocity of 6,000 ft/sec was used to derive these depth graduations. (Based on Figure 4, Chapman and Meneilly, 1990).

offset by faulting were made for several normal faults offshore of southwestern Louisiana. The authors report that corrections for folding in the fault hanging walls were made after measurements were taken, and that the only appreciable source of error (albeit small estimated errors) were associated with precisely reading the times of the horizons of interest from the vertical section display on the workstation.

The authors show that throw (taken as a proxy for displacement) decreases outward from a maximum located near the fault center toward the tipline, as was predicted. However, the observed outward throw decrease was not observed to be smooth but rather was characterized by several local throw maxima and minima. It was noted that these irregularities only became evident when the spacing between measurement stations along the fault traces were reduced from almost 3,300 ft to just over 400 ft (Figure 25). Thus, the lateral measuring resolution was a constraint on the ability to detect small-scale variations in throw on the fault surfaces. If the vertical resolution of the data is sufficiently high, excursions from the expected smooth vertical distribution of throw on a fault can be observed (Figure 26). Throw minima were observed to line up into roughly subhorizontal trends along several fault surfaces, possibly indicating linkage of faults in the dip direction.

The authors concluded that differences in mechanical properties of the sedimentary layering could account for the observed subhorizontal alignment of throw minima. However, these alignments were observed at different stratigraphic positions within the sediment column on different faults. This disparity indicates that dip linkage of neighboring faults is the more likely cause. Dip linkage is an analogous process to strike linkage and may produce relay zones in the area of fault overlap. Where faults link laterally, relay zones extend down dip. In the case of dip linkage, relay zones would be oriented roughly parallel to strike. Whether these relays are intact or breached, they would represent a localized area of minimum displacement oriented roughly perpendicular to the dip direction (Figure 27). This inference is supported by the high axial dimension ratios (length to depth) that characterize the faults in the study as being vertically restricted.

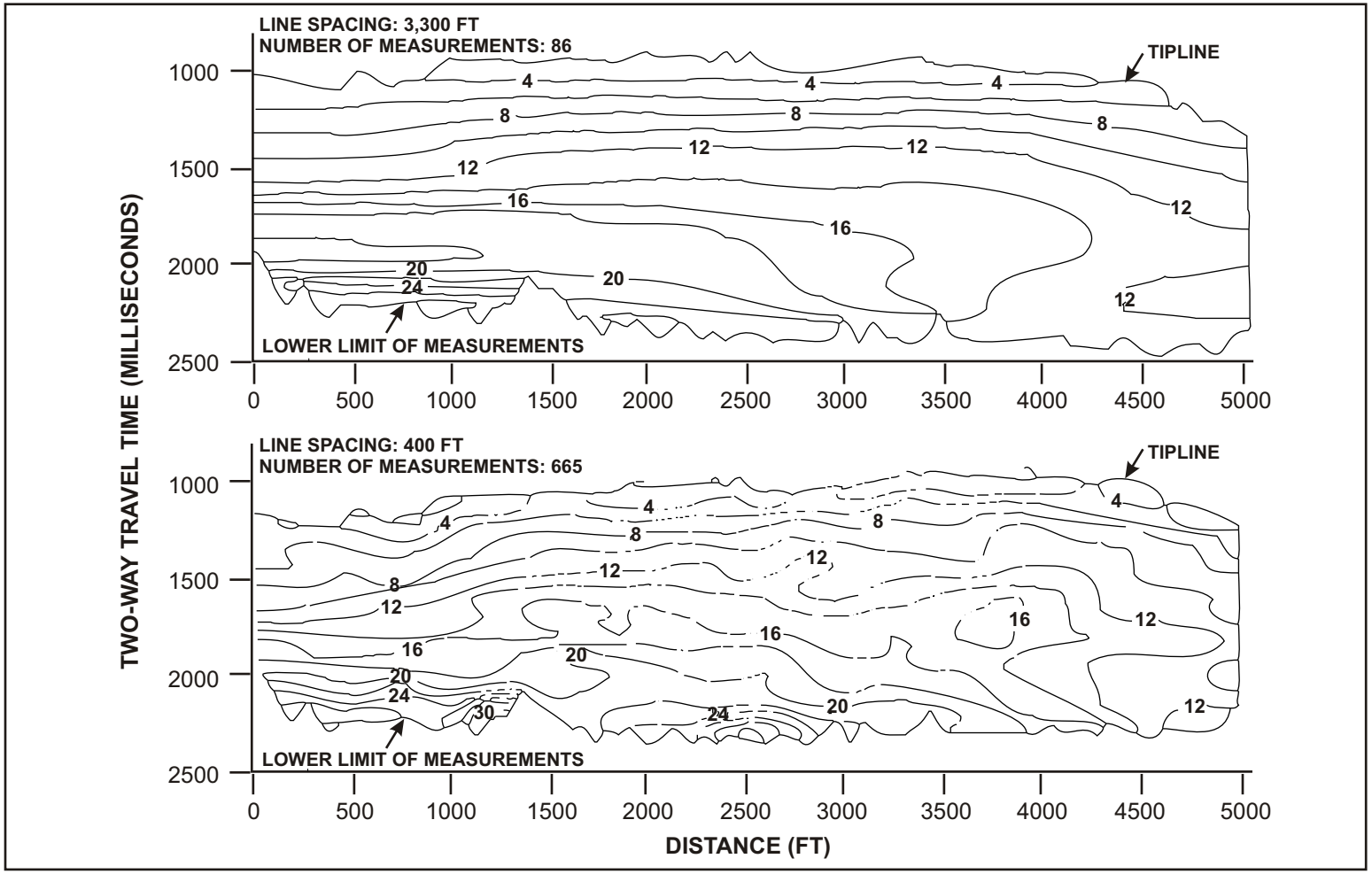

FIGURE 25: Comparison of lateral resolution of throw mapping for different measurement station spacings. Measurements taken at a line spacing of about 3,300 ft (top) versus a spacing of about 400 ft (bottom). As the spacing of measurements decreases, mapping resolution increases and small-scale irregularities in throw distribution on the fault surface become evident. Contoured values of throw in milliseconds. (Based on Figure 5, Mansfield and Cartwright, 1996).

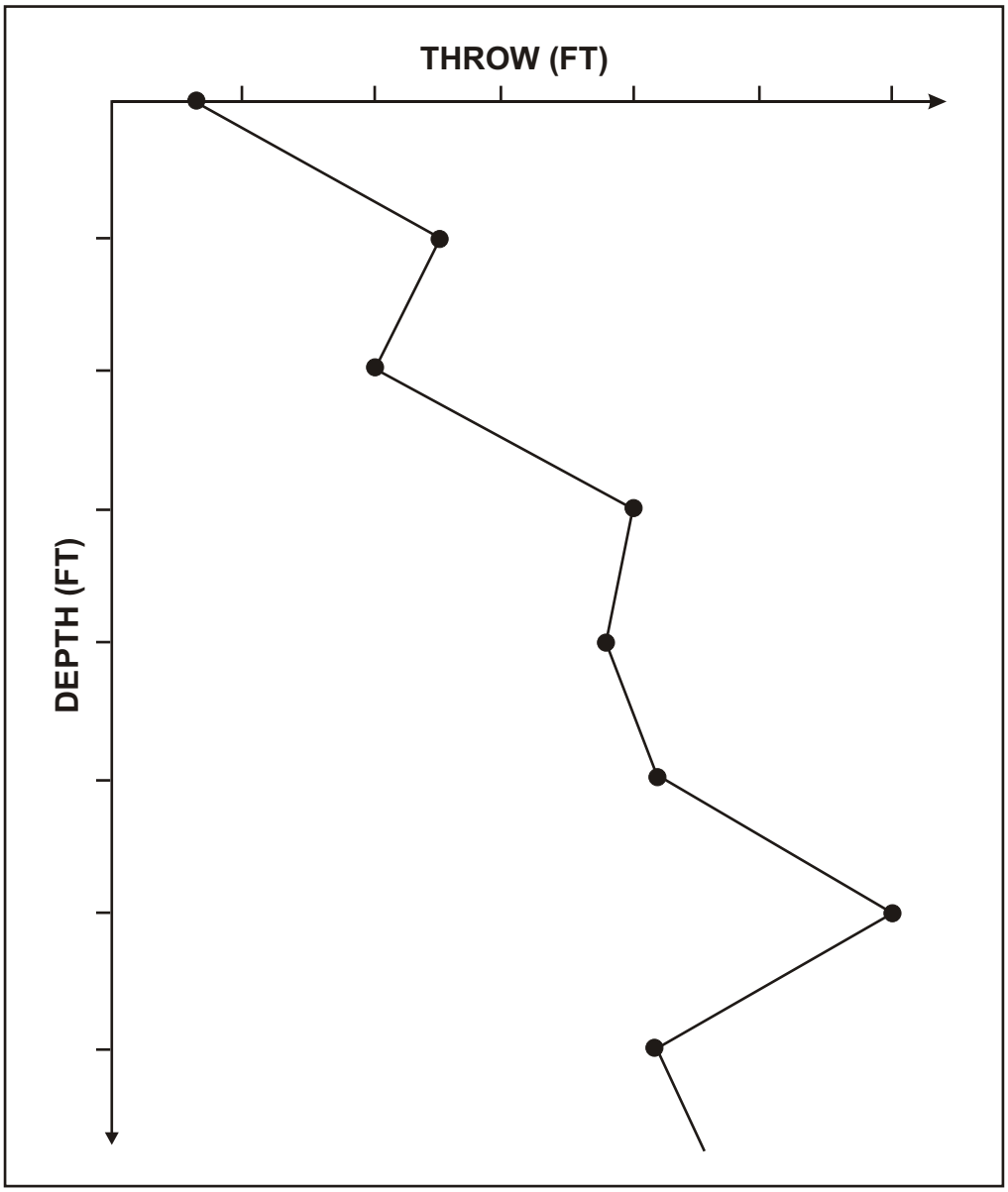

FIGURE 26: An example throw profile recorded midway along a fault, defined by eight different measurements. The departure from a smooth throw profile may be related to small-scale irredularities of throw on the fault surface that are visibile at the implied high resolution of mapping, or it may be the effect of fault linkage in the dip direction. (Based on Figure 6, Mansfield and Cartwright, 1996).

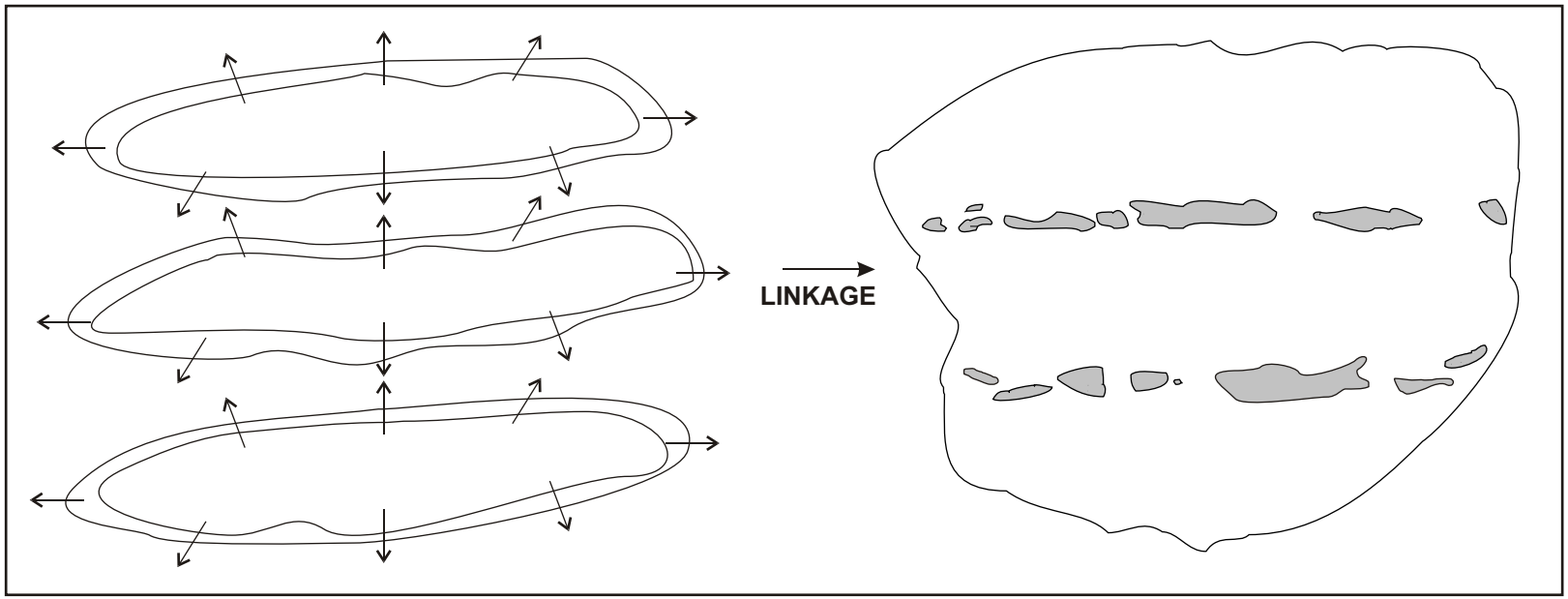

FIGURE 27: Vertical, or down-dip fault interaction. Vertically interacting faults would have high axial dimension ratios subparallel to strike, and the product of linkage between these faults would be a fault with relict suparallel-oriented displacement minima (shaded grey), corresponding to the areas of interaction between the former fault segments. (Based on Figure 12, Mansfield and Cartwright, 1996).

Needham et al. (1996) show how careful use of 3-D seismic data on the workstation can be used to constrain the geometry and displacement history of faults and how this knowledge can be applied to petroleum exploration in area where faults may provide fluid migration pathways or seals. The authors also discuss the advantages and potential dangers of fault interpretation on the workstation and advise on how to reduce the dangers. Workstation advantages (over interpretation of paper seismic records by hand) include rapid interpretation, objective automated mapping of horizons and faults based on geophysical criteria, and the ability to view a vertical section through a fault from any orientation and at any line spacing. Possible sources of error include the misinterpretation of horizons and faults. Automated horizon picking (horizon snapping) should be used to produce consistent horizon mappings, and analysis of fault displacement distributions can be used to make better fault interpretations. The authors, along with Cartwright et al. (1998), point out that over-simplified fault geometries assumed from 3-D mappings are generally more complicated, with interpretations of single faults often representing the actual case of two or more faults linked or in the process of linking along strike. Lateral resolution limits of 3-D seismic data may make it impossible to determine whether or not two faults are linked when examining the fault intersections with mapped horizons. If it must be determined whether or not a fault forms a continuous barrier to lateral fluid migration within a porous stratum, knowing if two faults are linked or if an unfaulted relay zone exists between the faults is critical. Fault displacement mapping is a useful tool for making such a determination. Cartwright et al. (1998) indicate that in some instances displacement mapping is the only viable means of making this critical determination for fault-bounded reservoirs.

RESEARCH METHODS

Methods used is this study are similar to those used in several other previous studies where horizon offsets at faults were measured in 2-D and 3-D seismic data sets, and in drifts and crosscuts in coal mines, to characterize fault displacement. These previous works include, but are not limited to Chapman and Meneilly (1991), Cartwright et al. (1995), Mansfield and Cartwright (1996), Needham et al. (1996), Nichol et al. (1996b), and Contreras et al. (2000).

High-resolution and Conventional Exploration 3-D Seismic Data Sets

A high-resolution (HR) 3-D seismic data set and a conventional (exploration) 3-D seismic data set were borrowed from a consortium of major petroleum companies operating a deepwater petroleum production development in an area of the upper continental slope offshore of Louisiana. The high-resolution data set is considered to be “high-resolution” because the spacing of the individual survey lines, the vertical data sampling interval, and the data frequency are superior to what is considered standard for industry conventional 3-D seismic data.

This high-resolution data set consists of a grid of orthogonal seismic inlines and crosslines producing rectangular bins 24.6 ft by 20.5 ft in size (inlines are spaced 24.6 ft apart and crosslines are spaced 20.5 ft apart). Each vertical seismic trace within the data volume is sampled at an interval of 1 millisecond, resulting in a dominant seismic frequency of about 200 HZ within the first one second below seafloor. Using the conventional seismic data set from this study as an example, typical industry conventional 3-D exploration data may be characterized by bin size on the order of 41.0 ft by 65.6 ft, a vertical trace sampling interval of one every 4 milliseconds, and a dominant frequency of about 35 Hz to 45 Hz in the upper portion of the sediment column. The high-resolution 3-D seismic data provides more resolving power because more data samples are present over a given lateral area (horizontal resolution) and per unit of vertical distance (vertical resolution). The high-resolution data has significant limitations, though. The quality of the data degrades rapidly below about one second below seafloor, whereas conventional 3-D seismic exploration data generally shows less degradation at equivalent two-way travel times. This is caused by attenuation of the higher frequency of the

sound source for the high-resolution data set. Figure 28 shows a side-by-side comparison of the advantages and disadvantages of the two types of 3-D data available for this study.

High-resolution 3-D Seismic Data Versus 2-D Seismic Data. Although no 2-D seismic lines were made available for this study, it is useful to briefly discuss the advantages and disadvantages of this data type. The vertical resolution associated with a standard 2-D seismic line is similar to the high-resolution 3-D data set used here. However, the high-resolution 3-D data set is judged to be more useful than 2-D seismic lines for the purposes of this study because the high-resolution 3-D data is a continuous volume of data. A series of 2-D seismic lines is typically arranged in a grid pattern with primary tracklines and crossing tielines spaced several hundred or several thousand feet apart. Any faults crossing the 2-D lines cannot be studied at any other interval along strike, or at locations of interest that fall between lines. Also, the orientation of these lines with respect to faults of interest may not be advantageous (for example, the primary tracklines may be oriented parallel or sub-parallel to the strike direction). With a 3-D seismic data set, the interpreter is permitted not only to view inlines and crosslines, but also arbitrary vertical seismic sections oriented at any angle to the main survey lines (Trabant, 1996).

Phase, Acoustic Impedance, Frequency, and Resolution. *Phase* is a seismic attribute that describes the distribution of reflected energy in a vertical seismic trace. A vertical seismic trace may be represented by a sinusoidal wave displaying variations in reflection strength and acoustic impedance in terms of alternating peaks (usually positive amplitudes) and troughs (usually negative amplitudes). *Acoustic impedance* is defined here as:

$$Z = \rho * v \qquad (2)$$

where Z is acoustic impedance, ρ is the density of the medium, and v is the velocity of sound in the medium. For the marine sedimentary environment, acoustic impedance is dependent mainly on lithology and diagenesis. Consolidated marine shales and well-cemented sandstones are

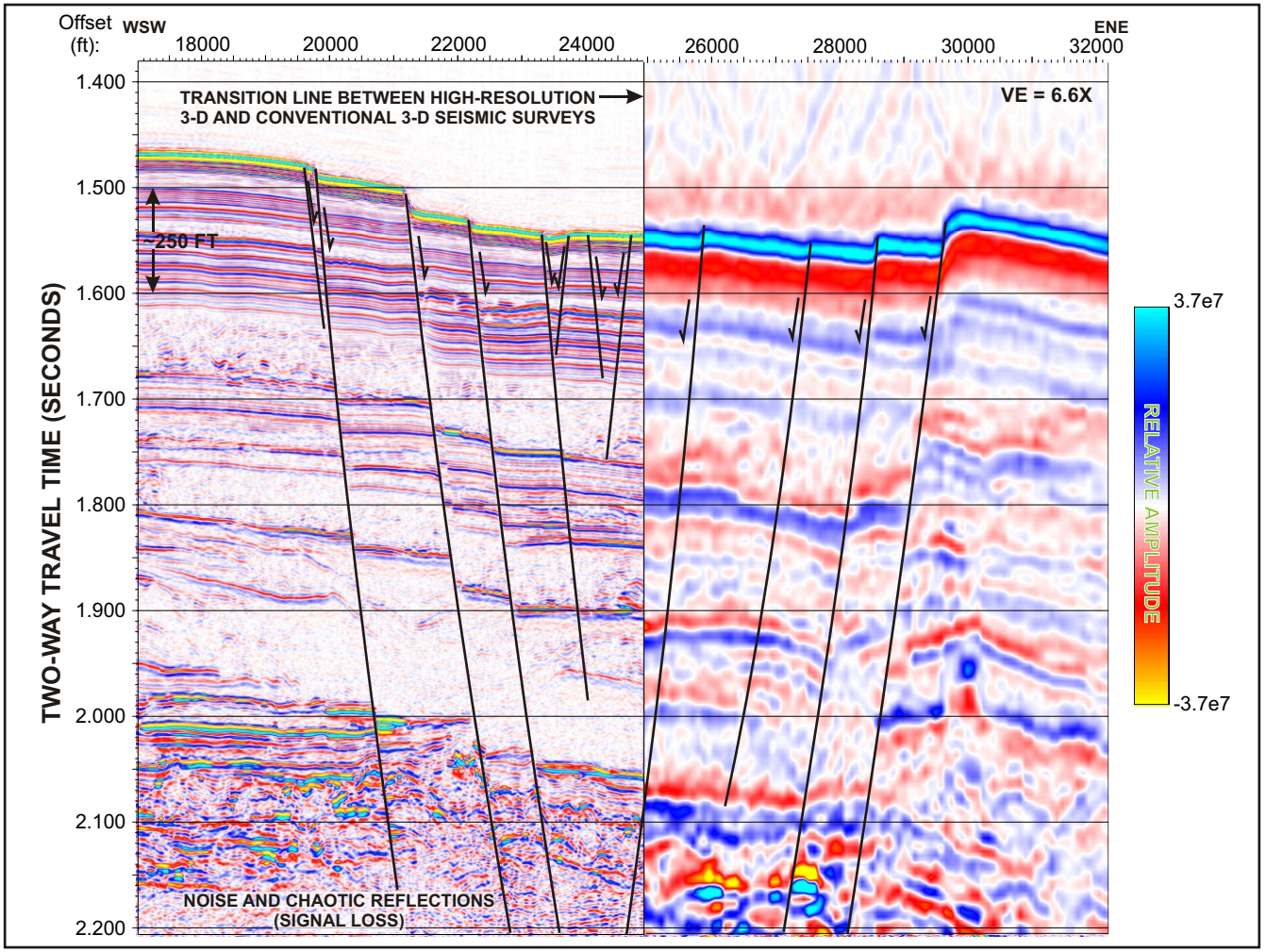

FIGURE 28: HR and conventional 3-D seismic data examples. HR seismic inline 1000 on left, and matching conventional seismic arbitrary line on right shown in adjacent vertical section panels. The resolution contrast between the high-resolution data and the conventional data is stark. Fault mapping is easier and more accurate with the high-resolution data than with the conventional data. Location of this figure shown on Figure 7.

dense and are characterized by low porosities. These transmit sound faster than unconsolidated clays (porosity around 50%) and uncemented or loose, poorly cemented sands.

For seismic data characterized by a phase of 0°, an increase in acoustic impedance between one acoustic medium and the next would be represented by a peak reflection at the contact, with most of the reflected energy being concentrated within the peak and less reflective energy contained within the preceding and trailing troughs (A. R. Brown, 2002, personal communication, private consulting geophysicist in Dallas, Texas). An example of an interface that produces this response is the seafloor. There, acoustic energy enters a higher impedance medium (generally fine-grained siliciclastics) from one of lower impedance (seawater). A decrease in acoustic impedance between one medium and the next would be represented by a trough reflection, with most of the reflected energy being concentrated in the trough. An example of this would be the contact between a fine-grained section (dense, tight shale) overlying a porous, gas- or water-filled sand.

Non-zero-phase data may vary significantly in the characteristics of reflections from the zero-phase case, with the physical contact that produces the reflection falling between adjacent peaks and troughs (Figure 29). Zero-phase data is generally preferable to data containing some other phase because the reflected energy maxima of peaks and troughs occur at lithologic contacts, or horizons (A. R. Brown, 2002, personal communication, K. J. Campbell, 2004, personal communication). Strong, conspicuous, and continuous reflections are most easily tracked and correlated laterally and provide the basis for mapping structural and stratigraphic features within a 3-D seismic volume. The vertical waveform along individual traces in the 3-D high-resolution seismic data set was assessed with respect to phase and was found to be approximately 45° from zero phase (0°). The phase of the data set was subsequently rotated by 45° to approximate the zero-phase condition for interpretation.

Frequency describes the number of cycles of peak-trough pairs that exist within a given vertical time increment, usually one second of two-way travel time, and provides a measure of the vertical resolving power of a seismic data set. The wave equation states that frequency is

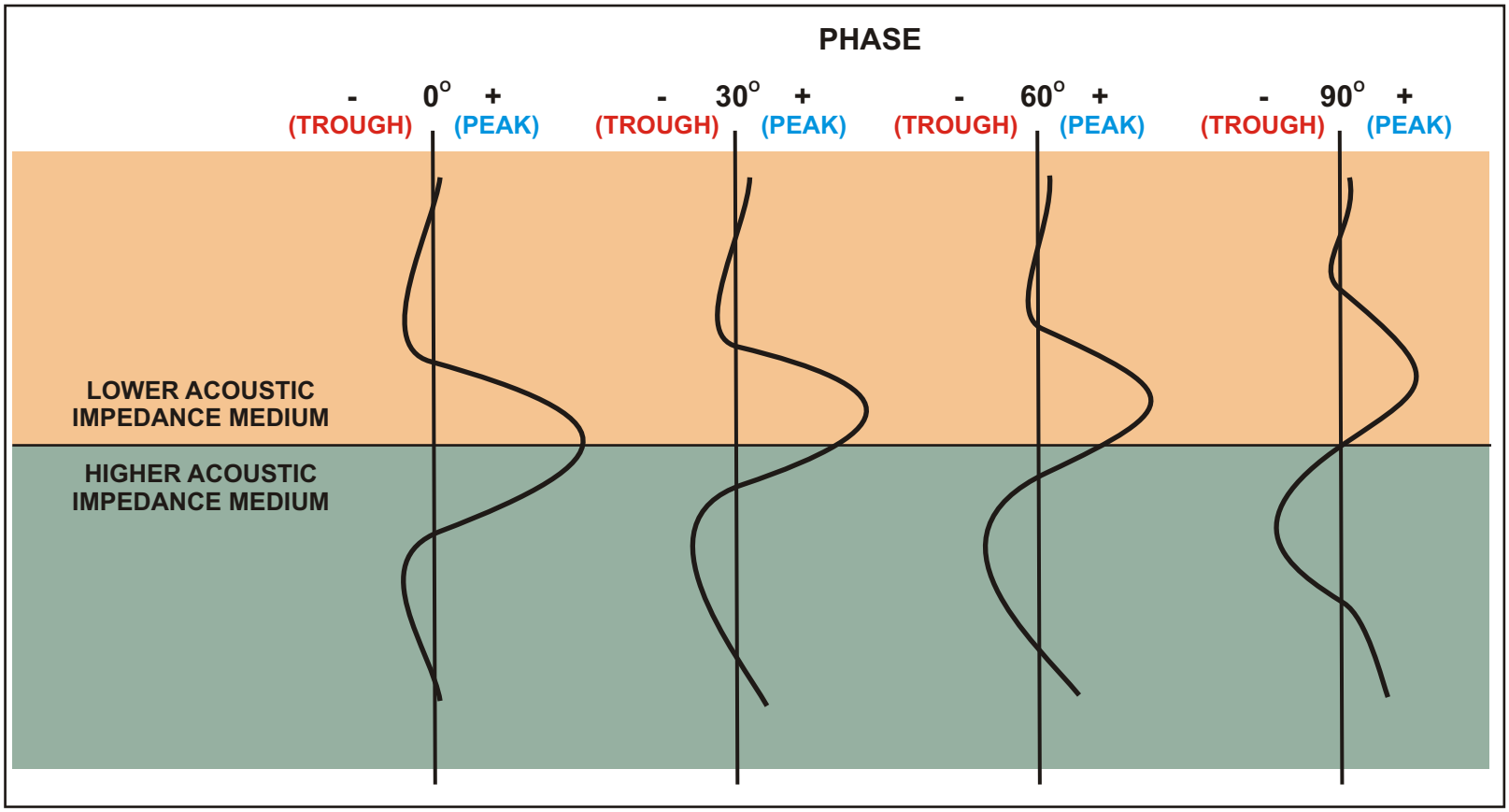

FIGURE 29: Effect of phase on the interaction between the seismic waveform and bedding. For the zero-phase case, lithologic contacts (boundaries representing acoustic impedance contrasts) are represented by either positive or negative amplitude maxima (peaks or troughs). For cases where phase varies, such as 30 degrees and 60 degrees above, the contact is not coincident with any amplitude maximum. For a phase rotation of 90 degrees from zero, the contact is represented by a zero amplitude (zero crossing).

equal to the speed of acoustic wave (or acoustic signal) propagation divided by the wavelength. This may be expressed mathematically as:

$$f = v / \lambda \quad (3)$$

where f is frequency, v is velocity, and λ is wavelength. As frequency increases, the resolution of the data increases because more reflections are present per vertical increment of time than at lower frequencies. Thus, if reflections correspond to contacts between individual stratigraphic layers, more layers can be differentiated at higher frequencies. The dominant frequency of the high-resolution 3-D seismic data set used in this study is about 200 Hz, and that of the conventional 3-D seismic data set is about 40 Hz.

The minimum thickness of a layer that can be differentiated for a given combination of acoustic velocity and frequency is termed the *limit of separability (LS)*, and is equal to one-quarter of the acoustic signal wavelength:

$$LS = v / (4 * f) \quad (4)$$

Thus, the limit of separability is also a measure of vertical resolution (Brown, 1999, A. R. Brown, 2002, personal communication). Using an average sediment column seismic velocity of 5,200 ft/sec two-way travel time, the limit of separability of the high-resolution 3-D seismic data set is about 6.5 ft and about 32.5 ft for the conventional 3-D seismic data set. Another measure of vertical resolution, the *limit of visibility (LV)*, describes the minimum separation between reflecting horizons required to make them distinguishable from each other for data of a given signal-to-noise (S/N) ratio. For quality data with good S/N, the LV is approximated by:

$$LV = v / (20 * f) \quad (5)$$

Using this relationship, the 3-D HR seismic data set LV is 1.3 ft, and the conventional 3-D seismic data set LV is 6.5 ft.

Horizon Selection and Mapping

Mapped horizons provide the references for measuring the vertical offset along a fault in a seismic vertical section. Six horizons (seismic reflectors) were selected for mapping within the

study area in the high-resolution 3-D seismic data set (Figure 30). These horizons were chosen primarily because they are regionally or locally continuous and (presumably) mappable across most or all of the study area.

Seafloor, the first horizon, was mapped across the entire data set as the first continuous peak reflector encountered in the data, and represents the modern water bottom. Horizons A, A2, B, and C are regional reflectors utilized by a major petroleum exploration company for stratigraphic correlation. Horizon A is a regionally continuous trough reflector interpreted to be an internal reflector within the young, parallel-stratified, pelagic draping clays. Horizon A2 is a generally continuous trough reflector just below the base of a thick, acoustically-chaotic, section of fine-grained mass movement deposits. Horizon B is a peak reflector interpreted as the top of a sand-prone, channelized stratigraphic interval. The presence of continuous sands and channels is likely result of deltaic distributary channel processes. Horizon C is a trough reflector within the sand-prone channelized interval. This horizon is interpreted to be an unconformity associated with episodic channelization. Both Horizons B and C are generally discontinuous within the study area because of deformation related to faulting. Horizon SP1 is a reflector between the seafloor and Horizon A that was mapped for this study to provide more control on fault throw in the shallow subsurface. It is a locally continuous trough reflector interpreted to be an internal reflector within the uppermost young, parallel-stratified sediments interpreted as pelagic draping clays.

These six horizons were mapped within the study area where they are continuous or are correlable across faults and erosional truncations with a high degree of certainty. Areas within the study area exist where mapping was not possible within reasonable certainty are shown on Figure 31.

The process of mapping horizons was accomplished on a PC-based seismic workstation running The Kingdom Suite 2-D/3-D seismic interpretation software. Versions 7.0 to 7.5 of this software were utilized for this study, and each subsequent version of the software represented improvements and refinements over older versions. The workstation allows for speedy and easy

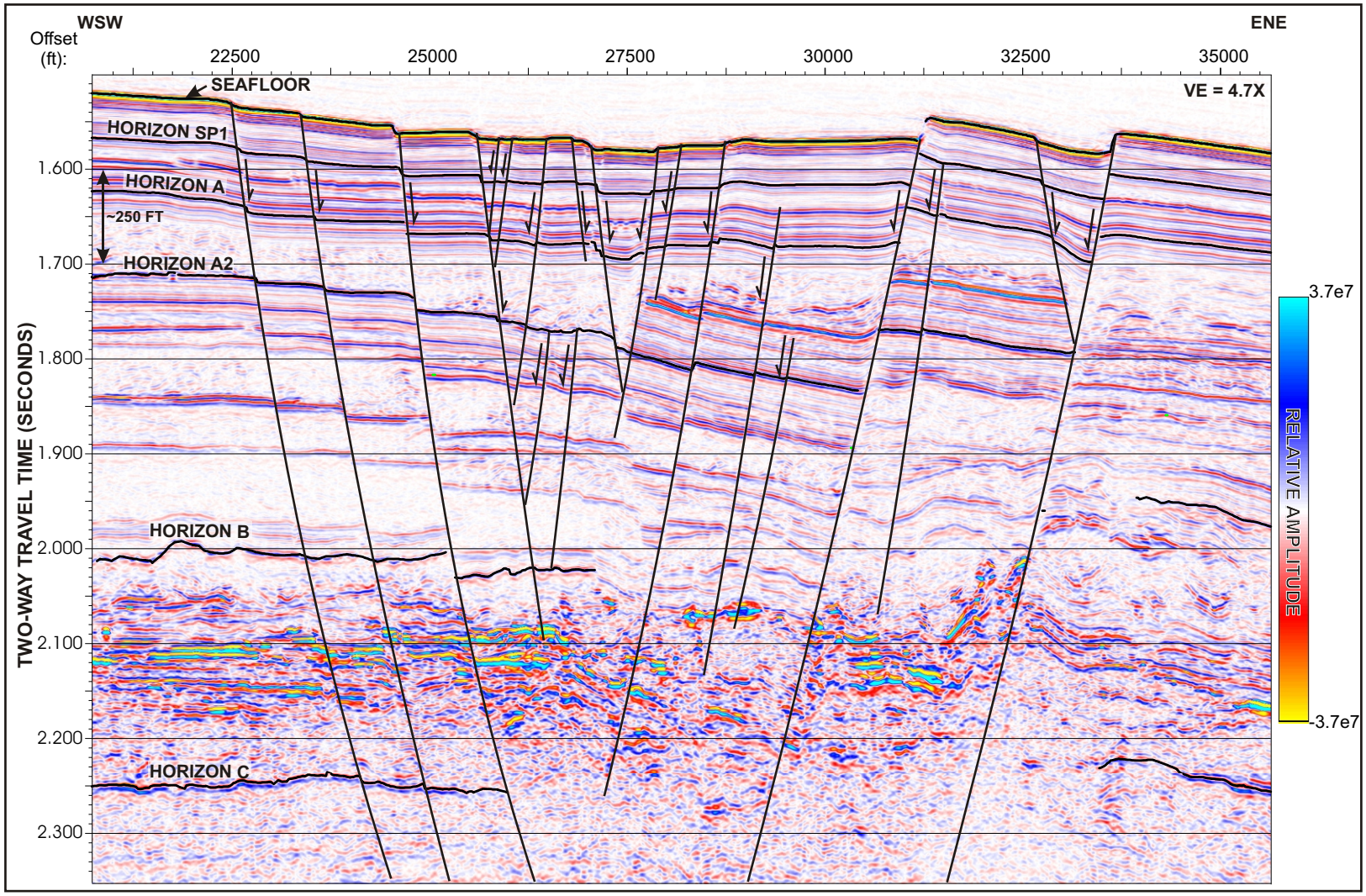

FIGURE 30: High-resolution seismic inline 760 showing mapped horizons used in this study. Location of this figure shown on Figure 7.

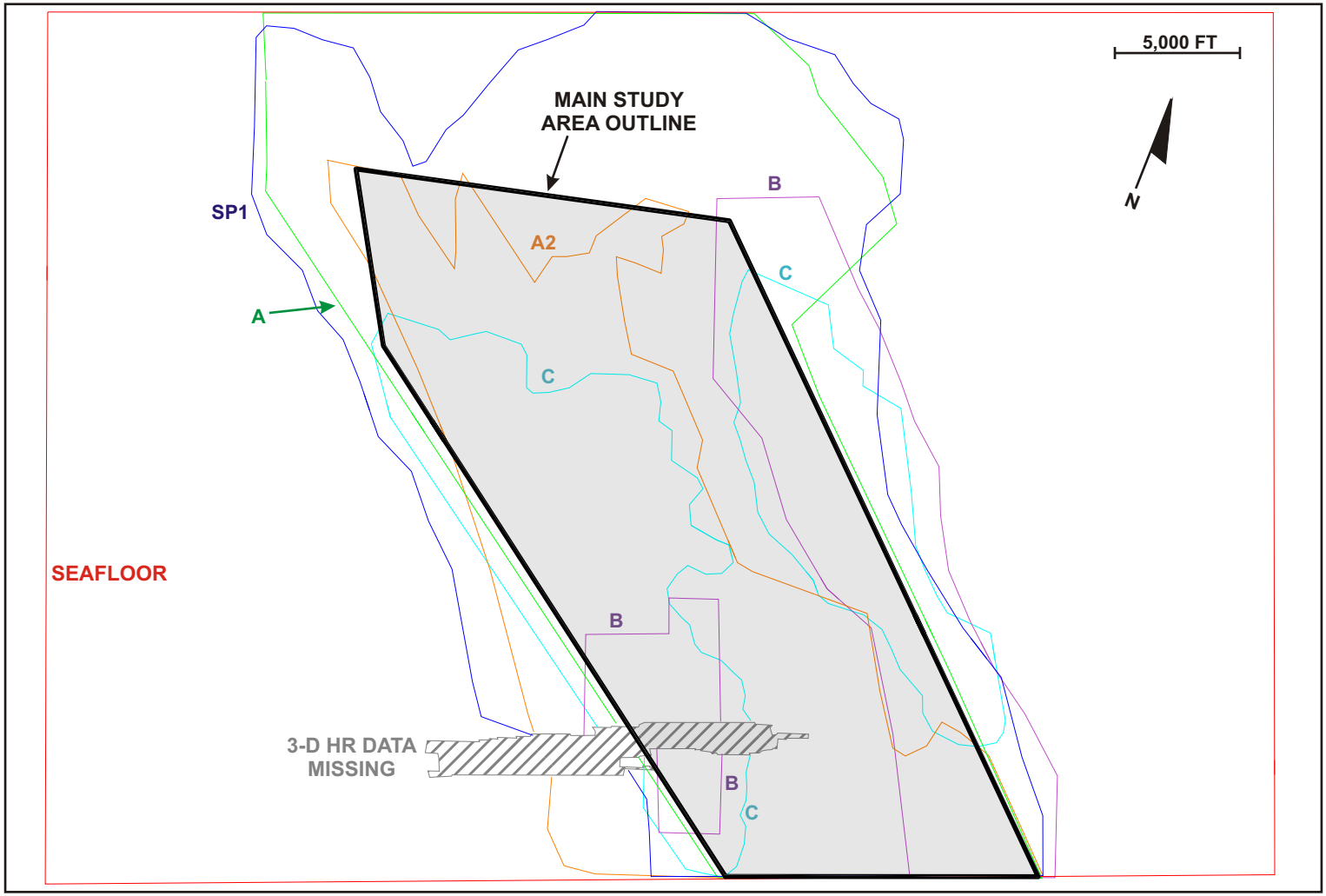

FIGURE 31: Map view of study area showing mappable extent of seafloor and five subsurface horizons. The main study area is shown as a dashed black polygon. Seafloor was mappable over the entire 3-D high-resolution (HR) data set. The subsurface horizons are SP1, A, A2, B, and C.

management and interpretation of a data set that is both complex and large, and provides tools that foster consistent methods of interpretation. The seismic workstation allows the user to digitize a horizon on a vertical section using either manual or automatic selection techniques. The automatic selection, or “snapping”, feature accepts user direction and maps the horizon along the highest amplitude of the chosen reflector. For zero-phase seismic data, the highest amplitude associated with a reflector corresponds stratigraphically to lithologic contacts or bedding planes. Using the snapping feature results in very consistently mapped horizons that follow the inferred stratigraphic contact and significantly decreases the time necessary for horizon mapping (A. R. Brown, 2002, personal communication, K. J. Campbell, 2004, personal communication). The snapping tool and extensions of it were used almost exclusively during the horizon mapping process.

The seafloor and subsurface horizons were picked initially on every tenth inline and crossline in the study area. Arbitrary vertical seismic sections were digitized in various orientations within the study area and were used to aid in horizon mapping in structurally and stratigraphically complex areas of the data set. Another software tool was used to laterally correlate reflectors because numerous faults offset the seismic reflectors in the study area. This tool, the *correlation polygon*, allows the user to visually restore fault offsets in vertical section to an unfaulted state. The user is then able to match reflectors in the hanging wall with their lateral equivalents in the footwall and map the reflector of interest across a fault with relative ease (Figure 32). The correlation polygon tool can also be used to allow the user to compare a portion of the vertical section to lateral equivalents at any other point along the vertical section line. This is useful in the correlation of reflectors across erosional truncations. This tool was used judiciously to avoid false correlations and in connection with other methods of lateral correlation to facilitate horizon mapping.

After initial picks were generated on a grid of every tenth inline and crossline, a software function for automatic picking was utilized to perform horizon mapping on the inlines and crosslines skipped in the process of generating seed picks. This task was repeated for each

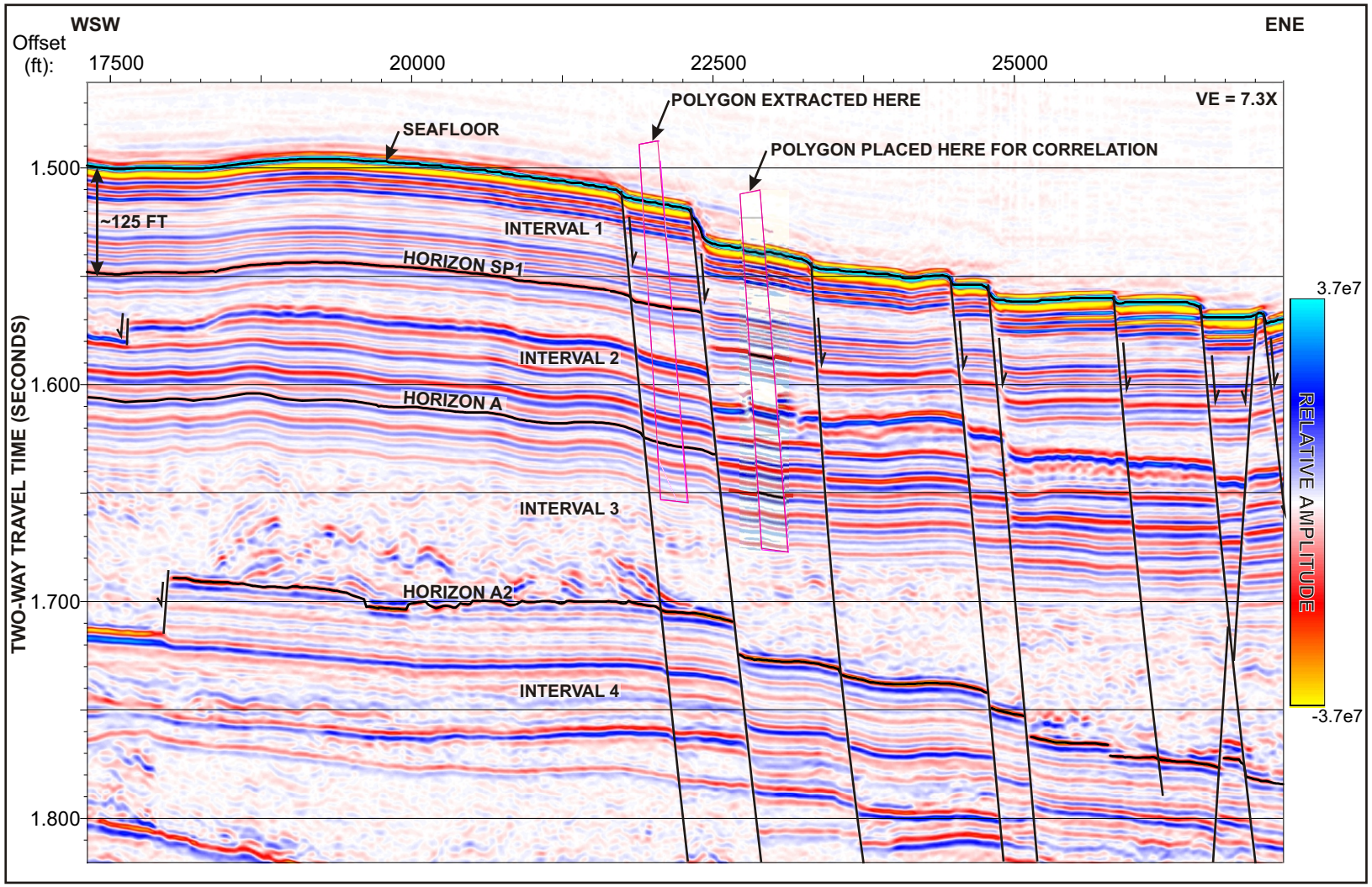

FIGURE 32: High-resolution seismic inline 840 showing the use of a correlation polygon in horizon mapping. The correlation polygon may be used to correlate reflectors across faults or other discontinuities. Location of this figure shown on Figure 7.

horizon, and the accuracy of the results was assessed by two principal means. First, *derivative maps* were computed for each horizon. For a given horizon, the derivative in the inline direction (change in the time component of a horizon pick from one trace to the next on an inline) and the derivative in the crossline direction were computed using map calculator functions in the seismic interpretation software. The resulting maps were examined for the presence of large and anomalous derivative values, which typically indicate the presence of significant variations in the travel time between a horizon at one trace versus the next trace. Such mispicks often represent excursions of the mapped horizon from the intended reflector (K. J. Campbell, 2004, personal communication). Mispicks can be located quickly using derivative maps, and are fixed by manually snapping the horizon to the correct reflector. A second method of checking the accuracy of automatic picking is by targeted examination of the picking results. It was quickly determined that most automatic picking errors were generated at faults; the automatic picker occasionally incorrectly and inconsistently mapped reflectors at fault offsets. These mapping errors were corrected by repeating the seed-picking process in the areas of interest at a closer interval; usually every third or fifth inline and crossline. The automatic picking function was then used to remap the intervening inlines and crosslines. The results of these corrective methods were almost invariably judged to be satisfactory, and improved the overall accuracy of horizon mapping.

Fault Selection and Mapping

Consistent mapping of fault planes in vertical section was necessary for accurate measurements of fault throw. The seafloor traces of all faults within the study area were first mapped on the workstation onto a seafloor rendering derived from the seafloor horizon (Figure 7). This map view presentation of the seafloor made detection and mapping of fault scarps simple and accurate, in that fault traces are visible in stark contrast to unfaulted seafloor. This seafloor fault trace map facilitated fault mapping in vertical section, as well as selection of faults for the throw measurement phase of this study.

The majority of faults within the study area strike roughly perpendicular to the inline direction of the 3-D high-resolution seismic data set. The seismic survey was designed and acquired specifically with this in mind. Thus, inlines are optimally oriented parallel to fault dip and allow for the measurement of fault throw in approximately a true dip section. Fault planes were initially mapped on every tenth inline within the study area. This mapping interval was selected to provide enough fault plane segments along any given fault to closely follow the three dimensional geometry of the faults while reducing the time required for laborious interpretation that would otherwise be required to map faults on every single inline. Seafloor fault traces shown on the gray-scale seafloor rendering were used to guide fault segment mapping in vertical section. This method proved to be optimal for the purpose of differentiating closely-spaced faults from one another, and it was not necessary to map fault segments on a smaller interval to insure mapping accuracy. However, it was decided to remap the faults on every fifth inline in the HR 3-D data set in the event that throw measurements were desired at shorter intervals along the faults.

The seismic interpretation software has no provision for automatic picking or snapping of faults, because the continuous reflectors required for automatic mapping that constitute horizons do not normally delineate fault planes. Faults can be mapped with snapping algorithms or by automated functions that can be applied to seismic data volume having special attributes not available with this data set. Thus, all fault mapping in this investigation was necessarily conducted manually. Every effort was made to digitize fault surfaces precisely, but the fault mapping is ultimately only as accurate as the resolution limits of the 3-D high-resolution seismic data.

Upon completion of fault mapping, all mapped faults were assessed for potential inclusion in the group of faults selected for horizon offset measurement. The fault selection criteria are summarized as follows:

1. The fault should have sufficient strike length so that several uniformly-spaced measurement stations will fall along the fault. Most of the faults within the study

area are sufficiently long that measurement stations spaced every twentieth inline along the seafloor trace of the fault provided a sufficient number of data points. Given an inline spacing of about 24.6 ft, the distance between stations is about 492 ft.

2. The fault should be located in a portion of the study area containing several of the mapped subsurface horizons. This allows several measurements of throw based on horizon offsets to be taken at each measurement station.
3. The fault should be sufficiently long in the dip direction. This is because fault throw scales with fault dimensions, and because it is preferable for a fault under study to intersect and offset the maximum number of mapped horizons (Chapman and Meneilly, 1991, Mansfield and Cartwright, 1996, Needham et al., 1996).
4. The fault should not be located within a dense population of faults. Such a complexly deformed area commonly contains chaotic bedding and poorly-defined fault offsets. This makes mapping of horizons and faults problematic and degrades the accuracy of measurements based on these mappings (Figure 33).
5. The fault should not be located near any other geologic features that degrade imaging of the fault or the seismic reflectors. Geologic conditions such as fluid seepage vents, landslides, and slumps causing such degradation should therefore be avoided. (Figure 33).

Of the fifty faults initially indicated for potential inclusion in this study, forty faults were selected for inclusion in this study. The selected faults are shown on Figure 7. Numerical designations were assigned to each during selection of faults for further study. (These designations generally increment by one, but in some cases faults are not numbered sequentially.)

Fault Displacement Components and Deformation Accommodated by Folding

Throw is the vertical component of displacement for a dip-slip fault and is directly measured at horizons offset by the fault (Peacock et al., 2000). The other components of fault

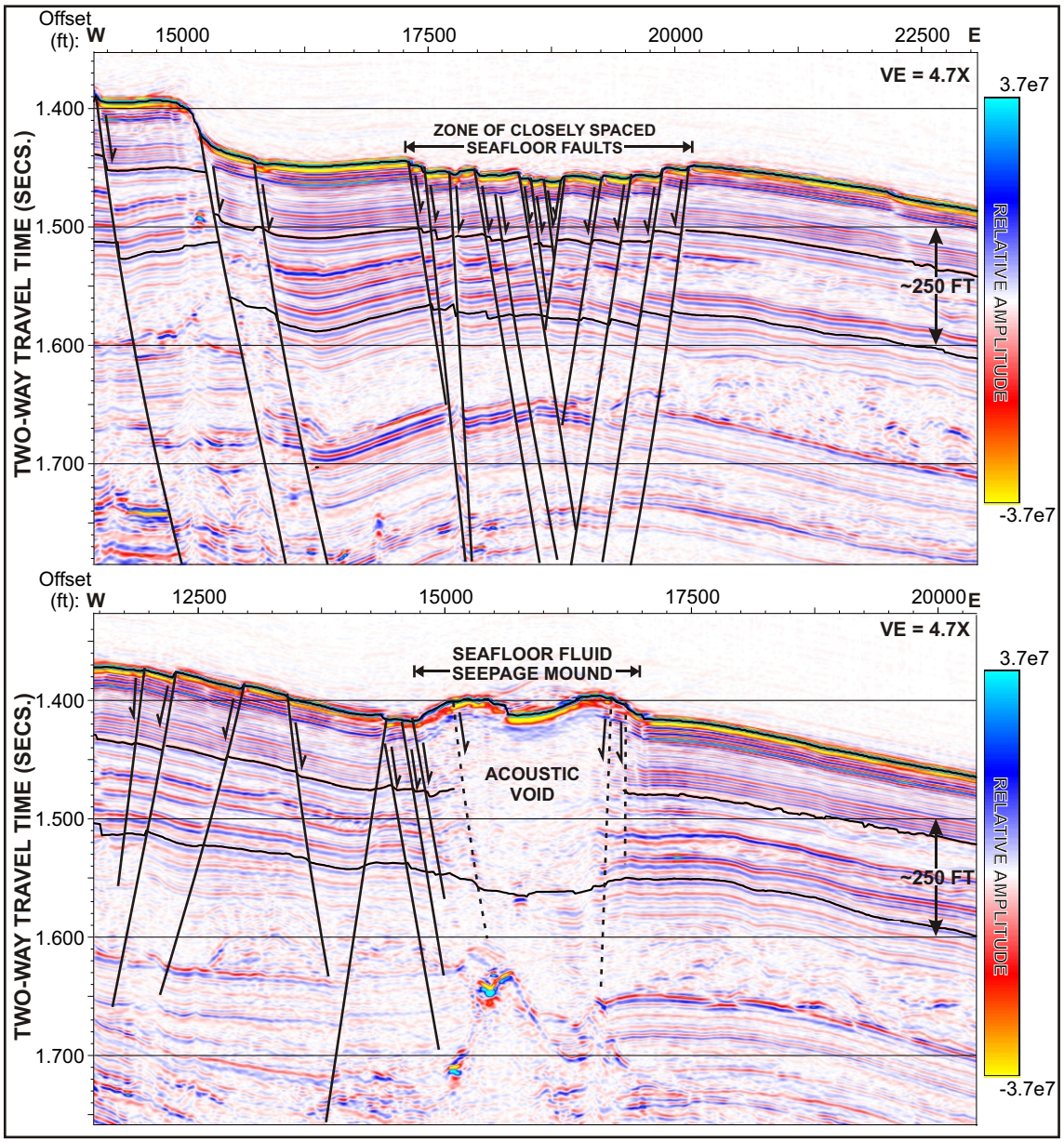

FIGURE 33: 3-D HR seismic arbitrary lines showing conditions considered adverse for this study. Upper arbitrary line shows faults spaced so closely that mapping of individual faults is of suspect accuracy. Lower arbitrary line shows acoustic wipeout associated with a fluid explusion mound, and the uncertainty associated with mapping faults or horizons in the vicinity of such a feature. Location of this figure shown on Figure 7.

displacement are *heave* and *strike-direction slip*. Heave is the horizontal component of displacement for a dip-slip fault and is equal to the throw at the horizon of interest multiplied by the cotangent of the fault dip angle (for depth intervals along the fault where the fault is characterized by constant dip, and there is no component of oblique slip). Dip angle is not directly quantified from seismic data and must be calculated. (Figure 34 shows how dip is calculated for fault segments that are planar in a dip-oriented vertical section. This process was used to estimate fault dips within the study area). Strike-direction slip is a component of fault displacement present on faults displaying oblique-slip characteristics.

Drag may be defined as deformation of strata on either side of a fault caused by displacement along that fault. This deformation is characterized by the formation of either anticlinal or synclinal folds in the deformed strata adjacent to the fault and is termed *drag folding* (Twiss and Moores, 1992). For normal faults, anticlinal drag folds (reverse drag) form in response to the horizontal extension produced by fault displacement. These rollover anticlines, therefore, partially accommodate hanging wall deformation (Figure 35). Synclinal drag folds (normal drag) form in response to resistance along the fault plane (Twiss and Moores, 1992, Peacock et al., 2000) and may also accommodate hanging wall deformation.

The presence of drag folds along a fault of interest introduces a serious complication to the process of measuring throw at offset horizons. The variation in the position of horizon truncations at fault planes caused by drag folding must be corrected either mathematically or graphically if measurements of vertical offset between correlable reflectors are to be accurately related to throw (Mansfield and Cartwright, 1996). Chapman and Meneilly (1990) describe a mathematical method for making this correction. Figure 35 shows how this correction is made for the cases of normal and reverse drag on a normal fault. The concept of this correction procedure is the removal of folding and restoration of the faulted horizon to a planar surface. A more careful examination of Figure 35 leads to a graphical “short cut” method for making this correction on the workstation during the collection of data. The straight-line projection of the horizon containing a drag fold intersects the fault such that the distance *T* is the true throw. By

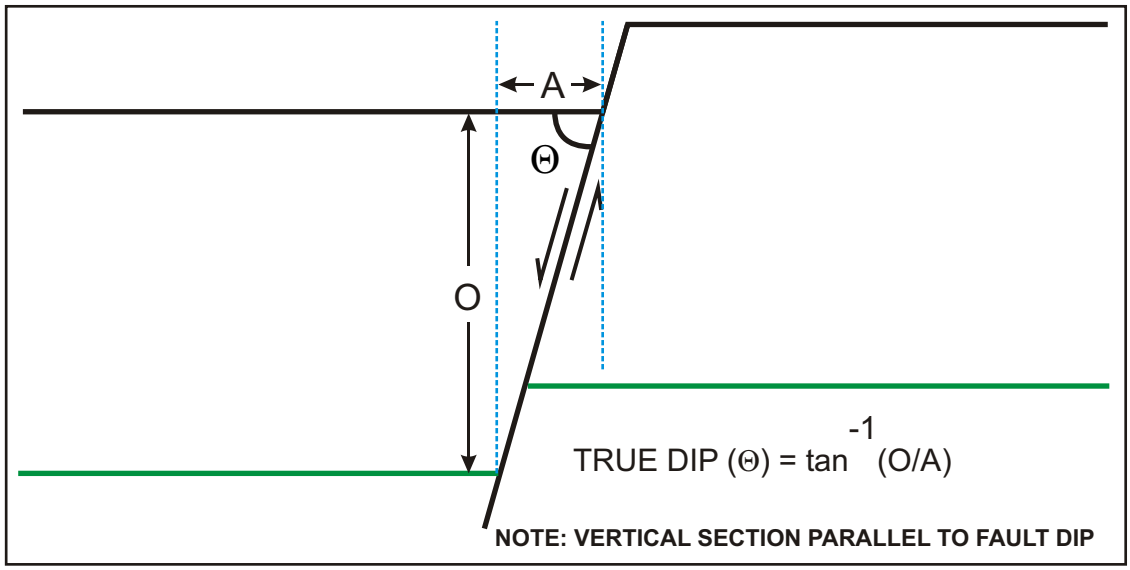

FIGURE 34: Method of calculating fault dip for a planar fault. **A** is the horizontal distance between the hanging wall fault cutoffs of two horizons (black and green). **O** is the vertical distance between the two horizons in the hanging wall. True dip of the fault is determined as $\Theta=\tan^{-1}(O/A)$.

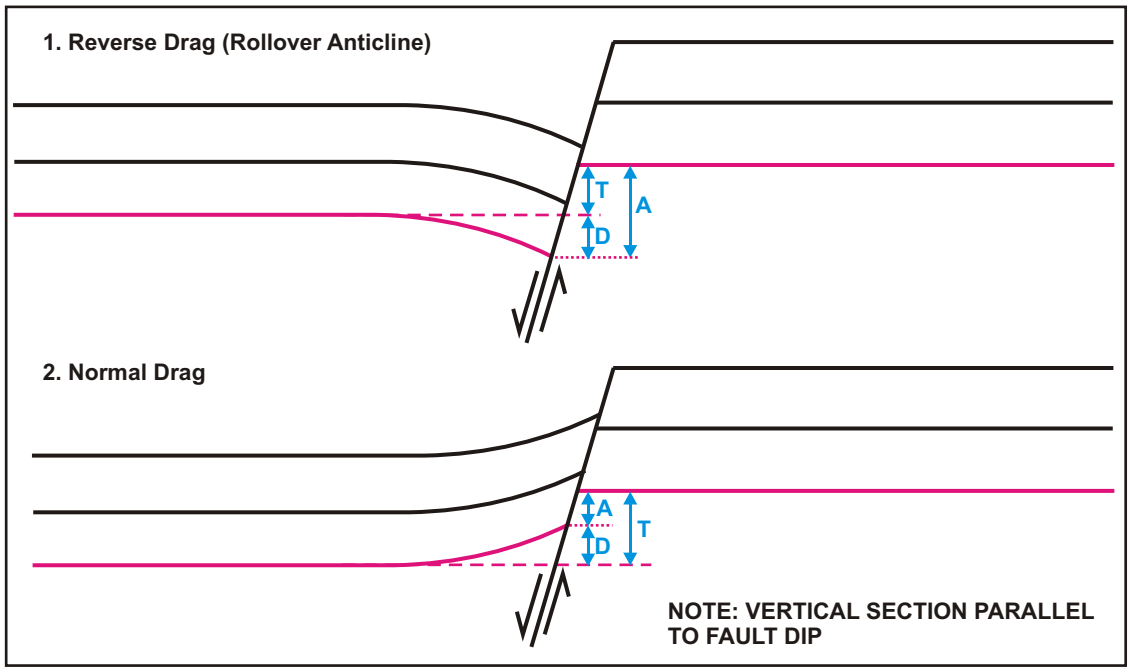

FIGURE 35: Graphical method of removing the effects of folding from measurements of horizon offset at a normal fault. In the above dip-parallel diagrams, **A** is apparent throw, **T** is true throw, and **D** is horizon deflection caused by folding. The dashed line is the projection of the unfolded horizon across the fault, and the dotted line is the projection of the truncation of the folded horizon across the fault. For the case of reverse drag (1), T=A-D. For the case of normal drag (2), T=A+D.

digitizing a correction horizon as a straight line like that shown in Figure 35, the effect of drag folding can be negated and measurement of throw can be made as if the folding did not exist. This graphical short cut was used to remove the effects of drag folding during the collection of horizon offset data. This short cut method was also used by Chapman and Meneilly (1990).

Conversion of Seismic Two-Way Travel Times to Depth

The processes used to convert seismic two-way travel times to depth are introduced briefly here. A discussion of depth conversion is warranted because the process is not straightforward and requires knowledge of variable water column and subsurface conditions.

Water Depth Conversion. Water depth at a given location may be determined by either direct or indirect means. Direct water depth measurements are made during the drilling of oil and gas wells and geotechnical borings. The driller records the length of the drill string when the seafloor is reached (Campbell, 1999).

Indirect methods of water depth determination require mathematical manipulation of geophysical data. 3-D seismic data or special bathymetric surveys provide depth below the sea surface in two-way time. If the vertical sonic velocity within the water column is known, then depth can easily be determined. A constant value of velocity in the vertical direction may be assumed for the water column and often is in everyday practice (Advocate and Hood, 1993, K. J. Campbell, 2004, personal communication). However, the velocity of sound in seawater is not constant with depth, and the application of a constant value of velocity may result in significant errors in water depth. Water column sonic velocities are dependent upon three parameters: temperature, salinity, and pressure (depth).

Velocimeters are tools utilized at the time of offshore geophysical survey work to collect information on the variations in temperature, salinity, and pressure within the water column as the instrument is dropped from the ship to the seafloor. These empirical data are used to develop a time-velocity relationship for conversion of seismic travel times to depth for the water column.

Advocate and Hood (1993) noted that constant vertical velocity functions can introduce significant error into water depth calculations from seismic two-way travel times on the order of hundreds of feet for water depths on the order of 5,000 ft. Obviously, such error is unacceptable for scientific and engineering purposes. Velocimeter drop data is desirable to have, but is not necessarily available or accessible for an area.

Using fourteen velocimeter profiles collected at different locations around the northern Gulf of Mexico in differing water depths and during different seasons, Advocate and Hood (1993) developed a relationship between two-way seismic travel time and water depth that considers variations in salinity, temperature, and pressure. Seismic travel time and seismic velocity pairs derived from the velocimeter data were plotted, and a best-fit curve was applied to the raw points. The resulting best-fit time versus velocity function can be manipulated into a useful relationship between two-way seismic travel time and water depth as:

$$D = 1/2(0.1105 - 5066.9193(T) + 468.6693(T^2) - 554.7107(T^3) + 340.7019(T^4) - 116.9910(T^5) + 20.7280(T^6) - 1.4658(T^7)) \quad (6)$$

D is water depth in feet, and *T* is two-way seismic travel time in seconds from the sea surface to the seafloor. This function has been found to be universally applicable across the Gulf of Mexico and in other areas of the world (K. J. Campbell, 2004, personal communication), with expected maximum errors of less than one percent (Advocate and Hood, 1993). This depth conversion function was used to convert seafloor seismic arrival times to water depth in this investigation.

Subsurface Depth Conversion. Conversion of two-way seismic travel times below the seafloor to accurate subsurface depths is carried out in a similar way to water column time-to-depth conversions. Subsurface vertical seismic velocities are dependent primarily on lithology, consolidation or compaction (amount of original porosity remaining), and the degree to which diagenetic processes have affected the mechanical properties of the sediments (such as cementation, precipitation, and recrystallization). In general, vertical seismic velocity increases with depth, but this increase is not necessarily linear. Thus, constant velocities are not feasible

for subsurface depth conversion, and simple first-order (linear) equations commonly yield inaccurate depth determinations.

Subsurface seismic velocity data that do account for nonlinearity and the variations in material properties of sediments are available from two sources: the seismic data itself (stacking velocities) and from downhole borehole seismic surveys done concurrently with the drilling of a well (checkshot time-depth pairs). Stacking velocities are readily derived from the data for any point of interest. However, because of certain assumptions and mathematical estimations used in deriving stacking velocities, depth values calculated with their use may be in error by as much as five percent or more (Brown, 1999).

Checkshot time-depth pairs are vertical velocity data that is collected during the process of drilling a well by measuring the travel time of acoustic signals sent from known depths in the wellbore to the surface. Although checkshot velocity surveys are only truly representative of subsurface seismic velocities at the wellbore, they are generally applicable within the vicinity of the survey well, provided that geological conditions are generally laterally homogenous (K. J. Campbell, 2004, personal communication). Checkshot surveys are considered to be one of the most accurate measures of subsurface vertical seismic velocities, with depth conversion errors on the order of 0.1% (Brown, 1999, A. R. Brown, 2002, personal communication).

The provider of the HR 3-D seismic data set also provided a fifth-order polynomial subsurface time-to-depth velocity function derived from checkshot survey data collected at an exploration well in the vicinity of the study area. This function was judged to provide the most accurate available depth conversions for this study area and was used for all subsurface time-to-depth conversions. The equation is as follows:

$$D = (1/2) * (4971.2*T + 1594.5*T^2 - 1341.3*T^3 + 627.51*T^4 - 96.362*T^5) \quad (7)$$

D is subsurface depth in feet, and T is two-way seismic travel time in seconds from the seafloor to the subsurface horizon of interest.

Throw Measurements, Data Recording, and Calculations

Data collection was accomplished by following a procedure designed to provide accurate and complete horizon offset data, present that data in a logical way, and maximize efficiency by automating several laborious data reduction processes. Microsoft Excel was found to be well suited for these purposes, though any spreadsheet application would have been sufficient.

A separate Excel spreadsheet was created for each fault selected for investigation. The spreadsheet organization and functions are described here. Refer to Figure 36, which shows an example spreadsheet used for data collection.

COLUMN 1. This column contains the location information for the measurements and computations in the succeeding columns. The column header lists the fault number for which measurements are taken (Figure 7), and the column entries are the horizons that are present at the fault and vertical seismic section intersection.

COLUMN 2. This column contains the seafloor two-way travel time to the top of the fault scarp for the fault and vertical section intersection of interest. The value recorded from the workstation is in units of two-way travel time seconds below sea surface (BSS). This value is the same for all horizons at this measurement location and can be considered to be the datum for all calculations.

COLUMN 3. The seafloor two-way travel times listed in Column 2 were converted to depth using the harmonic mean polynomial time-to-depth conversion function developed by Advocate and Hood (1993). This is the fault footwall scarp water depth.

COLUMN 4. The distances listed here are distances in two-way time in seconds BSS to the footwall cutoff of the horizon.

COLUMN 5. The values listed here are depth to the horizon footwall cutoffs in feet BSS. For a given horizon, the time listed in Column 2 is subtracted from the time listed in Column 4. The result is the two-way travel time difference between the seafloor and the horizon (*T* below). This difference is converted to depth below seafloor (*D*) or below

Velocity/Depth Function for Water Column:	Advocate & Hood (1993)												
Velocity/Depth Function for Sediment Column:	D=(4671.2 + (594.5*T) - (1341.3*(T^2)) + (627.51*(T^3)) - (96.362*(T^4)))*(T/2)												
1	2	3	4	5	6	7	8	9	10	11	12	13	14
Fault 1, Inline 1660 Horizon	Fault Scarp Water Depth	Fault Scarp Water Depth	Footwall Depth	Footwall Depth	Footwall Depth	Hanging Wall Depth	Hanging Wall Depth	Hanging Wall Depth	Throw	Throw (HW/FW depths)	Graph FW Depth BML	Graph Throw (HW/FW depths)	Notes
	(sec TWT BSS)	(feet BSS)	(sec TWT BSS)	(feet BSS)	(feet BML)	(sec TWT BSS)	(feet BSS)	(feet BML)	(sec TWT)	(feet)	(feet)	(feet)	
SF	1.398	3438.0	1.398	3438.0	0.0	1.421	3495.6	57.6	0.023	57.6	0.0	57.6	No drag observed.
SP1	1.398	3438.0	1.454	3579.6	141.6	1.485	3659.9	221.9	0.031	80.3	141.6	80.3	No drag observed.
A	1.398	3438.0	1.527	3770.6	332.6	1.562	3864.4	426.3	0.035	93.8	332.6	93.8	No drag observed.
Fault 1, Inline 1640 Horizon	Fault Scarp Water Depth	Fault Scarp Water Depth	Footwall Depth	Footwall Depth	Footwall Depth	Hanging Wall Depth	Hanging Wall Depth	Hanging Wall Depth	Throw	Throw (HW/FW depths)	Graph FW Depth BML	Graph Throw (HW/FW depths)	Notes
	(sec TWT BSS)	(feet BSS)	(sec TWT BSS)	(feet BSS)	(feet BML)	(sec TWT BSS)	(feet BSS)	(feet BML)	(sec TWT)	(feet)	(feet)	(feet)	
SF	1.393	3425.8	1.393	3425.8	0.0	1.413	3475.8	50.0	0.02	50.0	0.0	50.0	No drag observed.
SP1	1.393	3425.8	1.450	3570.0	144.1	1.471	3624.2	198.4	0.021	54.3	144.1	54.3	No drag observed.
A	1.393	3425.8	1.520	3753.1	327.2	1.543	3814.5	388.7	0.023	61.4	327.2	61.4	No drag observed.
Fault 1, Inline 1620 Horizon	Fault Scarp Water Depth	Fault Scarp Water Depth	Footwall Depth	Footwall Depth	Footwall Depth	Hanging Wall Depth	Hanging Wall Depth	Hanging Wall Depth	Throw	Throw (HW/FW depths)	Graph FW Depth BML	Graph Throw (HW/FW depths)	Notes
	(sec TWT BSS)	(feet BSS)	(sec TWT BSS)	(feet BSS)	(feet BML)	(sec TWT BSS)	(feet BSS)	(feet BML)	(sec TWT)	(feet)	(feet)	(feet)	
SF	1.394	3428.3	1.394	3428.3	0.0	1.421	3495.9	67.7	0.027	67.7	0.0	67.7	No drag observed.
SP1	1.394	3428.3	1.450	3569.8	141.6	1.478	3642.3	214.0	0.028	72.5	141.6	72.5	No drag observed.
A	1.394	3428.3	1.519	3750.2	321.9	1.549	3830.4	402.1	0.03	80.2	321.9	80.2	No drag observed.
Fault 1, Inline 1600 Horizon	Fault Scarp Water Depth	Fault Scarp Water Depth	Footwall Depth	Footwall Depth	Footwall Depth	Hanging Wall Depth	Hanging Wall Depth	Hanging Wall Depth	Throw	Throw (HW/FW depths)	Graph FW Depth BML	Graph Throw (HW/FW depths)	Notes
	(sec TWT BSS)	(feet BSS)	(sec TWT BSS)	(feet BSS)	(feet BML)	(sec TWT BSS)	(feet BSS)	(feet BML)	(sec TWT)	(feet)	(feet)	(feet)	
SF	1.393	3425.8	1.393	3425.8	0.0	1.419	3491.0	65.2	0.026	65.2	0.0	65.2	No drag observed.
SP1	1.393	3425.8	1.448	3564.8	139.0	1.474	3632.0	206.2	0.026	67.2	139.0	67.2	No drag observed.
A	1.393	3425.8	1.516	3742.4	316.6	1.574	3898.2	472.4	0.058	155.8	316.6	155.8	No drag observed.
Fault 1, Inline 1580 Horizon	Fault Scarp Water Depth	Fault Scarp Water Depth	Footwall Depth	Footwall Depth	Footwall Depth	Hanging Wall Depth	Hanging Wall Depth	Hanging Wall Depth	Throw	Throw (HW/FW depths)	Graph FW Depth BML	Graph Throw (HW/FW depths)	Notes
	(sec TWT BSS)	(feet BSS)	(sec TWT BSS)	(feet BSS)	(feet BML)	(sec TWT BSS)	(feet BSS)	(feet BML)	(sec TWT)	(feet)	(feet)	(feet)	
SF	1.393	3425.8	1.393	3425.8	0.0	1.436	3534.1	108.3	0.043	108.3	0.0	108.3	Displays normal drag. This
SP1	1.393	3425.8	1.447	3562.3	136.4	1.496	3689.6	263.8	0.049	127.3	136.4	127.3	Displays normal drag. This
A	1.393	3425.8	1.514	3737.1	311.3	1.578	3909.0	483.2	0.064	171.9	311.3	171.9	Displays normal drag. This
Fault 1, Inline 1560 Horizon	Fault Scarp Water Depth	Fault Scarp Water Depth	Footwall Depth	Footwall Depth	Footwall Depth	Hanging Wall Depth	Hanging Wall Depth	Hanging Wall Depth	Throw	Throw (HW/FW depths)	Graph FW Depth BML	Graph Throw (HW/FW depths)	Notes
	(sec TWT BSS)	(feet BSS)	(sec TWT BSS)	(feet BSS)	(feet BML)	(sec TWT BSS)	(feet BSS)	(feet BML)	(sec TWT)	(feet)	(feet)	(feet)	
SF	1.393	3425.8	1.393	3425.8	0.0	1.438	3539.2	113.4	0.045	113.4	0.0	113.4	Displays normal drag. This
SP1	1.393	3425.8	1.450	3570.0	144.1	1.497	3692.2	266.4	0.047	122.3	144.1	122.3	Displays normal drag. This
A	1.393	3425.8	1.510	3726.5	300.7	1.585	3928.1	502.3	0.075	201.6	300.7	201.6	Displays normal drag. This
Fault 1, Inline 1540 Horizon	Fault Scarp Water Depth	Fault Scarp Water Depth	Footwall Depth	Footwall Depth	Footwall Depth	Hanging Wall Depth	Hanging Wall Depth	Hanging Wall Depth	Throw	Throw (HW/FW depths)	Graph FW Depth BML	Graph Throw (HW/FW depths)	Notes
	(sec TWT BSS)	(feet BSS)	(sec TWT BSS)	(feet BSS)	(feet BML)	(sec TWT BSS)	(feet BSS)	(feet BML)	(sec TWT)	(feet)	(feet)	(feet)	
SF	N/A	#VALUE!	N/A	#VALUE!	#VALUE!	N/A	#VALUE!	#VALUE!	#VALUE!	#VALUE!	#VALUE!	#VALUE!	Apparent fluid expulsion feat
SP1	N/A	#VALUE!	N/A	#VALUE!	#VALUE!	N/A	#VALUE!	#VALUE!	#VALUE!	#VALUE!	#VALUE!	#VALUE!	Apparent fluid expulsion feat
A	N/A	#VALUE!	N/A	#VALUE!	#VALUE!	N/A	#VALUE!	#VALUE!	#VALUE!	#VALUE!	#VALUE!	#VALUE!	Apparent fluid expulsion feat
Fault 1, Inline 1520 Horizon	Fault Scarp Water Depth	Fault Scarp Water Depth	Footwall Depth	Footwall Depth	Footwall Depth	Hanging Wall Depth	Hanging Wall Depth	Hanging Wall Depth	Throw	Throw (HW/FW depths)	Graph FW Depth BML	Graph Throw (HW/FW depths)	Notes
	(sec TWT BSS)	(feet BSS)	(sec TWT BSS)	(feet BSS)	(feet BML)	(sec TWT BSS)	(feet BSS)	(feet BML)	(sec TWT)	(feet)	(feet)	(feet)	
SF	1.395	3430.7	1.395	3430.7	0.0	1.434	3528.8	98.1	0.039	98.1	0.0	98.1	Displays normal drag. This
SP1	1.395	3430.7	1.451	3572.3	141.6	1.503	3707.6	276.9	0.052	135.4	141.6	135.4	Displays normal drag. This
A	1.395	3430.7	1.514	3736.7	306.0	1.587	3933.0	502.3	0.073	196.3	306.0	196.3	Displays normal drag. This
Fault 1, Inline 1500 Horizon	Fault Scarp Water Depth	Fault Scarp Water Depth	Footwall Depth	Footwall Depth	Footwall Depth	Hanging Wall Depth	Hanging Wall Depth	Hanging Wall Depth	Throw	Throw (HW/FW depths)	Graph FW Depth BML	Graph Throw (HW/FW depths)	Notes
	(sec TWT BSS)	(feet BSS)	(sec TWT BSS)	(feet BSS)	(feet BML)	(sec TWT BSS)	(feet BSS)	(feet BML)	(sec TWT)	(feet)	(feet)	(feet)	
SF	1.397	3435.6	1.397	3435.6	0.0	1.454	3579.7	144.1	0.057	144.1	0.0	144.1	Displays normal drag. This
SP1	1.397	3435.6	1.453	3577.2	141.6	1.517	3744.2	308.7	0.064	167.1	141.6	167.1	Displays normal drag. This
A	1.397	3435.6	1.520	3752.2	316.6	1.597	3959.7	524.1	0.077	207.5	316.6	207.5	Displays normal drag. This
Fault 1, Inline 1480 Horizon	Fault Scarp Water Depth	Fault Scarp Water Depth	Footwall Depth	Footwall Depth	Footwall Depth	Hanging Wall Depth	Hanging Wall Depth	Hanging Wall Depth	Throw	Throw (HW/FW depths)	Graph FW Depth BML	Graph Throw (HW/FW depths)	Notes
	(sec TWT BSS)	(feet BSS)	(sec TWT BSS)	(feet BSS)	(feet BML)	(sec TWT BSS)	(feet BSS)	(feet BML)	(sec TWT)	(feet)	(feet)	(feet)	
SF	1.400	3442.9	1.400	3442.9	0.0	1.454	3579.3	136.4	0.054	136.4	0.0	136.4	Displays normal drag. This
SP1	1.400	3442.9	1.456	3584.5	141.6	1.514	3735.7	292.8	0.058	151.2	141.6	151.2	Displays normal drag. This
A	1.400	3442.9	1.515	3738.3	295.4	1.594	3950.6	507.7	0.079	212.3	295.4	212.3	Displays normal drag. This

FIGURE 36: Example of worksheet used in the data collection phase of this study. Horizon designations are the same as those given in the text. Two-way travel times are given in seconds BSS or BML, and depths are given in units of feet. Column numerical designations are keyed to the text. Text in column 14 has been truncated to improve presentation of the table in this figure.

mudline (BML) using the subsurface time-to-depth relationship given in the preceding section. The result of this computation is then added to the footwall water depth, given in Column 3.

COLUMN 6. The depths to footwall horizon cutoff in feet BML given here are a statement of the intermediate calculation given in the preceding column. The depth reported here is the sediment column thickness at the footwall cutoff for the corresponding horizon.

COLUMN 7. The values listed here are distances in two-way time in seconds BSS to the hanging wall cutoff of the horizon.

COLUMN 8. The values listed here are depths to the horizon hanging wall cutoffs in feet BSS. For a given horizon, the time listed in Column 2 is subtracted from the time listed in Column 7. The result is the two-way travel time difference between the seafloor and the horizon (T). The depth BML is computed identically as described for Column 5 using the fifth-order subsurface time-to-depth function.

COLUMN 9. As with Column 6, the depth to hanging wall cutoff in feet BML given here is a statement of the intermediate calculation given in the preceding column. The depth reported here is the sediment column thickness at the hanging wall cutoff for the corresponding horizon.

COLUMN 10. This column contains calculated values of throw for the corresponding horizon in two-way time seconds and is the difference between the hanging wall distance and footwall distance given to the horizon given in Columns 7 and 4, respectively.

COLUMN 11. This column contains calculated values of throw for the corresponding horizon in feet and is the difference between the hanging wall depth and footwall depth to the horizon given in Columns 9 and 6, respectively.

COLUMNS 12 AND 13. These columns are a restatement of Columns 6 and 11 and were repeated in the spreadsheet to make the process of graphing depth versus throw easier.

COLUMN 14. This column lists observations made during the measurement process. Many observations relate to drag and the process used to correct for it. Some notes were taken on data quality and other geological phenomena that have complicated the local geology.

The spreadsheet example shown in Figure 36 shows the measured and calculated values for measurement stations along one fault. Measurement stations are spaced every 20th inline (every 492 feet) for this example.

Data Analysis

Previous similar studies, such as those conducted by Barnett et al. (1987), Chapman and Meneilly (1990 and 1991), and Mansfield and Cartwright (1996), produced fault throw contour diagrams that display the results of the throw measurement analysis for a given fault. These studies focused mainly on very large faults imaged in 3-D exploration (conventional) seismic surveys and faults of moderate size encountered in coal mine drifts in the UK. Numerous continuous reflectors were mapped as horizons along the strike and dip lengths of those faults. Thus, these faults, although measured on a coarse seismic line grid, are well-constrained along strike and down dip. For this study, the available HR 3-D seismic volume allows for good control of fault characteristics along strike. However, the chaotic geometry of deep seismic reflectors and a zone of bright reflectors at depth that cause dimming of the underlying reflectors severely degrade the ability to map deeper horizons through the study area. This results in excellent characterization of the faults at shallow depths but poor or no control of the fault at depth. Thus, the dip length of the faults generally cannot be constrained using the 3-D HR seismic data. Therefore, the analysis presentation methods used previously in other studies are not well suited to the data collected here. This investigation focuses on fault throw characteristics that can be determined for the upper portions of the faults.

Each measurement station along a given fault yielded values of fault throw for all of the horizons cut by the fault. A plot of depth below the seafloor to the intersected horizons versus measured throw at the respective horizons yields a profile of the variation in fault throw with depth from the seafloor to the deepest encountered horizon (Figure 37). Such a vertical profile plot could be constructed for each measurement station along each fault selected for study. However, this display does not convey information about the lateral distribution of throw, which is the main focus of this investigation.

Horizontal profiles of distance along the fault versus throw were also constructed. For all of the faults investigated, the northern-most measurement station is considered to be the origin for lateral distance measurements. For each measurement station, the distance from the origin is plotted against the throw at each intersected horizon (Figure 37). This results in a graphic display of the variation of throw with distance along strike of the fault. This type of display is very useful for determining the distribution of throw along strike of the faults and constitutes most of the illustrative data examples presented in this investigation.

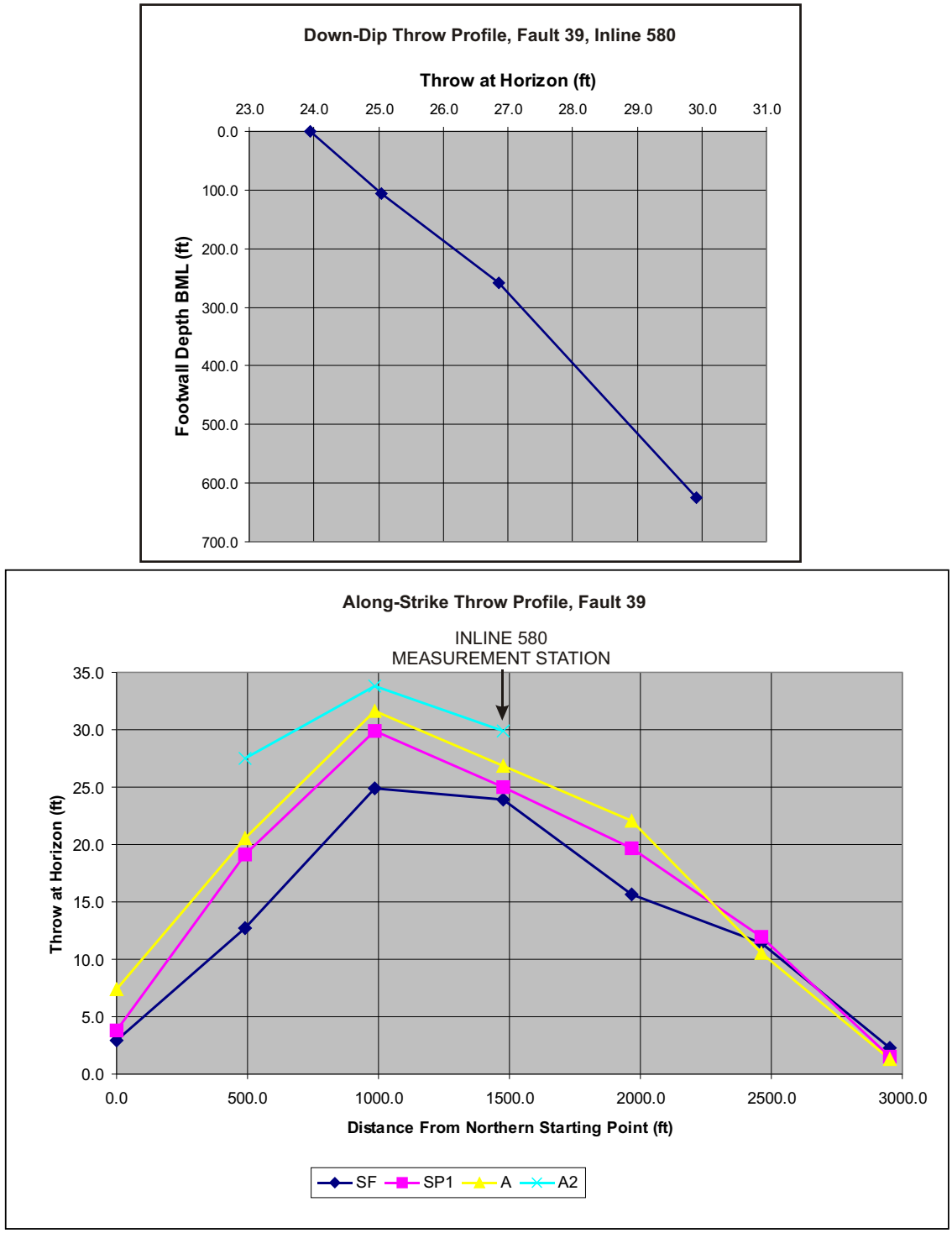

FIGURE 37: Examples of down-dip and along-strike throw profiles. Upper graph is a down-dip throw profile taken from Fault 39 at inline 580. Points represent, from shallowest to deepest depth BML, throw at Seafloor, SP1, A, and A2 horizons. Lower graph is an along-strike throw profile for Fault 39. Points along the four lines represent throw at the measurement stations along the fault for each of the horizons intersected by the fault.

RESULTS

This section contains results of the analysis of throw measurements of selected faults within the study area. Table 1 gives summary information on each fault included in this study, and selected representative data examples are also presented in graphical form. Appendix A contains along-strike throw profiles for 32 of the 40 faults in this investigation that are not described in detail and shown in figures accompanying the following discussion of results.

Fault Trace Characteristics and Measurements Taken

Of the fifty faults mapped in detail in vertical seismic sections, forty were selected for the purpose of taking throw measurements (Table 1). The ten faults that were omitted either fall outside the primary study area or are not imaged well enough in the seismic data to permit measurement of horizon offsets with reasonable confidence. The forty selected faults range in seafloor trace length between about 1,220 ft and 13,284 ft (about 2.5 miles), with an average trace length of about 5,000 ft and a median trace length of about 4,107 ft. The maximum relief across the seafloor scarp of a fault included in the study is about 144 ft. The average maximum seafloor fault scarp relief for a given fault included within the study ranges between 3.7 ft and 144 ft, with an average value of about 27 ft, and a median value of about 13.5 ft.

Throw measurements were taken at regular intervals along the trace of each fault. The first measurement station was at the northern end of the fault trace. Measurements were made nominally every 492 ft, corresponding to every twentieth seismic inline. For a few selected faults, measurements were made every 246 ft (every tenth seismic inline), with the purpose of examining the effect of lateral measurement resolution on the lateral distribution of throw on the fault. The ending measurement station was at the southern end of the fault trace. The number of measurement stations on the faults ranges from 3 to 28, with an average of 10. The total number of discrete measurements made of throw at horizons offset by the faults is 1,715.

Corrections Applied to and Limitations of Data

A limited number of corrections were applied to the throw measurement data. The only type of corrections applied were those intended to compensate for fault-related folding in the

TABLE 1. RESULTS SUMMARY TABLE FOR STUDY AREA FAULTS							
FAULT	**TRACE LENGTH (FT)**	**NUMBER OF MEASURE-MENT STATIONS**	**RESTRICTED OR UNRESTRICTED**	**LINKED OR SINGLE SEGMENT**	**DOWN-DIP THROW DISTRIBUTION NEAR FAULT CENTER**	**MEASUREMENT SPACING (FT)**	**NOTES**
1	14,572	28	restricted, north end	linked, 4 or 5 segments	throw increases down-dip	492	first measurement taken 984 ft from north end because of imaging problems
2	8,861	18	restricted, north end	linked, 2 or 3 segments	throw increases down-dip	492	
3	5,410	11	restricted, north end	linked, 2 segments	throw increases down-dip	492	
4	8,297	16	restricted, north end	linked, up to 5 segments; possibly seeing displacement irregularities along strike	shows throw max. within measurement depth range	246	map view trace geometry consistent with linkage and splay at north end
5	7,600	15	restricted, north end	linked, 2 or 3 segments	throw increases down-dip	492	
6	4,854	10	restricted, south end	single segment	throw increases down-dip	492	irregular (unsymmetrical) displacement geometry
7	13,890	25	restricted, south end	linked, 3 or 4 segments	throw increases down-dip	492	
8	4,652	9	unrestricted	single segment	throw decreases down-dip	492	unusual, unexpected fault characteristics
9	6,850	14	restricted, south end	linked, 2 or 3 segments	throw increases down-dip	492	
10	4,738	10	unrestricted	linked, 2 segments	unclear	492	unusual, unexpected fault characteristics

TABLE 1. CONTINUED							
FAULT	**TRACE LENGTH (FT)**	**NUMBER OF MEASURE-MENT STATIONS**	**RESTRICTED OR UNRESTRICTED**	**LINKED OR SINGLE SEGMENT**	**DOWN-DIP THROW DISTRIBUTION NEAR FAULT CENTER**	**MEASUREMENT SPACING (FT)**	**NOTES**
11	10,470	20	restricted, north end, possible branch	linked, 2 segments	throw increases down-dip	492	
12	9,565	17	restricted, both ends	linked, 3 or 4 segments	throw increases down-dip	492	
13	8,164	16	unrestricted	single segment	shows throw max. within measurement depth range	492	north end severely restricted; small displacement for fault length
14	6,733	13	restricted, near north end	linked, 3 segments	throw increases down-dip	492	
15	5,348	10	restricted, north end	linked, 2 segments	throw increases down-dip	492	north end displays restriction at crossing fault
16	3,755	7	restricted, north end	linked, 2 segments	shows throw max. within measurement depth range	492	abuts fault 35 (with antithetic dip)
24	2,205	5	restricted, south end	single segment	shows throw max. within measurement depth range	492	
25	1,220	3	unrestricted	single segment	shows throw max. within measurement depth range	492	
26	1,886	3	unrestricted	single segment	unclear	492	unclear characteristics for this fault

TABLE 1. CONTINUED							
FAULT	**TRACE LENGTH (FT)**	**NUMBER OF MEASURE-MENT STATIONS**	**RESTRICTED OR UNRESTRICTED**	**LINKED OR SINGLE SEGMENT**	**DOWN-DIP THROW DISTRIBUTION NEAR FAULT CENTER**	**MEASUREMENT SPACING (FT)**	**NOTES**
27	3,518	5	restricted, south end	single segment	throw increases down-dip	492	
28	2,535	5	restricted, south end	single segment	shows throw max. within measurement depth range	492	
29	2,733	5	unrestricted	single segment	throw increases down-dip	492	
30	2,760	4	unrestricted	linked, 2 segments	shows throw max. within measurement depth range	492	south end of fault outside data coverage
31	2,271	5	restricted, north end	linked, 2 segments	shows throw max. within measurement depth range	492	
32	4,064	9	restricted, north end	single segment	shows throw max. within measurement depth range	492	
33	1,805	8	restricted, north end	linked, 2 segments	throw increases down-dip	246	
35	1,532	4	restricted, south end	single segment	shows throw max. within measurement depth range	492	
36	7,392	14	unrestricted	linked, 3 segments	throw increases down-dip	492	northernmost 1,200 ft could not be measured (imaging problems)

TABLE 1. CONTINUED							
FAULT	**TRACE LENGTH (FT)**	**NUMBER OF MEASURE-MENT STATIONS**	**RESTRICTED OR UNRESTRICTED**	**LINKED OR SINGLE SEGMENT**	**DOWN-DIP THROW DISTRIBUTION NEAR FAULT CENTER**	**MEASUREMENT SPACING (FT)**	**NOTES**
37	2,821	5	restricted, both ends	single segment	unclear	492	displacement distribution is unexpected
38	2,660	6	unrestricted	single segment	unclear	492	
39	3,324	7	restricted, north end	linked, 2 segments	throw increases down-dip	492	
40	3,926	7	restricted, north end	linked, 2 segments	unclear	492	
41	6,423	20	restricted, south end	linked, at least 5 segments	throw increases down-dip	246	that constitute two different faults in the area of no data
42	3,058	6	unrestricted	single segment	shows throw max. within measurement depth range	492	
43	1,310	3	unrestricted	single segment	shows throw max. within measurement depth range	492	
44	1,505	4	restricted, south end	single segment	shows throw max. within measurement depth range	492	
45	5,683	11	unrestricted	linked, 3 segments	throw increases down-dip	492	
46	4,150	7	unrestricted	linked, 2 segments	throw increases down-dip	492	unclear characteristics for this fault

TABLE 1. CONTINUED							
FAULT	**TRACE LENGTH (FT)**	**NUMBER OF MEASURE-MENT STATIONS**	**RESTRICTED OR UNRESTRICTED**	**LINKED OR SINGLE SEGMENT**	**DOWN-DIP THROW DISTRIBUTION NEAR FAULT CENTER**	**MEASUREMENT SPACING (FT)**	**NOTES**
47	6,615	13	restricted, north end	linked, 3 segments	shows throw max. within measurement depth range	492	northernmost portion could not be measured because of imaging problems related to geologic conditions
48	1,930	4	unrestricted	single segment	shows throw max. within measurement depth range	492	

hanging wall and/or footwall. These corrections were made on only one or two horizons on a small minority of the faults. This process has been discussed previously in this work and resulted in the assignment of any fault displacement accommodated by folding back to the vertical translational offset (throw) across the fault.

Measurement limitations are related to the resolution limits and spatial limits of the 3-D HR seismic data. The maximum vertical resolution of the seismic data (limit of separability, discussed previously) is about 1.3 ft, and the lateral resolution limit is equal to the distance between measurement stations, either 246 ft or 492 ft. The deepest horizons considered to be locally mappable across study area faults are around 1,600 ft below the seafloor. However, the deepest mapped horizon along which measurements were routinely taken lies at a maximum depth of about 700 ft below the seafloor. Thus, study faults are generally well characterized by measurements to a maximum depth of about 700 ft depth, and poorly characterized (or uncharacterized) below this depth. In terms of lateral limitations, the study area is well within the interior of the available 3-D HR seismic data, except along the southeastern border of the study area. There, the study area boundary abuts the edge of the seismic data. Consequently, data is only available for the northern portion of Fault 30. All other faults lie completely within the available seismic data set.

Single- and Multi-segment Faults

Analysis of the fault throw measurement data shows that the lateral (along strike) and vertical (down dip) distributions of throw show generally predictable variations with distance or depth. These variations are interpreted to be the effects of fault growth by tipline propagation and fault segment linkage. It has been previously mentioned that linkage may occur along strike and down dip. However, because of limited depth of measurement and deteriorating seismic signal at depth, this discussion will focus exclusively on linkage along strike for the near-seafloor portions of the faults.

Seventeen of the forty study area faults show lateral distributions of throw consistent with the distribution expected for a single-segment fault (Table 1). These faults show a general

increase in throw from their tip areas to their centers at all of the horizons on which measurements were taken. In some cases, the throw maximum is not located at the midway point along the fault trace but rather at some point toward either tip. Figure 38 shows along-strike throw profiles for two representative cases, Faults 32 and 35. In each of these profiles, distance along strike is measured from the northern-most measurement station on the fault (nominally at the northern tip) and each point on the profiles represents a throw measurement at an offset horizon. For each measurement station there are several measurements of throw, with one for each offset horizon. Figure 39 is a grey-scale seafloor rendering map showing the locations and map view geometries of these faults.

These two faults display different trace lengths and throw maxima, and their lateral throw distributions are consistent with the interpretation of single-segment faults. An inspection of the fault traces on the seafloor images shows that they appear to be irregular (not smooth) and "dog-legged" in geometry. The trace of a true single fault segment growing by tipline propagation is expected to be essentially smooth because it is a continuous surface. This dog-legged surface trace geometry for Faults 32 and 35 is interpreted to be a remnant morphologic feature of faults formed by the linkage of three and two smaller faults, respectively, and is a characteristic of other study area faults with single-segment, along-strike displacement distributions. Doglegs are interpreted to represent breached relay zones between discrete fault segments.

The remaining twenty-three study area faults show lateral distributions of throw consistent with the distribution expected for a multi-segment fault (Table 1). These faults show localized, or smaller-scale throw maxima and minima along strike for some or all of the horizons on which throw measurements were taken. In addition, each of these faults shows the expected large-scale general increase in throw to a maximum in the central area of the fault trace from the tip areas. Figure 40 shows along-strike throw profiles for two representative cases, Faults 1 and 2. Figure 39 is a grey-scale seafloor rendering map showing the locations and geometries of these faults.

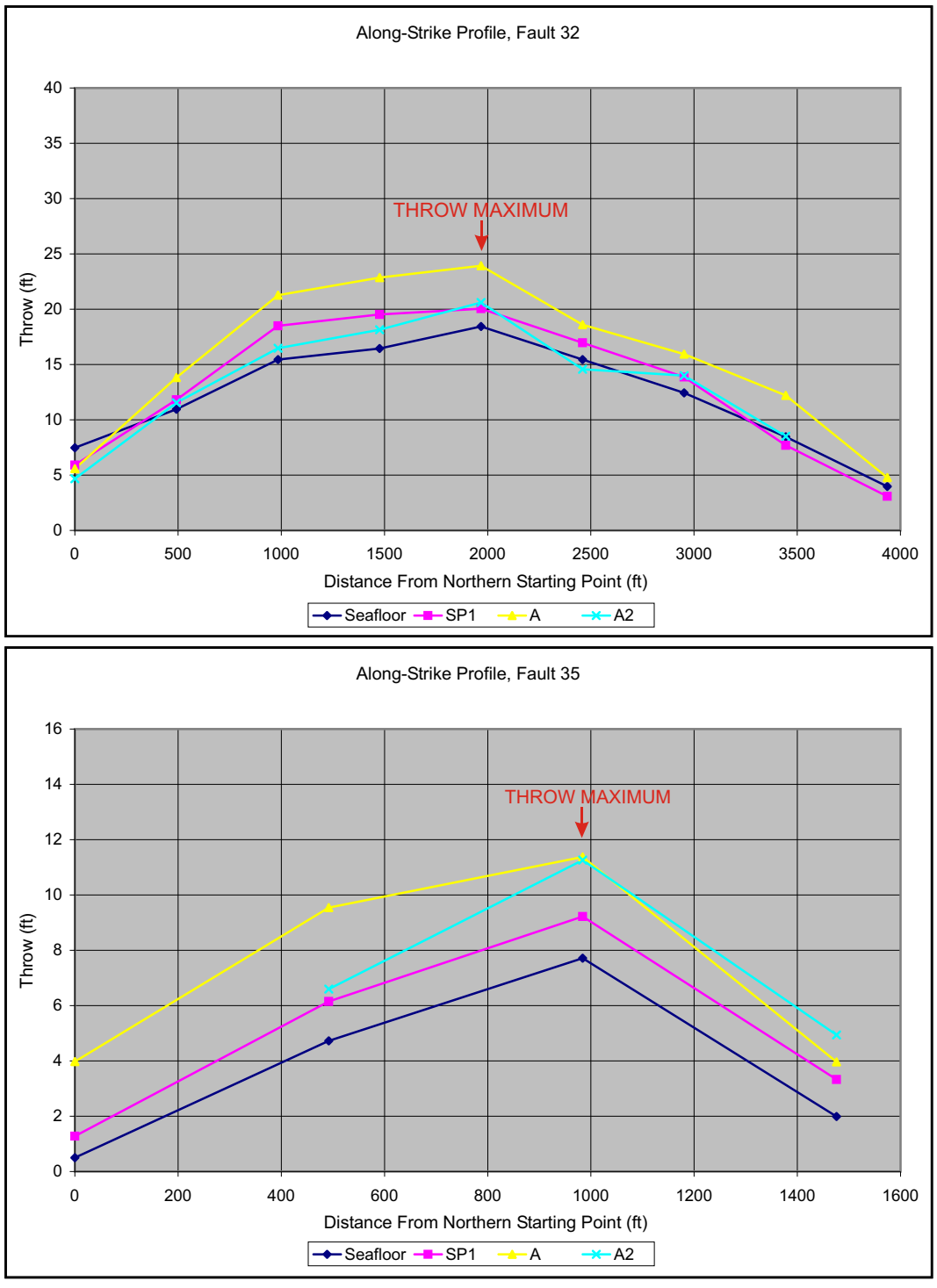

FIGURE 38: Along-strike throw profiles for four horizons offset by Faults 32 (upper) and 35 (lower). Throw at the horizons for each measurement station (indicated by symbols) are shown from northern starting point of measurements (zero distance) to the southern terminating measurement station. The lateral distribution of throw for each fault is characteristic of a single-segment fault, showing a central throw maximum and a decrease in throw toward minima at the tips.

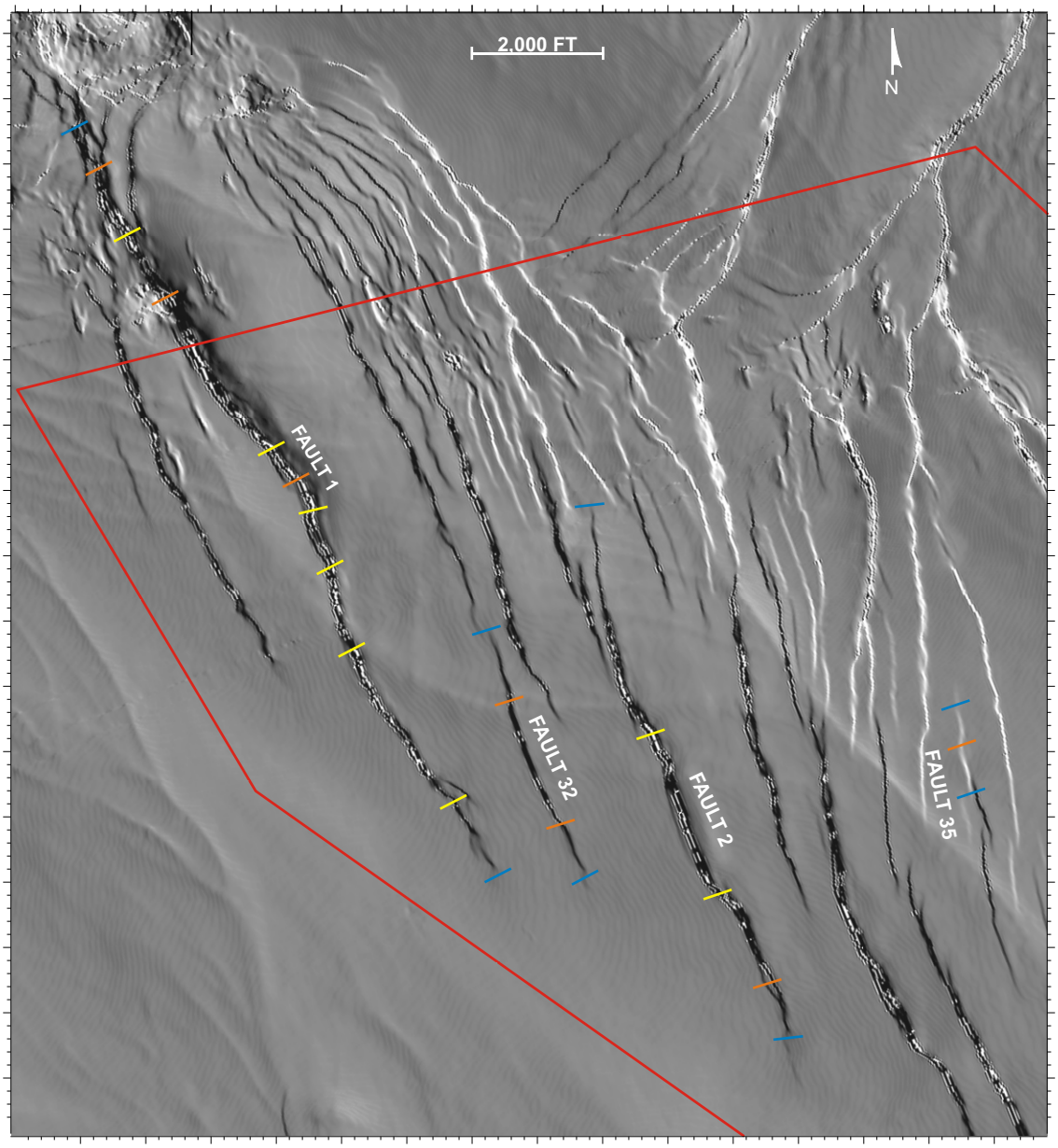

FIGURE 39: Grey-scale seafloor rendering map showing a portion of the study area including Faults 1, 2, 32, and 35 (FIGURES 38 and 40). The approximate locations of dog-legs, or locations along the fault traces where an abrupt bend in the trace occurs, are marked by yellow or orange bars. Blue bars mark the lateral tips of the fault traces. Yellow bars mark the interpreted approximate linkage points between inferred former single-segment faults that correspond to observed throw minima on the along-strike throw profile. Orange bars mark the interpreted approximate linkage points between possible former single-segment faults that cannot be correlated to throw minima observed on the along-strike profile. Red line marks the boundary of the main study area.

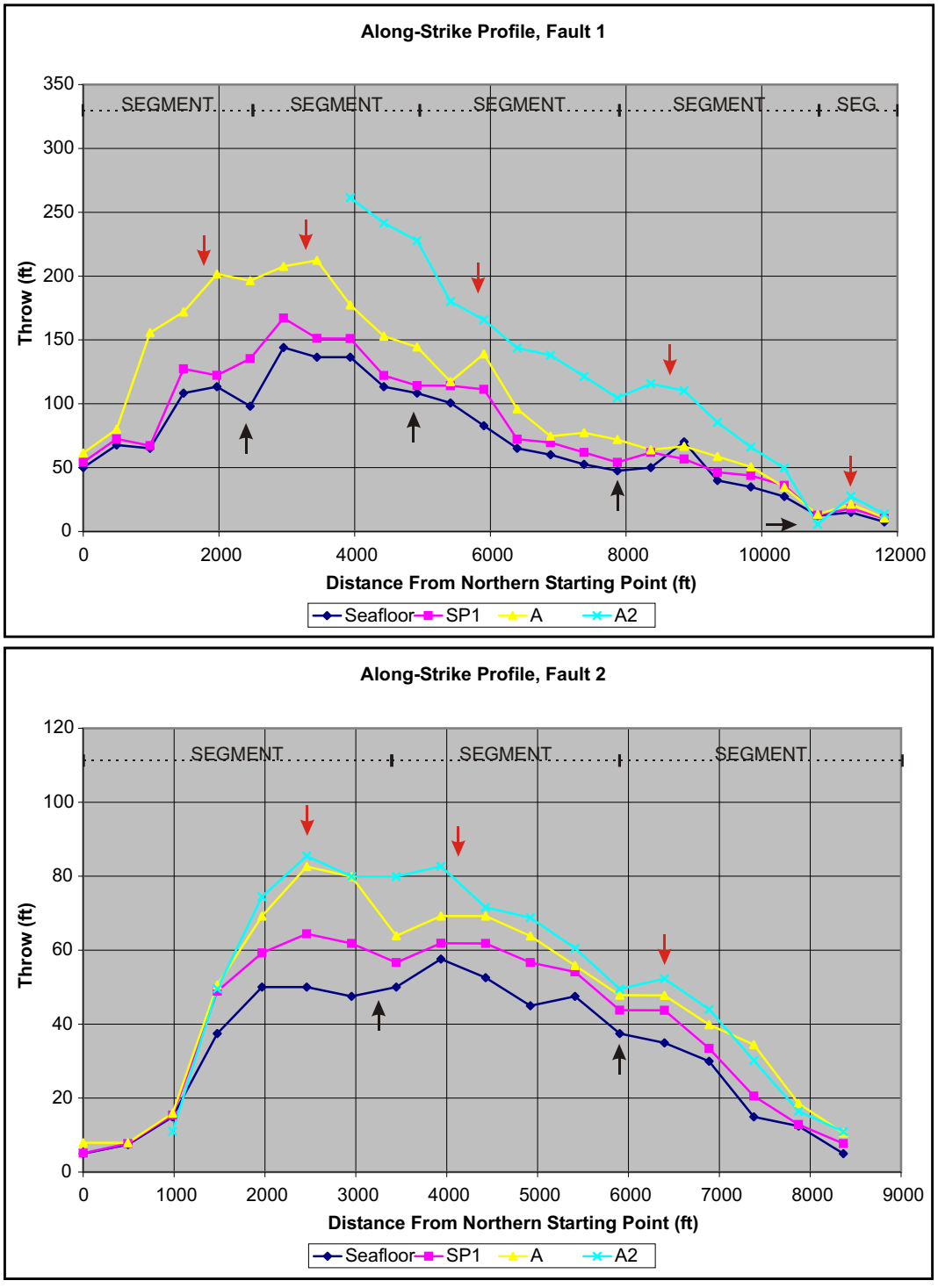

FIGURE 40: Along-strike throw profiles for four horizons offset by Faults 1 (upper) and 2 (lower). Throw at the horizons for each measurement station (indicated by symbols) are shown from northern starting point of measurements (zero distance) to the southern terminating measurement station. The lateral distribution of throw for each fault is characteristic of a multi-segment fault, showing several local throw minima (black arrows) and maxima (red arrows).

The localized throw maxima and minima present along Faults 1 and 2 are interpreted to be the result of linkage of several smaller faults, each with a discrete throw maximum, into the two respective faults. Local throw minima are inferred to correspond to the areas where segments linked. An inspection of the seafloor trace of Fault 2 (Figure 39) reveals a dog-legged morphology, and a count of discrete segments of the trace indicates that this fault may be the result of the linkage of three segments. The presence of three local throw maxima on the along-strike throw profile for this fault matches this interpretation, with the exception of a possible fourth former segment at the southern end of the fault that is not observed in the throw profile. Other multi-segment faults within the study area show the same general correspondence in the number of fault segments observed in map view and in throw profile. For Fault 1, however, the apparent presence of seven or more fault segments in map view contrasts with the interpretation of four to five throw maxima on the along-strike throw profile. Some other study area faults with a multi-segment lateral throw profile show the same discordant relationship between the number of fault segments apparent in map view versus the apparently lower number of segments evident in the faults' throw profiles.

Unrestricted and Restricted Faults

Analysis of the fault throw data shows that study area faults may also be characterized by the relative rate at which displacement changes from the nominally highest displacements at the central portion of the fault outward to the nominally lowest values at the lateral tip areas. Some faults display essentially linear lateral displacement gradients, but other faults display nonlinear, or variable, displacement gradients that tend to show the greatest deviations in the tip region.

Fourteen of the forty study area faults display generally linear lateral displacement gradients that are similar for each limb of a fault. (*Limb* is taken to refer to the lateral extent of a fault from the central (or near-central) region of maximum throw to the tip. Thus, each fault has two limbs that may be of equal or unequal length.) This condition is characteristic of faults that are unrestricted (Table 1). Figure 41 shows along-strike throw profiles for two representative

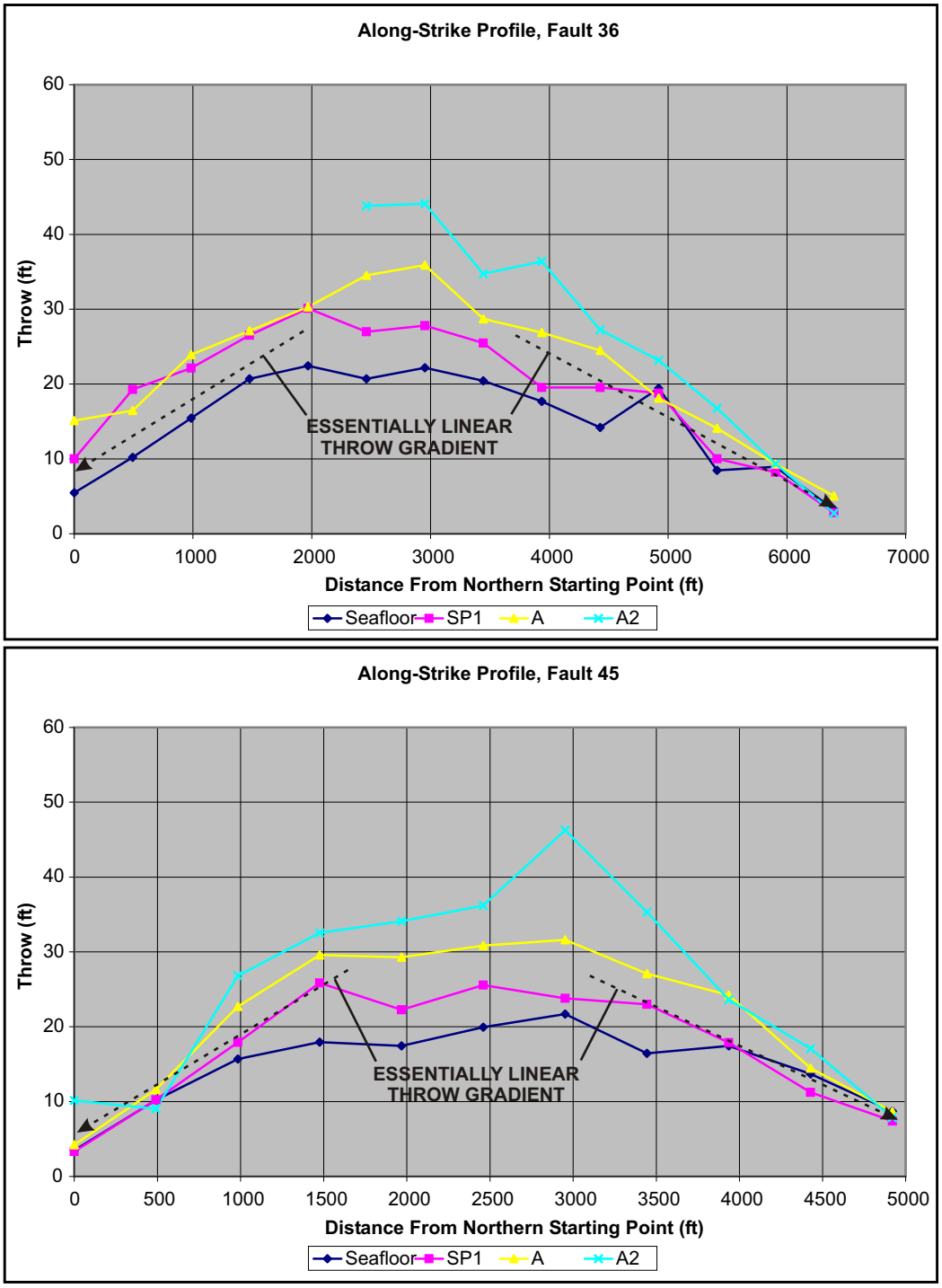

FIGURE 41: Along-strike throw profiles for four horizons offset by Faults 36 (upper) and 45 (lower). Throw at the horizons for each measurement station (indicated by symbols) are shown from northern starting point of measurements (zero distance) to the southern terminating measurement station. The change in throw from the central maximum outward toward the lateral fault tip area (throw gradient) is essentially linear, and the throw gradients for each limb of the fault are similar. These are characteristics of unrestricted faults.

unrestricted cases, Faults 36 and 45. Figure 42 is a grey-scale seafloor rendering map showing the locations of these two faults and their relationship to other faults in their vicinities. Figure 41 shows that the general throw gradient away from the central areas of both faults is linear (dashed, black arrows). In addition, the gradients are qualitatively interpreted to be similar to a first approximation.

The remaining twenty-six study area faults display lateral displacement gradients that are not generally linear nor are similar from one limb to the other. These characteristics are consistent with the interpretation that these faults are restricted at one or both of their tips (Table 1). Figure 43 shows along-strike throw profiles for two representative restricted cases, Faults 3 and 24. Figure 42 is a grey-scale seafloor rendering map showing the locations of these two faults and their relationship to other faults in their vicinities. The lateral throw profile for Fault 3 shows that the lateral throw gradient on the northern limb of the fault is non-linear and is higher than the southern limb. Note that the apparent fault center, where throw is at a maximum, is located closer to the northern fault tip than the southern tip. An inspection of Figure 42 reveals the presence of an overlapping fault tip at the north end of Fault 3. This neighboring fault is interpreted to restrict the lateral growth of Fault 3, resulting in the observed distribution of throw and the marked increase in throw gradient near the northern tip. The southern tip of Fault 3 displays no indications of restriction. The lateral throw profile for Fault 24 shows that the lateral throw gradient on the southern fault limb is non-linear and is higher than that for the northern limb. Again, the apparent fault center is located away from the midpoint along the fault trace, closer to the southern tip in this case. Figure 42 shows that an overlapping fault exists nearly along strike of and south of Fault 24. This fault is interpreted to impose a growth restriction on Fault 24, resulting in the observed throw gradient for the southern fault tip area.

Study area faults with restricted tips fall into three categories: faults with restricted northern tips, those with restricted southern tips, and those with both tips restricted (Table 1). Fifteen faults are restricted at their northern tips, and the majority are located southwest of a line

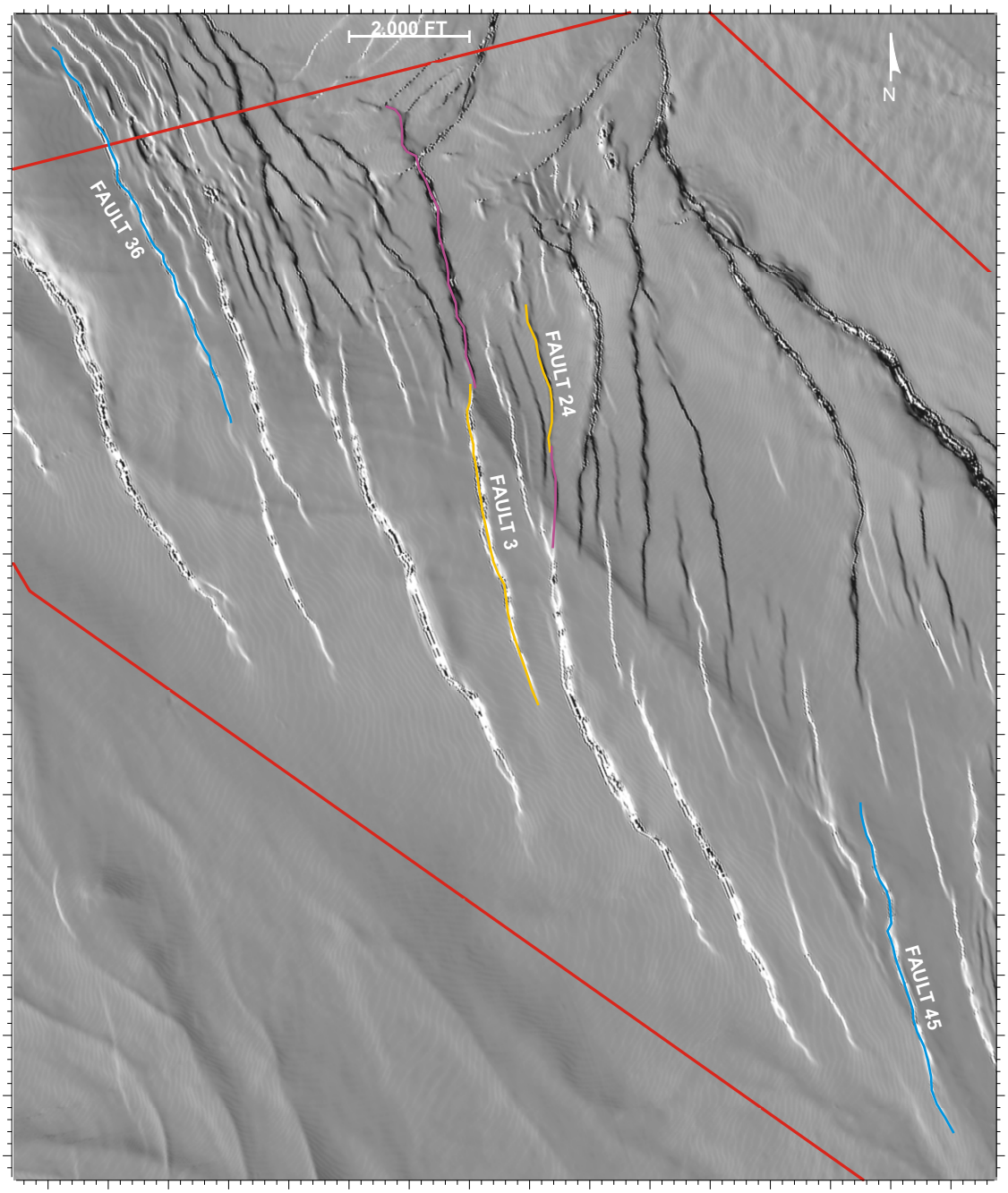

FIGURE 42: Grey-scale seafloor rendering map showing a portion of the study area including Faults 3, 24, 36, and 45 (FIGURES 41 and 43). The traces of Faults 36 and 45 are marked in blue, indicating that these faults are unrestricted. Note the absence of tips of other faults near the tips of Faults 36 and 45. The traces of Faults 3 and 24 are marked in orange, indicating that these faults are restricted. Each of these faults is restricted at one end, and the fault producing the restriction is marked in purple. Red line marks the boundary of the main study area.

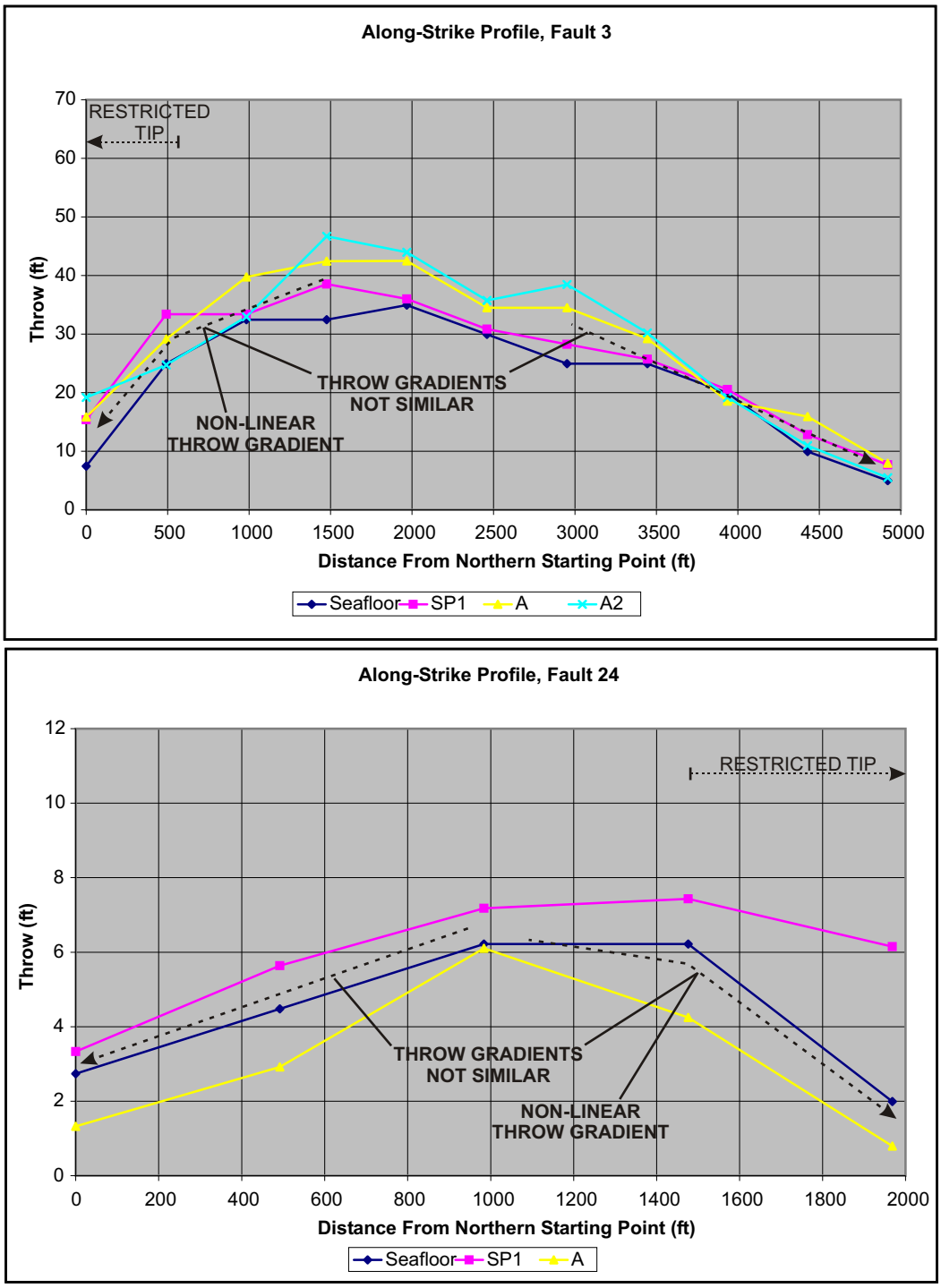

FIGURE 43: Along-strike throw profiles for horizons offset by Faults 3 (upper) and 45 (lower). Throw at the horizons for each measurement station are shown from northernmost to southernmost measurement stations along the fault. The change in throw from the central maximum outward to the lateral fault tip area (throw gradient) displays a nonlinear character (increasing in gradient toward the lateral fault tip areas) which is characteristic of restricted faults. Restriction may also exist in the form of contrasting throw gradients between the fault limbs.

marking the long axis of the seafloor graben (Figure 44). This position allows these faults to have the greatest chance for restriction along their northern tips. The southern fault tips border the poorly-defined southwestern graben boundary where no faults are observed at the seafloor. Nine faults are restricted at their southern tips and are evenly distributed on either side of the graben axis. Inspection of Figure 44 shows the relative positions of these faults with respect to the faults that impose restriction on the southern fault tips. Two faults are restricted at both tips, as indicated in Table 1 and shown on Figure 44.

Age of Faulting and Rates of Fault Movement

Knowing the amounts of displacement along horizons offset by a fault and the ages of those horizons can be used to determine the rate of fault movement through time. The magnitude of throw has been determined for several horizons at each fault included in this study. Horizon ages are not directly known, because results of direct age determination such as fossil markers and radioisotope analyses for the upper portion of the subsurface considered here are not available for this study. A method for estimating horizon ages from an idealized stratigraphic succession predicted from eustatic sealevel variations related to Milankovitch cyclicity is presented in Appendix B. This method has sufficient resolution for determining the ages of horizons deposited several tens of thousands to millions of years ago, but is not judged to be useful for short periods of time such as 10,000 years. Younes et al. (2005) report that regional, very shallowly-buried mass movement deposits related to mudvolcanoes in the vicinity of the study area are cut by seafloor faults very similar to and located in the same general area as the faults in this study. The authors report that the mass movement deposits are about 10,000 years old. Thus, the nearby and similar seafloor faults may be as old as about 10,000 years. A maximum age of 10,000 years is applied to the study area faults because no better determination of fault ages is available.

The available fault throw data and fault maximum age approximation can be used to determine generalized rates of fault movement. Using a period of 10,000 years, the maximum average rate of accumulation of throw along a fault is estimated to be about 1.4 ft per hundred

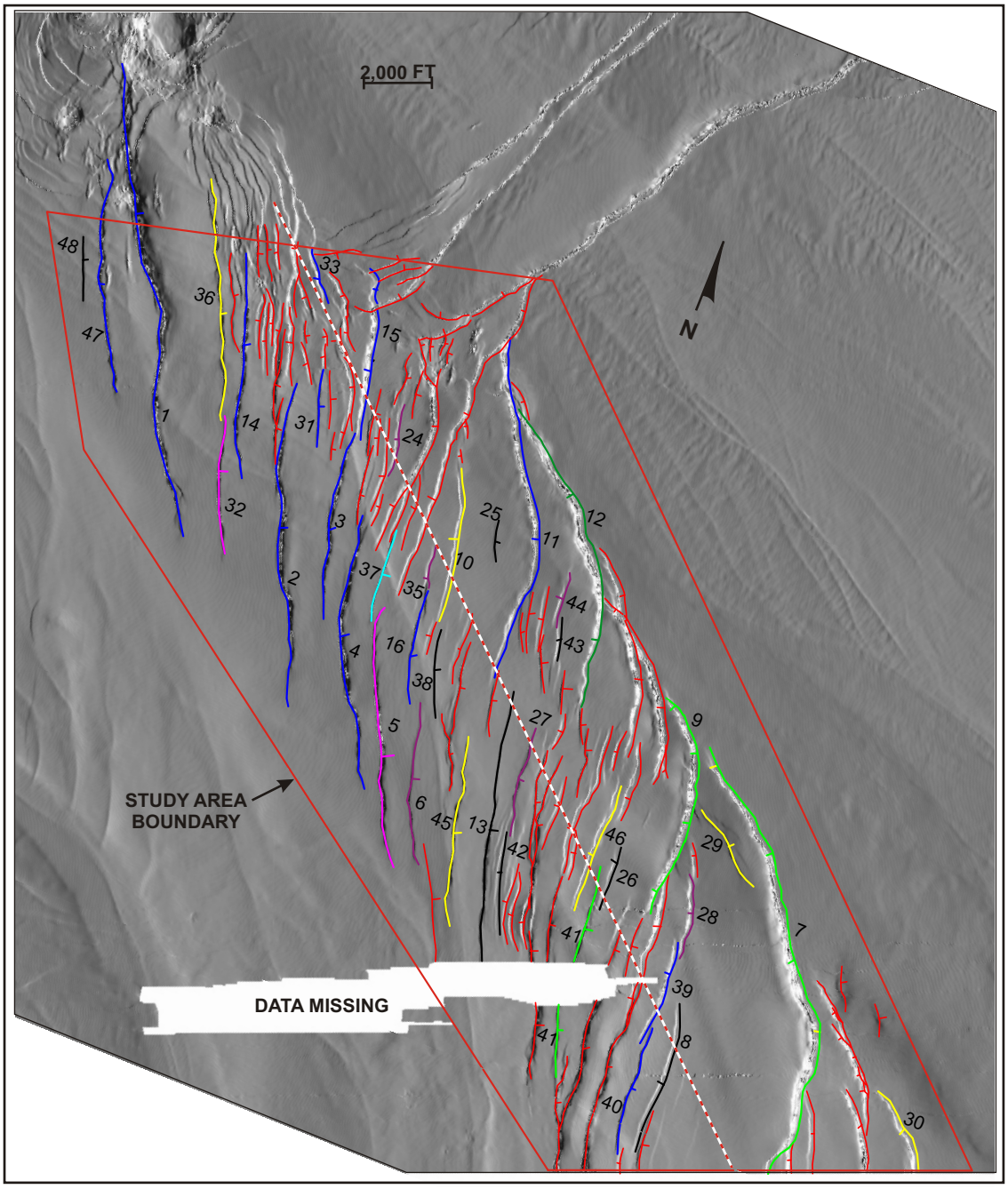

FIGURE 44: Grey-scale seafloor image showing study area fault traces color-coded by category. Red = faults not included in study; blue = multi-segment fault restricted at north end; light green = multi-segment fault restricted at southern end; dark green = multi-segment fault restricted at both ends; yellow = multi-segment, unrestricted fault; magenta = single-segment fault restricted at north end; purple = single-segment fault restricted at southern end; cyan = single-segment fault restricted at both ends; black = single-segment, unrestricted fault. Ticks show direction of fault dip. Dashed red and white line marks axis of seafloor graben.

years. Individual faults within the study area may have accumulated displacement at higher or lower rates over shorter periods of time. Also, although none is suspected, any small-scale and localized deposition or erosion of hanging wall or footwall strata would increase the uncertainty in estimated rates of movement.

Comparison of Throw and Trace Length

Plots of seafloor trace length versus maximum throw at the seafloor for each fault in the data set (or subset of the data set) in log-log space can be used to compare the similarity between the dimensional relationships between faults and to test the applicability of a power law in describing the relationship between these two dimensions. Figure 45 shows several plots of fault seafloor trace length versus maximum throw (known in the literature and previously discussed as D vs. L ratio) at the seafloor for the entire set of faults and for four selected fault subsets. The first plot shows D vs. L for all forty faults investigated in this study. A regression line shows the general trend of the data points, and the equation of this line gives the power law relationship between seafloor trace length and maximum throw at the seafloor that the regression line approximates. The R^2 value shown on the plot gives the relative agreement (or, conversely, scatter) of the data points with the regression line, with R^2 equal to 1 indicating perfect agreement between all data points and the regression line. The observed scatter in Plot 1 and R^2 equal to 0.694 are indicative of a reasonable fit between the power law function and real data.

D vs. L dimensional characteristics are also an important characteristic of the fault subsets grouped by presence or absence of restriction and single- or multi-segment character (Plots 2 to 5, Figure 45). Plots 2 and 3 show the unrestricted and restricted fault subsets, respectively. A similar correspondence of the fault data points to the power law regression line is observed in the unrestricted case as is seen in Plot 1. There are relatively more outlying data points in the second plot than in the first, and thus the R^2 value of 0.639 for plot 2 is lower than R^2 for the entire set of faults (Plot 1). The R^2 value of 0.750 and the relatively good correspondence of data points to the power law regression line for Plot 3 are indicative of good

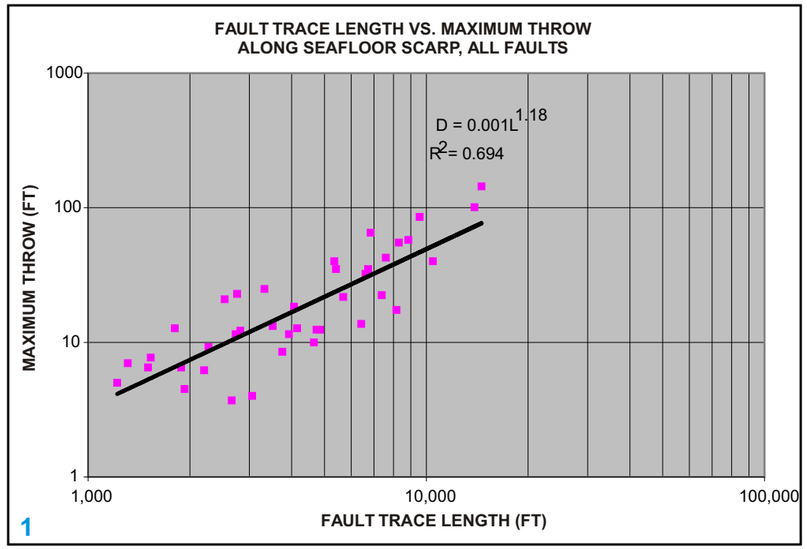

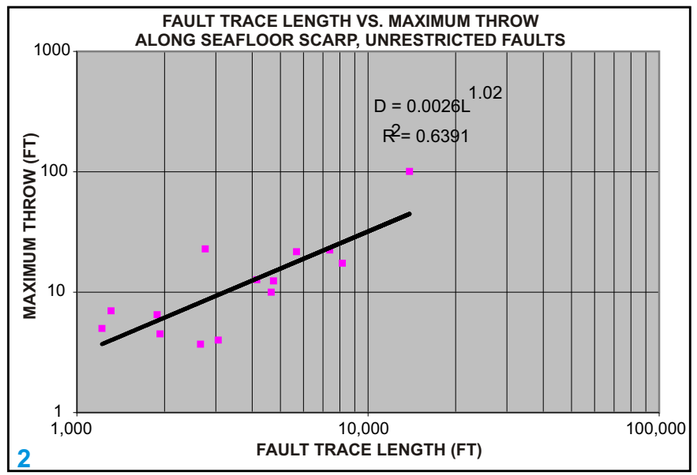

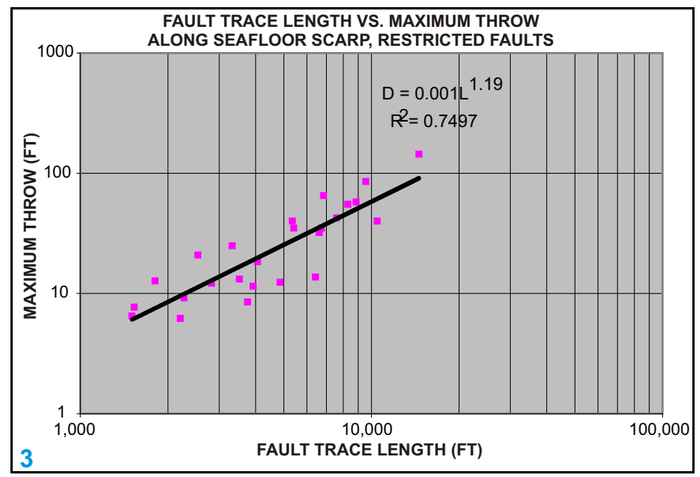

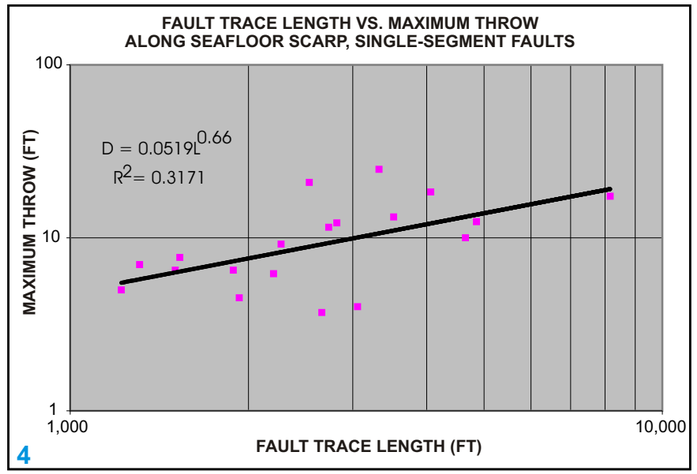

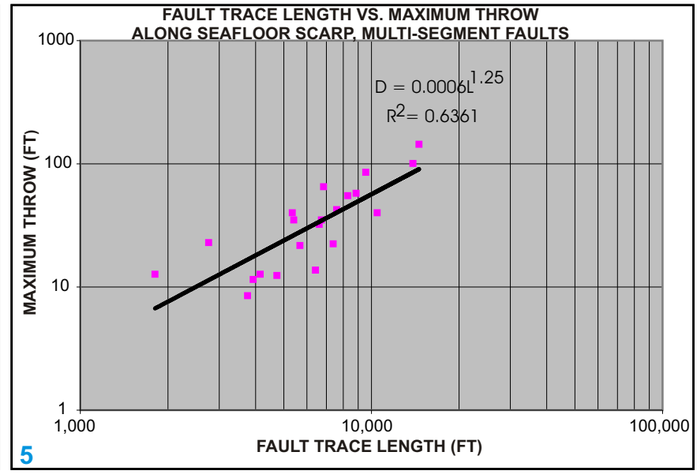

FIGURE 45: Log-log plots of fault seafloor trace length versus maximum fault throw at the seafloor. The five plots represent the whole fault set and four selected subsets, respectively. Each fault in the set or subsets is represented by a magenta square. Black lines are power law regression lines indicating the best-fit compromise function representing the trend of the individual points. The equation of each regression line and the R-square value are shown for each plot. Plot 1 contains all study faults. Plots 2 and 3 are plots of the unrestricted and restricted fault subsets. Plots 4 and 5 are plots of the single-segment and multi-segment subsets.

representation of the individual fault data points by the power law function. Plots 4 and 5 show the single-segment and multi-segment fault subsets, respectively. The fault data points in Plot 4 show a significant degree of scatter not seen in any of the other four plots. This scatter and the corresponding low R^2 value of 0.317 indicate poor representation of the data subset by the displayed regression line. Fault data points in Plot 5 show the same relative degree of correspondence to the displayed regression line as in Plot 2 and a similar value of R^2, here 0.636. With the exception of the single-segment fault subset (Plot 4), the full fault set and the unrestricted, restricted, and multi-segment fault subsets show a general adherence of the fault populations to a power law scaling relationship between the dimensional characteristics of seafloor trace length and maximum throw at the seafloor.

DISCUSSION

This section contains a discussion of the study results in four major areas. First, the characteristics of the whole fault set and the study area faults not included in the study will be examined as they appear on the modern seafloor. Second, the results describing the characteristics of single- and multi-segment faults and unrestricted and restricted faults will be discussed in relation to the expected behavior of faults predicted by the model of fault growth and interaction. Third, the power law scaling relationship between fault seafloor trace length and maximum throw at the seafloor will be examined in light of the power law regression curves computed for the full fault data set and selected fault subsets. Last, a discussion of mapping and measurement resolution and possible sources of error related to the mapping, measurement, and data analysis processes will be made.

Modern Faulted Seafloor Graben

The forty designated study area seafloor faults are shown along with the other seafloor faults not included in the study in Figures 7, 39, 42, and 44. One characteristic of the highly-faulted seafloor structural graben that is immediately noticed is the unusual angle between the axis of the graben and the general strike of the faults. A common characteristic of most structural grabens is a parallel or subparallel strike orientation of the associated internal network of conjugate normal faults with the axis of the graben. Graben-interior faults would be expected to be oriented nearly perpendicular to the axis of extension because the model for formation of most structural grabens assumes that they are predominantly extensional features (strike-slip motion is vastly subordinate or non-existent). This is the expected and intuitive result of extension on dip-slip faults, where the easiest means of accommodating extension is by purely normal offset parallel to the dip direction (Twiss and Moores, 1992). The study area faults strike approximately 35° to the axis of the graben, producing a left-stepping en echelon fault pattern in map view. This fault geometry is possibly the result of a complex combination of local extensional deformation of the shallow strata by an active salt ridge at depth and possible regional basinward translation of the Cenozoic overburden, with the strike-slip deformation

component resulting from differing rates of movement. This is the same end result referred to as wrench faulting by Younes et al. (2005).

The modern study area seafloor shown on Figures 7, 39, 42, and 44 also depicts the present state of growth and interaction of the individual faults and the overall maturity of the graben. Obviously, faulting is either presently active or has recently been active, because the seafloor fault scarps are fresh. Recent, very high depositional rates in the region would have already buried these faults if they were inactive. The faults themselves are characterized by traces with linear or curvilinear segments interrupted occasionally along strike by dog-leg bends. Faults are relatively closely spaced and are often close together in their tip regions. Figures 39 and 42 show that many faults that show an en echelon relationship to each other have a relay ramp connecting the footwall of one fault with the hanging wall of another in the tip areas where the faults are closest.

The northeast boundary of the graben is well defined, consisting of a discontinuous line of fault scarps. It is interesting to note that the portions of faults that make up the graben boundary are the northern extensions of graben-interior faults that are characterized by strikes that are contrary to the common strike direction of the other study area faults but are essentially parallel to the axis of the graben. In other words, the northern extensions of faults that form the northern graben boundary have curved into the boundary. The southwest boundary of the graben is very poorly defined, with no scarp or line of scarps marking the edge. The southernmost extents of faults along the southwestern graben margin do not show the pronounced deviation in strike that their counterpart faults along the northeastern margin do. A hint of this deviation is present on the southern extents of a few faults (Figures 7, 39, 42, and 44). This suggests that the southwestern graben margin is relatively immature with respect to the northeastern margin and may develop a similar discrete boundary in the future, with continued fault growth in this area.

Fault Segments, Restriction, and the Model of Fault Growth and Interaction

The occurrence and distribution of single-segment and multi-segment faults and unrestricted and restricted faults all within the same local area can be explained in terms of the model of fault growth and interaction which is based on work by numerous authors, including Barnett et al. (1987), Chapman and Meneilly (1991), Burgmann and Pollard (1994), Trudgill and Cartwright (1994), Cartwright, et al. (1995), Dawers and Anders (1995), Cartwright et al. (1996), Mansfield and Cartwright (1996), Needham et al. (1996), Nichol et al. (1996b), Contreras et al. (2000), and Willemse and Pollard (2000). This model can also be used to predict how the study area faults will behave in the future under similar conditions to those that produced the modern fault set.

Single- and Multi-Segment Fault Characteristics. All forty faults included in this study show throw characteristics of either single-segment or multi-segment composition. The model of fault growth and interaction states that individual faults composed of single segments or several linked segments represent different steps in the overall process of fault growth. Faults 32 and 35 (Figure 38) have previously been identified as examples of single-segment faults. Fault 24 (Figure 43) was identified as a restricted fault but also shows characteristics of a single-segment fault. These three examples of single-segment faults and the others identified in the fault set may represent the initial stage of the growth model, where small faults grow by tipline propagation at sufficient distance from other faults that they do not interact. Alternatively, these single-segment faults could represent faults composed of multiple segments that have endured sufficient post-linkage displacement that any along-strike local throw minima and maxima indicative of a multi-segment character have been smoothed away. This alternative case is supported by the observation that many of the single-segment faults have seafloor trace geometries containing linear or curvilinear segments connected by dog-legs, which are indicative of multi-segment character. This seafloor trace geometry is interpreted to persist after the displacement distribution returns to that of a single-segment fault. It is likely that both explanations for the single-segment fault character apply to faults within the study area.

Faults 1 and 2 (Figure 40) have previously been identified as examples of multi-segment faults. Fault 3 (Figure 43) and Faults 36 and 45 (Figure 41) have been identified as restricted and unrestricted faults, respectively, but also show characteristics of multi-segment faults. These five examples of multi-segment faults and the others identified in the fault set may represent a stage of fault growth where small faults linked together along strike after interacting, causing restrictions on the tips of the other faults. This linked characteristic follows from the predictions of Cartwright et al. (1995), Nichol et al. (1996b), and Willemse and Pollard (2000), shown in Figures 10, 11, 13, 17, and 18. In each of these real fault examples, local throw minima and maxima are visible to some degree in the along-strike throw profiles. As was observed with the single-segment category of faults, the number of fault segments determined from counting the apparent number of segments on the seafloor fault trace in map view differs from the apparent number of segments derived by counting local throw maxima in along-strike throw profiles. For example, Faults 1, 2, and 45 appear to consist of 8, 6, and 5 fault segments in map view, but the throw profiles for these faults reveal only the apparent presence of 5, 3, and 3 linked segments, respectively (Figures 40 and 41). Again, smoothing of the throw distribution with continued displacement causes eventual assimilation and loss of identity of the individual linked segments, except on the seafloor trace. Trudgill and Cartwright et al. (1994), Cartwright et al. (1995), and Cartwright et al. (1996), explain that the seafloor expressions of these formerly separated fault segments persist because fault movement occurs parallel to the dog-legs connecting the segments. If movement occurred perpendicular to the doglegs, as with a strike-slip fault, the dog-leg would be destroyed with continued fault displacement because it represents a barrier (roughness on the fault surface) to fault movement in that displacement regime. Thus, continued displacement eventually destroys these barriers geometries. The fact that some linked segments still maintain a vestige of their former lateral throw distributions is an artifact of more recent linkage of the segment into the larger multi-segment fault than for segments that were assimilated at an earlier point in the fault's history.

Unrestricted and Restricted Fault Characteristics. All forty faults included in this study show lateral throw characteristics of either laterally unrestricted or restricted fault tips. The model of fault growth and interaction states that unrestricted faults and those that are restricted at one or both lateral tips represent different steps in the overall process of fault growth. Within this study area, both types of faults are observed. This implies that this complexly faulted graben contains faults that are at various stages of the growth and interaction model. Faults 36 and 45 (Figure 41) have previously been identified as examples of unrestricted faults. These examples and the other faults within this category may represent a stage in fault growth where the fault has not grown by tipline propagation enough for its stress field to interact with the stress fields of other faults. The faults within the graben are closely spaced, and as a result, it is presumed that continued displacement on unrestricted faults in this graben would lead to new interactions as the faults grow closer together. In Figure 42 note that the northern and southern tips of Fault 36 are closer to other faults than is the case with Fault 45. With all other conditions and parameters of fault growth being equal, it is logical to conclude that Fault 36 would interact with other local faults sooner than would Fault 45.

Faults 3 and 24 (Figure 43) have previously been identified as examples of restricted faults. Faults 1 and 2 (Figure 40) and Faults 32 and 35 (Figure 38) have previously been identified as multi-segment and single-segment faults, respectively. These four faults also show characteristics of being restricted faults. All six of these examples of restricted faults and the others identified in the fault set are interpreted to represent a stage of fault growth in which faults are interacting at their tips. This interaction causes the observed growth restrictions at the interacting fault tip (or tips, if both limbs of the fault have restricted tips). This also represents the first part of the fault linkage process, in which restriction and local displacement gradients increase with increasing fault displacement as a consequence of locally arrested fault growth. With continued fault displacement the relay zone between the interacting and soft-linked faults accommodates a larger share of the strain in the area of fault overlap, and the linkage process would be expected to move into the terminal phase of hard-linkage by breaching of the relay

zone by a through-going fault. This follows from the predictions of several authors, including Trudgill and Cartwright (1994), Cartwright et al. (1995), Nichol et al. (1996b), and Willemse and Pollard (2000), shown in Figures 11, 13, 17, 18, 21, and 22.

In the previous section it was observed that a correlation exists between the location of a given restricted fault within the graben and the type of tip restriction that the fault displays (restricted northern tip, restricted southern tip, or restricted at both tips), as shown on Figure 44. This correlation is actually not related to position within the graben directly but rather to the local conditions that are associated with position. In the case of faults with northern tip restrictions, the majority of these faults are located in the southwestern portion of the graben because this position places these faults in relation to other faults such that northern tip restriction is more likely than southern tip restriction. For faults with southern tip restrictions, the same case applies to a more limited extent. More faults with which to interact are located near the southern tips of these faults than near the northern tips. About half of these southern-tip-restricted faults are located within the northeastern portion of the graben, with the balance being located in the central area of the graben or in its southwestern side. Two faults were identified that show restrictions at both tips (Faults 12 and 37). The locations of these faults place them in close proximity to other faults' tips or within their stress shadows, thereby causing the observed restrictions.

Power Law Scaling Relationship Between Trace Length and Maximum Seafloor Throw

Numerous authors, including Burgmann and Pollard (1994), Trudgill and Cartwright (1994), Cartwright et al. (1995), Dawers and Anders (1995), Cartwright et al. (1996), and Nichol et al. (1996a and b) have shown through extensive study and compilation of fault data from various settings around the world that a power law scaling relationship exists between trace length and maximum throw at the surface for groups of faults. As stated previously, the power law relationship describes maximum surface displacement, or maximum surface throw in this case, as the product of the displacement axis intercept and the fault trace length raised to the power *n*, which is the slope of the power law regression line in log-log space. This exponent is

reported to range between values of 1 and 2 in the literature (Cartwright et al., 1996). At least one set of authors, Nichol et al. (1996a), state that power law relationships are not applicable for fault sets where the dimensions span several orders of magnitude, because real fault data plotted in log trace length-log displacement space produce slightly non-linear (convex upward) trends. Given that the greatest variance in the same dimension (either throw or trace length) is two orders of magnitude for this set of fault data, the power law relationship is generally applicable to this data set because the span of data points on a log-log plot represents a very small and approximately linear segment of the relationship that Nichol et al. (1996a) have concluded exists. This is analogous to neglecting the curvature of a relatively short straight-line path on the surface a very large sphere.

Figure 45 shows the plots of D vs. L for the whole fault set and for four selected fault subsets. As discussed previously, each of these plots shows the relationships between each of the faults with respect to the rest of the fault population and with respect to the regression line that defines the power law relationship. The reported value of R^2 for each plot describes the relative scatter of the fault data points with the regression line. For a perfect fit between all points and the regression line, R^2 is equal to 1. None of the five plots show a perfect fit. The scatter that exists in the data points should be expected for real measurements, and this scatter can be explained in terms of the model for fault growth and interaction.

According to sources such as Burgmann and Pollard (1994), Dawers and Anders (1995), Cartwright et al. (1996), Mansfield and Cartwright (1996), and Nichol et al. (1996b), the processes of fault growth, interaction, and linkage are related and cyclical process that account for the growth of individual faults and the coalescence of two or more faults into a larger single fault. This process has been discussed previously and is shown in Figures 17 and 18. These processes are manifested in the faults present within the study area. Single-segment faults are interpreted to represent a stage of growth in which the fault has not yet linked with any other faults, or the fault has completed a cycle of linkage and has seen subsequent displacement and growth that have smoothed the displacement distribution along the fault to remove any vestiges

of multi-segment displacement distribution character. Multi-segment faults may represent the post-linkage stage, in which linkage has completed, but insufficient subsequent displacement has occurred to provide a mechanism for smoothing the displacement distribution. Unrestricted faults may be representative of faults that are growing primarily by tipline propagation and are not yet close enough to other faults to initiate interaction. Restricted faults, then, would represent those faults that are interacting and are beginning the linkage process. This is summarized graphically in Figure 46.

The processes of fault growth and linkage help to account for the scatter of data points observed in displacement vs. length plots for the entire fault set and for the four fault subsets (Cartwright et al., 1995, Dawers and Anders, 1995, Cartwright et al., 1996, and Nichol et al., 1996b). Data point scatter is symptomatic of the failure of individual faults to obey the power law described by the regression line shown on each plot in Figure 45 and on a single plot combining all five of the regression lines in Figure 47. This scatter is defined in terms of maximum displacement and trace length, therefore it is variations in the ratio of these dimensions that produce the observed distribution of data points. The lowest scatter (highest R^2 value) is associated with restricted faults, with unrestricted faults showing somewhat greater scatter. Scatter comparable to the unrestricted case is observed for the multi-segment fault case, whereas the greatest scatter (lowest R^2 value) by far is displayed by the single-segment group of faults. Lateral tip restriction and the early stages of linkage confine a fault to a certain length along strike (trace length in this case), with the displacement being the parameter that is free to increase. This results in the growth of the magnitude of displacement on a fault relative to trace length. When enough displacement accrues that the relay zone is accommodating a very large lateral displacement gradient (high strain), that relay zone ruptures and hard linkage occurs. It appears from the fault data presented here that this amount of displacement required for forcing linkage varies from one fault to another, but shows a good correlation to fault trace length. This is manifested in relatively low scatter in the restricted fault case. Conversely, single-segment faults in this study area appear to show much less adherence to a scaling

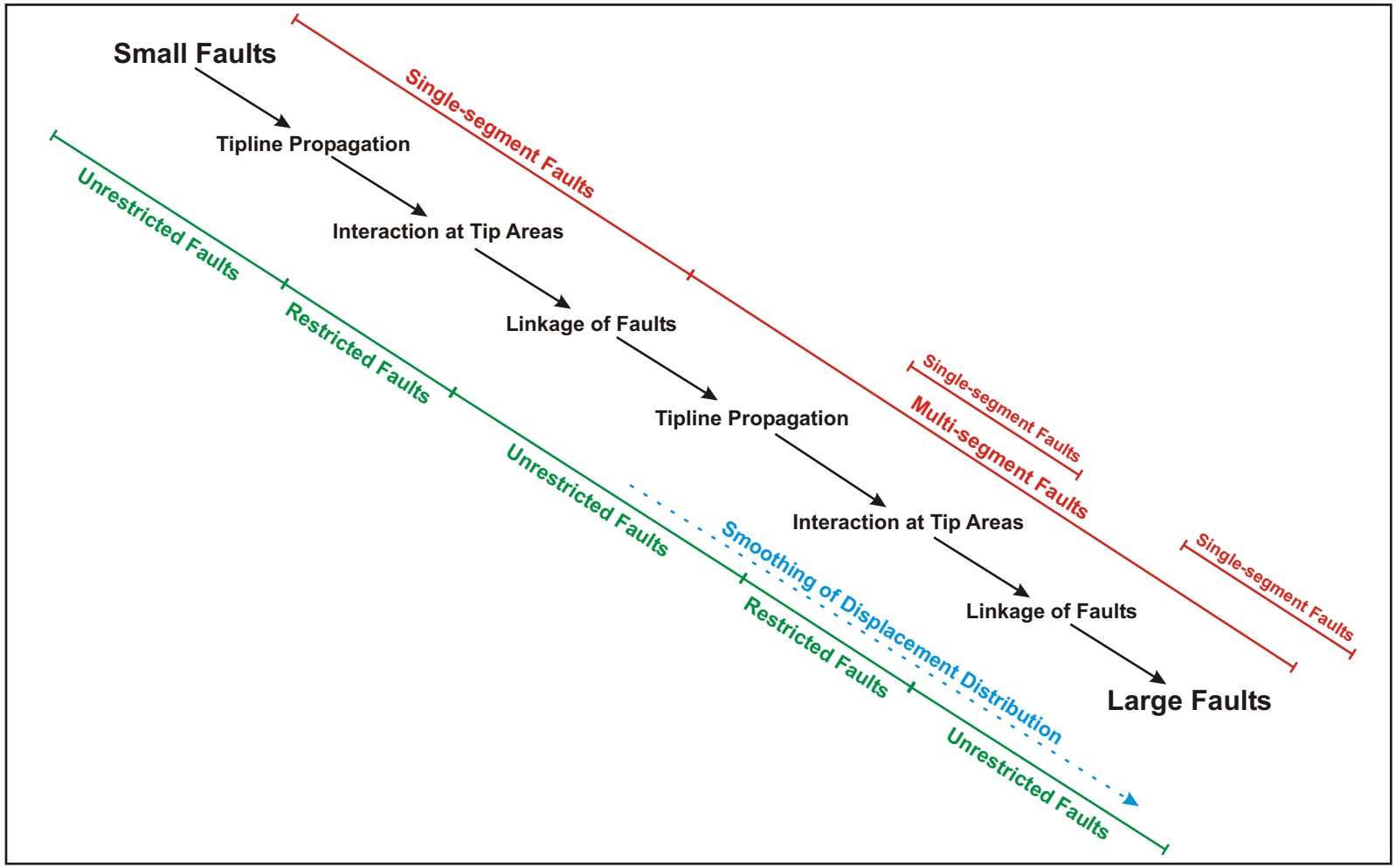

FIGURE 46: Generalized model of fault growth and interaction. Model shows the relationship between the stages and processes of fault growth and interaction and the categories of faults identified in this study. After faults link, the displacement distribution of the new single fault gradually smoothes from the distribution of linked faults to that of a single segment. This process can be disturbed before completion by the assimilation of other faults by linkage. This is shown as overlapping zones of single-segment and multi-segment fault character above.

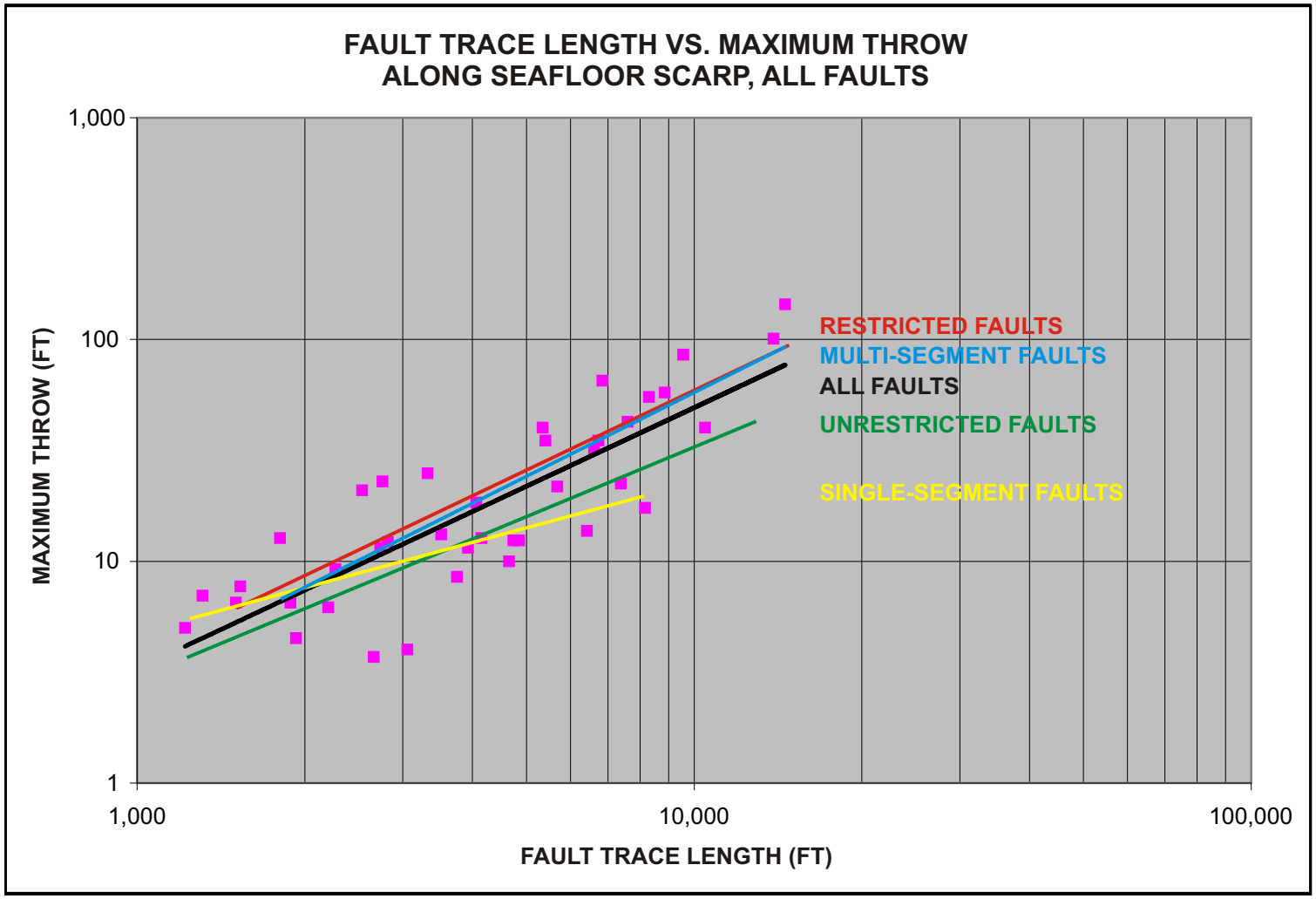

FIGURE 47: Plot 1 reproduced from Figure 45. The power law regression line for all faults is shown in black. Power law regression lines for the other four plots corresponding to the four categories of faults are shown for comparison. Note that unrestricted faults and single-segment faults trend toward lower values of throw for corresponding trace lengths. Magenta squares are individual fault data points.

relationship between displacement and trace length. Single-segment faults include both restricted and unrestricted faults. The difference between unrestricted and restricted lateral fault growth appears to account for most of the observed scatter in this subset.

Returning to Figure 47, the reasons for differences in the five displayed regression lines are evident in light of the connections to the fault growth and interaction model just discussed. The regression lines for restricted faults and multi-segment faults (red and blue lines, respectively) are very close to each other and overlap to some extent. These regression lines also display the highest displacement to trace length ratio (highest slope; *n* equal to 1.25 and 1.19, respectively, for the multi-segment and restricted faults subsets). This reflects the effect of restriction of trace length (by tip restriction) for both subsets of faults. In the case of multi-segment faults, tip restrictions may or may not be present. However, the restrictions that did exist before linkage may not yet be compensated-for by enhanced lateral tipline propagation. The unrestricted fault regression line (green line, *n* equal to 1.02) shows slightly shallower slope than the multi-segment and restricted cases. This is the result of a lack of relative shortening of the trace length that would have been caused by tip restriction. The single-segment fault regression line displays the lowest slope (*n* equal to 0.66), indicating the lowest scaled ratio of displacement to length. This subset is further characterized by nearly equal numbers of restricted and unrestricted faults, and many of these unrestricted faults are relatively small faults that may have no history of previous tip restriction. The result is that this fault subset is inferred to contain several faults that have very low individual ratios of displacement to trace length, skewing the subset toward a lower power law slope. The regression line for the entire fault set has a slope of n equal to 1.18, which shows the greatest agreement with the multi-segment, unrestricted, and restricted fault subsets.

Seismic Data Resolution and Procedural Error

The resolution of the HR 3-D seismic data set and procedural errors are the possible identified sources of error and uncertainty that could have affected the results of this investigation. The use of a HR 3-D seismic data set and procedures designed to limit or exclude

procedural errors are judged to have prevented the negative effects of these two factors on this study. The vertical resolution limits of the seismic data set were shown to be much smaller in magnitude than those of a conventional 3-D seismic data set. The excellent vertical resolution of this data set has allowed for not only the determination of very small quantities of throw, but also greater reliability of these determinations. The most probable sources of procedural error were identified and planned-for based on the experiences of previous authors doing similar work (Chapman and Meneilly, 1991, and Mansfield and Cartwright, 1996). As a result of this forethought, potential pitfalls associated with these issues were avoided. The primary potential errors identified were the failure to identify and account for fault deformation accommodated by folding (Chapman and Meneilly, 1991), inaccurate mapping of the horizons that were used to make throw measurements, and inaccurate mapping of the faults used in this study (Needham et al., 1996). Each of these potential sources of error was identified before work began and steps were taken to identify them when they occurred and to correct for them.

Other Related Questions

This research has answered several important questions regarding the use of HR 3-D seismic data in the investigation of active, shallow faults in the marine environment, their geometric characteristics, and the identification of fault growth and interaction. This research has also posed many other important questions that fall outside the scope of this work. Two important possible avenues for future work follow naturally from the work done thus far.

First, the relationships between individual faults are unclear. This investigation has dealt only with the characteristics of the individual faults and has made only a mention of the interactions between the study area faults. Developing an understanding of these relationships will add to the understanding of this faulted graben. The existing data set of measurement station locations and horizon offset throw measurements could be used, in part, to examine these relationships. Some key questions involve the distribution of throw in the zones of overlap between closely spaced, but unlinked faults, and the relationships between the faults at varying stratigraphic levels in the subsurface. In other words, how do the faults appear to be interacting

at one stratigraphic level as opposed to another? Many fault models envision that fault planes would appear to be shaped like ellipses or ovals (Figure 13). An assumption might be that two interacting faults would show restrictions first along the horizons that are nearest the down-dip middles of the faults, where the elliptical fault shape places these horizons within each others' stress fields before any of the other shallower or deeper horizons. Another key question is the distribution of throw in overlap areas (relay zones) for this fault set. Several workers have shown that this distribution can either be smooth, in that the aggregated throws in the relay zones represent just another smooth portion of the throw distribution along the faults. Other work has shown that the distribution indicates some type of aberration in the throw profile at the relay zone, having either greater combined throw or less combined throw (Contreras et al., 2000).

Second, can the point of origin of the faults within the subsurface be determined? Is the point of origin for the majority of faults located closer to the seafloor or closer to the shallow salt body that underlies the graben? To answer this question, some assumptions about the growth of the faults will need to be made, and some additional work will need to be done. The assumptions are: that the faults are the effect of shallow salt activity, and that the modern fault centers roughly represent the locations of the original nucleation points for the faults. Additional work will need to be done to map the entire fault surfaces, and not just the upper portions of most of the faults as was done in this investigation. By mapping the entire fault, the approximate location of the fault centers can be determined. This was not possible with the 3-D HR data because the deeper subsurface geology prevented accurate mapping of the faults and deep horizons offset by the faults. It is possible that the conventional 3-D seismic data set may be helpful in accomplishing this goal. It would also be interesting to examine the vertical displacement distribution along the faults for evidence of fault linkage down dip. Dip linkage produces patterns of localized displacement maxima and minima in the dip direction that are analogous to localized maxima and minima observed in along-strike throw profiles (Mansfield and Cartwright, 1996). Differentiating between single-segment faults and faults that are linked down dip is another necessary step in determining the original fault centers.

One final important point for further consideration is the idea that small values of throw especially at the tip areas of faults may not be quantifiable using the research procedures of this investigation. However, this work does suggest a means of estimating these small throws. Figures 38, 40, 41, and 43 show that no measurements of throw were made at the lateral tips of the investigated faults, because no zero values of throw are shown. Obviously, throws below the vertical resolution of the data cannot be detected. This means that the fault tips, which lay beyond the first and last measurement stations are not included in the along-strike plot of throw. By linearly extrapolating the tip area throw gradient toward the true tip area to zero throw, the lateral position of the tip can be estimated beyond the first and last measurement stations.

CONCLUSIONS

The following conclusions are warranted, based on the results and observations made during this investigation:

1. Faults within the study area that produce offsets at the seafloor are judged to be active faults over short geological periods of time: about the last 10,000 years in this case. Inactive faults would be blanketed by undisturbed marine clays. Such an undisturbed blanket is interpreted to not be present.
2. The use of a HR 3-D seismic data set in the analysis of shallow faulting by mapping throw at horizon offsets makes this approach possible for faults with relatively restricted trace lengths and small maximum throws because of the high vertical and lateral resolution of this data. Conversely, this analysis would either not be possible or would be subject to considerable error and uncertainty if 3-D conventional seismic data were used because of the low vertical and lateral resolution of that type of data.
3. By measuring throw at horizon offsets at measurement stations along a fault trace, it is possible to develop an understanding of the distribution of throw along strike of the fault.
4. Analysis of the resulting lateral throw distributions allows for the recognition of linked fault segments and restricted fault tips.
5. Correlations between fault throw characteristics and the map view characteristics of the faults are evident. Restricted fault tips are observed to be in proximity to other fault tips in map view, and the multi-segment characteristic of some faults is evident in the seafloor fault traces in map view.
6. The presence of and distributions of single- and multi-segment faults and unrestricted and restricted faults within the seafloor graben is explained by the model for fault growth and interaction proposed by several authors. Each type of fault (and their combinations) is characteristic of one or more of the steps in the cyclic processes of fault growth and interaction.

7. The whole fault set and selected subsets appear to roughly obey a power-law scaling relationship between maximum seafloor displacement and seafloor trace length. The power law exponent ranges between 0.66 and 1.25 for the four selected fault subsets, and averages 1.18 for the whole fault population. The whole-set power law exponent value agrees well with published values of 1 to 2.
8. The processes of fault growth and interaction described here comprise a good model for explaining how faults grow within a population of similar faults, such as the one in this investigation.
9. Several possible sources of error and uncertainty were identified in the methods used in this investigation. The use of HR 3-D seismic data instead of conventional 3-D seismic data and pre-investigation planning for the likely sources of error and uncertainty are judged to have significantly reduced their potential effects on the results of this investigation.
10. Fault analysis by mapping faults and offset horizons and subsequent measurement of throw at the horizon offsets is a useful tool in understanding how individual faults and populations of faults behave.

REFERENCES CITED

Advocate, D. M. and K. C. Hood, 1993, An empirical time-depth model for calculating water depth, Northwest Gulf of Mexico: Geo-Marine Letters, v. 13, p. 207-211.

Amery, G. B., 1978, Structure of continental slope, Northern Gulf of Mexico: The American Association of Petroleum Geologists Bulletin, v. 62, no. 2, p. 141-153.

Barnett, J. A. M., J. Mortimer, J. H. Rippon, J. L. Walsh, and J. Watterson, 1987, Displacement geometry in the volume containing a single normal fault: The American Association of Petroleum Geologists Bulletin, v. 71, no. 8, p. 925-937.

Bouma, A. H., C. E. Stelting, and J. M. Coleman, 1984, Mississippi Fan: internal structure and depositional processes: Geo-Marine Letters, v. 3, p. 147-153.

Brown, A. R., 1999, Interpretation of three-dimensional seismic data, fifth edition: American Association of Petroleum Geologists Memoir 42: Tulsa, American Association of Petroleum Geologists, 514 p.

Bryant, W. R., J. Lugo, C. Cordova, and A. Salvador, 1991, Chapter 2: physiography and bathymetry, *in* A. Salvador, ed., The Gulf of Mexico basin: The geology of North America, v. J: Boulder, Geological Society of America, p. 13-30.

Bryant, W. R. and L. B. Roemer, 1983, Structure of the continental shelf and slope of the Northern Gulf of Mexico and its geohazards and engineering constraints, *in* R. A. Geyer, ed., CRC handbook of geophysical exploration at sea: Boca Raton, CRC Press, p. 123-185.

Burgmann, R., and D. D. Pollard, 1994, Slip distribution on faults: effects of stress gradients, inelastic deformation, heterogeneous host-rock stiffness, and fault interaction: Journal of Structural Geology, v. 16, no. 12, p. 1675-1690.

Campbell, K. J., 1999, Deepwater geohazards: how significant are they?: The Leading Edge, v. 18, no. 4, p. 514-519.

Campbell, K. J., 1997a, Deepwater geohazards and engineering geology: meeting tough challenges: Houston Geological Society Bulletin, v. 40, no. 1, p. 9.

Campbell, K. J., 1997b, Fast-track development: the evolving role of 3-D seismic data in deepwater geohazards assessment and site investigation: Offshore Technology Conference, May 7-10, 1997, Houston, Texas.

Cartwright, J., R. Bouroullec, D. James, and H. Johnson, 1998, Polycyclic motion history of some Gulf Coast growth faults from high-resolution displacement analysis: Geology, v. 26, no. 9, p. 819-822.

Cartwright, J., C. Mansfield, and B. Trudgill, 1995, Fault growth by segment linkage: an explanation for scatter in maximum displacement and trace length data from the Canyonlands Grabens of SE Utah: Journal of Structural Geology, v. 17, no. 9, p. 1319-1326.

Cartwright, J., B. Trudgill, and C. Mansfield, 1996, The growth of normal faults by segment linkage, *in* P. G. Buchanan, ed., Modern developments in structural interpretation, validation, and modeling: Geological Society Special Publication No. 99: London, Geological Society, p. 163-177.

Chapman, T. J., and A. W. Meneilly, 1990, Fault displacement analysis in seismic exploration: First Break, v. 8, no. 1, p. 11-22.

Chapman, T. J., and A. W. Meneilly, 1991, The displacement patterns associated with a reverse-activated, normal growth fault, *in* A. M. Roberts, G. Yielding, and B. Freeman, eds., The geometry of normal faults: Geological Society Special Publication no. 56: London, Geological Society, p. 183-191.

Contreras, J., M. H. Anders, and C. H. Scholz, 2000, Growth of a normal fault system: observations from the Lake Malawi basin of the East African Rift: Journal of Structural Geology, v. 22, p. 159-168.

Davis, O. K., 2004, The astronomical theory of climate change: introduction to Quaternary ecology, <http:\\www.geo.arizona.edu/palynology/ geos462/21climastro.html>, accessed December 2005.

Dawers, N. H., and M. H. Anders, 1995, Displacement-length scaling and fault linkage: Journal of Structural Geology, v. 17, no. 5, p. 607 to 614.

Diegel, F. A., D. C. Schuster, J. F. Karlo, R. C. Shoup, and P. R. Tauvers, 1995, Cenozoic structural evolution and tectono-stratigraphic framework of the northern Gulf Coast continental margin, *in* M. P. A. Jackson, D. G. Roberts, and S. Snelson, eds., Salt tectonics: a global perspective: American Association of Petroleum Geologists Memoir 65: Tulsa, American Association of Petroleum Geologists, p. 109-151.

Fenton, C., D. Jayson, M. Gillies, and A. Parkin, 2002, Integrated geohazards evaluation and risk assessment for subsea facilities: Proceedings, 34th Annual Offshore Technology Conference, May 4-7, 2002, Houston, Texas, OTC Paper 14271, p. 1-7.

Galloway, W. E., P. E. Ganey-Curry, X. Li, and R. T. Buffler, 2000, Cenozoic depositional history of the Gulf of Mexico Basin: The American Association of Petroleum Geologists Bulletin, v. 84, no. 11, p. 1743-1774.

Griggs, J., 2001, Daisyworld and glaciation, Milankovitch cycles and climate change: Earth climate systems, <http:\\http://geosciences.ou.edu/~jgriggs/intro2.htm>, accessed December 2005.

Imbrie, J., J. D. Hays, D. G. Martinson, A. McIntyre, A. C. Mix, J. J. Morley, N. G. Pisias, W. L. Prell, and N. J. Shackleton, 1984, The orbital theory of Pleistocene climate: support from a revised chronology of the marine $\delta\,^{18}O$ record: *in* A. Berger, J. Imbrie, J. Hays, G. Kukla, and B. Saltzman, eds., Milankovitch and climate, part I, series C: mathematical and physical sciences volume 126: Dordrecht, Holland, D. Reidel Publishing Company.

Mansfield, C. S. and J. S. Cartwright, 1996, High resolution fault displacement mapping from three-dimensional seismic data: evidence for dip linkage during fault growth: Journal of Structural Geology, v. 18, no. 2-3, p. 249-263.

Martin, R. G., 1977, Northern and Eastern Gulf of Mexico continental margin; stratigraphic and structural framework, *in* A. H. Bouma, G. T. Moore, and J. M. Coleman, eds., Framework, facies, and oil-trapping characteristics of the upper continental margin: American Association of Petroleum Geologists Studies in Geology 7: Tulsa, American Association of Petroleum Geologists, p. 21-42.

Nave, C. R., 2000, Inverse square law, light: hyperphysics, <http://hyperphysics.phy-astr.gsu.edu/hbase/vision/isql.html#c1>, accessed November 2005.

Needham, D. T., Y. Yielding, and B. Freeman, 1996, Analysis of fault geometry and displacement patterns, *in* P. G. Buchanan, ed., Modern developments in structural interpretation, validation and modeling, Geological Society Special Publication no. 99: London, Geological Society, p. 189-199.

Nichol, A., J. J. Walsh, J. Watterson, and P. A. Gillespie, 1996a, Fault size distributions—are they really power law?: Journal of Structural Geology, v. 18, no. 2-3, p. 191-197.

Nichol, A., J. Watterson, J. J. Walsh, and C. Childs, 1996b, The shapes, major axis orientations and displacement patterns of fault surfaces: Journal of Structural Geology, v. 18, no. 2-3, p. 235-248.

Peacock, D. C. P., R. J., Knipe, and D. J. Sanderson, 2000, Glossary of normal faults: Journal of Structural Geology, v. 22, p. 291-305.

Peel, F. J., C. J. Travis, and J. R. Hossack, 1995, Genetic structural provinces and salt tectonics of the Cenozoic offshore U.S. Gulf of Mexico: a preliminary analysis, *in* M. P. A. Jackson, D. G. Roberts, and S. Snelson, eds., Salt tectonics: a global perspective: American Association of Petroleum Geologists Memoir 65: Tulsa, American Association of Petroleum Geologists, p. 153-175.

Pratt, T. L., J. F. Dolan, J. K. Odum, W. J. Stephenson, R. A. Williams, and M. E. Templeton, 1998, Multiscale seismic imaging of active fault zones for hazard assessment: a case study of the Santa Monica fault zone, Los Angeles, California: Geophysics, v. 63, no. 2, p. 479-489.

Pratt, T. L., J. H. Shaw, J. F. Dolan, S. A. Christofferson, and A. Plesch, 2002, Shallow seismic imaging of folds above the Puente Hills blind-thrust fault, Los Angeles, California: Geophysical Research Letters, v. 29, no. 9, p. 18-1 to 18-4.

Reading, H. G., and B. K. Levell, 1996, Controls on the sedimentary rock record, *in* H. G. Reading, ed., Sedimentary environments: processes, facies, and stratigraphy, third edition: Oxford, Blackwell Publishing Limited, p. 5-36.

Rowan, M. G., M. P. A. Jackson, and B. D. Trudgill, 1999, Salt-related fault families and fault welds in the Northern Gulf of Mexico: The American Association of Petroleum Geologists Bulletin, v. 83, p. 1454-1484.

Shackleton, N. J., and N. D. Opdyke, 1973, Oxygen isotope and paleomagnetic stratigraphy of an equatorial Pacific core V28-238: oxygen isotope temperatures and ice volumes on a 10^5 and 10^6 year time scale: Quaternary Research, v. 3, p. 39-55.

Stow, D. A. V., H. G. Reading, and J. D. Collinson, 1996, Deep seas, *in* H.G. Reading, ed., Sedimentary environments: processes, facies, and stratigraphy, third edition: Oxford, Blackwell Publishing Limited, p. 395-453.

Trabant, P. K., 1996, Use of 3-D exploration seismic data for geohazards analysis: Proceedings, 28th Annual Offshore Technology Conference, May 6-9, 1996, Houston, Texas, OTC Paper 386, p. 1-8.

Trudgill, B., and J. Cartwright, 1994, Relay-ramp forms and normal-fault linkages, Canyonlands National Park, Utah: Geological Society of America Bulletin, v. 106, p. 1143-1157.

Twiss, R. J., and E. M. Moores, 1992, Structural geology: New York, W. H. Freeman and Company, 532 p.

Uchupi, E., 1975, Physiography of the Gulf of Mexico and Caribbean Sea, *in* A. E. M. Nairn and F. G. Stehli, eds., The ocean basins and margins: volume 3, the Gulf of Mexico and the Caribbean: Woods Hole, Woods Hole Oceanographic Institution, p. 1-64.

Walsh, J. J., J. Watterson, W. R. Bailey, and C. Childs, 1999, Fault relays, bends and branch-lines: Journal of Structural Geology, v. 21, p. 1019-1026.

Willemse, E. J. M. and D. D. Pollard, 2000, Normal fault growth: evolution of tipline shapes and slip distribution, *in* F. K. Lehner, ed., Aspects of tectonic faulting: New York, Springer Publishing Company, p. 193-226.

Woodbury, H. O., I. B. Murray, Jr., P. J. Pickford, and W. H. Akers, 1973, Pliocene and Pleistocene depocenters, outer continental shelf, Louisiana and Texas: The American Association of Petroleum Geologists Bulletin, v. 57, p. 2428-2439.

Worrall, D. M., and S. Snelson, 1989, Evolution of the northern Gulf of Mexico, with emphasis on Cenozoic growth faulting and the role of salt, *in* A.W. Bally and A.R. Palmer, eds., The geology of North America, an overview: The geology of North America, v. A: Boulder, Geological Society of America, v. A, p. 97-138.

Younes, A. I., J. L. Gibson, and R. C. Shipp, 2005, Geohazard assessment of the deepwater Princess Field in the Northeastern Gulf of Mexico: example of evaluating complex faulting in a subsea development: Proceedings, 37th Annual Offshore Technology Conference, May 2-5, 2005, Houston, Texas, OTC Paper 17577, p. 1-11.

APPENDIX 1: ADDITIONAL FAULT THROW PROFILES

This appendix contains along-strike throw profiles for the 32 faults that are not shown as data examples in the main body of this work. These throw profiles are designated as Figure 48, and follow this page. The same convention for displaying throw across the fault at the horizons offset by the fault at each measurement station is used in Figure 48 as was used in Figures 38, 40, 41, and 43 presented in the main body of this text.

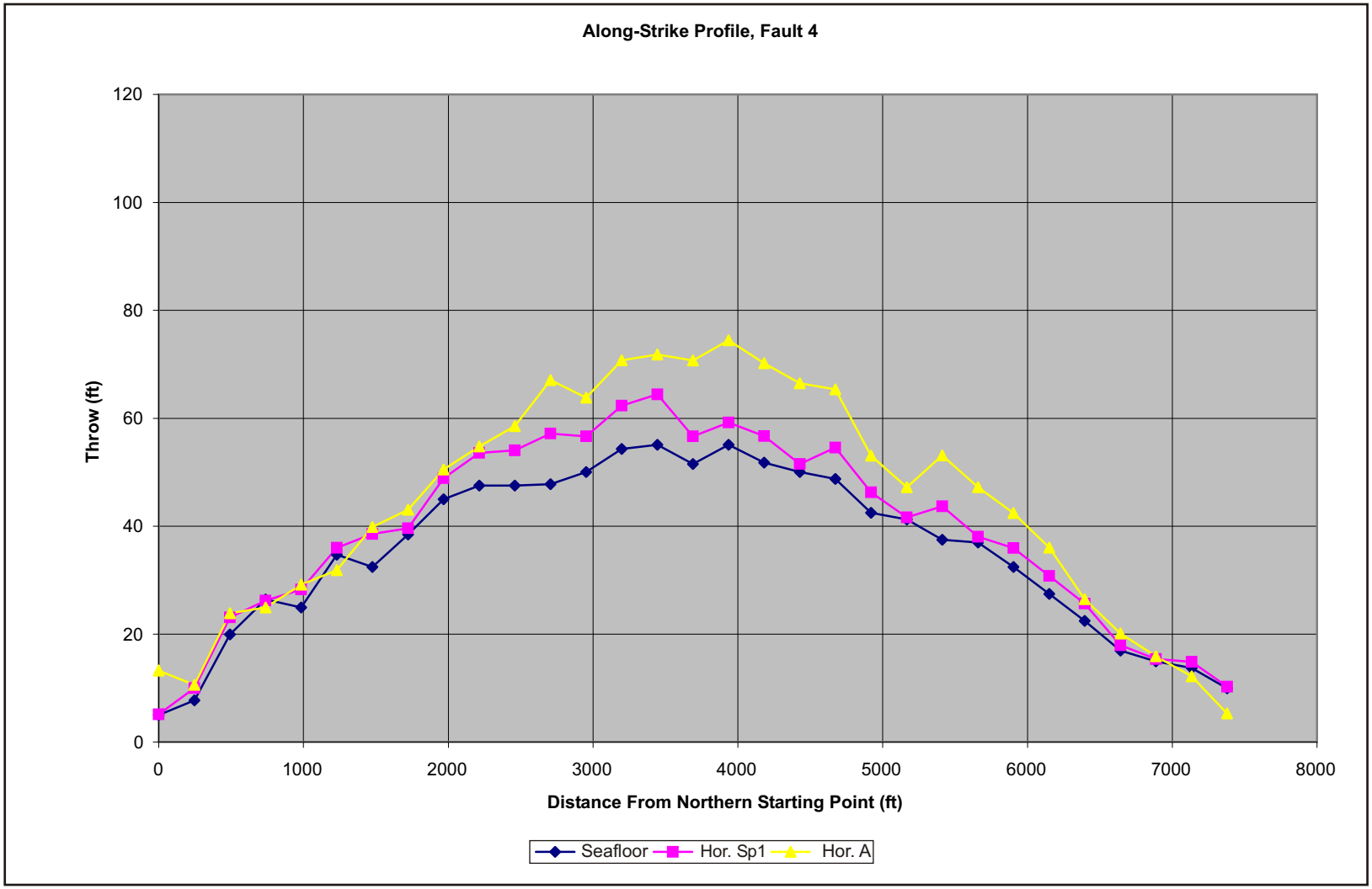

FIGURE 48: Along strike throw profiles for Faults 4-16, 25-31, 33, 37-44, and 46-48. These are along strike throw profiles for the balance of the 40 faults that were not discussed and shown in data examples in the Results section of this work.

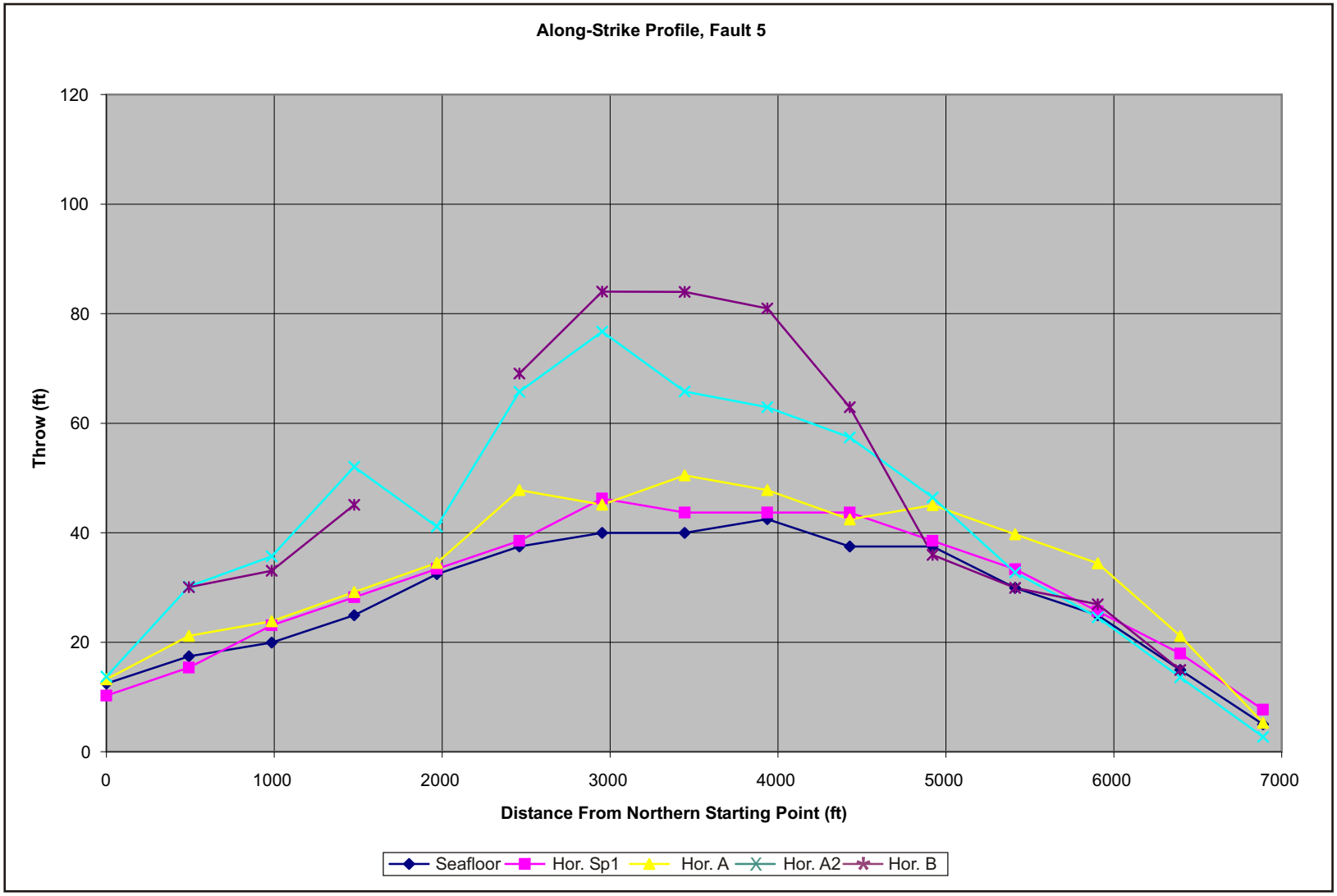

FIGURE 48 Continued.

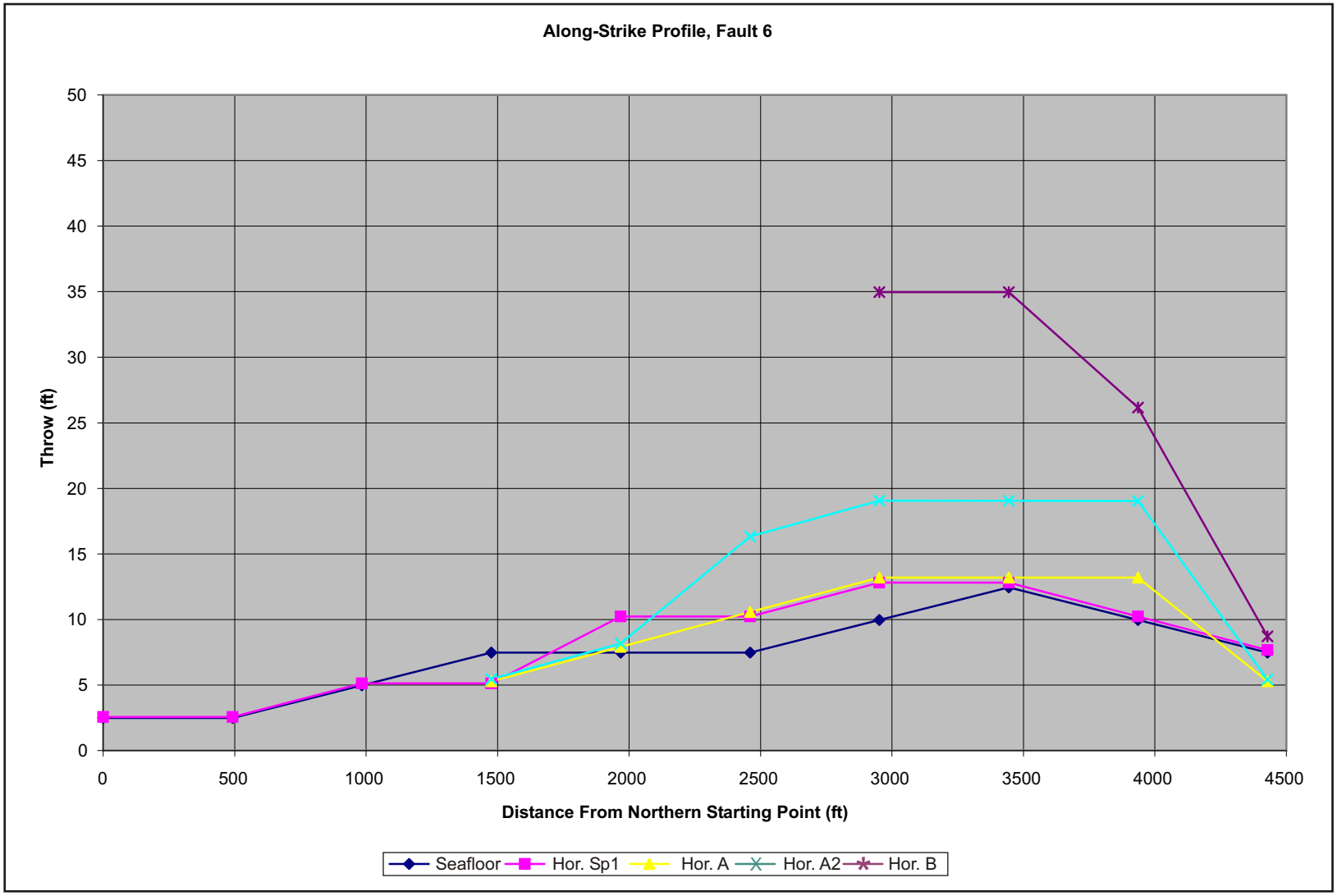

FIGURE 48 Continued.

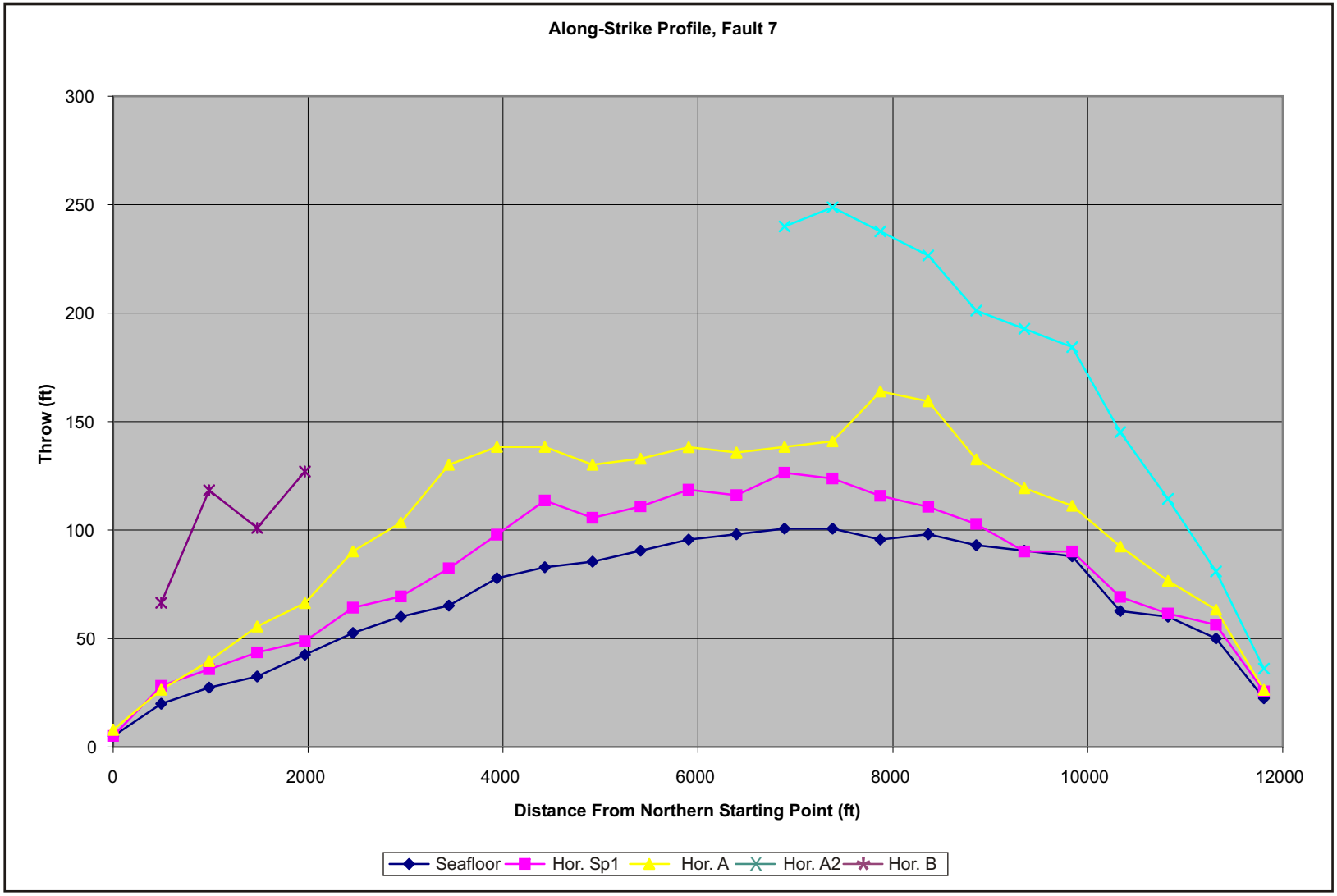

FIGURE 48 Continued.

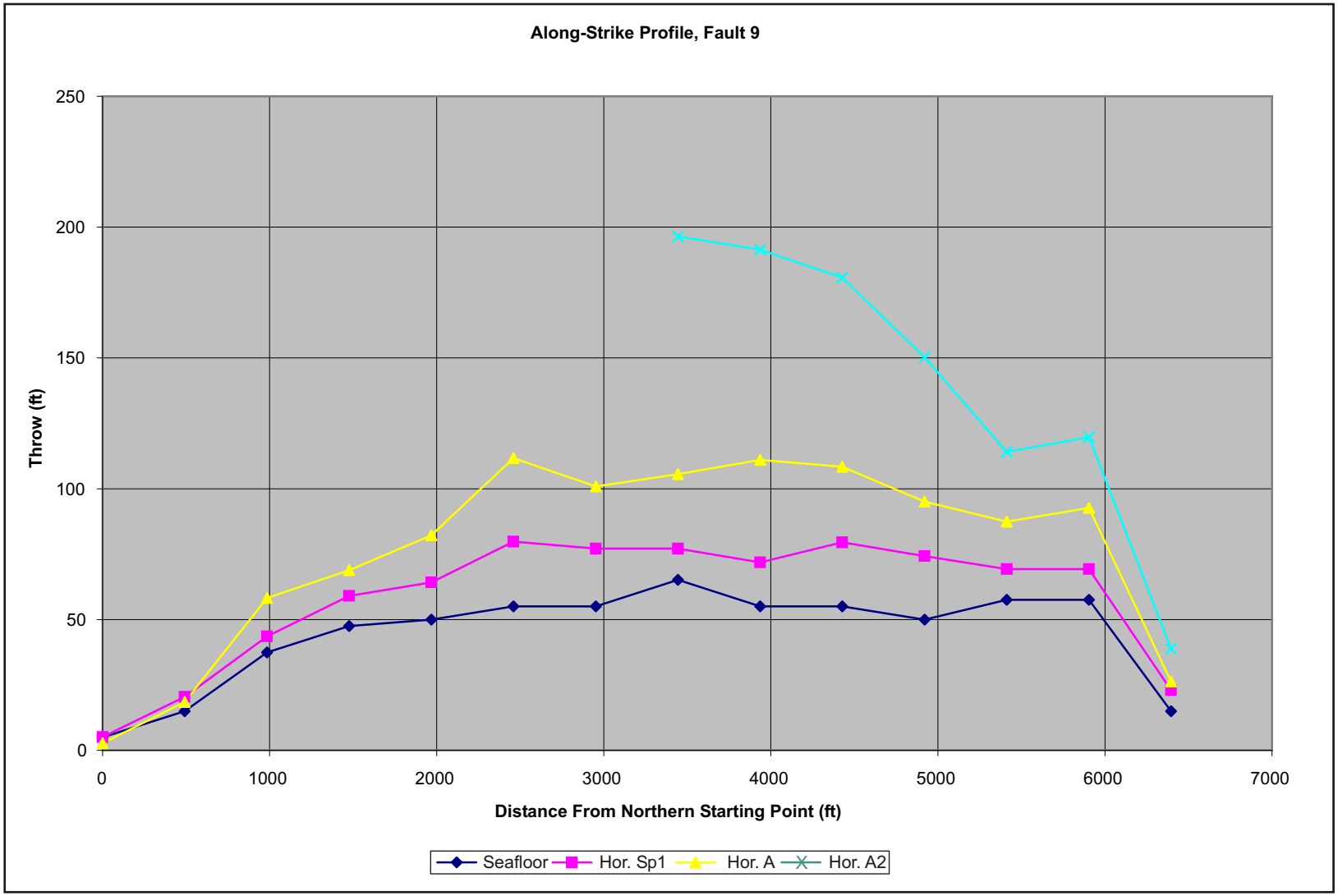

FIGURE 48 Continued.

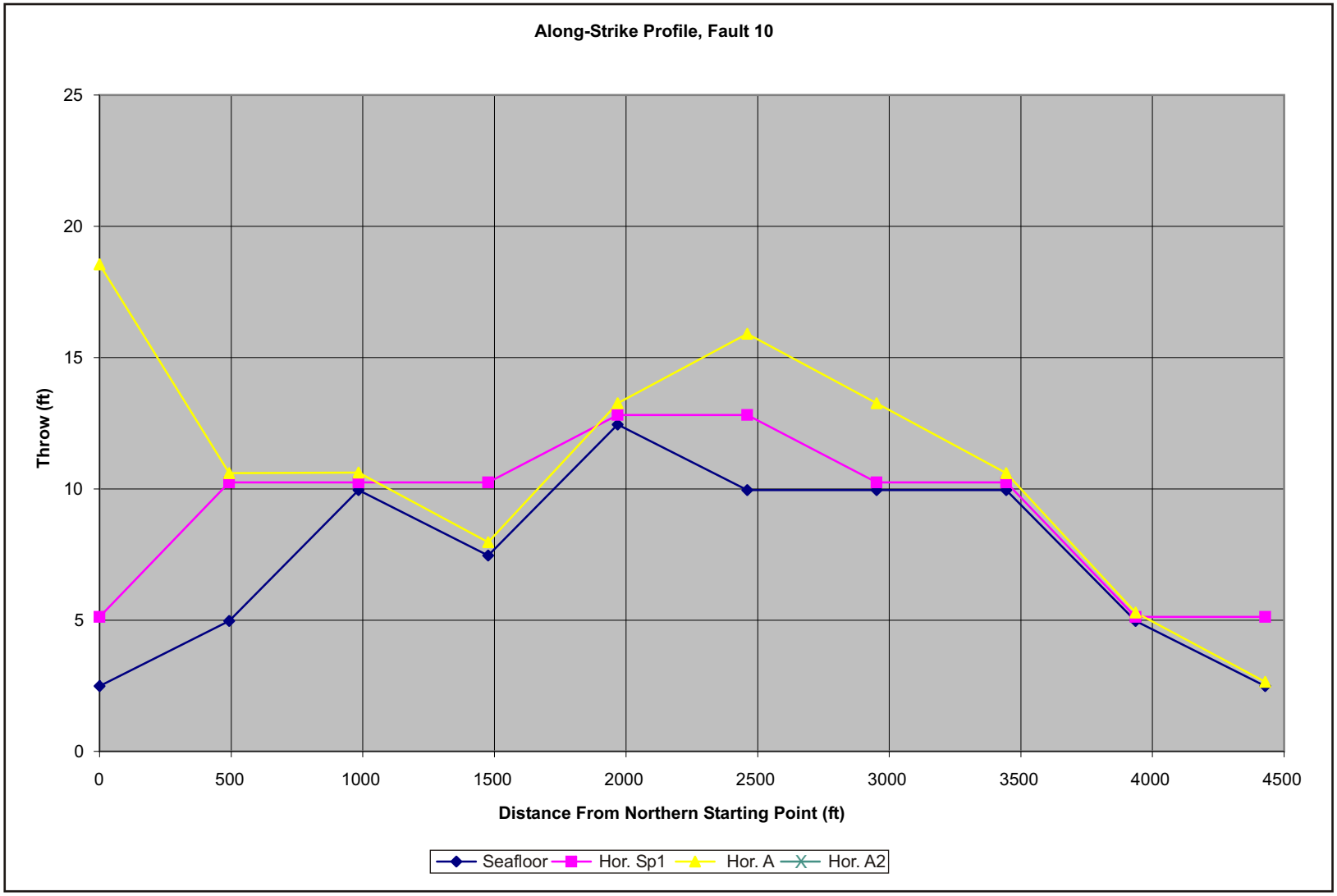

FIGURE 48 Continued.

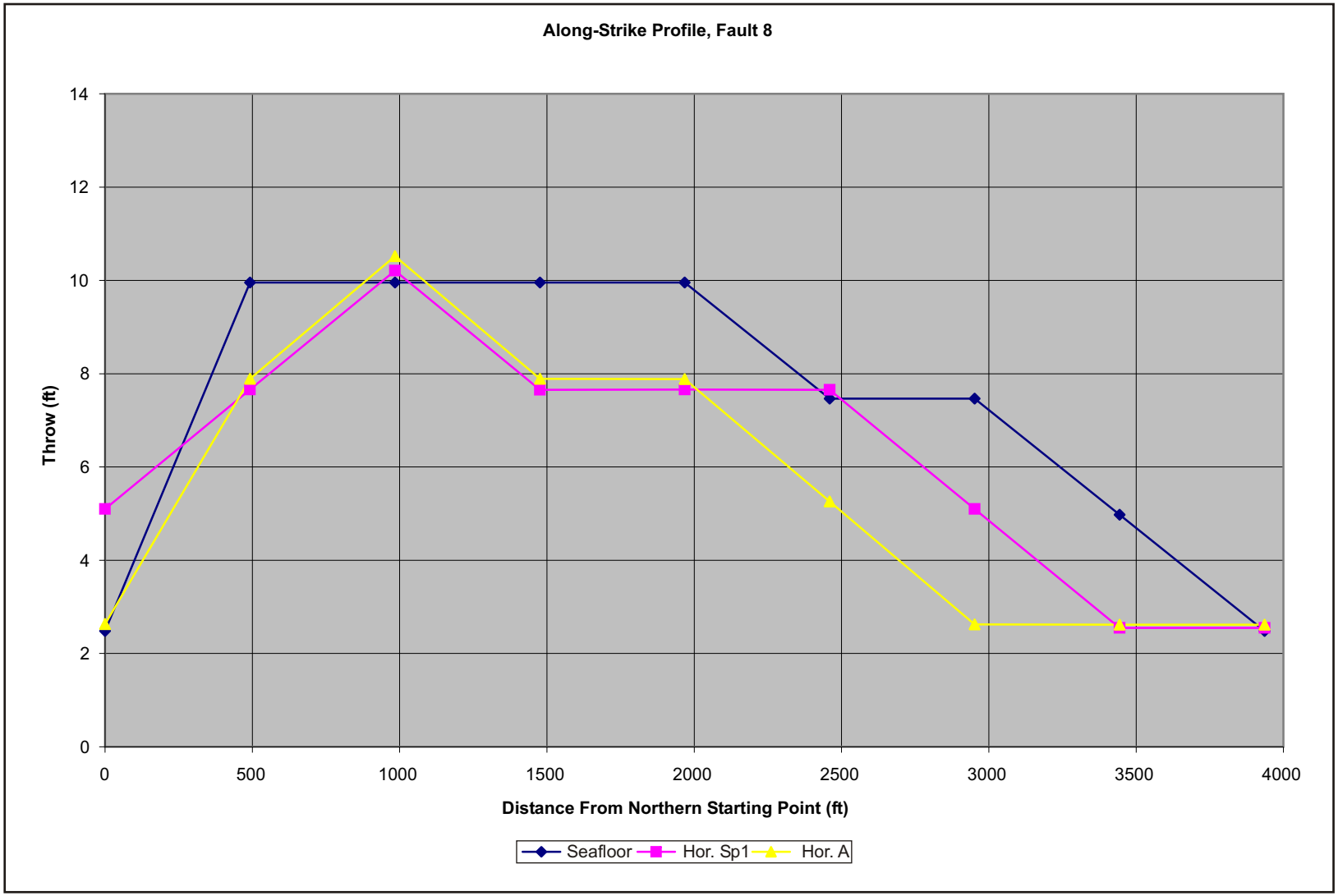

FIGURE 48 Continued.

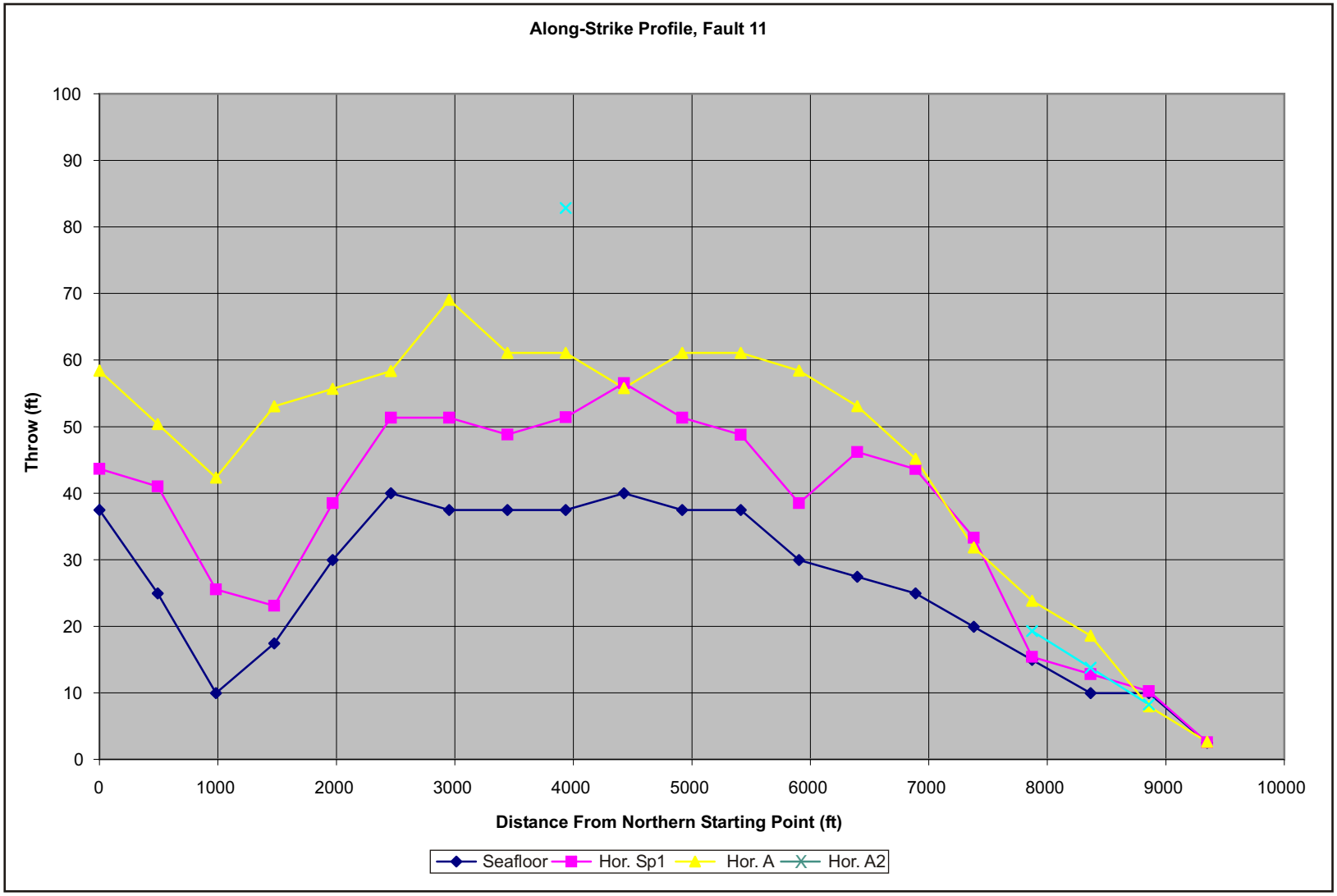

FIGURE 48 Continued.

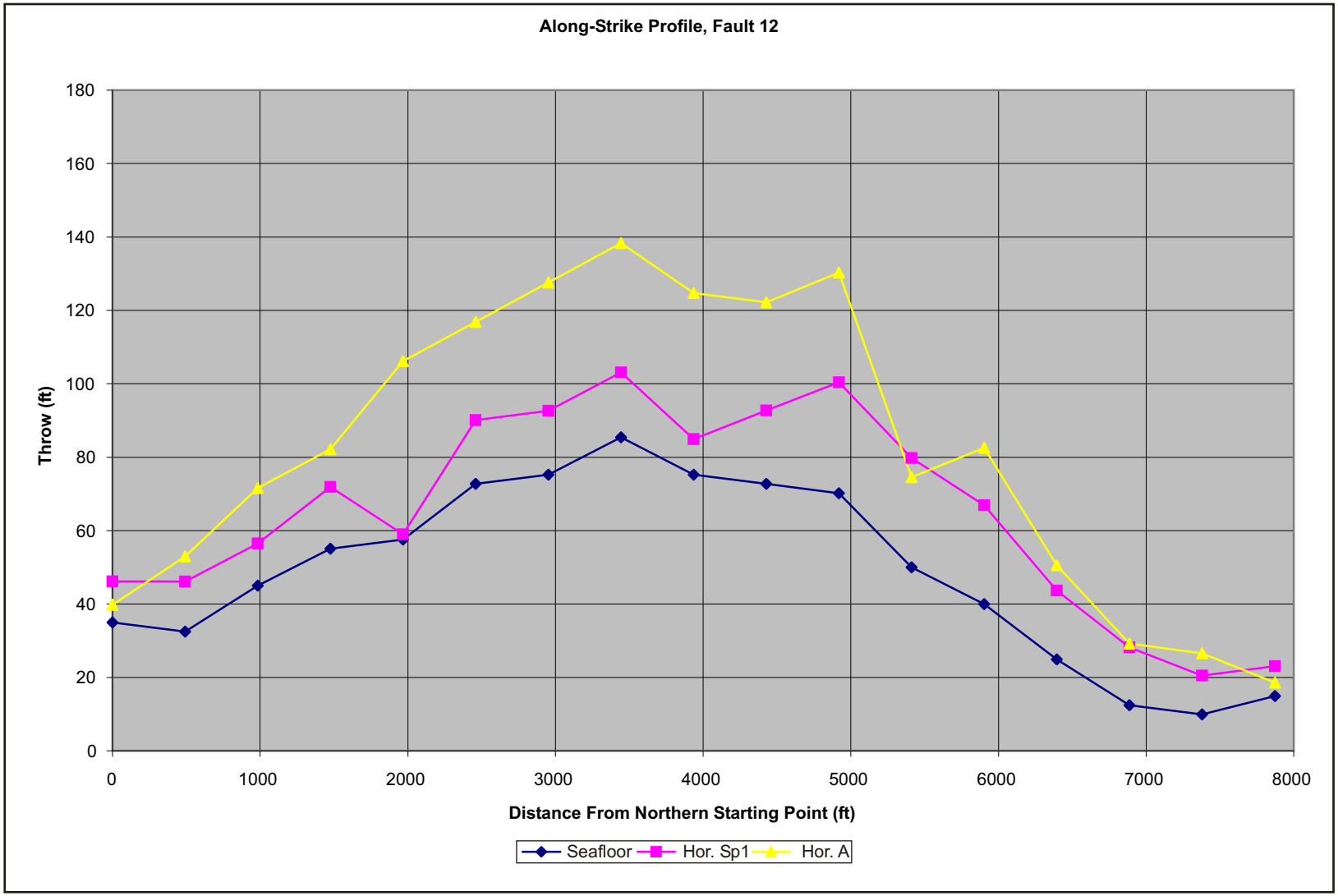

FIGURE 48 Continued.

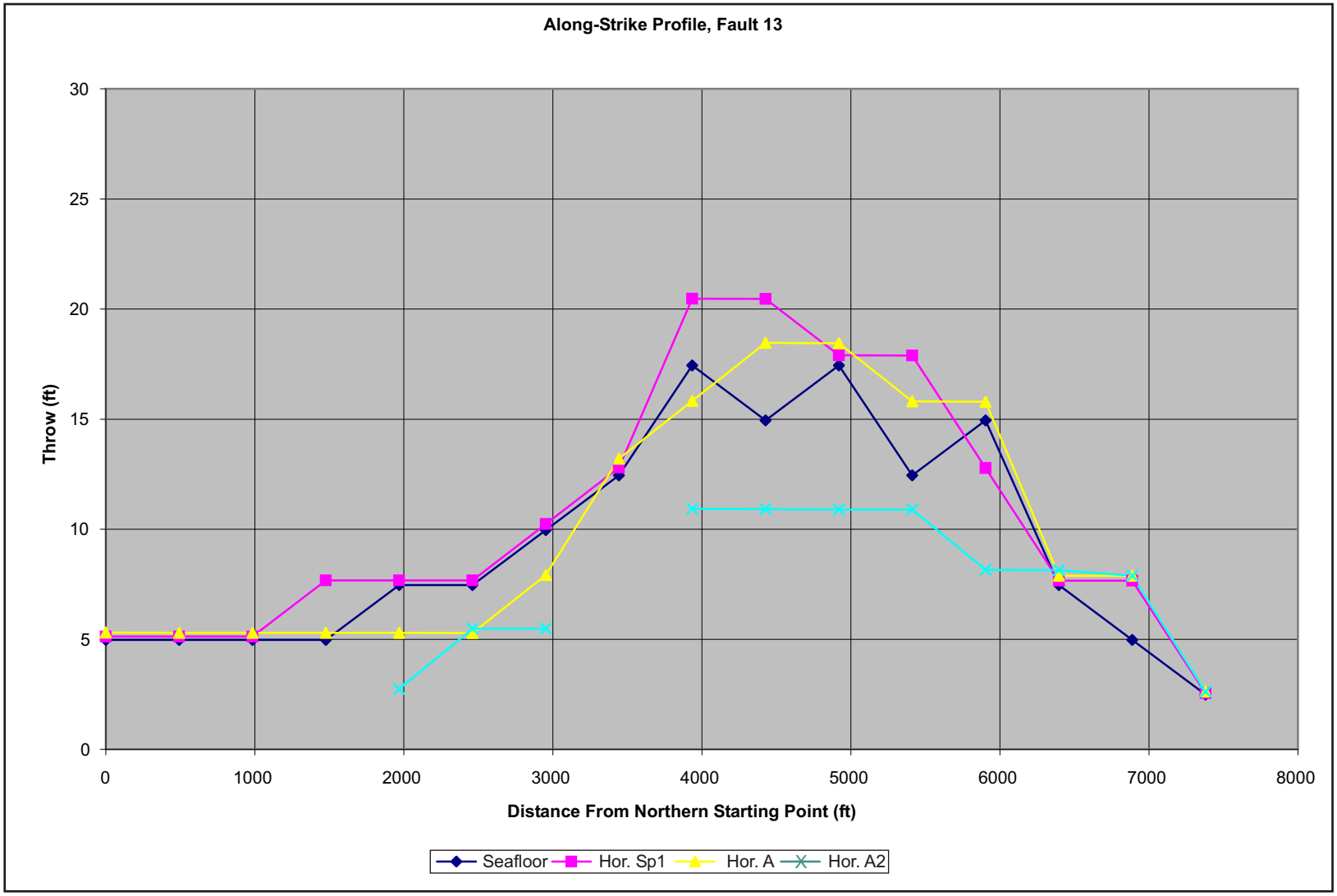

FIGURE 48 Continued.

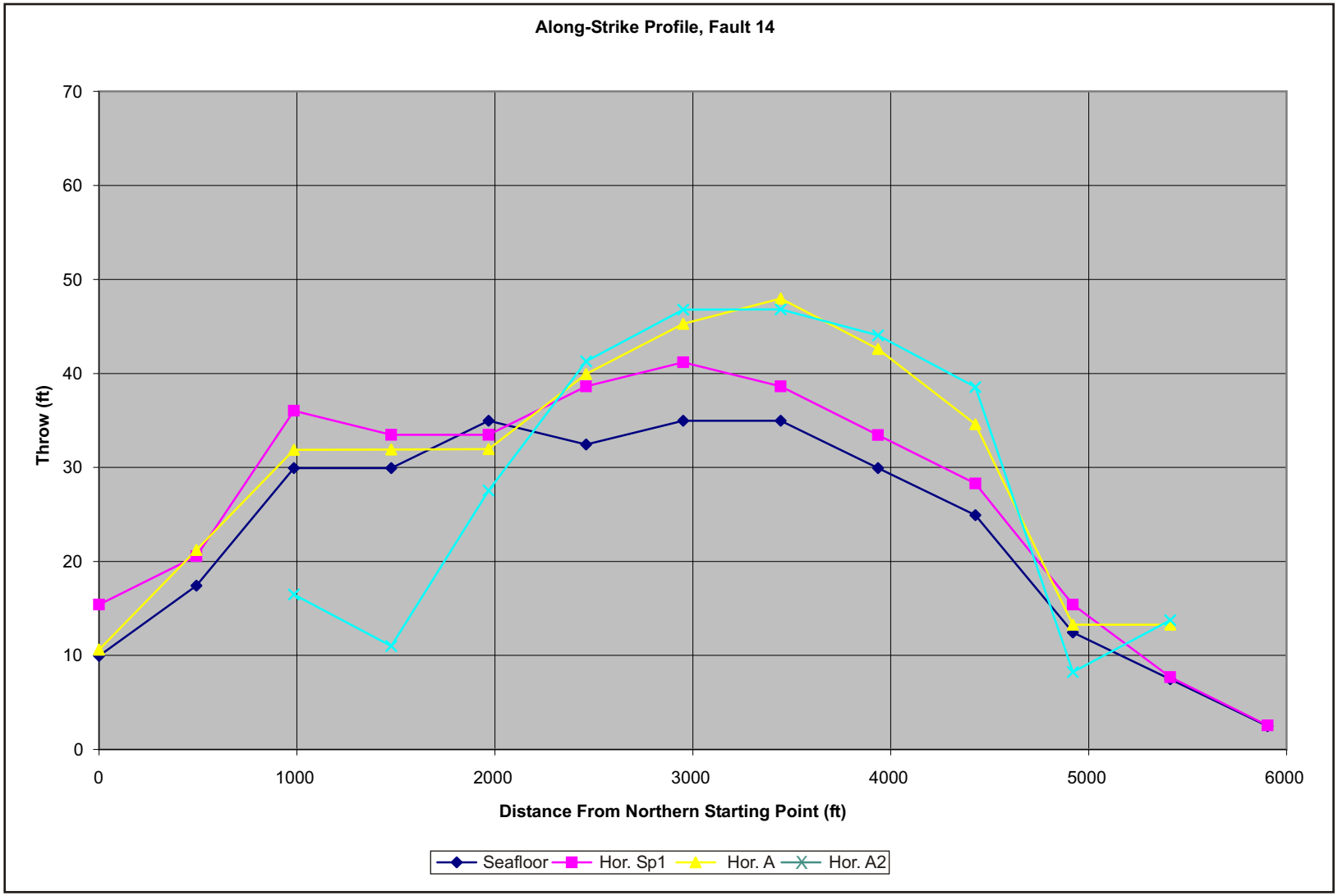

FIGURE 48 Continued.

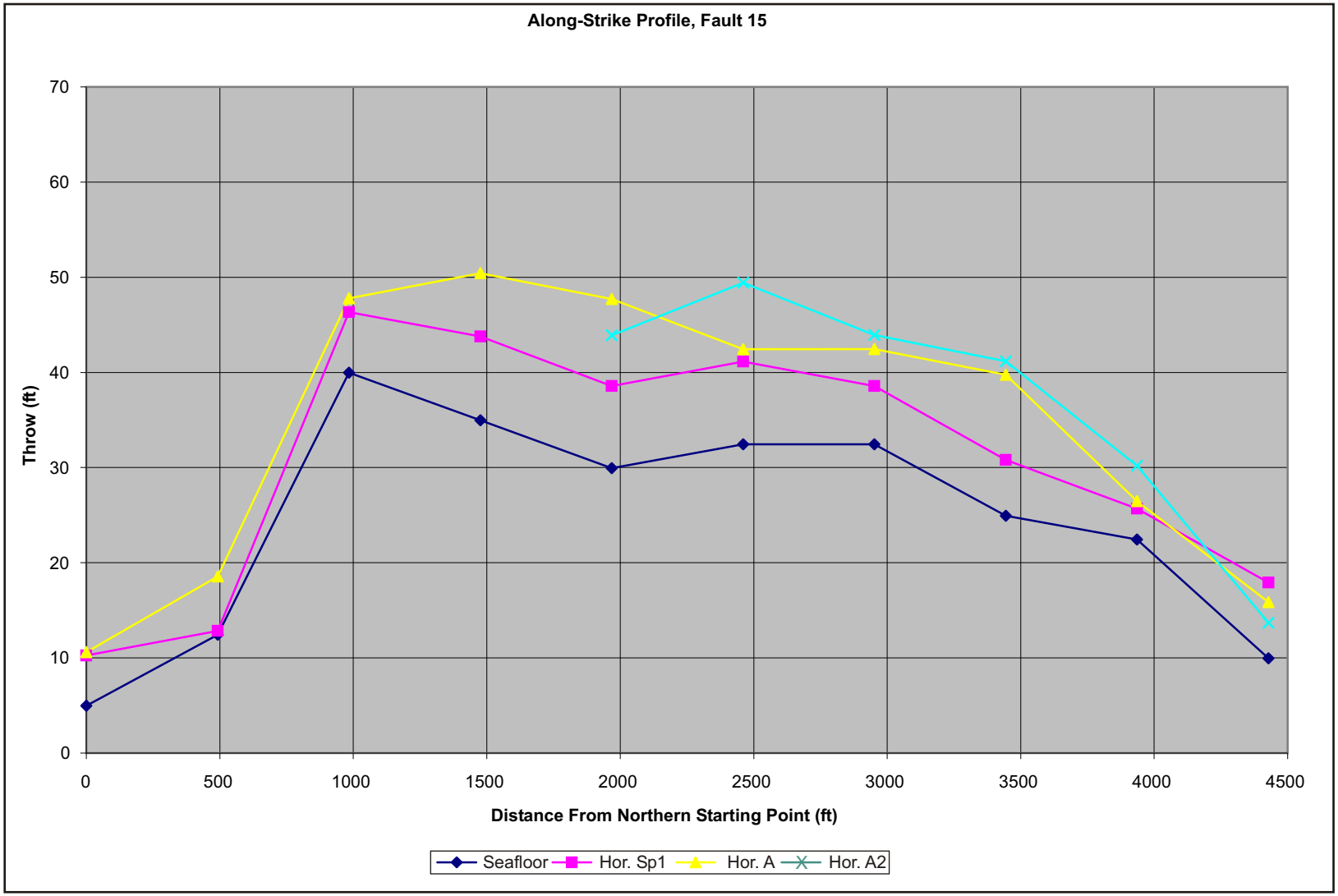

FIGURE 48 Continued.

FIGURE 48 Continued.

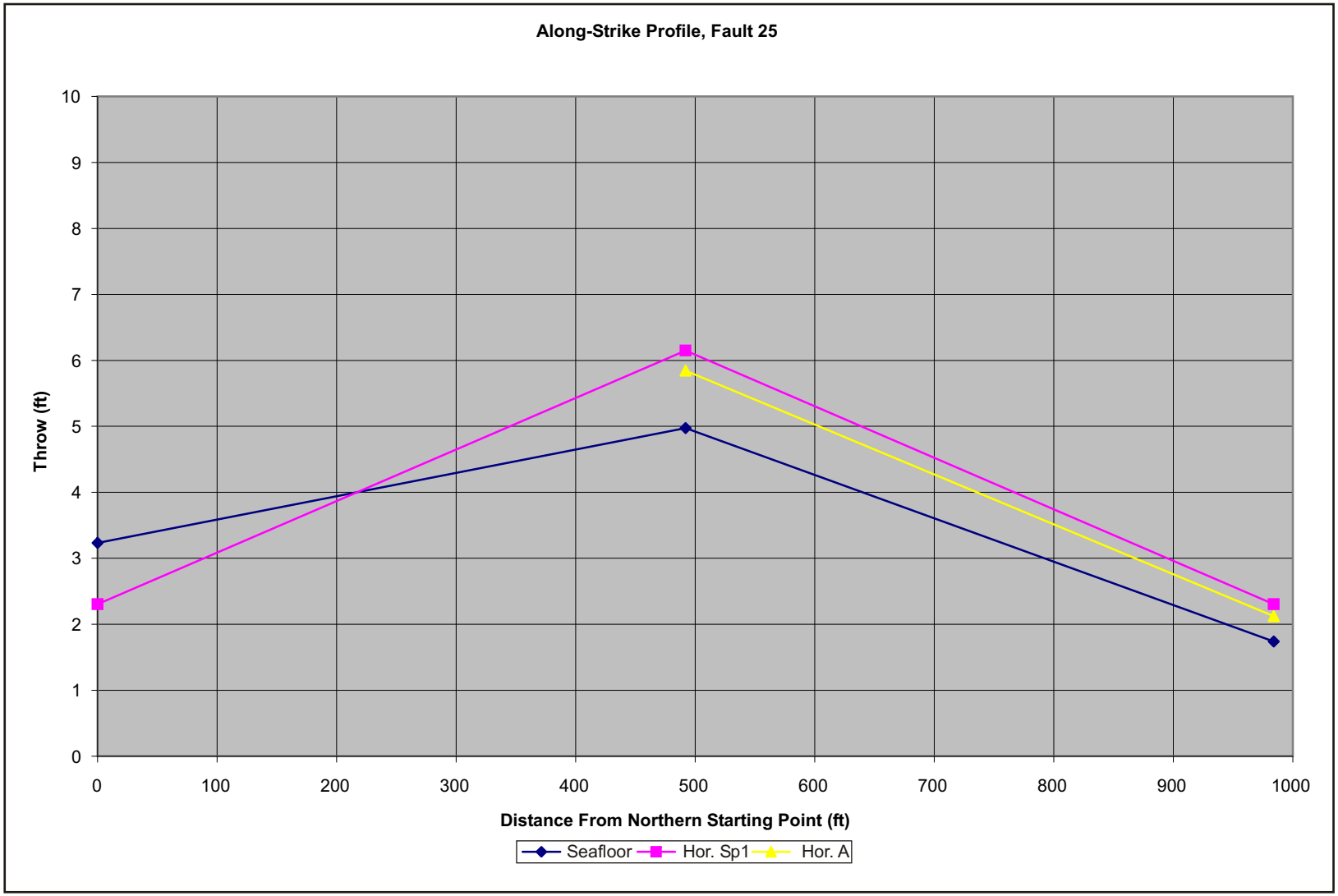

FIGURE 48 Continued.

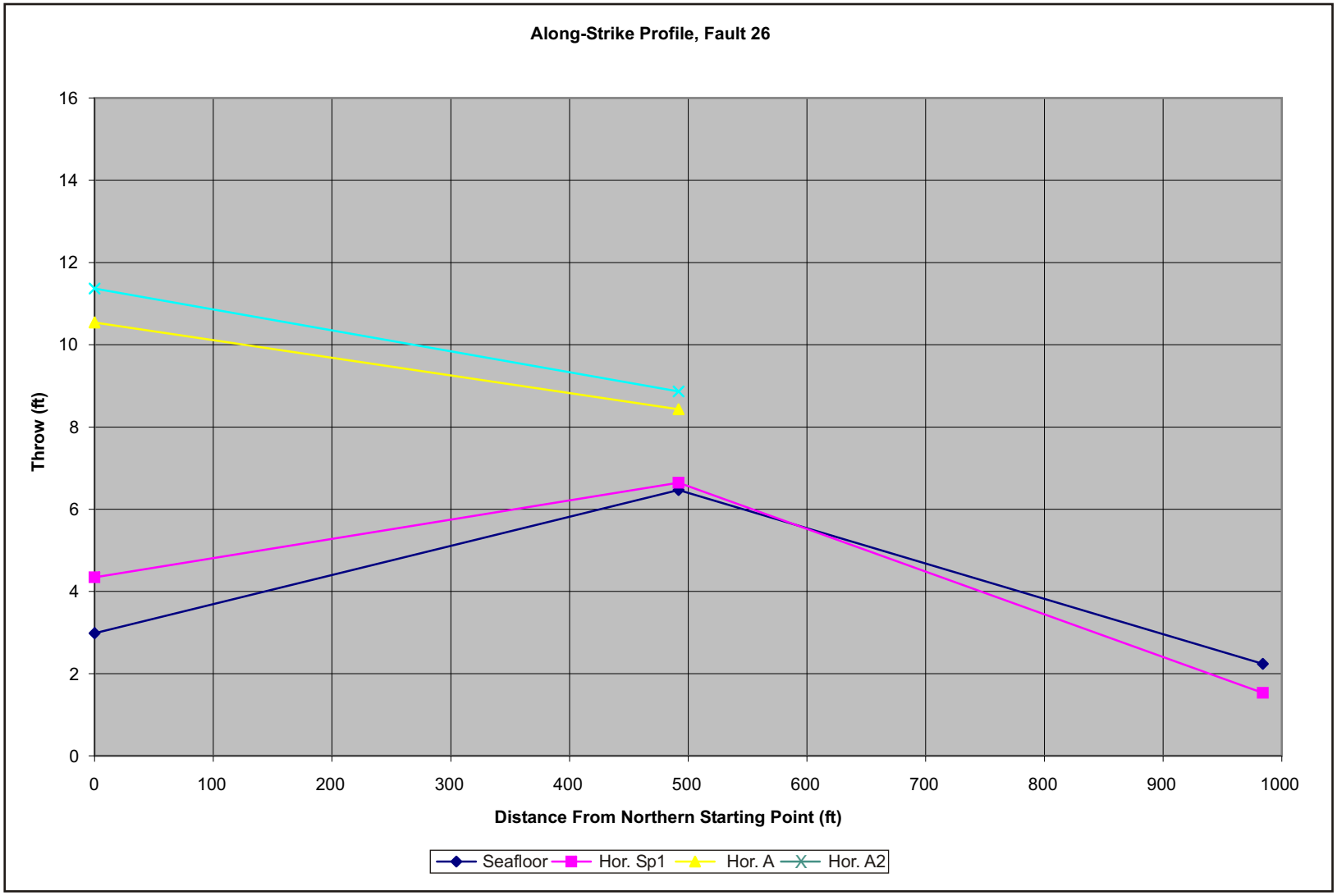

FIGURE 48 Continued.

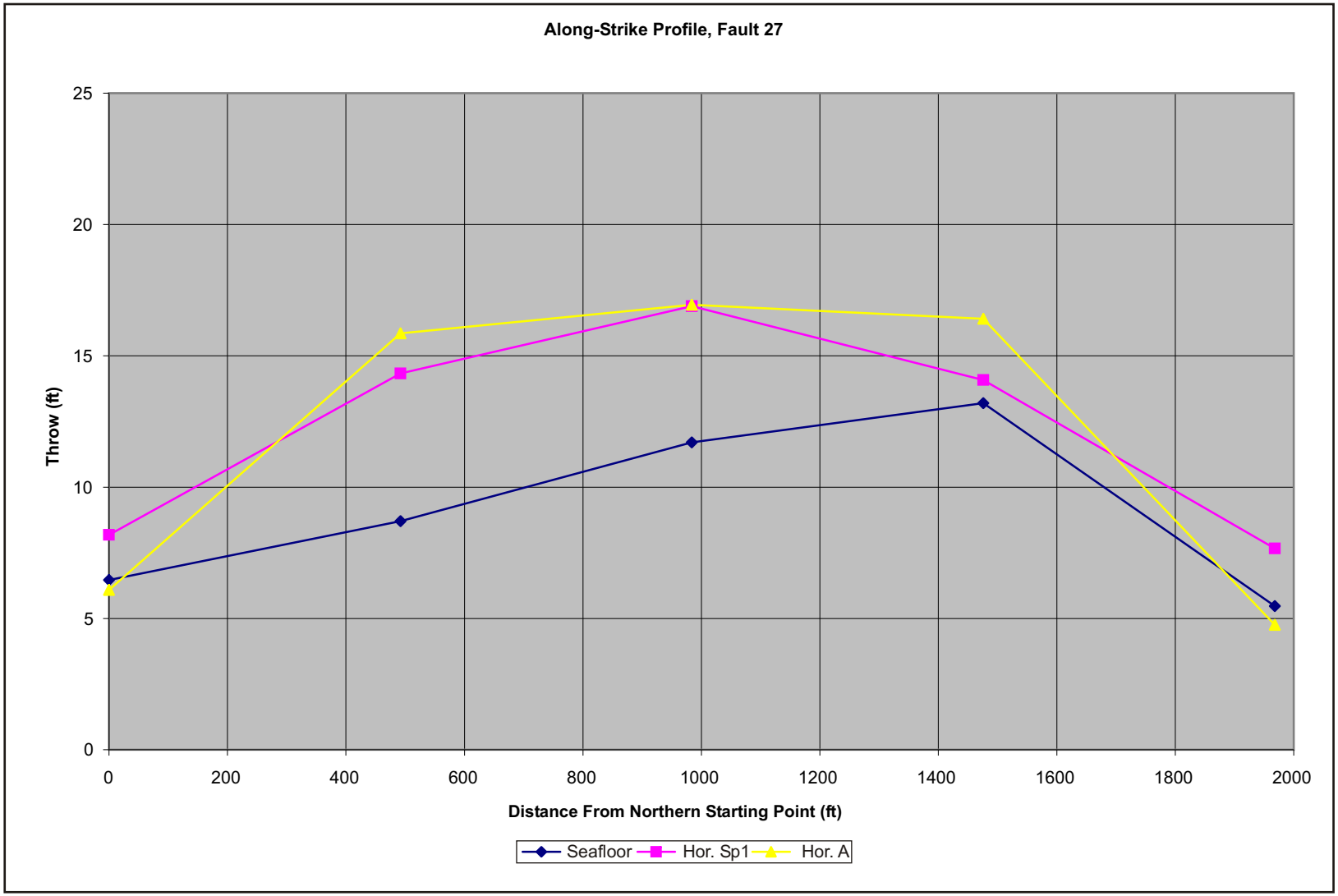

FIGURE 48 Continued.

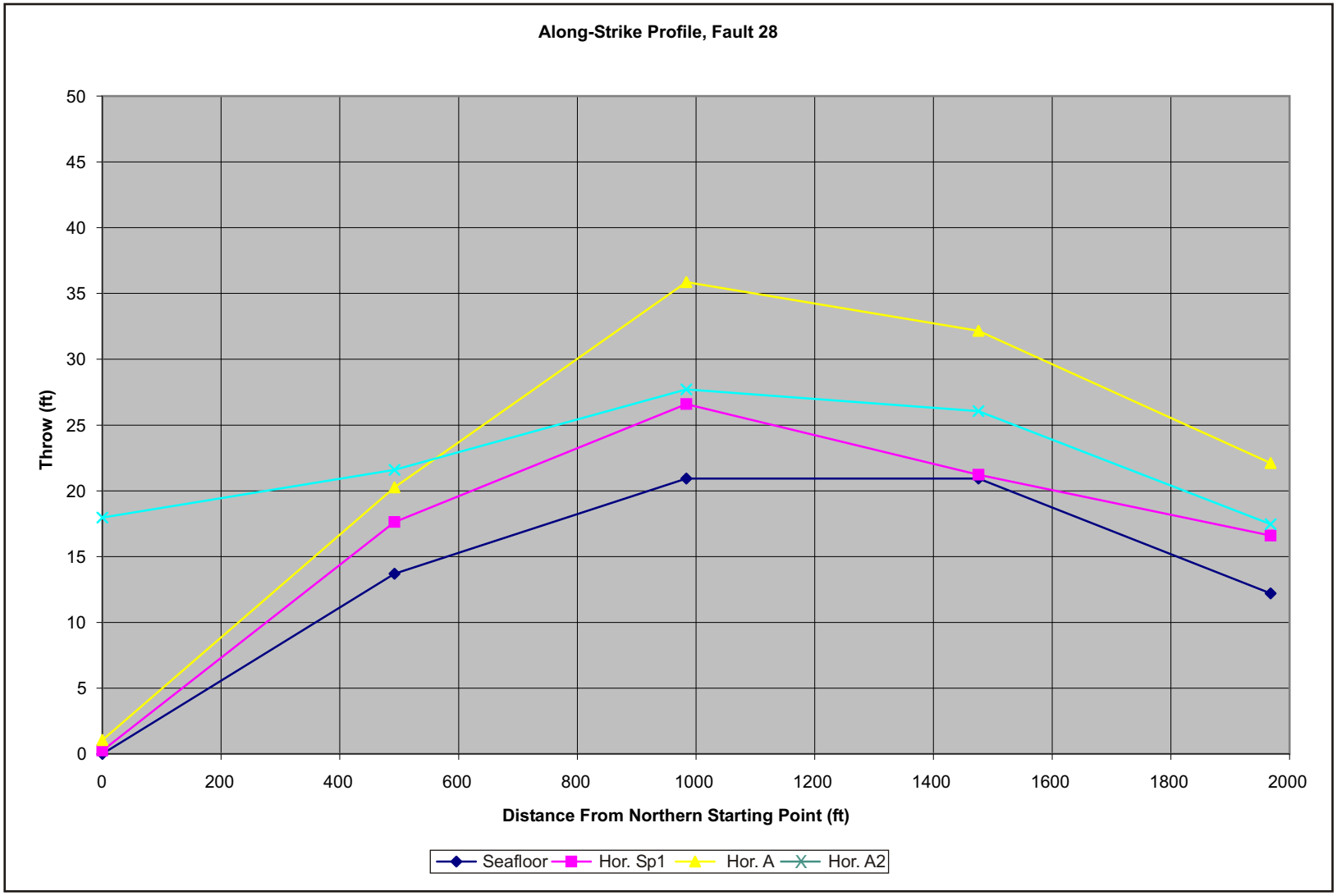

FIGURE 48 Continued.

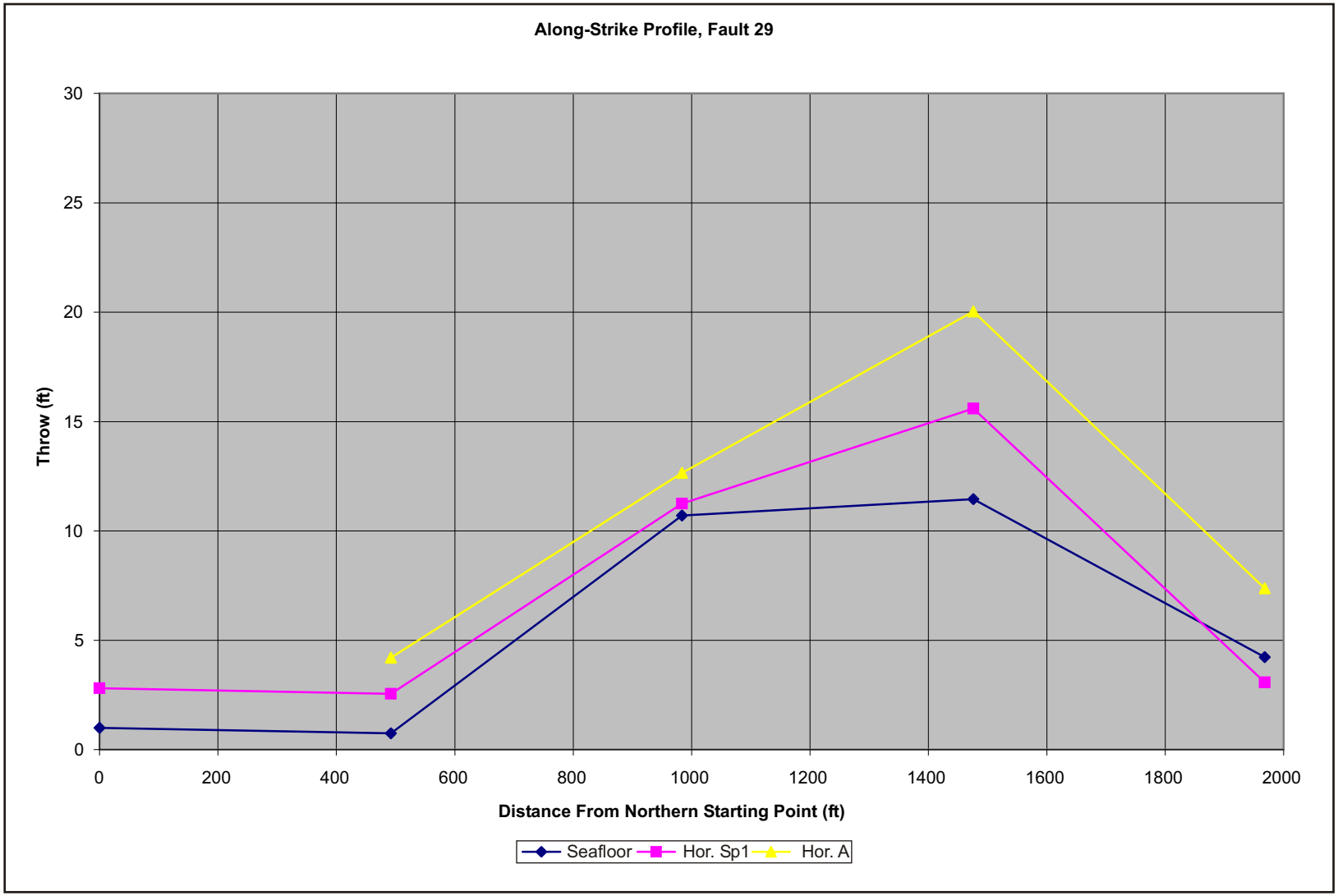

FIGURE 48 Continued.

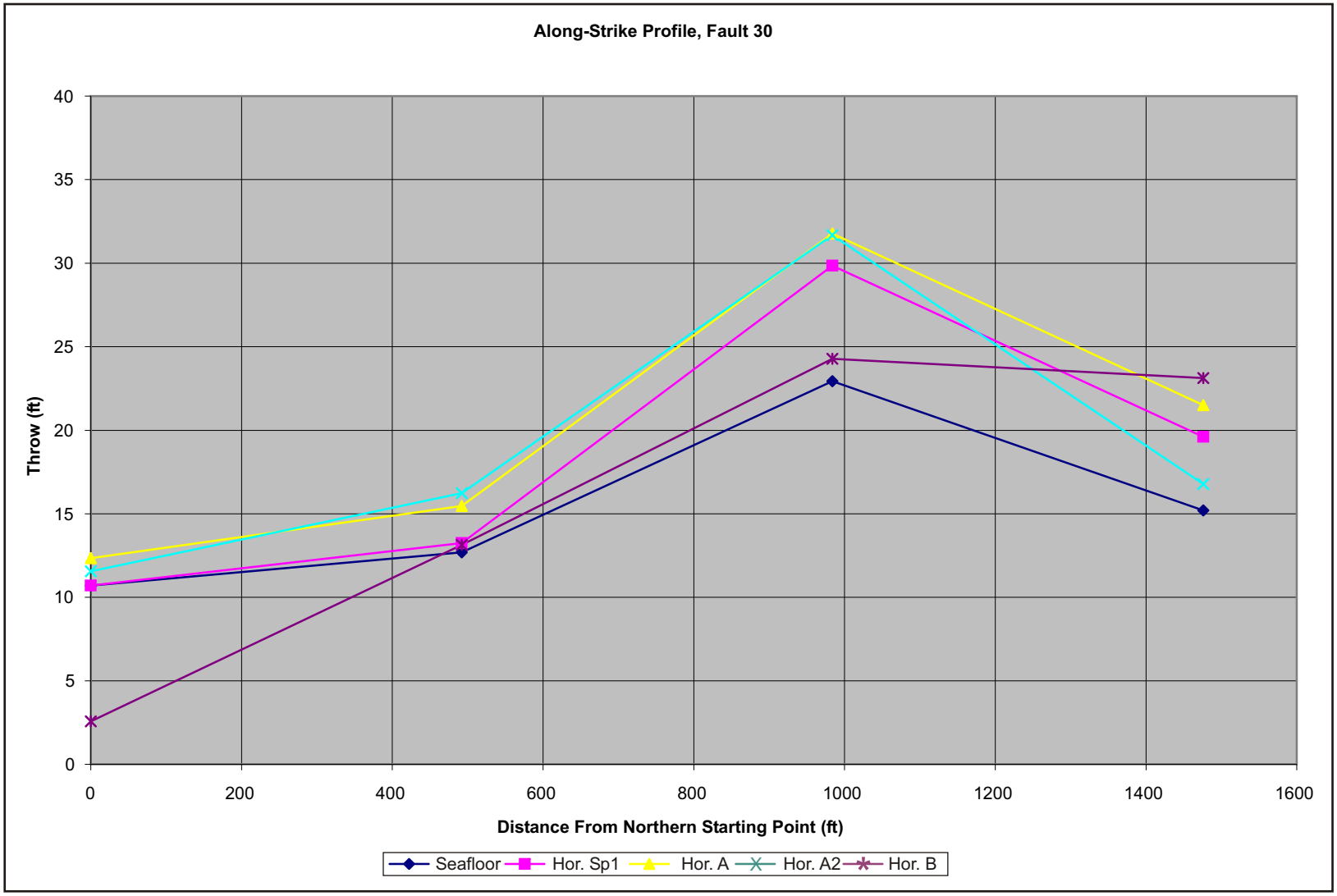

FIGURE 48 Continued.

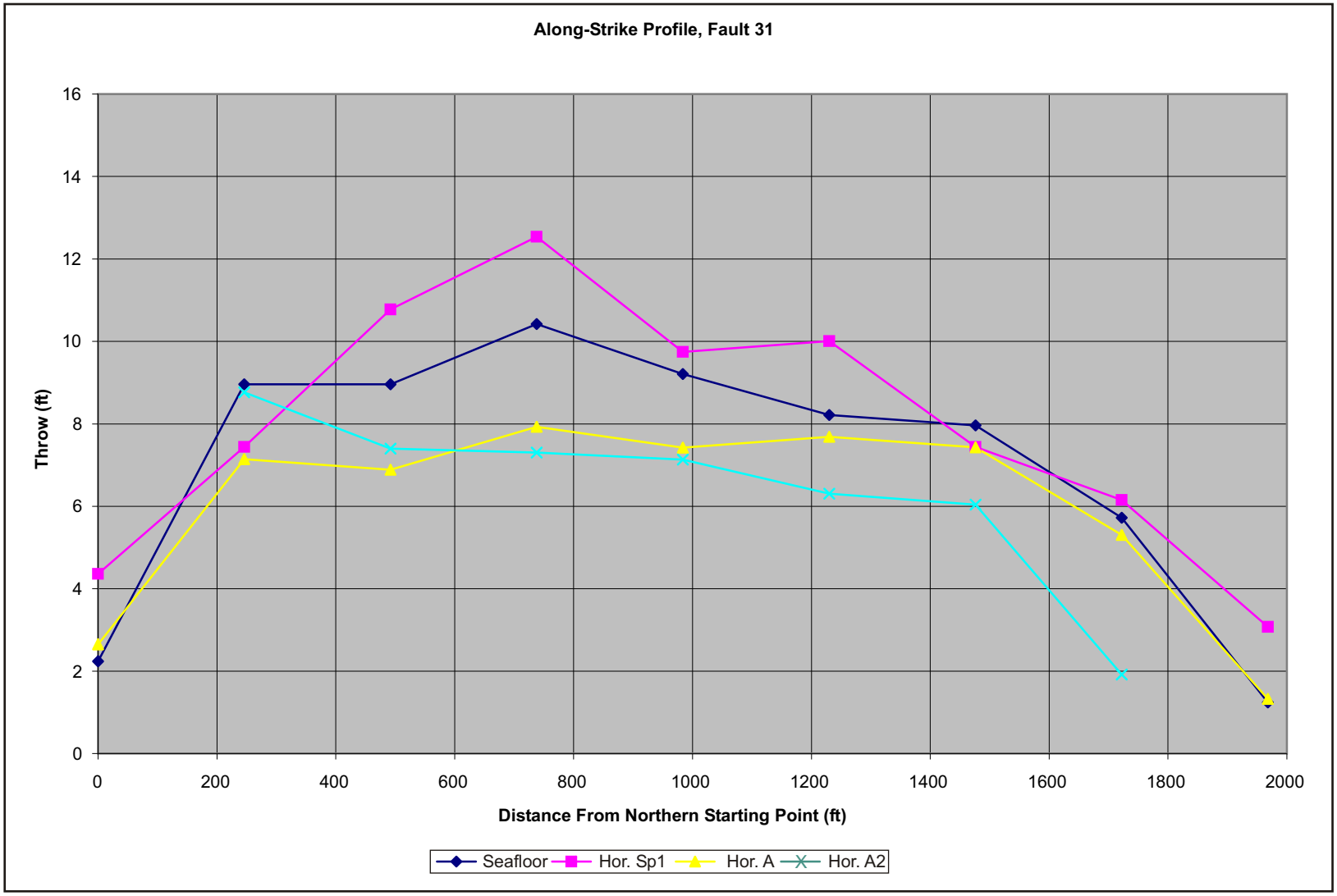

FIGURE 48 Continued.

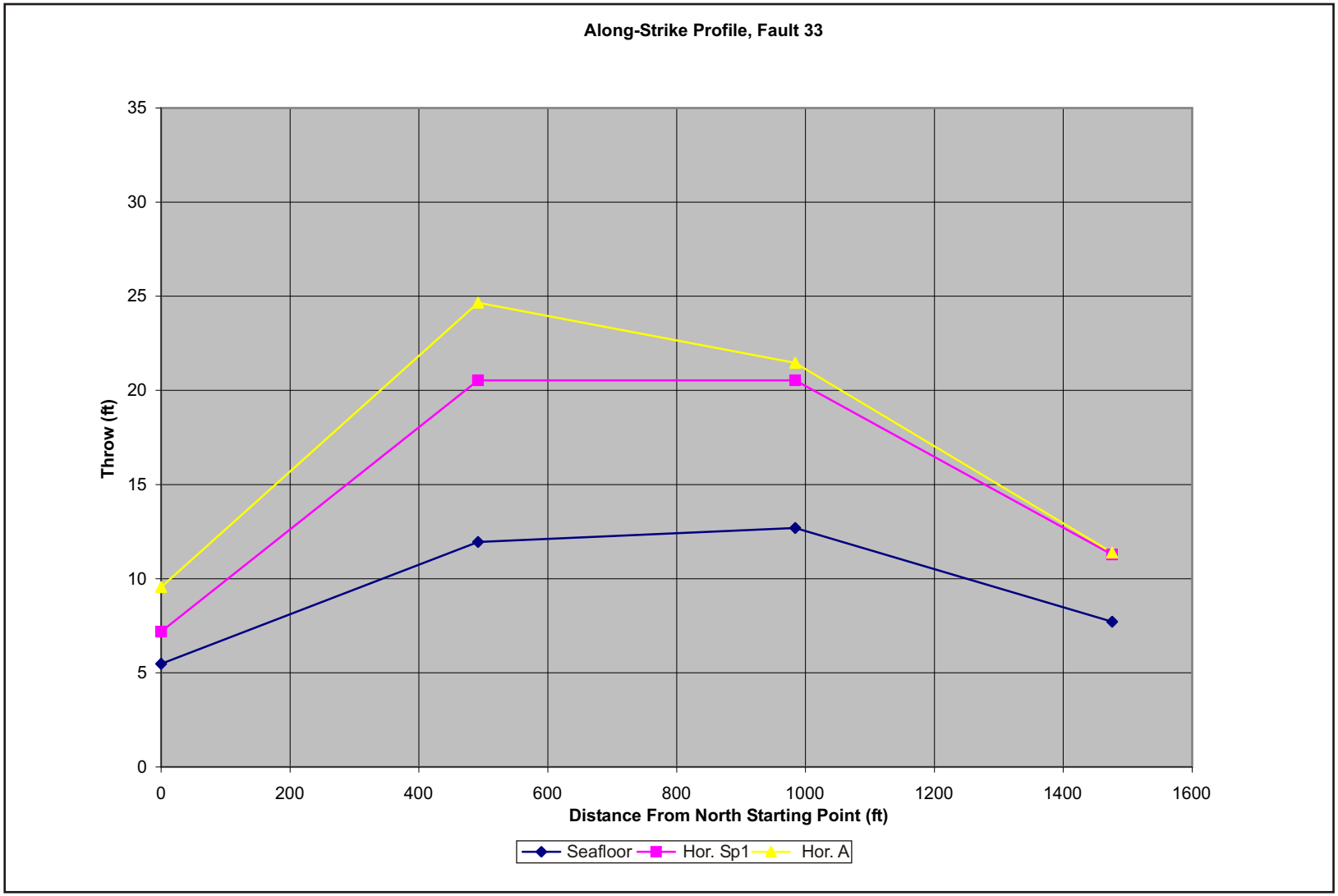

FIGURE 48 Continued.

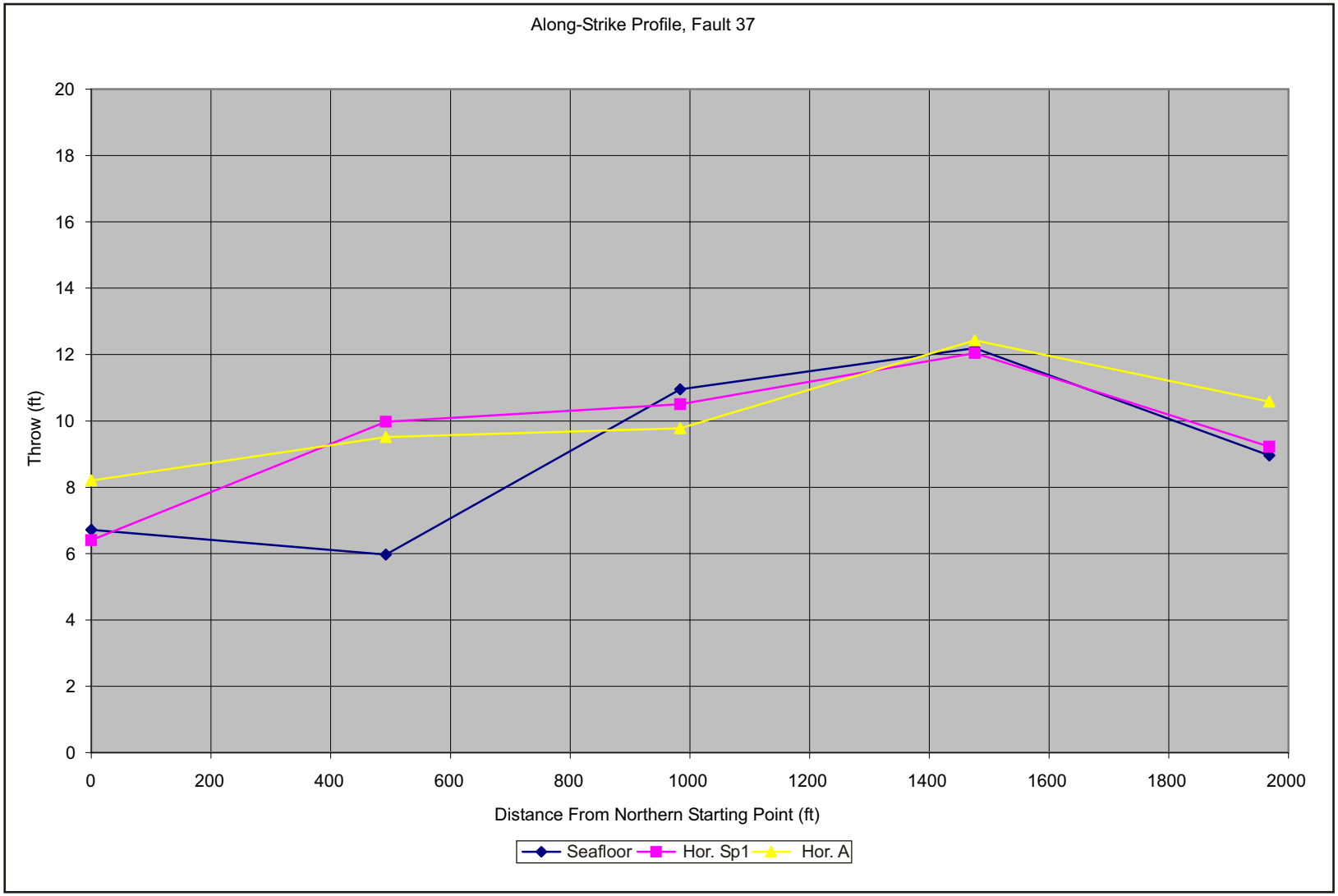

FIGURE 48 Continued.

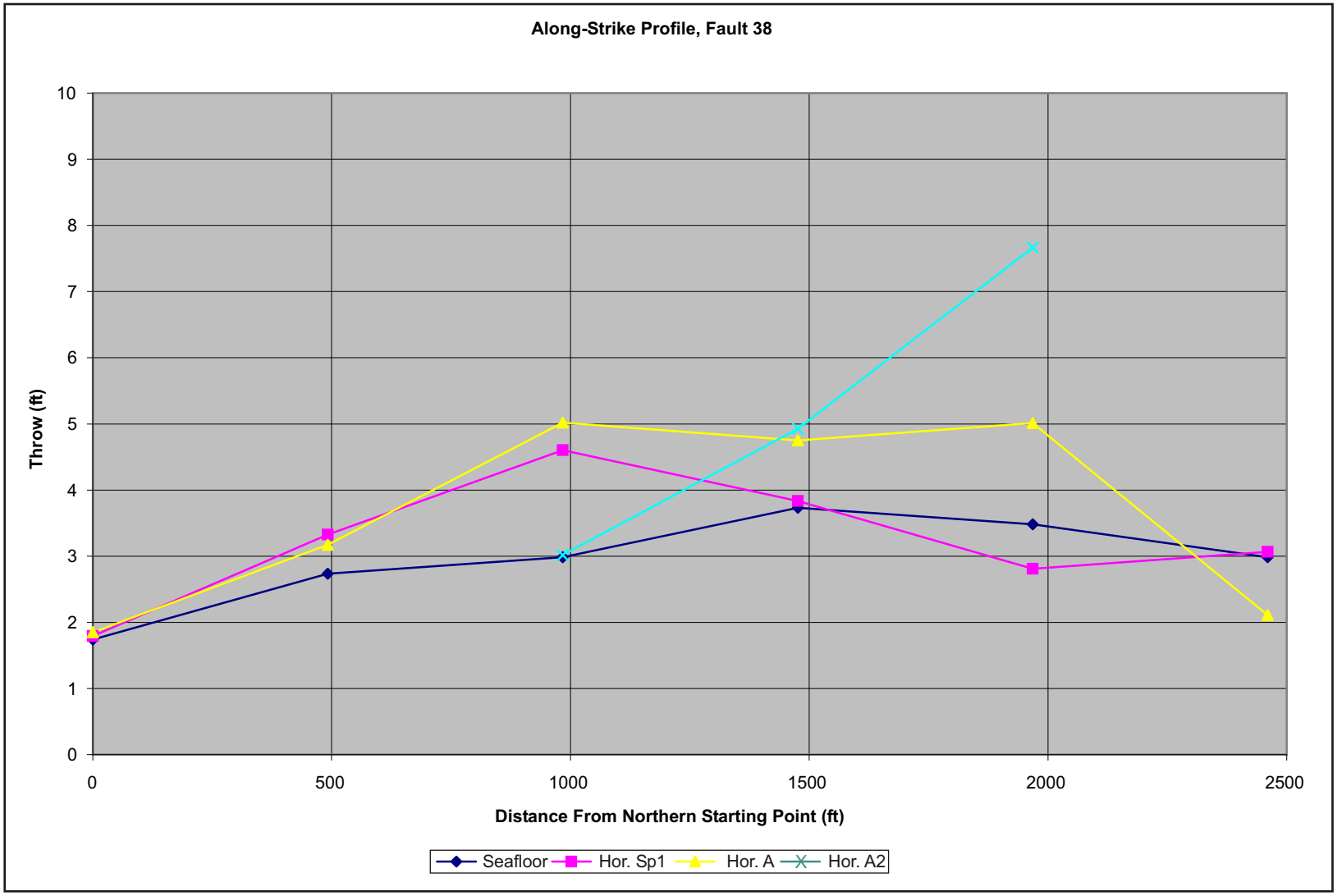

FIGURE 48 Continued.

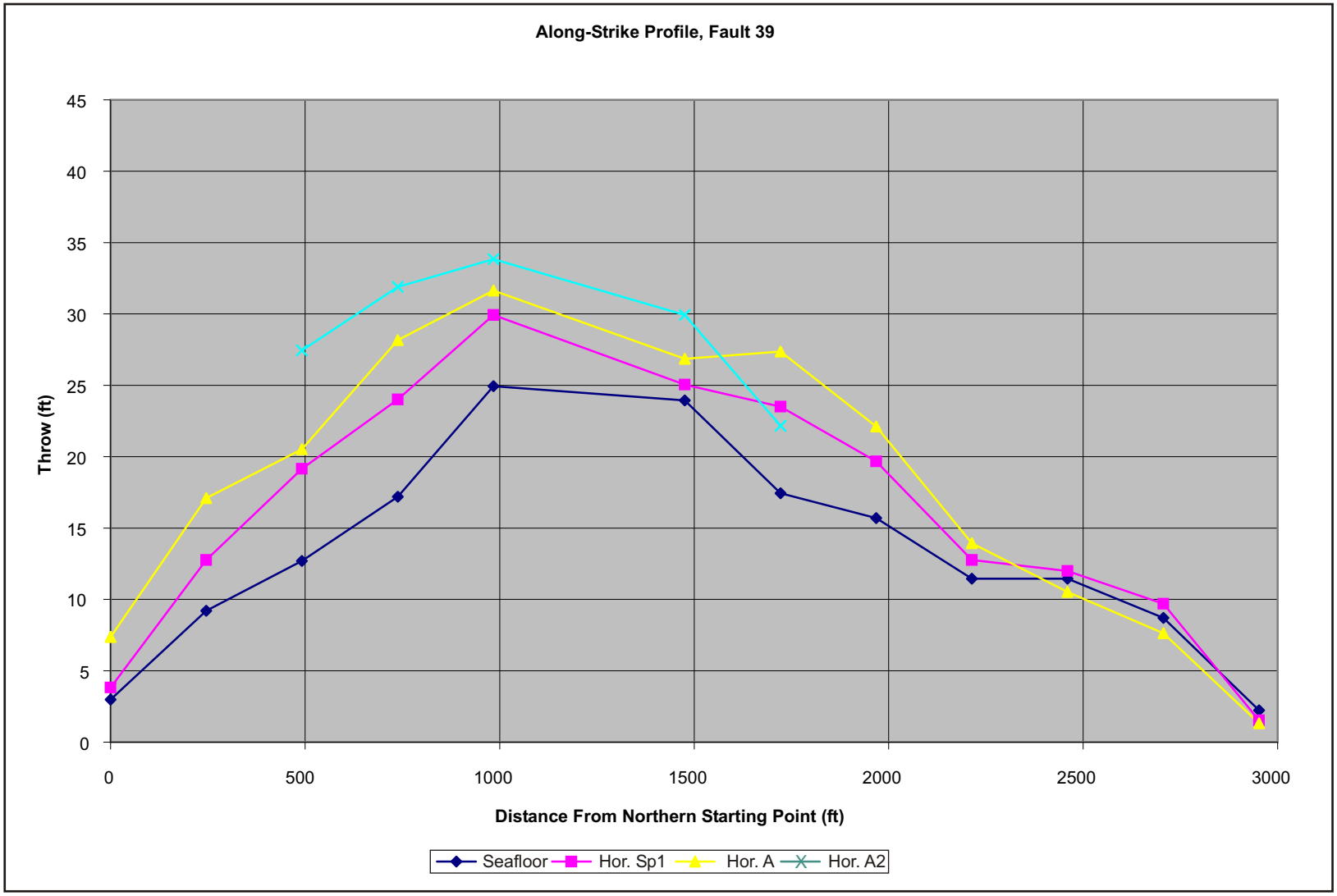

FIGURE 48 Continued.

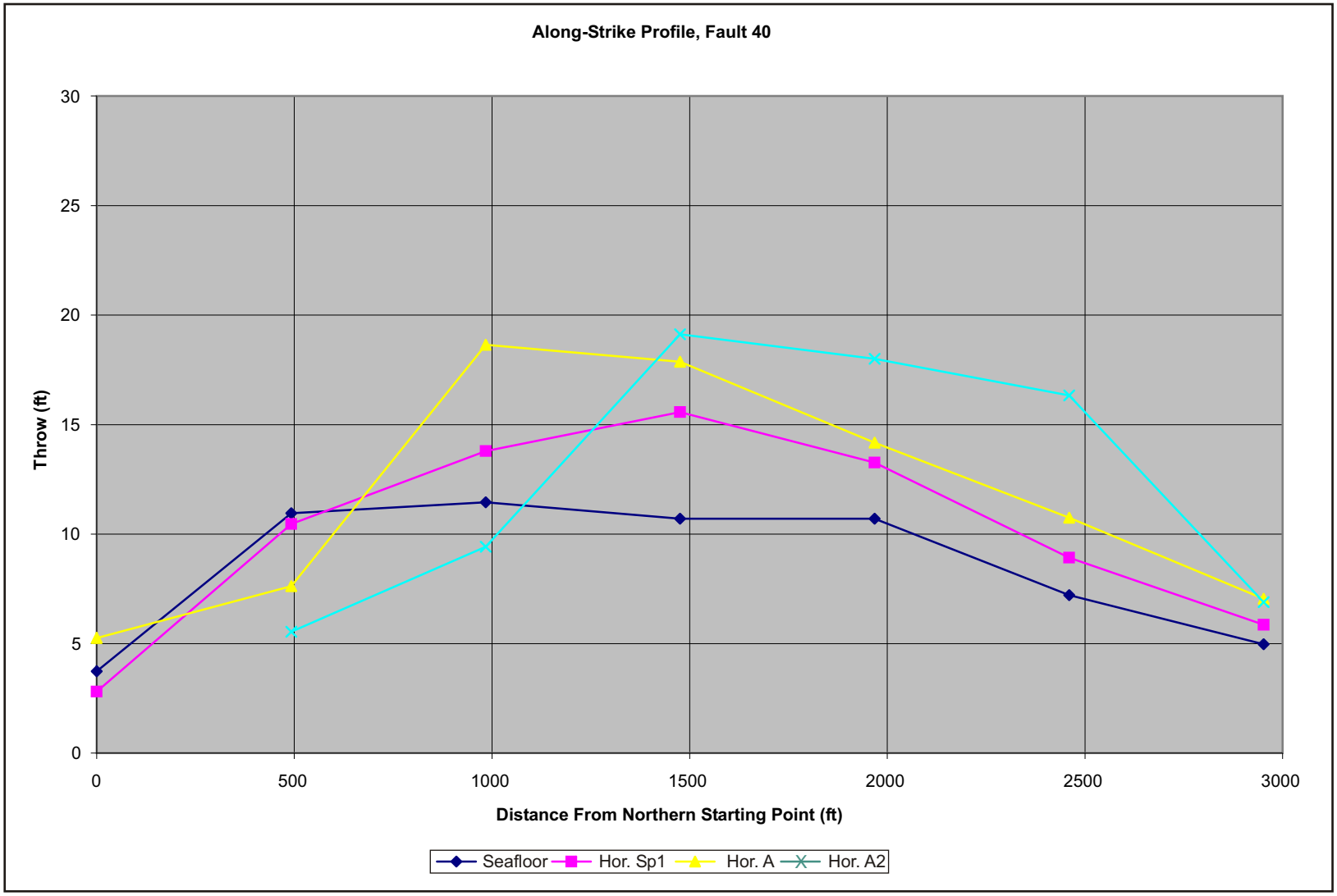

FIGURE 48 Continued.

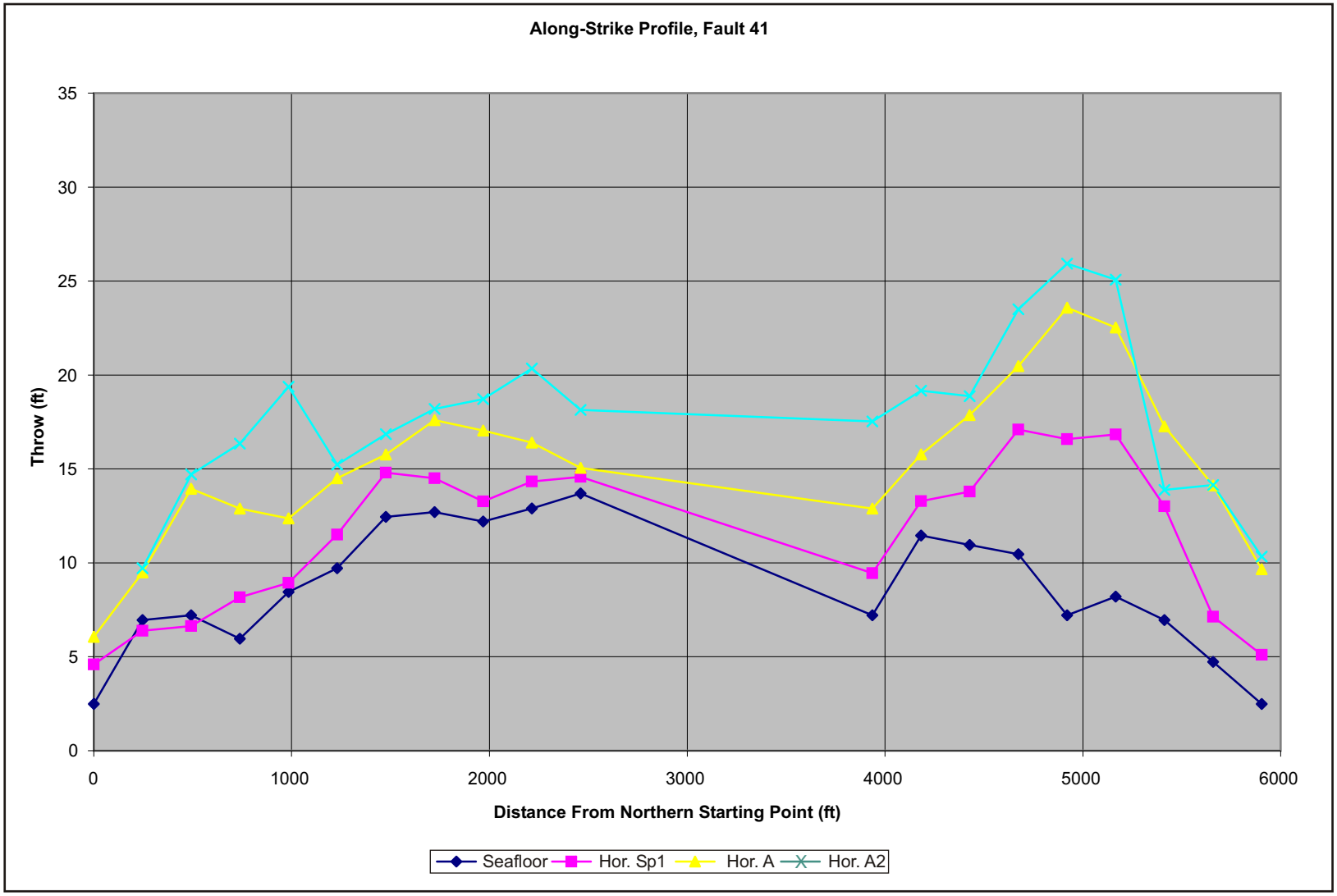

FIGURE 48 Continued.

FIGURE 48 Continued.

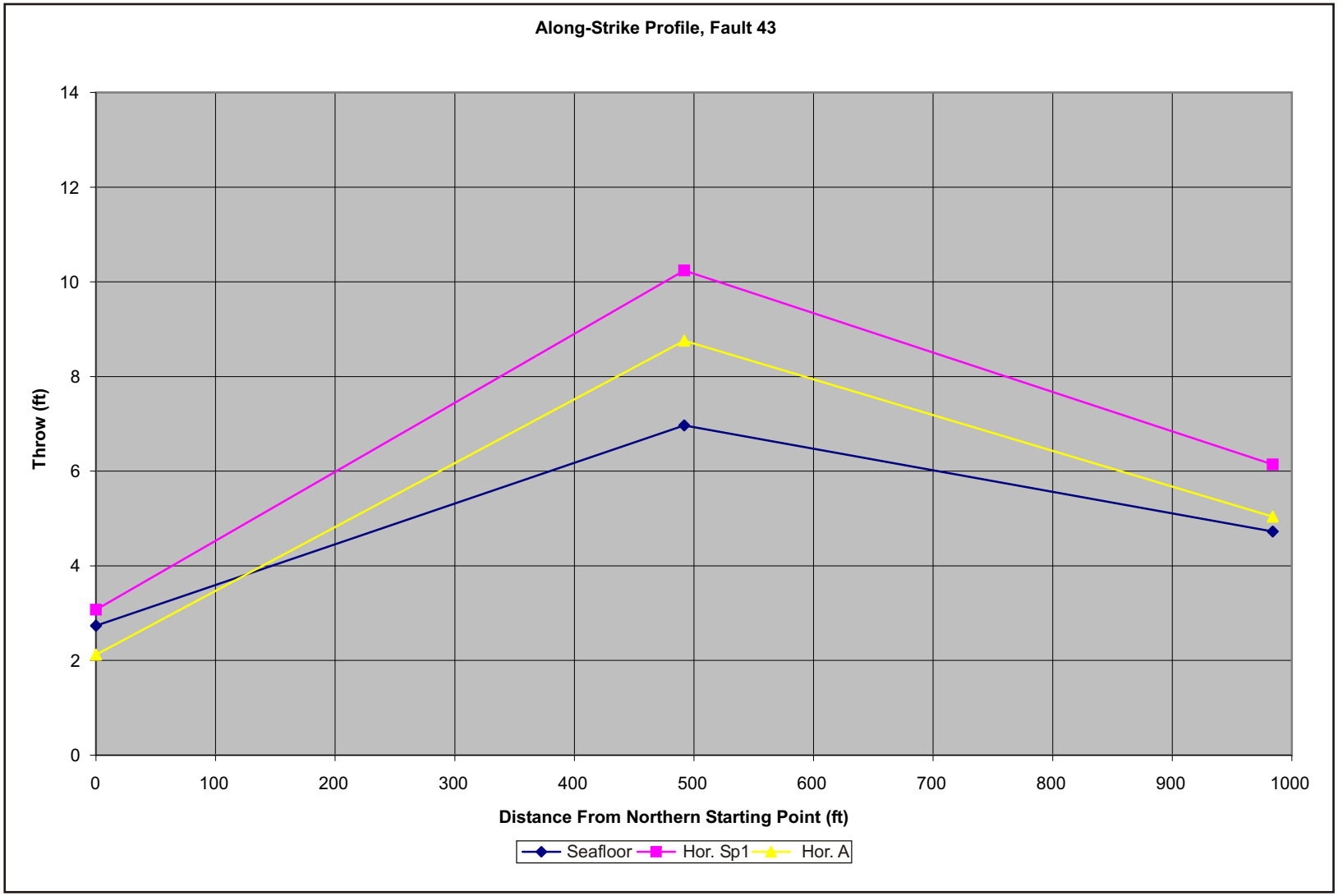

FIGURE 48 Continued.

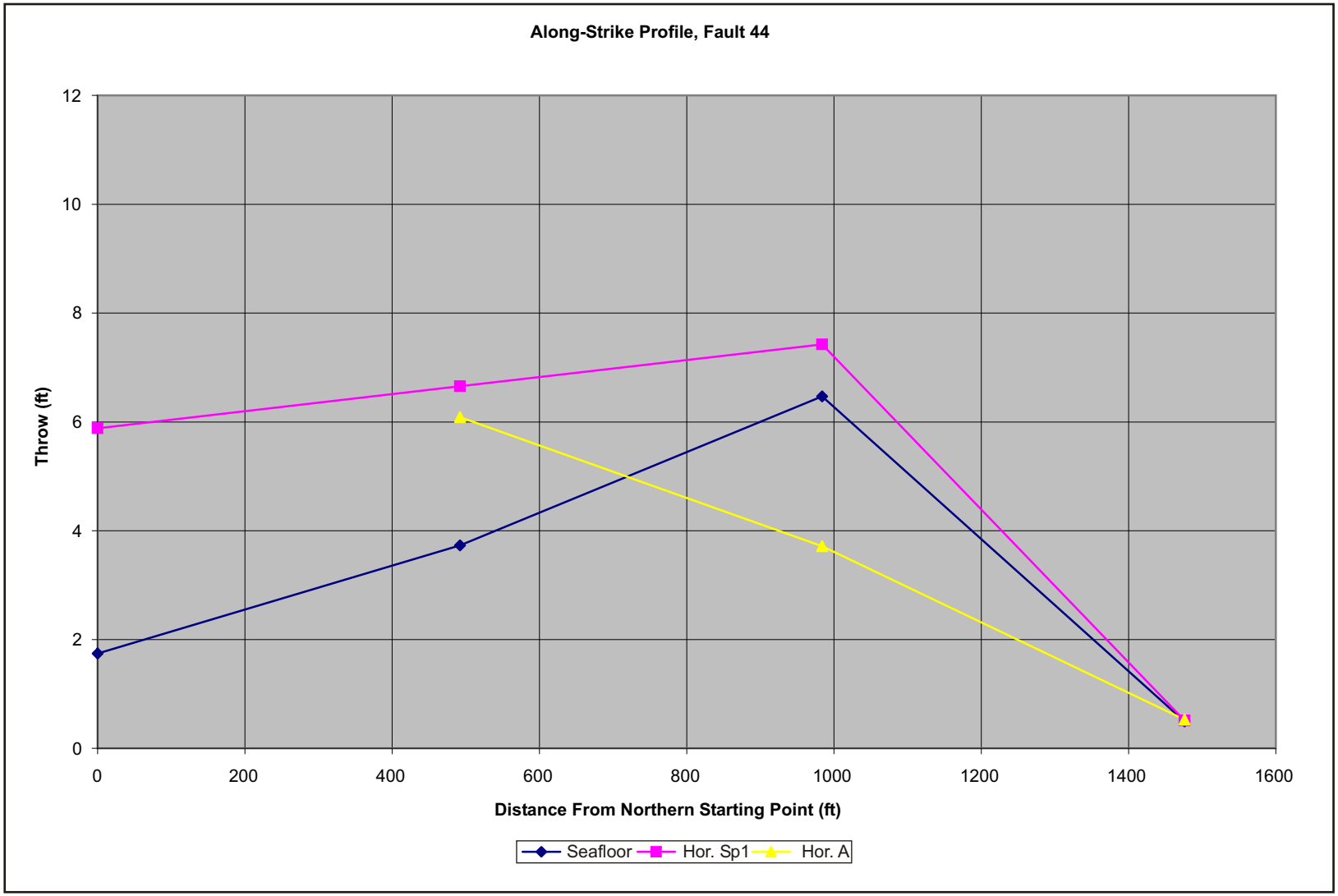

FIGURE 48 Continued.

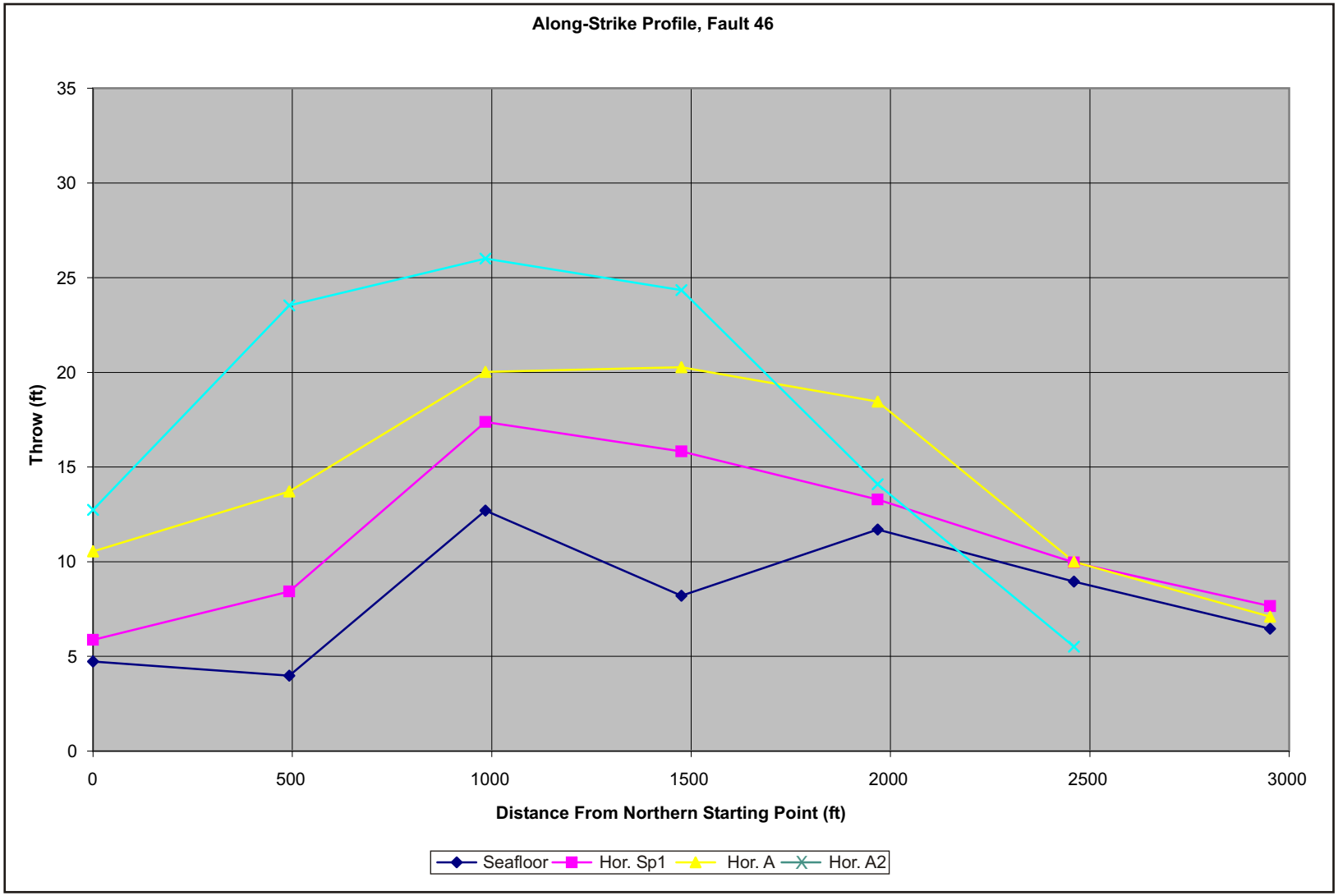

FIGURE 48 Continued.

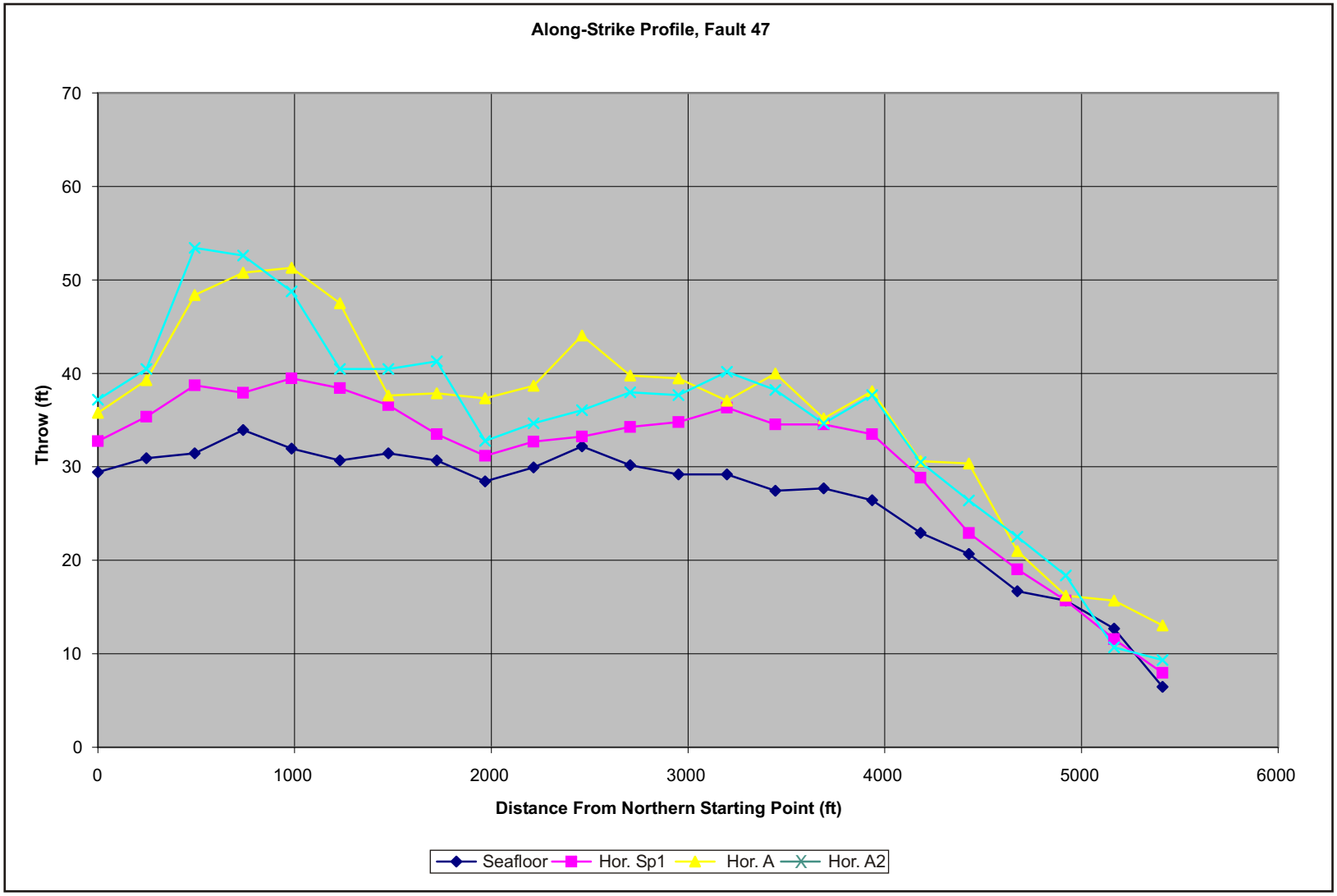

FIGURE 48 Continued.

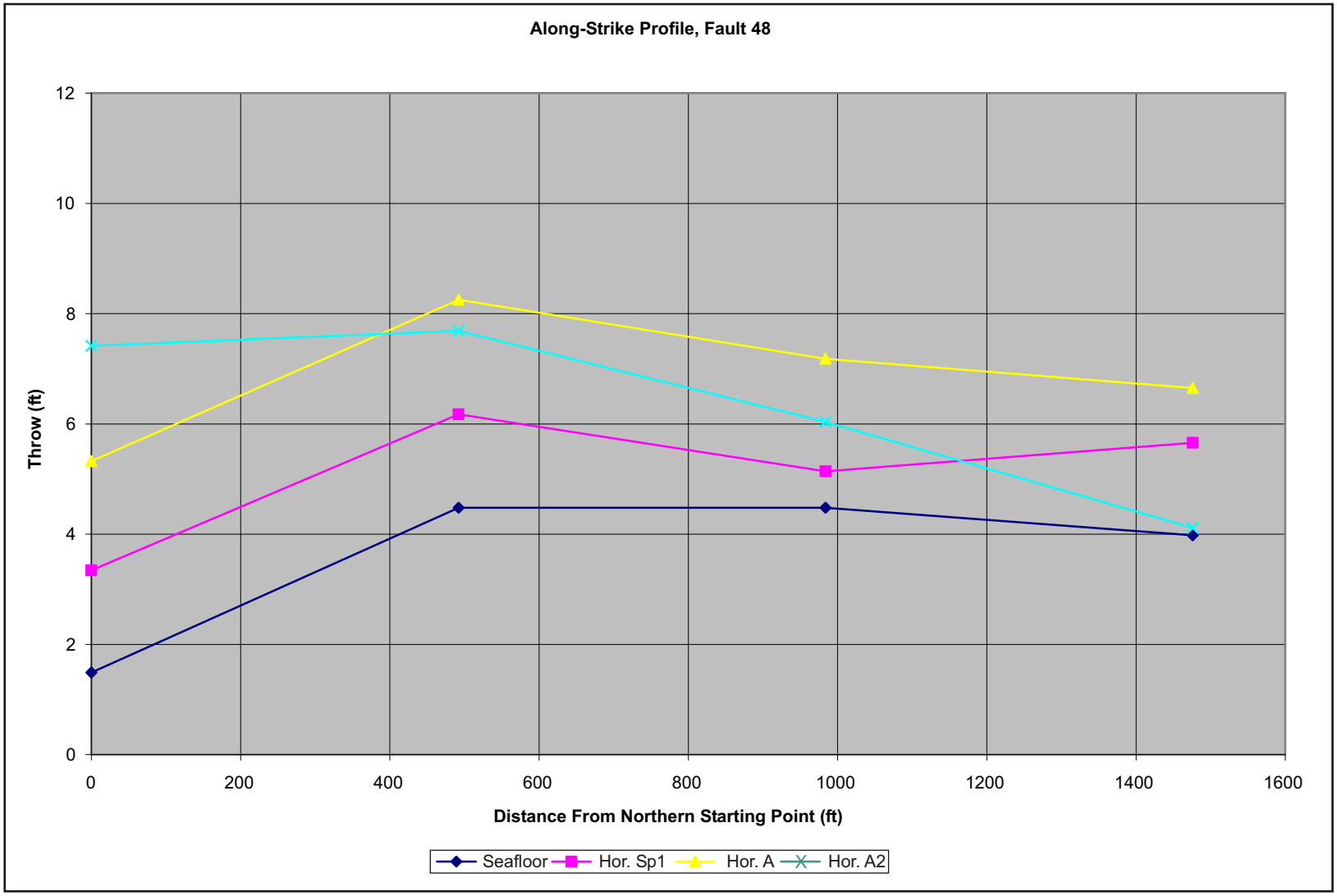

FIGURE 48 Continued.

APPENDIX 2: STRATIGRAPHIC DATING WITH SEQUENCE STRATIGRAPHY AND $\delta^{18}O$ DATES

A component of this research project is the assessment of the rate of movement along the faults within the study area. No direct instrumented measurements of movement—or any of the components of displacement—are possible because of the deep marine environment and because of the inferred very long time periods required for collecting meaningful measurements. Therefore, an indirect method of determining rates of movement is required. The numerous seismic reflectors (equivalent to sediment bedding planes) offset by the faults could be used to determine average rates of movement. This requires that we know the amount of offset of a given reflector across the fault and the age of the reflector. The offset—the components of displacement, in this case throw—can be measured with reasonable accuracy and precision from a vertical seismic section intersecting the fault parallel to the true dip. The age of the reflector can be determined or estimated from some absolute dating method. Biostratigraphy, magnetostratigraphy, and radioisotope dating are viable methods. No absolute dates for sediments are available for the study area in public records and literature. Available radiocarbon dates for shallow sediments are known at a nearby location, however, reliable correlation of reflectors into this study area is not possible. Absolute dates for regional marker horizons present within the study area were supplied by a petroleum exploration and production company operating in the Gulf of Mexico, but these horizons are below the practical depth limit of this study and are unusable.

A method of estimating the ages of unique stratigraphic packages was suggested by an industry professional consultant (P. K. Trabant, 2004, personal communication, consulting geologist in Austin, Texas). This method allows for the assignment of absolute ages to relatively young, shallow sediments deposited in generally quiescent deepwater settings, and does not require the local determination of absolute ages of the strata of interest by sampling and testing. The physical mechanisms exploited in this age estimation method are the predictable variations in the Earth's orbital and rotational

parameters. These variations affect terrestrial climate through the process of orbital forcing (Milankovitch cyclicity).

Milutin Milankovitch and Parameters of Earth's Orbit and Rotation

Serbian astrophysicist Milutin Milankovitch (1879-1958) developed a model for external control of terrestrial insolation based on the Earth's orbit and rotation. His model, expanding on earlier work by others dated to the 1840's, describes the dependence of seasonal and total insolation upon observed variations in three parameters of the Earth's orbit and axial rotation: eccentricity, obliquity, and precession (Davis, 2004).

Eccentricity. The Earth's orbit around the Sun deviates slightly from a perfect circular shape, and is therefore said to be elliptical in shape. Furthermore, the elliptical orbit displays a time-dependent, cyclical variation in shape. An ellipse's eccentricity is the parameter that defines the deviation from a perfect circle in terms of the lengths of the ellipse's semimajor and semiminor axes. Earth's elliptical orbit varies between eccentricities of 0.0005 (more circular) and 0.0607 (more elliptical) over a period of nearly 100,000 years (Davis, 2004; Figure 49).

Orbital eccentricity affects Earth's total insolation in the following way: The intensity of sunlight at a point in space is a function of distance from the light source (Nave, 2000). As distance from the Sun increases linearly, the intensity of sunlight decreases proportionally with the square of the distance. The constant of proportionality is 4π. Thus, variations in the Earth/Sun separation distance result in variations in total insolation. This effect is accentuated when the orbital eccentricity is greater and reduced when the eccentricity is less.

Obliquity. The Earth's axial tilt, or obliquity, varies with time. This variation in tilt is analogous to the wobble of a spinning top, and is related to the uneven distribution of mass within the Earth (Reading and Levell, 1996, Davis, 2004). Obliquity is measured as the angle between the rotational axis and the normal to Earth's orbital plane. Earth's obliquity varies between 21.5° and 24.5° over a period of about 41,000 years (Griggs, 2001, Davis, 2004), and is currently 23.5° (Figure 49). Obliquity primarily affects seasonal insolation at Earth's high

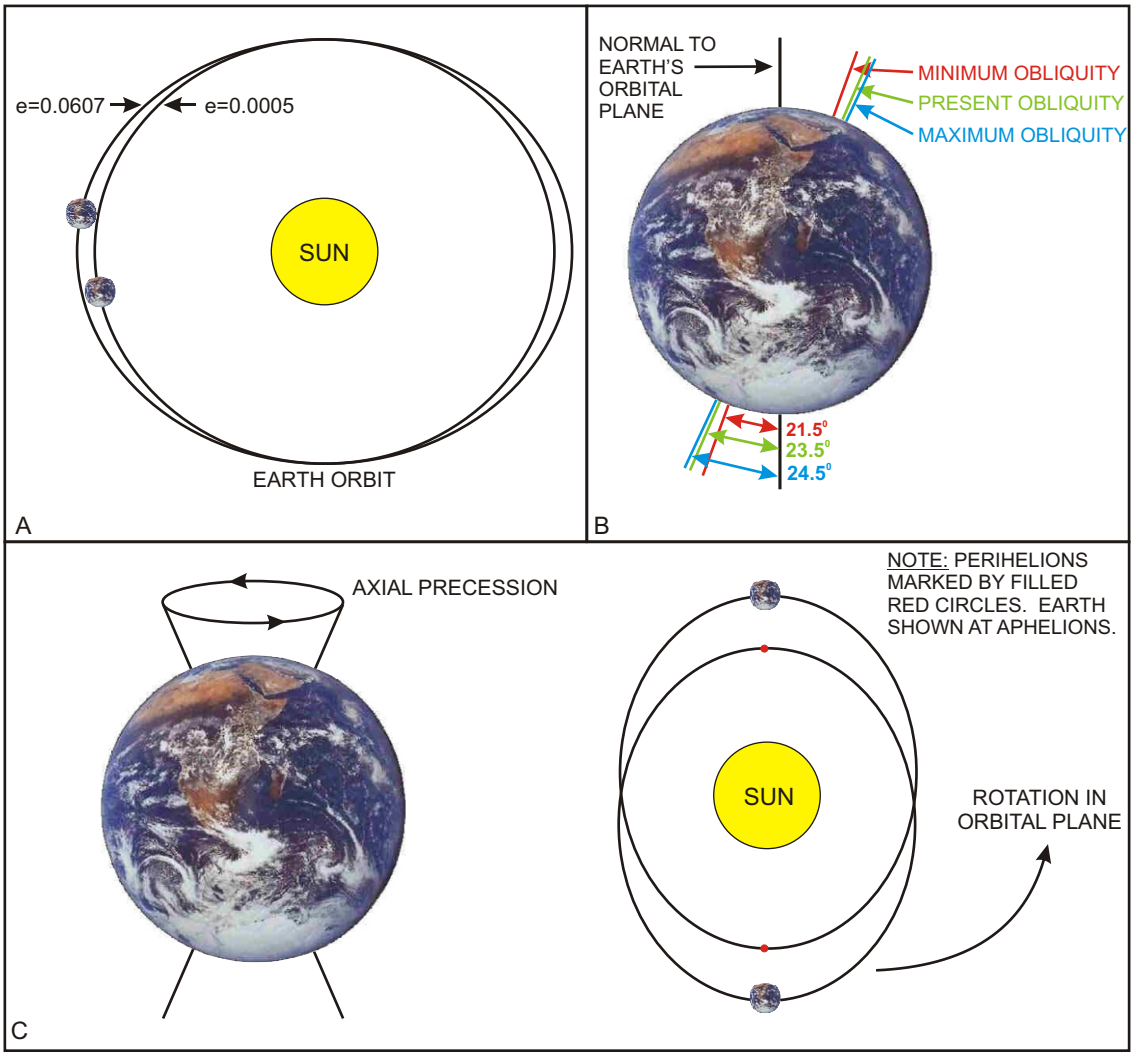

FIGURE 49: Components of Earth's orbital and rotational parameters governing insolation in Milankovitch's theory of astronomical forcing of climate. A. Eccentricity of Earth's orbit varies on a 98,000 year cycle and affects total insolation. B. Axial obliquity varies on a 41,000 year cycle. This parameter dictates the amount of sunlight reaching high latitudes. C. The Earth's rotational axis precesses (traces a circle). The orbital plane also rotates, causing aphelion and perihelion to occur at different seasons through time. Rotational and orbital precession occur on 19,000 year and 23,000 year cycles, respectively. These parameters dictate the timing of the seasons. With eccentricity, precession dictates season insolation for the hemispheres. (Drawings are not to scale, and angular relationships are approximate or exaggerated unless stated.)

latitudes, and thus the degree to which the Earth experiences seasons. When obliquity is at a minimum, high latitudes experience less summertime direct sunlight than when obliquity is at maximum (Reading and Levell, 1996).

Precession and Orbital Rotation. In addition to variations in the angle of obliquity, Earth's rotational axis also precesses. That is, from the point of view of an Earth-bound observer, the rotational axis traces a circular path in the sky over an absolute period of about 26,000 years. Axial precession is caused by the combined gravitational effects of the Sun and the Moon on Earth's equatorial bulge as they move relative to the Earth (Reading and Levell, 1996). Earth's orbital plane also rotates around the Sun, causing the locations of aphelion (farthest distance from the Sun) and perihelion (closest approach to the Sun) to change with time from the point of view of a stationary observer. The effect of this orbital rotation is to reduce the precessional cycle to two characteristic periods of about 19,000 years and 23,000 years (Reading and Levell, 1996) as shown in Figure 49. Precession causes the seasons, marked by the winter and summer solstices and the vernal and autumnal equinoxes, to occur at progressively different times of the year.

Combined Effects. As discussed previously, the degree of obliquity affects the degree of seasonality experienced by high latitudes by controlling the directness of sunlight received during the winter. Eccentricity affects the distance between the Earth and Sun throughout the year, and affects total insolation through an inverse square relationship. Precession affects seasonal insolation in conjunction with eccentricity by progressively varying the timing of the seasons with respect to aphelion and perihelion (Davis, 2004). The eccentricity, obliquity, and precession cycles repeat over different time periods (Figure 50), and the effects of any one orbital or rotational parameter may act to amplify or to degrade the effects on insolation caused by the other parameters. Imbrie et al. (1984) recognized that consolidating the time variations in these parameters, which they termed ETP, would lead to means of predicting past variations in this composite parameter (Figure 50).

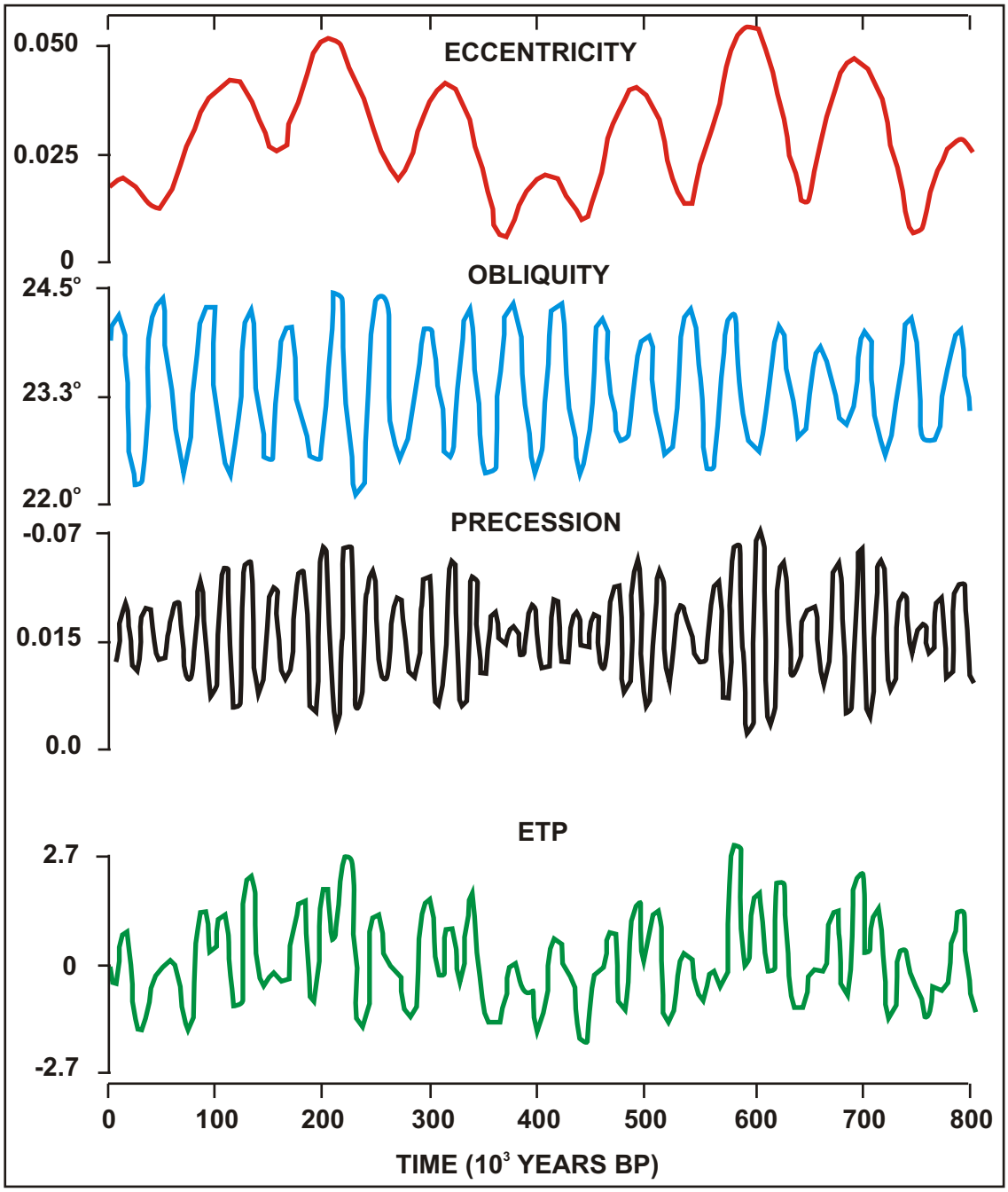

FIGURE 50: Variations in eccentricity, obliquity, and precession over the past 800,000 years. The cyclic nature of variation in these parameters of Earth's orbit and rotation are readily observed: approximately 100,000 years for eccentricity, 41,000 years for obliquity, and 19,000 and 23,000 years for precession. Obliquity is shown in units of degrees, and precession is shown as values derived by Imbrie et al. (1984) called precession index, and is analogous to angular momentum. The bottom curve labeled ETP (Eccentricity, Tilt (obliquity), Precession), is constructed by normalizing the upper three curves and summing them. Units of ETP are standard deviation. (Based on Figures 2 and 3 of Imbrie et al., 1984).

Milankovitch Cycles, Climate, and Oxygen Isotopes

Milankovitch Cycles and Climate. Several non-human factors are known to affect climate on Earth, including changing atmospheric composition, volcanism, geographic distribution of land masses and ocean basins, variations in solar output, and variations in Earth's orbital and rotational parameters. These factors operate on differing time scales, ranging from years to millions of years. If attention is focused on a short period of time, the past several hundred thousand years for example, several factors affecting climate appear to be constant because of their very long-term variability, and would therefore not cause appreciable climatic variations on our scale of observation. The global distribution of continents and oceans varies on a scale of tens to hundreds of millions of years, and falls into this category. Volcanism may affect atmospheric composition and airborne particulate matter on the short terms (a few years to hundreds of years). Variations in solar output are not well understood, but are thought to operate on short (years or decades) or long (millions of years) scales. On the scale of long-term climatic variation, the composition of the atmosphere has varied relatively little since the appearance of abundant land plant life in the Devonian, and subsequent radical modification of Earth's atmosphere. Beginning with Milankovitch and his contemporaries and continuing to the present with the work of Imbrie et al. (1984) and others, orbital forcing is recognized as a control over insolation whose signal is recorded in the fossil record. Orbital forcing also affects climate over the scope of time considered here.

Oxygen Isotopes and Climate. Imbrie et al. (1984) describes the relationship between the combined Milankovitch parameters (ETP) and a specific indicator of paleoclimate: oxygen isotope variations in the marine fossil record. The relative abundance of ^{18}O versus ^{16}O in the tests of forams (small, near-surface dwelling marine organisms) is partially dependent upon the growth and retreat of continental glaciers. This is because water containing ^{16}O is preferentially sequestered in glaciers and other land ice in relation to water containing ^{18}O (Shackleton and Opdyke, 1973, Imbrie et al., 1984). Therefore, ^{18}O is relatively more abundant in seawater during periods of glacial growth than during glacial retreat and interglacial periods.

Measurements of the relative abundances of ^{18}O and ^{16}O in foram tests at various depths within deep-sea cores collected around the world led investigators (for example, the works of C. Emiliani, dated 1955-1956 and not referenced here; Shackleton and Opdyke, 1973; Imbrie et al., 1984) to develop a relationship between oxygen isotope abundance and depth. Deep-sea sediments, typically consisting of clay and siliciclastic sand and silt, accumulate at slower, but more constant rates than shallow water sediments. The investigators applied estimated depositional rates to the thickness of sediment studied in each core, yielding isotopic oxygen composition versus time (Figure 51). Conversion of depth in the deep-sea cores to time was further calibrated with the use of radiocarbon age determinations and the recognition of a conspicuous and precisely dated magnetic reversal event. Iterative statistical calculations were also used to further calibrate the Milankovitch cycle with the observed oxygen isotope data, and variables such as changes in sedimentation rate and time lag in the effects of climate on oceanic oxygen isotopic composition were also considered (Imbrie et al., 1984). Oxygen isotope composition is usually reported as the excursion in ^{18}O abundance versus a standard value ($\delta^{18}O$). Negative values of $\delta^{18}O$ are related to warmer climates and retreat of glaciers, and positive values are related to cooler climates and glacial growth (Davis, 2004).

Oxygen Isotopes and Milankovitch Cycles. Imbrie et al. (1984) compared their ETP curve to foram $\delta^{18}O$ versus time curves from several deep-sea cores taken in the Atlantic and Indian Oceans, and in the Coral, Caribbean, and Weddell Seas (Figure 52). By applying certain digital filters and spectral analyses to the oxygen isotope data and to the components of the Milankovitch cycle, they determined that a strong correlation exists between oxygen isotope distribution in the recent marine microfossil record and Milankovitch cyclicity (Figure 52). It is estimated that 77% of the magnitude of excursions in $\delta^{18}O$ in marine sediments from baseline values is attributable to Milankovitch mechanisms (Imbrie et al, 1984). Thus, a controlling relationship exists between orbital forcing, climate, and glaciation. Glaciation, in turn, affects oceanic oxygen isotope ratios.

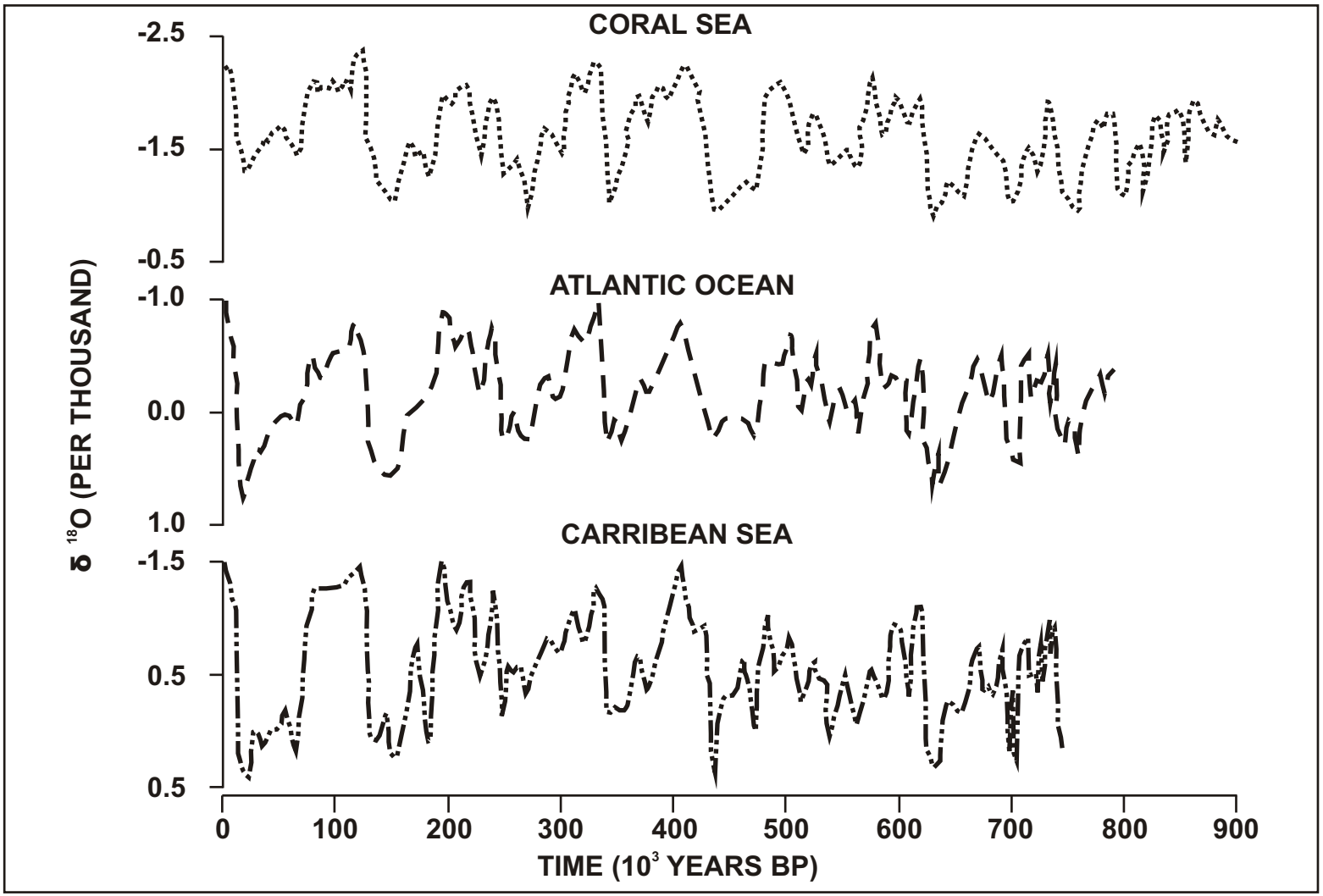

FIGURE 51: Oxygen isotope composition of foram tests as a function of time for three deep-ocean core locations. (Based on Figure 6, Imbrie, et al., 1984).

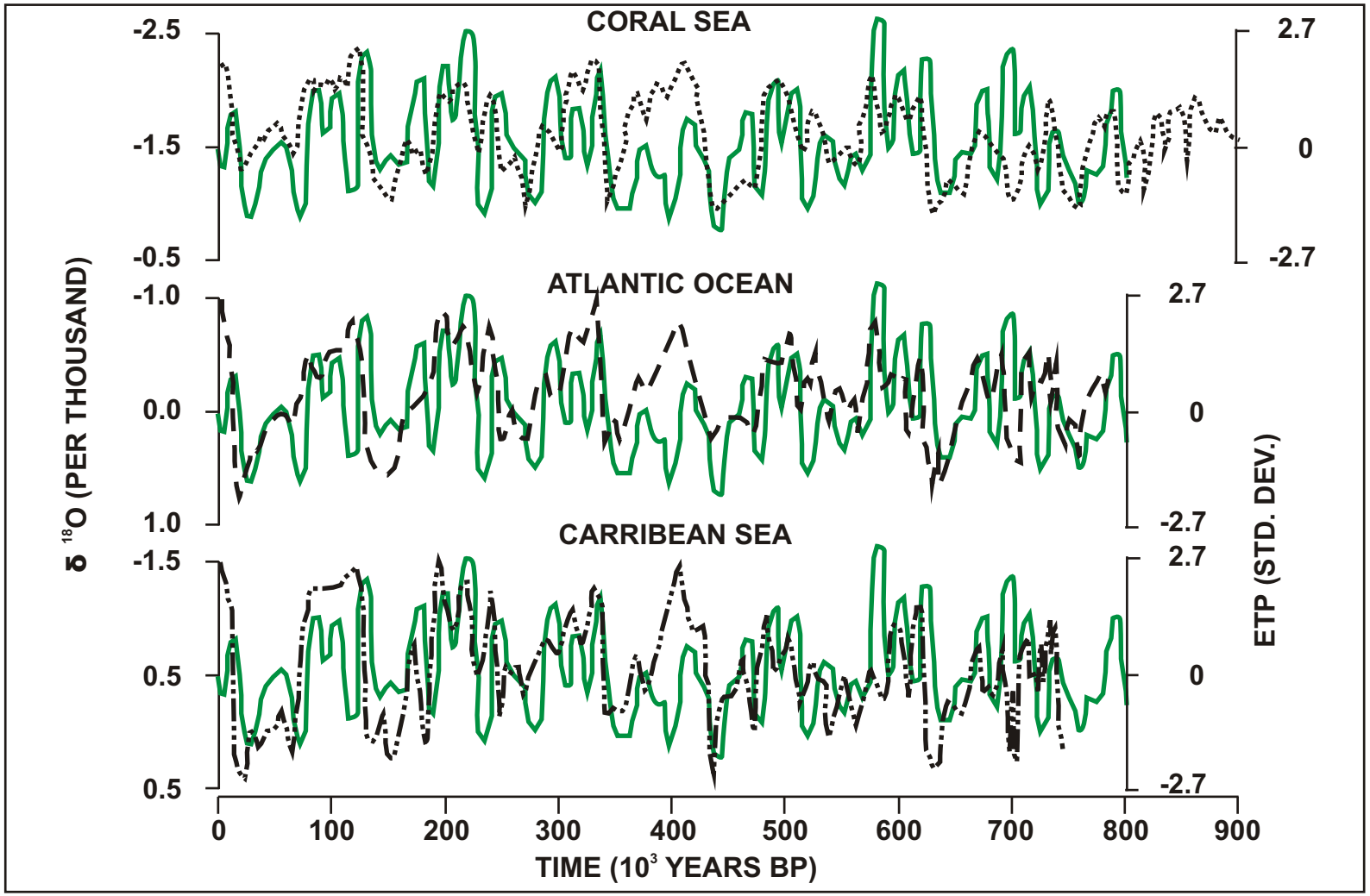

FIGURE 52: Oxygen isotope composition of foram tests as a function of time for three deep-ocean core locations shown with ETP curve. (Based on Figures 2, 6, and 8, Imbrie, et al., 1984).

The integration of oxygen isotope data from numerous deep sea cores collected worldwide with the ETP curve was used to produce SPECMAP, a charting of predicted $\delta^{18}O$ excursions for a shallow deep sea stratigraphic section representing continuous sediment accumulation with no unconformities (Imbrie et al, 1984, P. K. Trabant, 2004, personal communication).

SPECMAP and Sequence Stratigraphy

Glacial growth and retreat is recognized as a primary cause of eustatic sea level variations over the shorter time intervals applicable to recent Cenozoic marine sedimentation. Variations in eustatic sea level and the rate of basinal subsidence (or uplift) together affect relative sea level, and ultimately the marine depositional environment. For the northern Gulf of Mexico, where recent sediment deposition is dominated by clastics derived from the Mississippi River, the result of fluctuations in relative sealevel are stratigraphic packages predicted by the EPR sequence stratigraphic model developed by Vail and Mitchum (Reading and Levell, 1996).

For deepwater marine areas of the northern Gulf of Mexico, clastic sediments consist mostly of blanketing, parallel-stratified hemi-pelagic and pelagic marine clays, chaotically-deposited clay-prone slope failure deposits, turbidites, and fine- to coarse-grained deltaic sediments (Stow et al., 1996, Galloway et al., 2000, K. J. Campbell, 2004, personal communication). Blanketing clays commonly form condensed sections in the deepwater environment during a relative sea level highstand, when distal areas are sediment-starved. The condensed section contains a maximum flooding surface (MSF) and is the lateral equivalent of the transgressive and highstand system tracts (TST and HST). Failure deposits are common in the northern Gulf of Mexico deepwater sediment column, and represent local or upslope sediment slope failures that occur primarily during a relative sea level fall.

Periods of glacial retreat are associated with relative highstands of sea level (eustatic sea level rise), and HST deposits such as condensed sections can be attributed to these interglacials. A direct relationship exists between $\delta^{18}O$ and stratigraphy because negative

excursions of $\delta^{18}O$ can also be attributed to interglacial periods, (P. K. Trabant, 2004, personal communication). This correspondence is the basis for the use of the $\delta^{18}O$/ETP chart (SPECMAP) as a means of assigning absolute ages to stratigraphic events in marine stratigraphic successions where the sedimentary record is complete (no unconformities related to erosion or to nondeposition). This relationship and the connection to orbital forcing are illustrated in Figure 53. Absolute ages assigned by this process are subject to the time lag errors noted by Imbrie et al. (1984). They indicate that error scales with estimated age BP, ranging between 2,000 years and 5,000 years up to about 800,000 years BP.

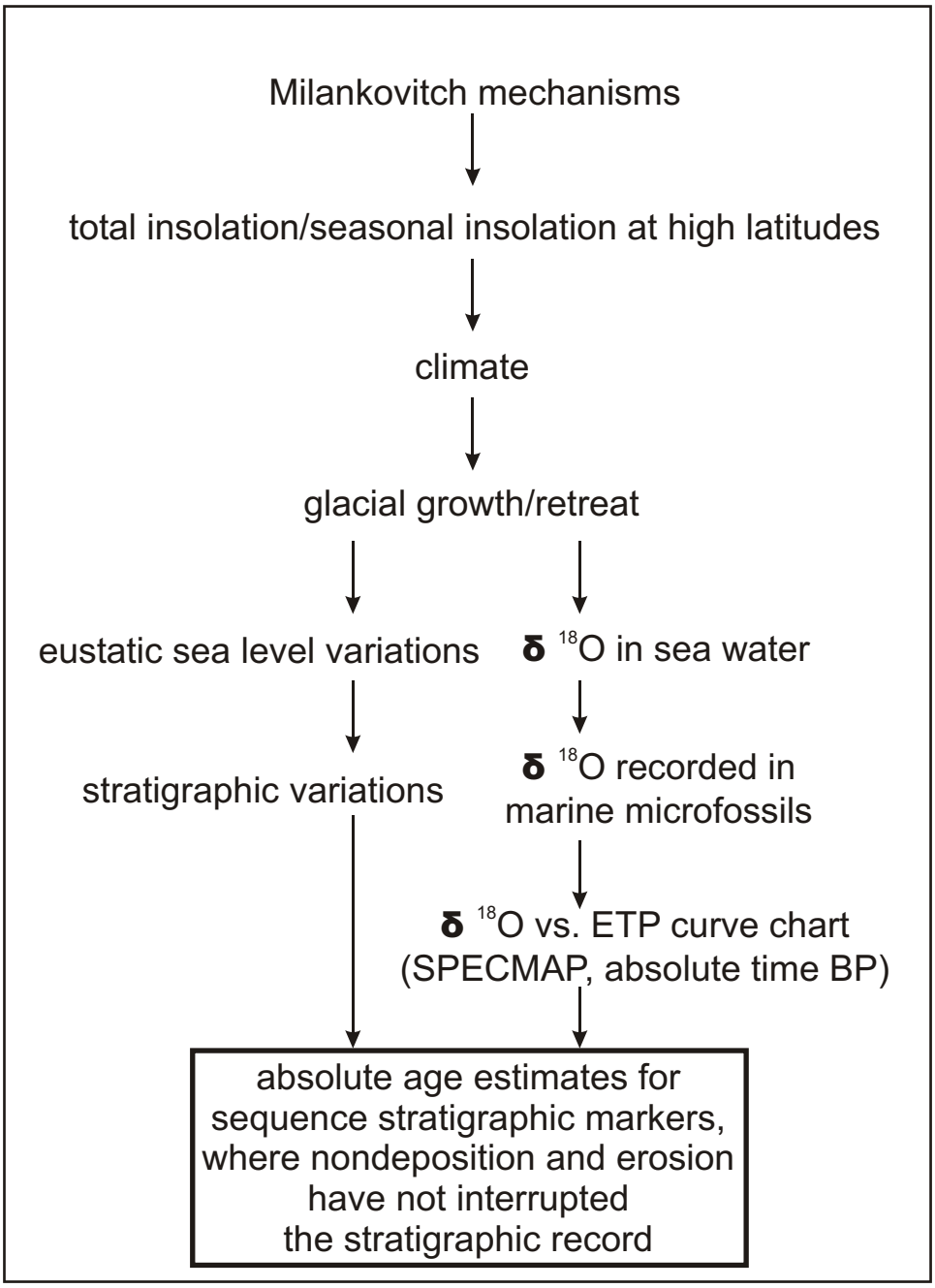

FIGURE 53: Relationships between Milankovitch mechanisms, climate, glaciation, $\delta^{18}O$, stratigraphy, and absolute ages.

VITA

Mr. Scott Ashley Wegner was born March 5, 1975, to Mrs. La Verna Ann Wegner and Mr. John Lee Wegner in Houston, Texas. His sole sibling is Ms. Amy Dawn Wegner. Scott Ashley Wegner received his primary education from Houston public schools. He graduated in June 1993, in the top ten percent of his class. His undergraduate education was undertaken entirely at Texas A&M University, where he earned the degree of Bachelor of Science in Geology in May 1999. His graduate education was also accomplished at Texas A&M University, where he earned the degree of Master of Science in Geology in May 2006.

Scott Ashley Wegner is employed as a practicing professional geologist with Fugro GeoServices, Inc., where he is a deepwater shallow geologic hazards interpreter and engineering-geologic analyst. He is an active member of the Association of Engineering Geologists, the American Association of Petroleum Geologists, and the Houston Geological Society. His permanent professional address is 6100 Hillcroft, Houston, TX, 77081. His email address is swegner@fugro.com.